Naval Surface Warfare Center
Dahlgren Division

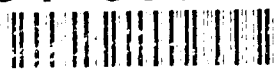# Technical Digest

September 1993

AD-A276 448

94-06538

Advanced Materials Technology

About the cover: Advanced materials enable modern systems such as spacecraft, submarines, ships and missiles to survive and operate in a variety of harsh environments. Designs formed with computer-colorized scanning electron micrographs are fibers (right) and the fracture surface of a matrix composite (center), from an investigation of phosphate bonding of silicon nitride ceramics and ceramic-matrix composites (article on page 16). Potential applications include engine parts, aerodynamic leading edges, and radomes.

*Naval Surface Warfare Center
Dahlgren Division*

Technical Digest

September 1993

2

Guest Editor's Introduction

Advanced Materials Technology

The ability of modern naval systems to withstand a wide diversity of harsh environments, from the depths of the oceans to the outer reaches of space, depends in large part on the development of new and advanced materials. Although progress in this technology has been more rapid over the last half century than at any time in recorded history, we are continually challenged by requirements for advanced materials with properties that will enhance operational characteristics such as range, speed, accuracy, response time, altitude, readiness, and operability. This issue of the *Technical Digest* describes some of the ways in which the Naval Surface Warfare Center (NSWC) Dahlgren Division is investigating new concepts, new methods of evaluation, and new applications.

The Dahlgren Division conducts full-spectrum research, development, test and evaluation (RDT&E), and fleet support on advanced materials and materials processes for application to ordnance and weapon systems. We emphasize various core technologies such as advanced ceramics, warhead materials, electrochemistry, polymer science, acoustic materials, composites, magnetostrictive materials, semiconductor materials, thermal management materials, radiation sensor materials, energetic materials, biotechnology, surface science, and nondestructive evaluation. Spin-off technologies for dual use are also actively pursued. This issue of the *Digest* includes articles on engineered materials, energetic materials, and the characterization of materials.

Engineered Materials

The field of engineered materials — that is, those materials designed specifically for a given application or class of applications — encompasses a broad spectrum of technologies with diverse applications. Materials such as plastics, lightweight alloys, composites, and ceramics play increasingly critical roles in every area of modern military technology. Plastics offer the advantages of low density, corrosion resistance, ease of fabrication, good electrical and thermal insulating properties, color selection or transparency, and in some instances, high damping characteristics and impact and shock resistance. A *Technical Digest* article by Hartmann et al. addresses the technology developed to tailor polyurethane properties so as to obtain a very wide range of acoustic properties in a known, controllable manner. These materials are used in coatings for underwater mines, submarines, and sonar domes. Commercial applications in the form of foams, injection molding, and rubber compounds have been found for these types of materials.

Ceramics and composite materials provide the means to overcome the extreme environments and challenging requirements encountered in space, in high-speed missile and aircraft structures, and in rocket propulsion systems. Our work in these areas has resulted in the development of mullite whiskers

3

and felt as reinforcements for radomes, engine parts, tactical missile launchers, and hot gas filtration systems. Talmy et al. discuss recent advances in low-cost methods of processing ceramic composites based on the development of phosphate bonding for the matrix material. The authors demonstrate that this approach applies not only to missile systems, but can also be used to develop building materials such as bricks, blocks, and tiles from fly ash, a waste product of coal combustion in electrical plants.

Since the mid-1940s, the Division has been extensively involved in RDT&E of advanced electrochemical power sources (batteries) for naval weapons. Virtually every naval weapon system requires electrical energy to perform one or more of the complex functions of target detection, fuzing, countermeasures, ignition, deployment, guidance, control, and propulsion. Over the years, we have co-developed with industry a number of advanced batteries for mines, missiles, projectiles, bombs, rockets, sonobuoys, and torpedoes, including those currently in the fleet. Smith and James present an article on recent advances in high-energy, rechargeable lithium power sources under development as an alternative for current state-of-the-art silver oxide/zinc cells used for underwater vehicle propulsion. These batteries are expected to increase significantly the range of these underwater vehicles.

One of our priorities is the development of new materials such as tungsten, aluminum composites, and tantalum for use in weapon systems. Tungsten is an important element of many high-strength superalloys used in projectiles and as preformed fragments in anti-missile warheads. Mansour and Vasanth have investigated W-Ni-Fe alloys, and discuss in their article the attributes of x-ray absorption fine-structure spectroscopy for determining the effect of composition in the corrosion characteristics of tungsten superalloys exposed to seawater simulation. They conclude that the corrosion products are similar to those of Fe_2O_3. The chemistry and structure of Ni in the corroded alloys are similar to those of metallic Ni, and the tungsten component of the alloy is least affected by the corrosion process. This finding will contribute to developing more corrosion-resistant superalloys.

Aluminum alloys have been the traditional choice of low-cost material for missile air frames, torpedo hulls and mines. Divecha et al. discuss the development of a low-cost process for producing large-diameter tubes of silicon carbide aluminum matrix composites, resulting in significantly increased strength and stiffness compared to conventional aluminum alloys. Because of its high density, tantalum is being investigated for possible use in explosively formed projectiles for warheads. J. Clark and Garrett elaborate on the role of processing in controlling the preferred orientation of grains. They describe the development of an advanced processing schedule that produces tantalum with strong crystallographic orientation to achieve optimum material performance.

The Division's early research in magnetic materials focused primarily on magnetic influence sensors for mines. The resulting materials acquired "NOL" names (for Naval Ordnance Laboratory, now the Division's White Oak Detachment) such as ORTHONOL, PARABONOL, THERMONOL, and BISMANOL. From this rapid evolution of new materials came new magnetometers, ordnance locators and magnetic amplifiers. This early work also resulted in the development of the soft magnetic materials used in such military and commercial applications as electronics, transformers, motors, signal processors, memories, recorders, and sensors. Some later R&D efforts are just now starting to mature, with the potential of sweeping advances.

An article by A. E. Clark describes a new generation of magnetic materials with application to military sensors such as sonar transducers and magnetometers, as well as commercial sensors used for the precise measurement of acceleration and strain. These new magnetostrictive materials also provide an experimental basis for studying the emerging technology of Chaos, or the control of Chaos in complex systems. One immediate spinoff of this technology is the potential control of chaotic heart arrhythmia.

4

The rapidly expanding field of electronic circuitry presents new opportunities for innovative materials research. The growth of fluorides on silicon wafers, for example, is receiving considerable attention for possible use as insulating layers. Chu et al. describe the results of studies on the growth of BaF_2 on oriented silicon wafers in a molecular beam epitaxy apparatus under ultrahigh vacuum conditions. They found that the quality of the epitaxial insulating film is a direct result of the interatomic interactions in the first few atomic layers of fluoride deposition.

The final article in this section deals with research conducted by Rish and Pham to develop liquid crystal for thermal control of insulated suits for Navy divers. The authors show that liquid crystal valves allow the thermal conductivity of the suit's insulation to be varied depending on the ambient water temperature and the diver's exertion level. This approach effectively insulates the diver in extremely cold ambient temperatures, but provides an outlet (valve) for excess heat in warm temperatures and during high levels of exertion, thus allowing the diver to remain under water longer.

Energetic Materials

After World War II, the Naval Ordnance Laboratory, White Oak assumed responsibility for the development, testing and evaluation of explosive molecules and compositions. Our chemical synthesis groups have been responsible for the synthesis, scale-up and evaluation of a number of new explosive molecules. Many of these molecules augment standard explosives such as HMX, RDX and TNT, providing special capabilities not found elsewhere. The most important of these are HNS, TATB, DIPAM and DATB. Developed during the 1950s and 1960s, each has been used in subsequent explosive compositions developed for use by the Navy, other military services, NASA, and the Department of Energy. HNS (hexanitrostilbene), for example, was first used in an explosive composition developed for use in NASA's Apollo moon missions.

The early compositions belonged to the HBX family of meltcast, TNT-based explosives. HBX-3, the first explosive composition developed in NOL, is used as the main charge in many Navy underwater mines. H-6, developed to provide maximum airblast and fragmentation, is used in Mk 80 series bombs, demolition charges, mines, and warheads for missiles such as Talos, Terrier, Sparrow, Bullpup, the Standard Missile, and Tomahawk. PBXN-103, the first castable PBX explosive, consists of aluminum/ammonium perchlorate

with an energetic plastic binder. It was developed to increase underwater shock energy and energy in the explosive bubble caused by the detonating gases. The second castable PBX was PBXN-105, which is used as the explosive fill in the Navy's Mk 48 heavyweight torpedo.

New nanostructure materials are being investigated to further enhance underwater explosive performance. Beard et al. discuss one such investigation that resulted in increasing the energy release rate from an additive fuel by using nano-size aluminum particles that are consumed in fractions of microseconds. Typical aluminum particles, on the other hand, measure tens of microns in size and require a number of microseconds to be consumed in a detonation.

As explosive compounds become more energetic they tend to become more sensitive. We therefore continue to explore methods of increasing the energy while decreasing the sensitivity of these compounds. An article by Bardo on intercalated materials demonstrates theoretically that high-performance explosive crystals can be designated with direction shock sensitivity properties identified with specific crystal axes. Correct use of this directional sensitivity can lead to less sensitive and higher energy compounds.

Characterization of Materials and Environmental Effects

Frequently, advances in materials development and utilization precipitate from concurrent advances in the ability to analyze materials. The past decade has not only

5
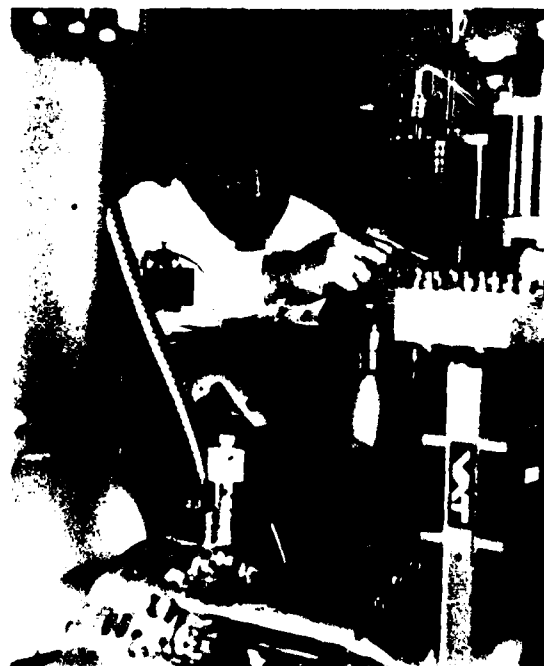
brought new technologies capable of analyzing chemistry and structure down to the atomic level, but it has also provided tremendously expanded utilization of older technologies via computer automation. The expansion in both sophistication and availability of advanced materials characterization technologies is slowly peeling away the layers of the mysterious "black art" often associated with materials synthesis or performance. Occasionally new materials characterization techniques show that previously held assumptions concerning chemistry or structure were overly simplistic or invalid. Several *Digest* articles highlight the close relationship between advanced materials characterization technologies and progress in materials synthesis and utilization.

Liu and Vernon describe an electromagnetic technique for nondestructive evaluation of carbon-carbon composites used in naval strategic weapon systems. The capability of carbon-carbon composites to retain excellent mechanical properties and dimensional stability in hostile environments makes them prime candidates for future space structures. Because the technique allows anomalies to be detected early in the material processing stage, corrections can be made to achieve the desired mechanical properties in braided, thin-wall tubes for satellites.

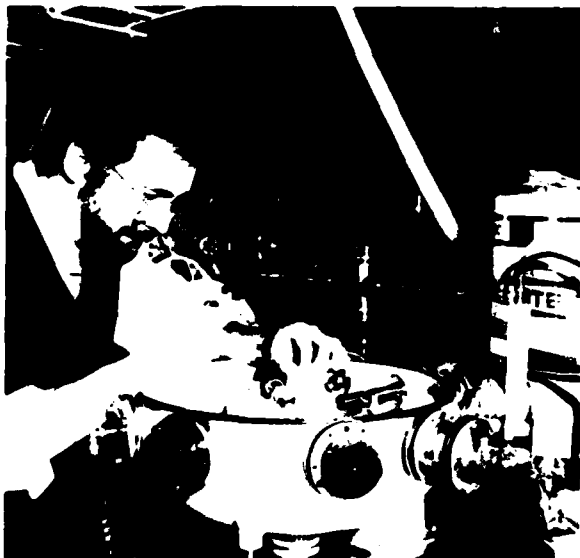Environmental effects can degrade materials whether they are exposed to the thin atmosphere of space or the corrosive environment of the ocean. Several Digest articles address these environmental effects on materials. For example, satellite flights by NASA in the early 1980s revealed that many polymers and some metals are susceptible to surface recession from exposure to high fluence levels of atomic oxygen. In the first article, Foltz describes the effects of oxygen on a carbon-carbon matrix

material and a space mirror made of foam metal, both of which were flown on space shuttle flight STS-46 in July 1992. The samples were mounted on a retrievable platform and were returned to Earth in August 1992. Postflight examination revealed that carbon-carbon composites are indeed susceptible to atomic oxygen attack. In another example, Land et al. discuss the use of the Division's Van de Graaf accelerator as a valuable tool for ion beam analysis of surface and near-surface material samples. They subjected mirrors intended for space application to a simulated space environment. Ion-beam analysis showed their susceptibility to damage.

Relative to the ocean environment, Jones-Meehan et al. present case histories of microbiologically influenced corrosion of copper and monel piping material used in seawater piping systems on surface ships. Using environmental scanning electron microscopy, the authors discovered that an aerobic, copper-tolerant bacterium (isolated from copper-containing coating) produced large amounts of extracellular polymer that had metal binding ability, thereby resulting in a fivefold increase in the corrosion rate of Cu metal. They also found that anaerobic bacteria (sulfate reducers) selectively dealloyed nickel from copper alloys, leaving spongy, copper-rich pits. This research is expected to pave the way for developing improved, corrosion resistant materials and protective coatings.

In the final article, Chakrabarti et al. discuss the development of a very sensitive dosimeter made from calcium sulfate. This dosimeter may be used to measure an individual's exposure to a nuclear radiation environment resulting from nuclear powered ships and submarines. The authors point out that its robustness offers the potential to perform battlefield dosimetry.

Acknowledgments

The Guest Editor

CARL E. MUELLER, head of the Dahlgren Division's Weapons Materials Division, holds a B.S. degree in chemical engineering from Clarkson University, Potsdam, New York, and M.S. and Ph.D. degrees in chemical engineering from the University of Maryland. He joined the White Oak Detachment (then the Naval Ordnance Laboratory) as a chemical engineer in 1961. Subsequently he gained extensive experience in the fields of electrochemistry, corrosion technology, materials science and engineering, systems analysis, and operations research. He was extensively involved in research, development, test and evaluation of advanced power sources for mines, missiles, sonobuoys, and torpedoes. Under his leadership as head of the Electrochemistry Branch from 1980 to 1987, the Division became lead laboratory for naval electrochemistry technology. During that period he also served as 6.2 Block Program Principal for Electrochemistry Technology, Associate for Development in the Research and Technology Department, Strategic Business Unit Manager for Electrochemistry Technology, and Program Manager for Dahlgren Division's Small Business Innovation Research (SBIR) Program. He received the Navy Meritorious Civilian Service Award in 1984 for technical and managerial contributions to the field of electrochemistry. In 1985, he was selected for the Navy Science and Technology Exchange Program, in which he served as SBIR Program Manager for the Department of the Navy, reporting to the Assistant Secretary of the Navy for Research, Engineering and Systems. He joined the staff of the Office of Chief of Naval Research (OCNR) in 1987 as Navy SBIR Program Manager and Special Assistant for OCNR Small Business Programs. For his performance as Program Manager, he received a Congressional Citation and the Navy Meritorious Civilian Service Award. Since 1988 he has headed the Weapons Materials Division.

Polyurethane Technology Offers Wide Range of Acoustic Properties

Bruce Hartmann, Gilbert F. Lee, and John D. Lee

Scientists at the Dahlgren Division's White Oak Detachment have developed the technology to tailor the properties of polyurethanes to obtain a very wide range of acoustic properties in a known, controllable manner. For example, the sound absorption in polyurethanes has a maximum value that can be designed, by varying molecular weight or chemical constituents, to occur anywhere from 0.1 Hz to 1 MHz. This range covers applications from motor mounts to submarine hull coatings. In addition, the material can be formulated to have very high absorption or very low absorption. High sound absorption is needed for coatings on surface ships, submarines, and mines, while low sound absorption is needed for sonar windows and transducer potting compounds. Finally, materials can be designed to absorb over a wide frequency range or be tuned to a particular frequency band.

Introduction

The goal of this work is to relate the acoustic properties of polymers to their molecular structure. Acoustic properties are of importance to the Navy in numerous applications, and most often it is a polymer that is used. The different applications lead to a variety of requirements. In some cases, such as for a coating on a surface ship, submarine, or mine, high sound absorption is needed. In other cases, such as for a sonar window or transducer potting compound, low sound absorption is needed. While these two problems sound different, they can both be solved with an understanding of the relation between the molecular structure of polymers and their acoustic properties. One reason polymers are used in these applications is that their properties vary over a wide range. This advantage also creates a problem in that it is difficult to know which polymer to choose among the thousands on the market. An additional problem is that most of these polymers are proprietary materials. For these reasons, it is vital that the Navy be able to specify the acoustic properties of polymers in terms of their molecular structure.

This article begins with a description of the acoustic properties, describes the molecular structure of the polymers, and finally demonstrates the relation between structure and properties. The polymers studied are polyurethanes because their molecular structure can be varied to provide an extremely wide range of properties.

8

Acoustic Properties

This section considers acoustic properties of polymers from a phenomenological point of view. In other words, we focus on what can be determined about acoustic properties without considering molecular structure.

The first step is to recognize that acoustic properties can be expressed either in terms of sound speed and absorption, or equivalently, in terms of complex modulus. In the sound speed and absorption representation, there are two types of sound speeds: longitudinal (c_l) and shear (c_s). Associated with each of these sound speeds is an absorption $(\alpha_l$ and $\alpha_s)$. In the complex modulus representation, there are two complex moduli, bulk $(K^* = K'+iK'')$ and shear $(G^* = G'+iG'')$. The relations between these two representations are well established and it is a matter of convenience as to which to use. To a first approximation, sound speed is proportional to the square root of the real part of the modulus and sound absorption is proportional to the ratio of the imaginary part to the real part, G''/G', which is referred to as the loss factor.

For this work, measurements of complex modulus were made using a resonance device in which a sample in the shape of a bar is excited into resonance at various harmonics. Typically, four or five resonant peaks can be determined in a range of 1.5 decades centered at about 1 kHz. The real (G') and imaginary (G'') parts of the complex shear modulus (G^*) are calculated at these resonant frequencies. The measurements are repeated as a function of temperature. Time-temperature superposition is then used to shift the measured data to form a master curve of G' and loss factor over approximately 20 decades of frequency at a reference temperature of 25°C.

Typical data for a polyurethane is shown in Figure 1. Qualitatively, the modulus increases from a lower value at low frequency to a higher value at high frequency with a transition between the two centered at a transition frequency. The loss factor goes through a maximum at the transition frequency. It has been well established that this behavior is due to the glass transition occurring in the polymer.[1] At the glass transition, large segments of the polymer chain become free to move; this transition from glassy behavior to rubbery behavior affects many physical properties of polymers, including volume expansivity, specific heat, and mechanical properties. The nature of this transition is significant because many studies have been done on the effect of the glass transition on other properties, and the conclusions reached will carry over to the acoustic case.
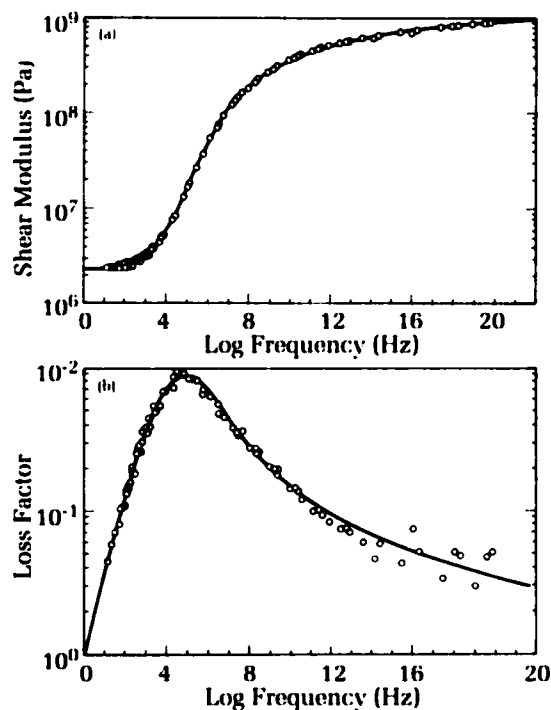
Figure 1. Typical dynamic mechanical data for a polyurethane. (a) Shear modulus vs frequency; (b) Loss factor vs frequency.

As shown in Figure 1, the glass transition dominates the acoustic behavior of polymers. The low frequency value of the modulus is referred to as the rubbery modulus and the high frequency value as the glassy modulus. The loss factor (proportional to absorption) has a glass transition peak at 100 kHz in this example. For applications in which high absorption is desired, such as a hull coating, the transition frequency should be near the application frequency. Conversely, if low absorption is desired, such as for a sonar window, the transition frequency should be different from the application frequency.

Another qualitative feature of the data worth noting is that the transition is very broad, covering many decades of frequency, and asymmetrical, being skewed to high frequency.

Analytical Model

It is an advantage to describe the qualitative features of the glass transition using an analytical model. With a model, acoustic properties can be represented with a few parameters, which then can be used in computer prediction of acoustic performance and in interpolating properties that were not actually measured. There are many analytical models to choose from in the literature. However, it is advantageous to select a model whose parameters are

9

COMPLEX MODULUS AND LOSS FACTOR

Polymers have some of the characteristics of an elastic solid and some of the characteristics of a viscous liquid, and they are referred to as viscoelastic materials. For such materials, the modulus (ratio of stress to strain) is not a simple constant of proportionality as it is for an elastic solid. There is a component of the strain in phase with the applied stress and a component out of phase. Such behavior is described by making the modulus complex. For example, if a shear stress is applied to a viscoelastic material, the shear modulus is given by

$$G^* = G' + iG'',$$

where the superscript * identifies the modulus as a complex number, G' is the real part of the modulus, and G'' is the imaginary part of the modulus. When a periodic stress (such as a sound wave) propagates through a viscoelastic material, some of the energy is absorbed as a result of the phase lag between stress and strain. A detailed analysis of this process shows that the energy absorption depends on the ratio G''/G', known as the loss factor. Thus, if $G'' = 0$, the material is an elastic solid with a purely real modulus and no absorption of sound energy. For finite G'', the material is viscoelastic with a complex modulus and absorption of sound waves.

10

related to the molecular structure of the polymer rather than being curve-fitting parameters.

An analytical model of the glass transition known as the Havriliak-Negami equation was found to represent the master curve data generally within the accuracy of the measurements. The qualitative features of the model are a rubbery modulus at low frequency, G_0, a glassy modulus at high frequency, G_∞, and a transition between the two limiting values at a transition frequency. It is theoretically preferable to express the transition frequency in terms of the equivalent relaxation time associated with it, $\tau = 1/2\pi f$. The width of the transition is governed by a parameter α, with values between zero and one, and the asymmetry is governed by a parameter β, also with values between zero and one. The specific form of the model is

$$(G_0-G_\infty)/(G^*-G_\infty) = (1+(i\omega\tau)^\alpha)^\beta \qquad (1)$$

where $\omega = 2\pi f$ is the circular frequency of the measurement. The complex modulus measurements can then be summarized in terms of five parameters: G_0, G_∞, τ, α, and β.

An example of the fit of the analytical model to the typical polyurethane experimental data is shown in Figure 1. The solid lines in this figure were calculated using Equation (1). As can be seen, the fit is very good. The high frequency modulus, G_∞, is about 1 GPa, a value typical of most polyurethanes. The low frequency modulus, G_0, is about 2 MPa. For polyurethanes in general, this value ranges from 1 to 10 MPa. The loss factor peak occurs at about 100 kHz, corresponding to a relaxation time of about 1 μs. This value varies over many decades of frequency for other polyurethanes. The value of α for the data in Figure 1 is 0.6. Other polymers vary from 0.3 to 0.8. Finally, β is 0.04 and varies from 0.0003 to 0.5 in other systems.

Glass Transition Temperature

The characteristic temperature at which the glass transition occurs is known as the glass transition temperature, T_g. The characteristic time at which the transition occurs is the relaxation time τ from Equation (1). Theoretically, we expect these two parameters (T_g and τ) to be related since they are both measures of the glass transition. As discussed earlier, τ is determined from the data obtained in the complex modulus measurement. The glass transition temperature is determined using a differential scanning calorimeter (DSC) measurement of the heat flow into a sample under controlled heating conditions. We postulated that these two independent parameters, determined in completely different manners, should be related by an Arrhenius relation between the log of τ and the reciprocal glass transition temperature.

To verify this assumption, τ and T_g were evaluated for 20 different polyurethane systems of varying molecular weight, isocyanate type, polyglycol type, chain extender type, and concentration of hard segment. The Arrhenius plot is shown in Figure 2. There is a good correlation, with $r^2 = 0.91$. The activation energy calculated from the slope of this line is 118 kJ/mol, a reasonable value for the glass transition of a polymer. Other relations that have been shown to hold for T_g, such as dependence on molecular weight and molecular structure, can now be applied to acoustic properties as well.
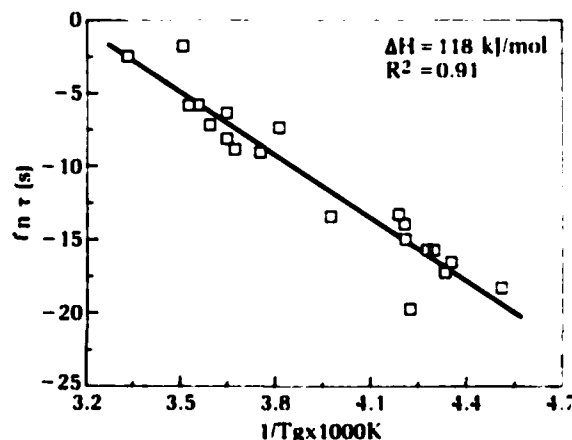
Figure 2. Log relaxation time vs reciprocal glass transition temperature for polyurethanes.

The correlation between T_g and τ is used in the tailoring of polymers for a particular acoustic application in the following manner. An acoustic designer may need a polymer with a loss factor maximum at a particular frequency, which is related to τ. The chemist who is asked to synthesize the polymer may not understand how τ is related to molecular structure, but is very familiar with T_g. Therefore, this correlation bridges the chasm between acoustic designer and chemist.

Molecular Structure

This section presents the molecular structure of polymers from the synthesis point of view. In other words, we focus on what can be determined without considering acoustic properties directly.

11

Polyurethanes are alternating block copolymers made up of soft segments of aliphatic chains from a polyglycol and hard segments of groups from a diisocyanate and a chain extender. Since the soft and hard segments are chemically dissimilar, they tend to be incompatible and thus separate into different phases. Separate glass transitions can occur in each phase, and either one or both phases can be crystalline. Microphase separation can occur, and the hard segment can be crystalline or amorphous. As will be shown below, we have found that the presence or absence of hard-segment crystallinity is the dominant factor in determining the acoustic properties of polyurethanes.

Polyurethane chemistry will be illustrated with a particular polymer system. Most of the systems to be discussed will be variations of this basic system. The basic polyglycol is poly (tetramethylene ether) glycol (PTMG)

$$HO-[-(CH_2)_4O-]_n-H.$$

The basic diisocyanate is 4.4'-diphenylmethane diisocyanate (MDI)

$$OCN-C_6H_4-CH_2-C_6H_4-NCO.$$

The basic chain extender is 1.4-butanediol (BDO)

$$HO-(CH_2)_4-OH.$$

Four molecular weights of PTMG (nominally 650. 1000. 2000. 2900) were used to react with MDI to form prepolymers. Typically, three moles of MDI were used to react with one mole of polyglycol. The prepolymers were then chain extended with BDO. The isocyanate index of the mixture was 1.05, which ensures that there is a five percent excess of isocyanate for cross-linking during the cure.

One variation of the above basic system that was investigated[2] was replacing MDI with methylene bis (4-cyclohexylisocyanate) (H$_{12}$MDI)

$$OCN-C_6H_8-CH_2-C_6H_8-NCO.$$

Although the molecular structures of MDI and H$_{12}$MDI are similar. H$_{12}$MDI comprises a mixture of three geometric isomers: trans-trans, cis-trans, and cis-cis. The presence of these three geometric isomers tends to prevent hard segment crystallinity in the H$_{12}$MDI-based polymers. The hard segment in MDI-based polyurethanes, on the other hand, is crystalline. Hard segment crystallinity will be shown later to have a significant effect on acoustic properties.

Another variation of the basic system considered[1] was replacing PTMG with polypropylene glycol (PPG)

$$HO-[-CH_2CH(CH_3)O-]_n-H.$$

The presence of the pendant methyl group in PPG inhibits hard-segment crystallinity in PPG-based polymers. This system thus represents another technique for reducing the degree of hard-segment crystallinity in comparison with the basic system.

Acoustic-Chemistry Relation

In this section we describe the increased insight into the problem when we know the relation between acoustics and chemistry.

A determination of hard-segment crystallinity is made using a DSC, which measures the heat flow into a sample under controlled heating conditions. In the DSC thermograms shown in Figure 3, the top plot is the basic polyurethane. In addition to the glass transition that gives rise to the desirable acoustic properties, hard-segment melting can also be seen. In the bottom plot, the polymer is the same except that MDI has been replaced with H$_{12}$MDI. Due to the three geometric isomers, hard-segment crystallinity is prevented, as is obvious from the lack of a melting peak.

The shear modulus of these crystalline and non-crystalline polymers is shown in Figure 4. Crystallinity in the MDI polymer has raised the rubbery modulus by about a factor of ten, while having little effect on the glassy modulus.

The loss factor of the same polymers is shown in Figure 5. The non-crystalline polymer has a high loss peak, while the crystalline polymer has a low loss peak. This is a general
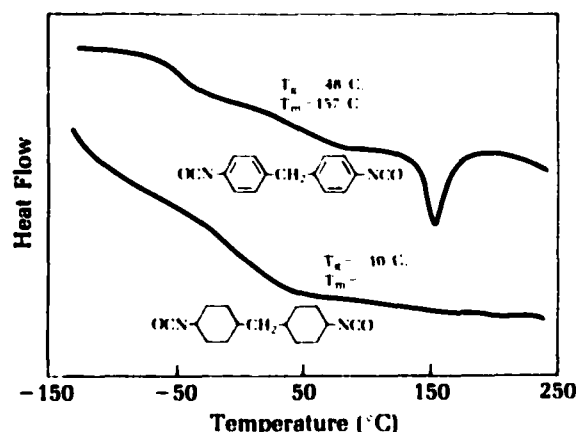
Figure 3. DSC thermograms for PTMG1000/ BDO polyurethanes synthesized with different isocyanates.

12
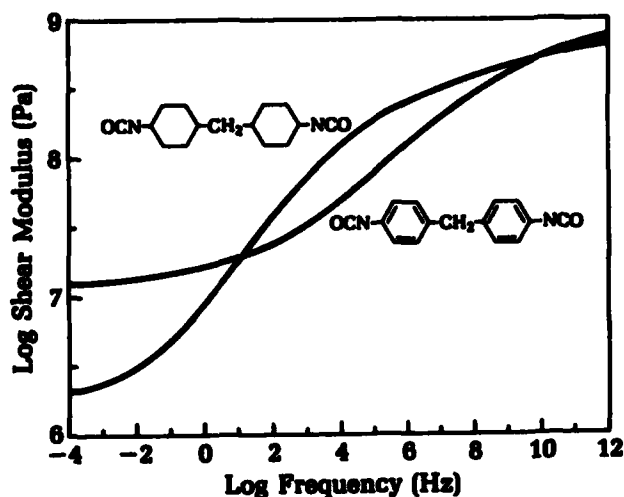
Figure 4. Shear modulus for PTMG1000/BDO polyurethanes synthesized with different isocyanates.

Figure 5. Loss factor for PTMG1000/BDO polyurethanes synthesized with different isocyanates.
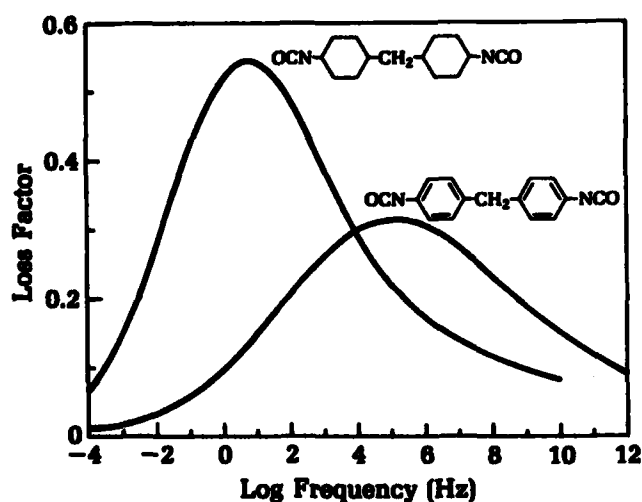
relation: whenever the rubbery modulus is low, the loss peak will be high; when the rubbery modulus is high, the loss peak will be low. This behavior has been observed for a variety of compositions.

It was concluded that the absence of hard-segment crystallinity is the dominant factor in producing a high-loss peak; the method by which crystallinity is prevented from occurring is not relevant. To verify this assumption, a variation of the basic crystalline polyurethane was prepared in which the degree of crystallinity was reduced not by changing the isocyanate, but by changing the polyglycol. PTMG was replaced with PPG. In this case, the pendant methyl group inhibits crystallinity. There is a small amount of crystallinity, but much less than in the PTMG polymer. The same qualitative behavior, namely a high loss factor, is shown in Figure 6.

Up to now only the height of the loss peak has been considered. Now let us consider the frequency at which the peak occurs. As shown before, τ determines this location and is correlated with T_g (Figure 2). Since T_g varies with molecular weight, we expect that τ will likewise vary with molecular weight. Verification of this assumption is shown in Figure 7. The loss peak can be moved anywhere from 0.1 Hz to 1 MHz by increasing the molecular weight.

Conclusions

We have developed a methodology to tailor the properties of polyurethanes to meet requirements for applications that include hull coatings, sonar windows, transducer potting compounds, and motor mounts. This ability to design material properties not only allows us to

13
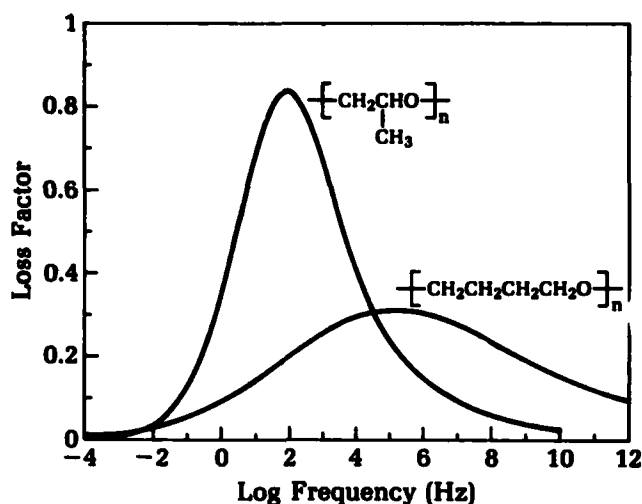
Figure 6. Loss factor for MDI/BDO polyurethanes synthesized with different glycols.

Figure 7. Loss factor for polyurethanes of different molecular weight.
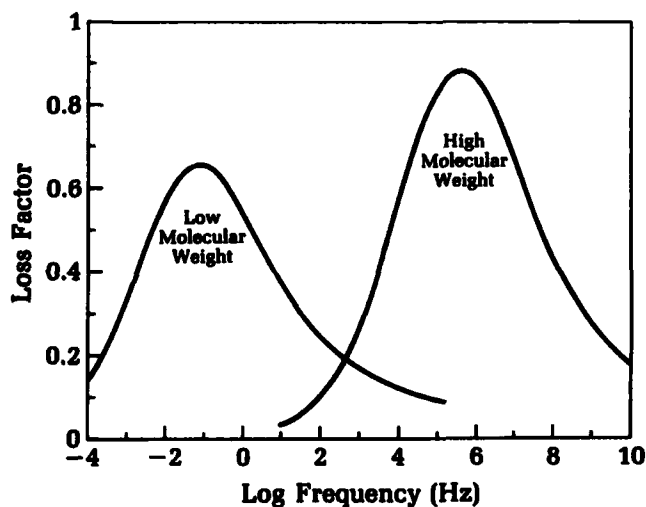
optimize material performance, but eliminates the need for proprietary materials.

Based on the analysis conducted here, the following specific conclusions were reached:
- Glass transition temperature and relaxation time are correlated. Glass transition temperature depends on molecular structure, and relaxation time determines the frequency at which the loss factor peak occurs. The correlation of glass transition temperature and relaxation time then allows us to relate peak location to molecular structure. For example, based on the known variation of glass transition temperature with molecular weight, the peak can be moved anywhere from 0.1 Hz to 1 MHz. Materials with loss peaks at low frequency are required for motor

mounts, while materials with loss peaks at high frequency are needed for hull coatings.
- Non-crystalline polymers have a high, narrow loss peak, while crystalline polymers have a low, broad loss peak. Because the degree of crystallinity depends on molecular structure, the height and width of the loss peak are determined by molecular structure. For example, the presence of pendant groups inhibits crystallinity and produces a high loss factor. Hull coating materials require a trade-off between high loss and broad band behavior.
- Crystallinity raises the rubbery modulus by about a factor of ten with little effect on the glassy modulus. High rubbery modulus is needed in order to minimize

14

the effect of static load on the performance of motor mounts.

Acknowledgment

References

1. Hartmann, B., "Relation of Polymer Chemical Composition to Acoustic Damping," *Sound and Vibration Damping With Polymers*, R. D. Corsaro and L. H. Sperling, eds., ACS Symposium Series 424, American Chemical Society, 1990, Ch. 2.
2. Lee, J. D., Lee, G. F., and Hartmann, B., "Damping Properties of Aliphatic Polyurethanes from Methylene bis(4-cyclohexyl isocyanate)," *Proceedings of Damping '91*, Vol. III, p. GDF-1, Aug 1991.
3. Hartmann, B. and Lee, G. F., "Dynamic Mechanical Relaxation in Some Polyurethanes," *Journal of Non-Crystalline Solids*, Vol. 131, 887 (1991).

The Authors

BRUCE HARTMANN received a Ph.D. degree in physics from American University. He has been a scientist at the White Oak Detachment since 1960 and has been the head of the Polymer Physics Group since 1975. His specialty is structure-property relations in polymers, particularly the acoustic properties of polyurethanes. He has published over 50 papers in the open literature and a like number of government publications. He is a member of the American Physical Society, the Society of Rheology, and the Acoustical Society of America. Among his awards are the Navy Meritorious Civilian Service Award, the Technology to Sea Excellence Award, and the Independent Research Excellence Award.

GILBERT F. LEE received an M.S. degree in chemical engineering from Tufts University. He has been employed at White Oak since graduation in 1974 and is a member of the Polymer Physics Group specializing in the dynamic mechanical characterization of polymers. He has published 25 papers in the open literature and 10 government publications. Among his awards are the Technology to Sea Excellence Award and the Independent Research Excellence Award.

JOHN D. LEE received a B.S. in chemical engineering from the University of Maryland and has been employed at White Oak since his graduation in 1977. He is a member of the Polymer Physics Group, specializing in the synthesis and development of polyurethanes for dynamic mechanical applications. He has published 13 papers in the open literature and 8 government publications. He is a member of the American Chemical Society. Among his awards are the Outstanding Young Scientist of the Year Award, the Technology to Sea Excellence Award, and the Independent Research Excellence Award.

Development of Phosphate-Bonded Silicon Nitride Ceramics and Ceramic-Matrix Composites

I. G. Talmy, C. A. Martin, D. A. Haught, A. H. Le, and A. E. Janovsky

The preparation of nonoxide ceramics (nitrides, carbides, etc.) and ceramic-matrix composites normally requires expensive methods such as hot pressing or hot isostatic pressing. Phosphate bonding offers a low-temperature, pressureless processing technique for such materials. Phosphate-bonded ceramics can be prepared at temperatures below 1000°C and used at much higher temperatures. Silicon nitride monolithic ceramics containing Al, B, Si, and Zr phosphates as binders have been developed at the Naval Surface Warfare Center, Dahlgren Division. Ceramic composites were also prepared using a variety of ceramic whiskers and fibers with phosphate-bonded Al_2O_3 and Si_3N_4 matrices. The mechanical, thermal, and electrical properties and environmental stability of the materials were characterized. The flexural strength of Si_3N_4 ceramics ranged from 40 to 95 MPa, and the strength of composites ranged from 30 to 120 MPa, depending on composition. All the materials had good water stability and exhibited low and thermally stable dielectric constant and loss tangent. While not as strong as conventionally processed Si_3N_4, phosphate-bonded ceramics are suitable for many military applications including engine parts, radomes, and antenna windows.

Introduction

Numerous problems in weapons systems, industrial processes, and consumer goods can be solved using ceramic materials because of their high thermal stability, wear resistance, hardness, and stiffness. However, the broad application of ceramics is substantially limited by the high processing costs. Most advanced ceramics, particularly nonoxide ceramics, require complicated processing, including the use of very high temperatures and pressures to prepare parts, thus resulting in high cost. A major thrust in the ceramic community is the search for less expensive methods of preparing ceramics, such as chemical bonding routes.

Chemical bonding techniques are based on the formation of strong bonds as the result of low-temperature (room temperature to a few hundred degrees C) chemical reactions. These reactions take place *in situ* during processing. The most common chemical bonding technique is based on the formation of hydrates, as in cements. Another possible technique is based on the formation of metal phosphates.

16

Phosphate bonding has been used for many years in manufacturing conventional refractories, protective coatings, and high-temperature adhesives. Phosphates can be formed in ceramics by direct reaction between selected oxides and phosphoric acid (H_3PO_4), or by the addition of a solution of phosphate hydrates which decompose during firing and bond with the particles in the body. Aluminum, chromium, boron, zirconium, and other phosphates have been reported in the literature.[1-4] Many metal phosphates have an attractive combination of properties, including high thermal stability (up to 2000°C) and strength, low thermal expansion, and good chemical resistance.

Phosphate bonding can be particularly useful for the preparation of nonoxide ceramics such as silicon nitride, silicon carbide, and boron nitride. Nonoxide ceramics are currently being developed for many applications because of their high strength, toughness, hardness, and special thermal and electrical properties. However, due to the highly covalent nature of the atomic bonding and the resultant low diffusion rates, they are difficult to prepare fully dense by inexpensive techniques such as pressureless sintering. Ordinarily, techniques such as hot pressing or hot isostatic pressing (HIP) are used. Pressureless sintering of nonoxide ceramics can be accomplished by using oxide additives which form low melting liquid phases, but these phases deteriorate high-temperature properties. Phosphate bonding techniques can provide a means for low-cost, low-temperature processing of nonoxide ceramics in applications where their very high-strength potential (750 to 1000 MPa) is not required. Although phosphate bonding does not result in fully dense, high-strength nonoxide ceramics, it allows exploitation of their unique properties, e.g., electrical. For example, silicon nitride (Si_3N_4) has dielectric properties (low and thermally stable dielectric constant and loss tangent) suitable for advanced radome applications.

Phosphate bonding can also be very useful for the preparation of both continuous and discontinuous fiber ceramic composites. Such composites are most commonly produced by hot pressing or HIP, which are expensive, and in addition, high processing temperatures may be detrimental to fibers and may also create problems with the fiber/matrix interface.

Phosphate bonding allows the preparation of continuous fiber ceramic composites by well developed techniques used in the polymer matrix composite field. The general concept is the same: a continuous tow or cloth is infiltrated with a liquid or paste matrix precursor, which later solidifies. In the case of phosphate-bonded ceramics, the matrix precursor is a *mixture of ceramic particles and phosphoric acid or phosphate hydrate solution instead of a* liquid polymer. The temperatures needed to cure phosphate binders are in the range of room temperature to 300°C, not that different from the temperatures used in the polymer field. A subsequent firing at up to 900°C may be employed depending on the application. Layup and shape-forming methods such as vacuum bagging, pressing, and autoclaving are all applicable to phosphate-bonded composites.

This article describes the results of an ongoing project investigating the application of phosphate-bonding techniques in the preparation of monolithic and discontinuous fiber reinforced Si_3N_4 ceramics as well as continuous fiber ceramic composites with oxide and nonoxide fibers and various phosphate matrices.

Monolithics and Discontinuous Fiber Composites

This section describes the experimental procedure for the preparation and testing of aluminum, boron, and zirconium phosphate-bonded silicon nitride ceramics, both monolithic and composites, reinforced with whiskers and platelets. Discussion of the material properties follows.

Experimental Procedure

Silicon nitride powder of 97.8 percent purity, 2 percent oxygen, 90 percent alpha phase, and particle size 0.7 μm was used in this study. The phosphate phases were formed in the materials as a result of the reaction of aluminum oxide (alumina, Al_2O_3), boric acid (H_3BO_3), and zirconium oxide (zirconia, ZrO_2) with phosphoric acid. The powders used in the experiments were 0.3 μm alumina (99.99 percent purity, alpha phase), 0.05 μm alumina (99.99 percent purity, mixed gamma and alpha phases), boric acid (99.99 percent purity), and zirconia powders with surface area 3.2 and 22 m²/g. Discontinuous reinforcements used were Si_3N_4 and SiC whiskers from Tateho, grades SNW1-S and SCW1-S-105, respectively, and SiC platelets from American Matrix. The platelets were -375 mesh, with an aspect ratio of ten. The phosphoric acid was 85 weight percent concentration, 99.99 percent purity.

Starting materials were combined in proportions to form 20 to 30 volume percent aluminum phosphate ($AlPO_4$), boron phosphate (BPO_4), and zirconium phosphate (ZrP_2O_7) in Si_3N_4 ceramics during firing. The binder content was selected because it resulted in the highest strengths in a previous experiment.[5] Five compositions in the Al-B phosphate system were also prepared with the following $AlPO_4$:BPO_4 ratios: 100:0, 75:25, 50:50, 25:75, and 0:100. (The desired composition is used in

17

this article as nomenclature, regardless of the actual phase composition achieved.) Each batch was mixed by first combining the Al_2O_3, H_3BO_3, or ZrO_2 with H_3PO_4, and then adding Si_3N_4. For comparison, ceramics were also prepared from a mixture of silicon nitride with 25 weight percent H_3PO_4. All raw mixtures were sieved through a 500-μm screen. Specimens of size 5 x 5 x 60 mm were pressed at 50 to 100 MPa in a steel die and fired at temperatures up to 900°C in air.

For whisker- and platelet-reinforced composites, aluminum phosphate was chosen as the binder. The binder content was fixed at 30 volume percent. The whisker and platelet contents were 30 and 20 volume percent, respectively. Silicon nitride comprised the balance of the compositions. For comparison, control samples without reinforcement were also prepared. Compositions were mixed in a centrifugal ball mill using rubber-coated steel media. Dry ingredients were mixed first, followed by addition of phosphoric acid and further mixing. Disc-shaped specimens were die pressed at 10 MPa followed by isopressing at 350 MPa, and fired at 700°C in air. After firing, all specimens were sectioned into bars, ground, and polished to 6 μm.

Fired specimens were characterized by porosity (measured by Archimedes method), dimensional changes, phase composition (x-ray powder diffraction), and flexural strength (4-point bending) at room temperature and 800°C. Thermal shock resistance of selected compositions was evaluated by residual strength after abrupt air cooling of samples from 1000°C and 1125°C. Dielectric properties (dielectric constant and loss tangent) were measured from room temperature to 1000°C at 35 GHz by Dr. William Ho at Rockwell International Science Center in Thousand Oaks, California.

The water stability of the materials was determined from retained strength and changes in phase composition (determined by x-ray powder diffraction) after boiling specimens in water for one hour.

Results and Discussion

The flexural strength and phase composition of ceramics based on the Si_3N_4 - H_3PO_4 system are shown in Figures 1 and 2 for firing temperatures from 300°C to 1100°C. The ceramics exhibited strengthening due to the formation of silicon metaphosphate, $Si_3(PO_4)_4$, during firing as a result of the reaction of H_3PO_4 with the surface silica on silicon nitride particles. The maximum strength of 65 MPa was observed after firing at 900°C. Further increase in firing temperature resulted in a dramatic decrease in strength, which is attributed to the decomposition of silicon metaphosphate. Figure 2 shows the absence of $Si_3(PO_4)_4$ and the appearance of SiO_2 in samples fired at 1100°C.

The properties of die-pressed ceramics in the $AlPO_4$-BPO_4-Si_3N_4 system are given in Figures 3 and 4. Both strength and linear changes were found to be a strong function of starting alumina powder particle size, firing temperature, and composition. The strength of specimens prepared from 0.05 μm Al_2O_3 was found to be a function of $AlPO_4$:BPO_4 ratio and firing temperature, increasing with both BPO_4 content and firing temperature. The highest strength was observed in materials based on pure BPO_4 binder after firing at 900°C. Linear changes of all specimens were negligible.

Ceramics prepared using 0.3 μm Al_2O_3 exhibited different behavior. The strength of specimens fired at 700°C was nearly constant up to $AlPO_4$:BPO_4 ratio of 50:50, with a slight decrease at higher BPO_4 content. Linear changes for all compositions were also negligible. However, after firing at 900°C, the
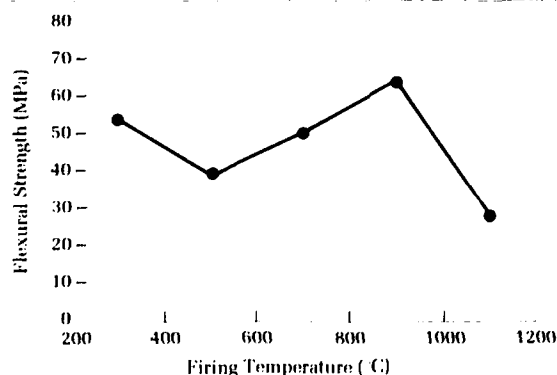

Figure 1. Flexural strength of ceramics prepared from Si_3N_4/25% H_3PO_4 mixtures.
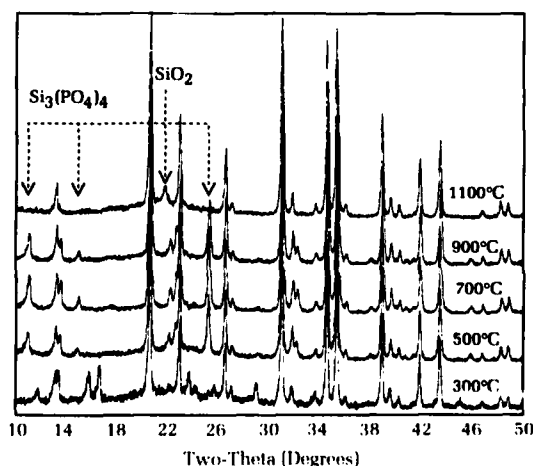
Figure 2. X-ray diffraction patterns of Si_3N_4/H_3PO_4 mixtures fired at 300°C to 1100°C.

18
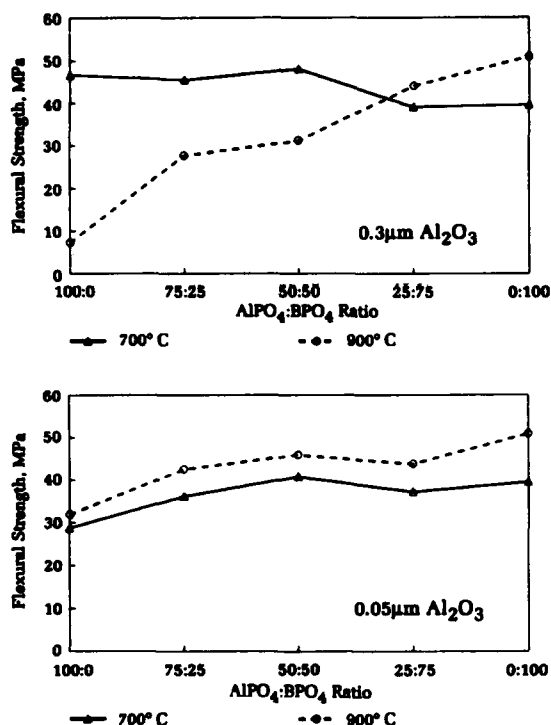
Figure 3. Flexural strength of $AlPO_4/BPO_4$ bonded silicon nitride.
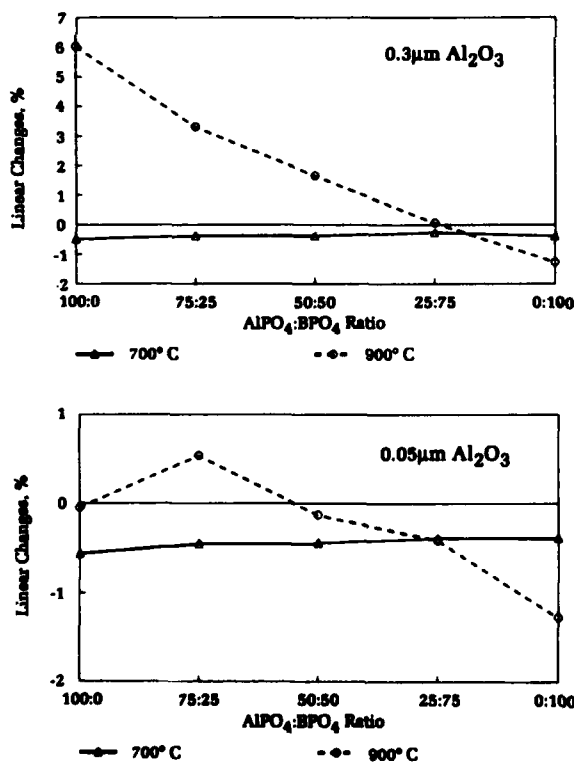
Figure 4. Linear changes of $AlPO_4/BPO_4$ bonded silicon nitride.

100 percent $AlPO_4$ specimen exhibited very low strength (about 7 MPa), which proportionally increased with BPO_4 content up to a maximum of 50 MPa. Compositions with BPO_4 content above 75 percent exhibited an increase in strength at the higher firing temperature, with values at both temperatures similar to those for samples based on 0.05 μm alumina. Samples with higher $AlPO_4$ content showed significant expansion when fired at 900°C (6 percent for ceramics based on pure $AlPO_4$).

This behavior can be explained by the difference in the phase composition, which is depicted in the x-ray diffraction patterns in Figure 5 for materials based on aluminum phosphate. Specimens prepared using 0.05 μm Al_2O_3 contained aluminum orthophosphate, $AlPO_4$, after firing at both temperatures. In contrast, specimens prepared using 0.3 μm Al_2O_3 contained aluminum metaphosphate, $Al(PO_3)_3$, if fired at 700°C, or a mixture of $Al(PO_3)_3$ and $AlPO_4$ if fired at 900°C. It is hypothesized that materials based on 0.05 μm alumina form $AlPO_4$ directly, while materials based on 0.3 μm alumina form $Al(PO_3)_3$ as an intermediate to $AlPO_4$. It is presumed that $Al(PO_3)_3$ decomposed above 800°C to form $AlPO_4$. This decomposition is accompanied by the formation of gaseous P_2O_5, which can explain the expansion upon firing and low strength of materials based on 0.3 μm alumina. The phases observed in the 30 volume percent BPO_4 specimen were Si_3N_4 and BPO_4, and the intermediate compositions followed rule of mixtures behavior.

The flexural strength of zirconium phosphate-bonded silicon nitride is shown in Figure 6 as a function of binder content and firing temperature for materials based on 3.2 m²/g zirconia. Strength of the ceramics increased with increasing binder content and firing temperature, with the highest strength of
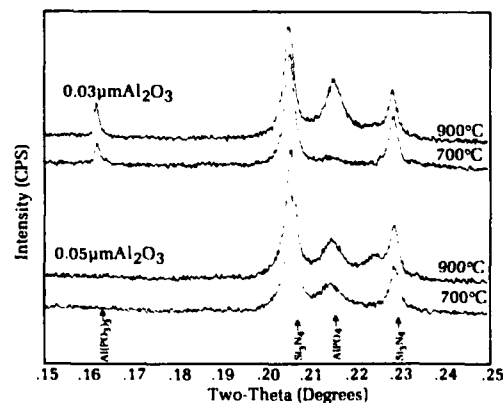
Figure 5. Phase composition of $Si_3N_4/30$ volume percent $AlPO_4$ ceramics as a function of Al_2O_3 particle size and firing temperature.

19

95 MPa observed for specimens containing 30 volume percent ZrP_2O_7 and fired at 900°C. As shown in Figure 7, the materials contained ZrP_2O_7 as well as a large amount of unreacted zirconium oxide. The use of higher surface area zirconia (22 instead of 3.2 m²/g) promoted the reaction between ZrO_2 and H_3PO_4, although the ceramics still contained a significant amount of unreacted zirconia (Figure 8). Figure 9 shows that the strength of ceramics based on the higher surface area ZrO_2 was lower compared to the strength of those based on 3.2 m²/g zirconia, presumably due to the poor packing of the finer zirconia. The significant increase in strength of high surface area ZrO_2 based materials after isostatic pressing is further evidence of the poor packing. Specimens containing 25 percent zirconium phosphate (based on 22 g/cm² zirconia) exhibited an increase in flexural strength from 79 MPa at 25°C to 92 MPa when measured at 800°C. Materials of the same composition showed very high thermal shock resistance; the strength was

practically unchanged after abrupt cooling from 1000°C and 1125°C.

The microstructure and properties of aluminum phosphate-bonded silicon nitride ceramics containing whiskers and platelets are shown in Figure 10 and Table 1. The control (isopressed) sample exhibited much higher strength compared to die-pressed samples of the same composition (Figure 3). The increase in strength can be attributed to higher relative density, which is the result of isopressing. The addition of SiC platelets and Si_3N_4 whiskers did not significantly change the open porosity of the composites, while the addition of SiC whiskers significantly increased porosity, possibly due to packing considerations. The introduction of whiskers resulted in a decrease in strength. This decrease is less significant for the SiC whisker composites, considering the increased porosity compared to the Si_3N_4 whisker composites. The introduction of SiC platelets resulted in little change in strength. Linear changes for all specimens were found to be less than one percent. Scanning-electron micrographs of fracture surfaces of the
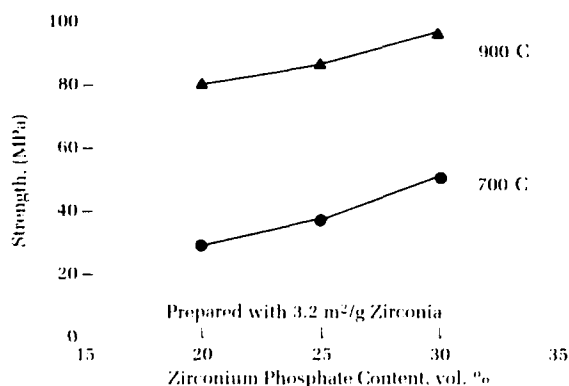
Figure 6. Flexural strength of ZrP_2O_7 bonded $Si_3 N_4$ fired at 700°C and 900°C.

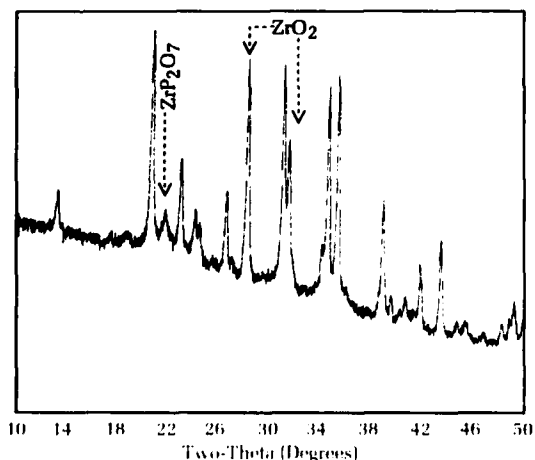**Figure 7.** X-ray diffraction pattern of Si_3N_4/30% ZrP_2O_7 fired at 900°C prepared with 3.2 m²/g ZrO_2.
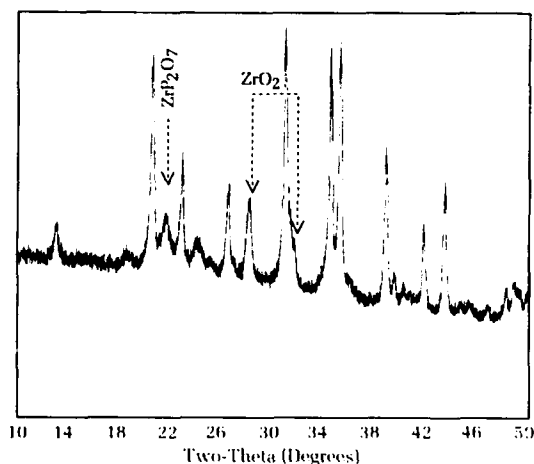
Figure 8. X-ray diffraction pattern of Si_3N_4/30% ZrP_2O_7 fired at 900°C prepared with 22 m²/g ZrO_2.
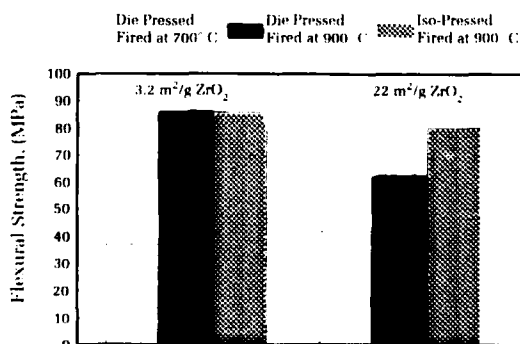
Figure 9. Flexural strength of Si_3N_4/25% ZrP_2O_7 vs firing temperature and forming technique.

20

SiC Whiskers	SiC Platelets	Si₃N₄ Whiskers
2 μm	20 μm	2 μm
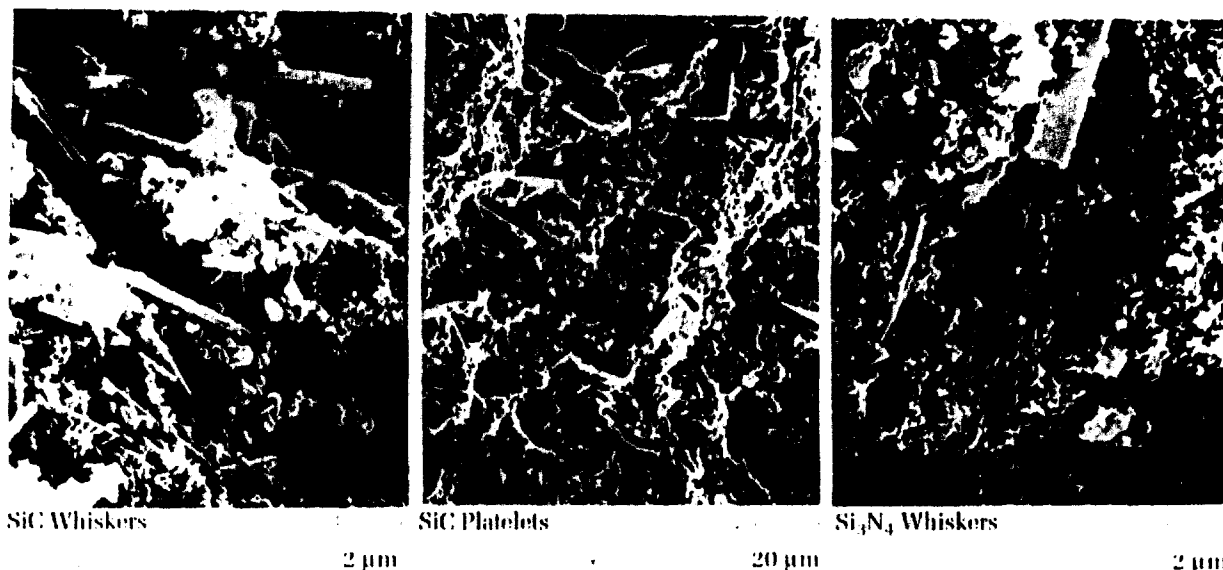
Figure 10. Scanning electron micrographs of $AlPO_4/Si_3N_4$ matrix composites with discontinuous reinforcement.

composites (Figure 10) show that there is no noticeable reaction between the reinforcement and matrix.

The results of dielectric property measurements on aluminum, boron, and zirconium phosphate-bonded silicon nitride, as well as on a silicon nitride whisker-containing composite, are shown in Table 2 along with the goals for advanced radome materials. The room temperature dielectric constant of all materials was below 5, and the change to 1000°C was below 7 percent; the loss tangent of all materials was very low. The values of dielectric properties make phosphate-bonded silicon nitride materials promising candidates for advanced radome applications.

The results of the water stability tests are given in Figures 11 through 13. Firing at 900°C compared to 700°C resulted in significantly higher retained strength for all materials (Figure 11). Boron phosphate-bonded silicon nitride showed the lowest retained strength at both firing temperatures. This behavior is reflected in the x-ray diffraction data (Figures 12 through 13). The substantial loss of BPO_4 in the material fired at 700°C explains the dra-

matic decrease in strength. No noticeable change in the phase composition was observed for the $AlPO_4$- and ZrP_2O_7-bonded ceramics.

Continuous Fiber Composites

This section describes the experimental procedure for the preparation and testing of phosphate-bonded ceramic matrix composites reinforced with continuous fused silica and Nicalon fibers. Test results are discussed as a function of matrix composition, fiber type, interface coating, and processing techniques.

Experimental Procedure

The raw materials for the matrix were the same as those described earlier, with the

Table 1. Flexural Strength and Open Porosity of $AlPO_4/Si_3N_4$ Matrix Composites

Reinforcement	Strength, MPa	Porosity, %
None	85.0	18.0
SiC whiskers	51.3	28.1
SiC platelets	89.5	18.6
Si₃N₄ whiskers	47.9	20.0

Table 2. Dielectric Properties of Phosphate-Bonded Ceramics

Specimen Composition Si₃N₄ +	Dielectric Constant		
	20°C	% change to 1000°C	Loss Tangent
30% $AlPO_4$	4.03	5.2	0.0055
30% $AlPO_4$/30% Si₃N₄ whiskers	4.17	5.35	0.0050
30% BPO_4	3.99	6.5	0.0120
30% ZrP_2O_7	4.98	6.5	0.0031
Radome Material Goals	<9	<7	<0.1

21
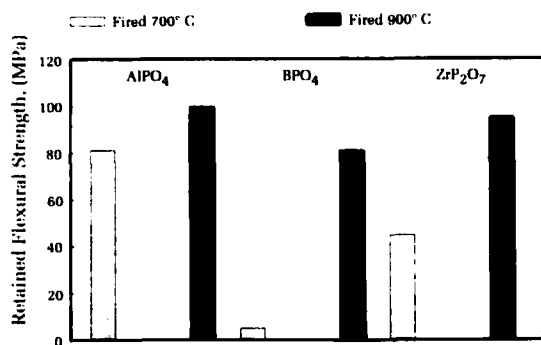
Figure 11. Retained strength of Si_3N_4 containing 30 percent binder after one hour boiling in water.
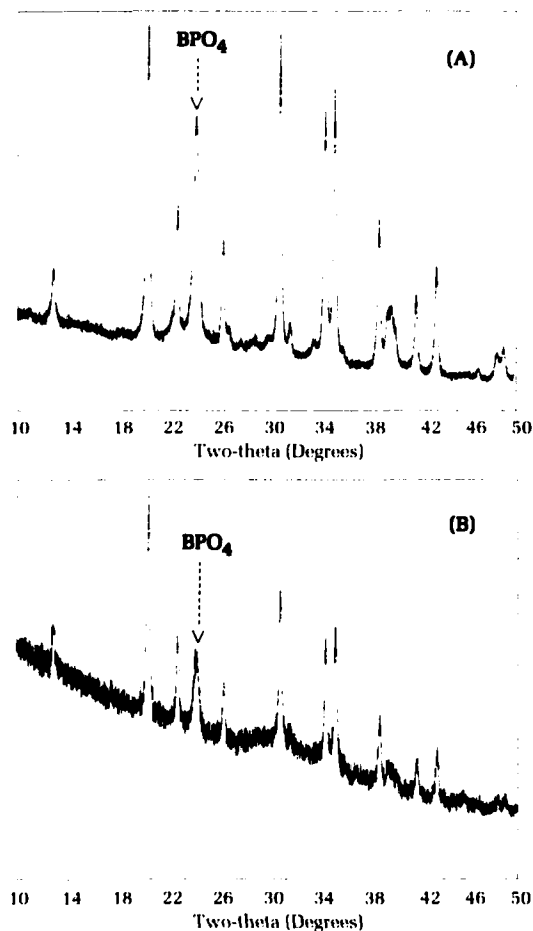
Figure 12. X-ray diffraction patterns of Si_3N_4/30% BPO_4 fired at 700°C (A) before and (B) after boiling in water.

Figure 13. X-ray diffraction patterns of Si_3N_4/ 30% BPO_4 fired at 900°C (A) before and (B) after boiling in water.

were: a CVD (chemical vapor deposition) carbon coating applied to Nicalon by the manufacturer; a boron nitride (BN) coating on the silica fibers applied by Synterials Inc. of Reston, Virginia, using CVD; and a phenolic-based carbon coating applied to the silica fibers using an in-house developed method.

The matrix starting components were mixed as described above. All the mixtures had a pasty consistency. Composites were prepared by applying a thin layer of the matrix material paste to the fabric and laying up a specimen.

22   substitution of a larger particle size of alumina (3.5 μm, Alcoa A-17). Matrix compositions and their designations are given in Table 3.

The fabrics evaluated were two fused silica (HPQY-1 from FMI and Astroquartz from J.P. Stevens) and one Si-C-N (Nicalon from Nippon Carbon). The three interface coatings evaluated

Table 3. Matrix Compositions for Continuous-Fiber Composites

Designation	Filler (vol. %)		Binder (vol. %)	
	Al_2O_3	Si_3N_4	BPO_4	ZrP_2O_7
SN/BP	0	45	55	0
SN/BP/ZP	0	25	37.5	37.5
AO/ZP	25	0	0	75

using either 0 – 0 or 0 – 45 degree orientations. The specimens were vacuum bagged, pressed, and autoclaved. The composites were then de-bagged and fired in air if no interface coating was used, or in nitrogen if a coating was used.

Selected compositions were reimpregnated with aluminum phosphate, zirconium phosphate, or boron phosphate using monoaluminum phosphate (MAP) solution, zirconia/phosphoric acid mixture, or boric acid/phosphoric acid mixture. The monoaluminum phosphate solution was vacuum impregnated, while the other mixtures were pressure impregnated due to their higher viscosity. After impregnation, specimens were autoclaved and fired in nitrogen.

After firing, the composites were sectioned into 60 x 10 x 3 mm bars and characterized by microstructure, porosity, and flexural strength (3-point bending).

Results and Discussion

The strength and porosity of composites containing fused silica fibers are shown in Table 4 as a function of matrix composition, fiber type, interface coating, and reimpregnations. The effect of fiber type can be seen by comparing specimens 1 and 3. Both specimens had low strength, and fiber type did not have a significant effect. The effect of matrix composition can be seen by comparing specimens 3 and 5. Again, the strength was low and nearly the same for both. Comparison of 2 with 1 and 4 with 3 shows that reimpregnation with zirconium phosphate resulted in a very significant increase in the strength of the specimens prepared with HPQY-1 cloth. This can probably be attributed to a difference in interface coating on the two cloths. Although the coatings were intended to be the same, the HPQY-1 cloth appeared darker than the Astroquartz after coating application, indicating some difference in the coatings. The effect of monoaluminum phosphate solution reimpregnation can be evaluated by comparing specimens 5 and 6, and although the porosity was significantly reduced, the strength increase was very small. The great importance of the interface coating can be seen by comparing specimens 5 and 7, where the use of the in-house carbon coating was found to result in the highest strength observed, 55 MPa. The effectiveness of the interface coatings in protecting the fibers can also be seen in the microstructures (Figure 14), showing a dramatic difference in the pullout lengths for samples with the BN and in house carbon coatings.

Table 4. Flexural Strength and Open Porosity of Silica Fiber/Phosphate Matrix Composites

No.	Matrix	Interface Coating	Fiber Type	Reimpreg-nation	Strength MPa	Porosity %
1	SN BP ZP	BN	AQ	none	17	40
2	SN BP ZP	BN	AQ	ZrP O	12	
3	SN BP ZP	BN	HPQY	none	19	36
4	SN BP ZP	BN	HPQY	ZrP O	40	
5	SN BP	BN	HPQY	none	22	45
6	SN BP	BN	HPQY	MAP	25	26
7	SN BP	C	HPQY	none	55	

*In house coating

CVD C/BN

1 mm

In-House Carbon

1 mm

23

Figure 14. Fracture surface of Si_3N_4/55 percent BPO_4 matrix, SiO_2 fiber composites with different fiber coatings.

Table 5. Flexural Strength and Open Porosity of Nicalon Fiber with ZrP_2O_7/25% Al_2O_3 Matrix Composites

No.	Interface Coating	Layup	Reimpreg-nation	Strength MPa	Porosity %
1	none	0-0	none	52	26
2	none	0-0	ZrP_2O_7	26	20
3	none	0-45	none	46	–
4	none	0-45	BPO_4	63	23
5	CVD C	0-0	none	69	28
6	CVD C	0-0	MAP 1x	120	23
7	CVD C	0-0	MAP 2x	64	–

Strength and porosity of Nicalon fiber composites with ZrP_2O_7/25 percent Al_2O_3 matrix are shown in Table 5 as a function of layup architecture, interface coating, and reimpregnation. The effect of layup architecture can be seen by comparing specimens 1 and 3. The composites with the 0 – 45 degree layup exhibited slightly lower strength, which is to be expected since fewer fibers are in the optimum orientation in the flexural test specimens. The effect of the CVD carbon interface coating can be seen by comparing specimen 5 with 1; the carbon coating yielded a significant increase in strength, indicating the importance of protective interface coatings for nonoxide fibers as well. Reimpregnations were found to reduce porosity of the specimens, but the effects of reimpregnations on strength depended on the interface coating and the phosphate used. Reimpregnation with zirconium phosphate (comparing 2 with 1) resulted in a decrease in strength of nearly 50 percent, whereas reimpregnation with boron phosphate (comparing 4 with 3) yielded a significant increase in strength. This difference can be attributed to the curing temperatures of the two phosphates. Reimpregnation with MAP (comparing 5 and 6) was found to nearly double the strength. However, a second reimpregnation (sample 7) resulted in a decrease in strength. Because the specimens were fired to 700°C after each reimpregnation, it is believed that the CVD carbon interface coating was insufficient to protect the fibers during the second cycle.

Summary

Techniques have been demonstrated for low-cost, low-temperature processing of monolithic silicon nitride ceramics and composites with both discontinuous and continuous reinforcement using phosphate bonding. Silicon nitride ceramics bonded with silicon, aluminum, boron, and zirconium phosphates were prepared and characterized by strength, dielectric properties, and water stability. The flexural strength of the ceramics ranged from 40 MPa to 96 MPa. Phase composition and mechanical properties of aluminum phosphate-bonded silicon nitride exhibited strong dependence on firing temperature and alumina particle size. The use of 0.05 μm alumina resulted in stable phase composition and properties, and is recommended for further development. Ceramics bonded with zirconium phosphate exhibited the highest room temperature strength. These compositions also exhibited excellent thermal shock resistance and strength retention up to 800°C. All the materials had low and thermally stable dielectric constant and loss tangent, which together with good strength make them promising candidates for electromagnetic window applications. Phosphate-bonded silicon nitride showed high water stability when fired at 900°C.

Ceramic composites were prepared with a variety of whiskers (SiC, Si_3N_4), fibers (fused silica, Nicalon), and phosphate-bonded Al_2O_3 and Si_3N_4 matrices. Properties of the materials were characterized as a function of matrix composition, fiber type, fiber/matrix interface, and phosphate reimpregnations. Three types of interface coatings were evaluated (CVD carbon, CVD BN, and an in-house developed carbon coating). The highest strength of 120 MPa was observed for a composite containing Nicalon fibers in a zirconium phosphate/alumina/aluminum phosphate matrix. Interface coatings and reimpregnations were found to be crucial for increasing strength and require further development and optimization.

Acknowledgments

References

1. Kingery, W. D., "Fundamental Study of Phosphate Bonding in Refractories: I. Literature Review, II. Cold Setting Properties, III. Phosphate Adsorption by Clay and Bond Migration," *J. Am. Cer. Soc.*, Vol. 33, 1950, pp. 239-250.

24

2. Gonzalez, F. and Halloran, J., "Reaction of Ortho phosphoric Acid with Several Forms of Aluminum Oxide," *Am Cer. Soc. Bull.*, Vol. 59, 1980, pp. 727-738.
3. Hummel, F., "Properties of Some Substances Isostructural with Silica," *J. Am. Cer. Soc.*, Vol. 32, 1949, pp. 320-326.
4. Rouanet, A., et al., "Rare Earth Orthophosphates at High Temperatures," Akakemii Nauk SSSR, *Neorganicheskie Materialy*, Eng. translation, Vol. 17, 1981, pp. 104-109.
5. Talmy, I. G. and Martin, C. A., "Phosphate-Bonded Non-Oxide Ceramics," *Proc. 14th Conference on Metal Matrix, Carbon, and Ceramic Composites*, NASA CP-3097, Part 1, pp. 309-316.

The Authors

INNA G. TALMY is the senior research ceramist of the High Temperature Materials Group at the White Oak Detachment, which she joined in 1983. She received both M.S. (1957) and Ph.D. (1965) degrees in ceramic science and engineering from the Institute of Chemical Technology in Moscow, Russia. Previously, Dr. Talmy worked in the ceramic departments of Institutes of Chemical Technology in Moscow, Russia, and Prague, Czechoslovakia. Her primary research interests are in the field of dielectric ceramics and ceramic-matrix composites. Dr. Talmy directed the development of celsian ceramics for future radomes and mullite whiskers and mullite-whisker felt. Under her leadership, a new generation of candidate radome materials employing chemical (phosphate) bonding is currently under investigation. The use of phosphate technology for ceramic-matrix composites, high temperature adhesives and coatings is also being developed. Her work has resulted in numerous publications and patents. Dr. Talmy's work has been recognized by several awards such as the Navy Meritorious Civilian Service Award (1990) and the John Adolphus Dahlgren Award (1991).

CURTIS A. MARTIN received a B.S. degree (1979) and M.S. degree (1982) in materials engineering from Virginia Polytechnic Institute and State University. After graduation, he worked in the field of refractory materials at Lafarge Calcium Aluminates in Chesapeake, Virginia. In 1985, he joined the White Oak Detachment as a member of the High Temperature Materials Group. Mr. Martin has been involved in several projects developing ceramic materials for applications in missiles and other weapon systems. His research has resulted in several patent disclosures and articles. For the past four years, he has served as an officer of the Baltimore-Washington Section of the American Ceramic Society.

DEBORAH A. HAUGHT received a B.S. in chemical engineering from Virginia Tech in 1985 and then joined White Oak as a member of the High Temperature Materials Group. Ms. Haught completed work on an M.S. degree in materials science from the University of Virginia in 1989 and is presently pursuing a masters degree in engineering management from George Washington University. Her principal involvements are in the development of celsian ceramics for future radomes, mullite whiskers and mullite-whisker felt, and the development of new classes of ceramic materials employing phosphate technology. These achievements have led to numerous publications and patents as well as the Research and Technology Department Young Professional of the Year Award in 1991. In addition to her research responsibilities, Ms. Haught is actively involved in program management for the Weapons and Spacecraft Material Block Program. In 1992, she became the group leader of the High Temperature Materials Gr   ).

ANH H. LE received a B.S. (1978) and Ph.D. (1982) in physical chemistry from the American University. In 1983, he joined White Oak as a research chemist. He has conducted research in nuclear submarine lead-acid batteries and corrosion studies of materials (such as metals, metal alloys, metal-matrix composites and amorphous alloys) in different environments. His experience also includes synthesis, processing, and characterization of ceramic materials with emphasis on solid state and surface chemistry. Currently, he is a member of the American Ceramic Society and an adjunct professor in the Chemistry Department of the American University.

AMY E. JANOVSKY began working at the White Oak Detachment as a high school summer intern in 1988, sponsored by the Science and Engineering Apprentice Program. The following year, she started studying chemical engineering at Virginia Tech and entered the cooperative education program. Working with High Temperature Materials Group scientists, she has been involved in all major research areas, especially in the development of celsian and phosphate-bonded ceramics for advanced radome application. She has made significant contributions to the projects. Ms. Janovsky will receive her B.S. degree in chemical engineering in December 1993.

25

Building Materials Prepared From Phosphate-Bonded Fly Ash

I. G. Talmy, D. A. Haught and C. A. Martin

Recent experiments have demonstrated that phosphate-bonding techniques developed at the White Oak Detachment for processing ceramics and ceramic-matrix composites can also potentially be used to convert fly ash, a waste product, into a new, cost effective family of building materials.

Fly ash, a waste by-product of coal combustion in electrical power plants, represents a significant environmental problem. An estimated 80,000,000 tons of fly ash are generated per year in the United States alone. Only about 20 percent of this amount is utilized, and the rest is dumped. Fly ash has complex chemical composition containing mostly SiO_2 and Al_2O_3 (up to 80 percent), with Fe_2O_3, CaO, MgO, Na_2O, K_2O, SO_3 and other oxides as the remainder. It may also contain traces of hazardous elements such as arsenic, lead, barium, and mercury. The chemical composition varies significantly depending on coal deposits and power plant operating parameters.

Various options of using fly ash are being considered, the most promising being: in cement as a substitute for shale; in concrete as a substitute for cement and sand, and as aggregates; in road construction as a filler to bitumen and as a substitute for sand in the foundation layer; in bricks as a substitute for clay; and for soil stabilization. These possible ways of utilization do not lead to massive consumption of the wastes since fly ash is not the major component. The development of alternative uses of fly ash would be of great practical value, especially if it is the major component of the products.

The White Oak Detachment has developed phosphate-bonding techniques for the low-cost processing of ceramics and ceramic-matrix composites. The method, described in detail in the previous article, is based on the chemical reaction between certain metal oxides, hydroxides, salts or other compounds with phosphoric acid or other phosphorous-containing compounds. As a result of the reactions, strong polymeric-like bonds are formed assuring the high strength of final products. Phosphate bonding technology offers significant advantages such as low temperature firing, readily available commodity raw materials, and near-net shape parts, resulting in overall low-cost processing.

Phosphate bonding is very promising for utilization of fly ash since it contains many oxides conventionally used for this technology. Chemical reactions of phosphorous-containing compounds with Al_2O_3 and SiO_2 (predominant components of fly ash) are slow, and result in the formation of strong bonds. Compared to that, reactions with CaO and MgO (present in some types of fly ash in amounts exceeding 20 percent) are vigorous even at room temperature, and represent a serious and challenging processing problem.

Experiments at White Oak have shown that phosphate bonding of fly ash holds the potential of providing a new family of building materials such as bricks, tiles, and porous aggregates to be used as fillers in lightweight concretes and plastics. Ceramics were prepared using four different types of fly ash which significantly varied in chemical composition. The bending strength of
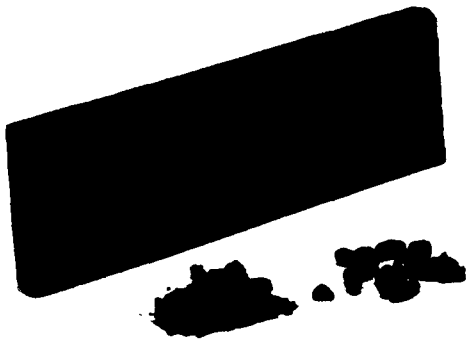
Figure 1. The tile shown here and the porous aggregates in the right foreground were prepared from fly ash (left foreground) using phosphate-bonding techniques.

the products ranged from 15 MPa to 28 MPa (compared to 18 MPa for common bathroom tiles). Porous aggregates with density below 1 g/cm^3 were successfully produced. Figure 1 shows a tile and porous aggregates prepared from fly ash using the developed technology.

The preliminary results indicate that the method can be applied to the production of building materials with fly ash as the major component. Variations in the composition of the fly ash will not significantly affect the manufacturing process or properties of the final product. The technology based on phosphate bonding can be easily transferred to existing plants and facilities. One of the important advantages of the process is the formation of water insoluble metal phosphates, including hazardous metal phosphates which will prevent contamination of the environment from leaching.

Future work will be concentrated on optimization of processing parameters, thorough characterization of the products, and the development of industrially feasible and low-cost processing methods.

The Authors

INNA G. TALMY is the senior research ceramist of the High Temperature Materials Group at the White Oak Detachment, which she joined in 1983. She received both M.S. (1957) and Ph.D. (1965) degrees in ceramic science and engineering from the Institute of Chemical Technology in Moscow, Russia. Previously, Dr. Talmy worked in the ceramic departments of Institutes of Chemical Technology in Moscow, Russia, and Prague,

Czechoslovakia. Her primary research interests are in the field of dielectric ceramics and ceramic-matrix composites. Dr. Talmy directed the development of celsian ceramics for future radomes and mullite whiskers and mullite-whisker felt. Under her leadership, a new generation of candidate radome materials employing chemical (phosphate) bonding is currently under investigation. The use of phosphate technology for ceramic matrix composites, high temperature adhesives and coatings is also being developed. Her work has resulted in numerous publications and patents. Dr. Talmy's work has been recognized by several awards such as the Navy Meritorious Civilian Service Award (1990) and the John Adolphus Dahlgren Award (1991).

DEBORAH A. HAUGHT received a B.S. in chemical engineering from Virginia Tech in 1985 and then joined White Oak as a member of the High Temperature Materials Group. Ms. Haught completed work on an M.S. degree in materials science from the University of Virginia in 1989 and is presently pursuing a masters degree in engineering management from George Washington University. Her principal involvements are in the development of celsian ceramics for future radomes, mullite whiskers and mullite-whisker felt, and the development of new classes of ceramic materials employing phosphate technology. These achievements have led to numerous publications and patents as well as the Research and Technology Department Young Professional of the Year Award in 1991. In addition to her research responsibilities, Ms. Haught is actively involved in program management for the Weapons and Spacecraft Material Block Program. In 1992, she became the group leader of the High Temperature Materials Group.

CURTIS A. MARTIN received a B.S. degree (1979) and M.S. degree (1982) in materials engineering from Virginia Polytechnic Institute and State University. After graduation, he worked in the field of refractory materials at Lafarge Calcium Aluminates in Chesapeake, Virginia. In 1985, he joined the White Oak Detachment as a member of the High Temperature Materials Group. Mr. Martin has been involved in several projects developing ceramic materials for applications in missiles and other weapon systems. His research has resulted in several patent disclosures and articles. For the past four years, he has served as an officer of the Baltimore-Washington Section of the American Ceramic Society.

27

Lithium Rechargeable Batteries for Underwater Vehicle Propulsion

Patricia H. Smith and Stanley D. James

The Naval Surface Warfare Center, Dahlgren Division, is developing a high energy, rechargeable lithium battery that will significantly extend the capabilities of naval underwater vehicles such as the SEAL delivery vehicle. The lithium/cobalt oxide battery under investigation has the potential to double vehicle range and greatly improve battery lifetime (charge-discharge cycle life), storability, and low-temperature operation. It would replace the silver oxide/zinc battery, currently the principal power source for underwater vehicle propulsion. The lithium/cobalt oxide electrochemical couple has been successfully demonstrated in 30-amp-hour capacity, hermetic cells. Projections indicate that, at the 400-amp-hour cell size used in the SEAL vehicle, this battery will meet program goals, resulting in a more durable, energy-dense, and cost-effective power source for naval vehicles.

Introduction

In collaboration with Alliant Techsystems Inc., Power Sources Center (Horsham, Pennsylvania), the Naval Surface Warfare Center, Dahlgren Division, White Oak Detachment, is investigating the feasibility of using lithium rechargeable batteries for underwater vehicle propulsion. Many underwater vehicles are currently powered by silver oxide/zinc (AgO/Zn) cells. Although AgO/Zn is the most energetic high-rate secondary battery now available, its energy density (55- to 65-watt-hours per pound) limits its usefulness. Other major disadvantages of this system include: (1) limited number of charge-discharge cycles before failure, (2) a substantial drop in energy density near the end of cycle life, and (3) a poor wet stand life.

The ultimate objective of our lithium rechargeable battery effort is to develop a 400-amp-hour cell displaying the following characteristics:

Energy Density:	100-watt-hours per pound
Rate Capability:	C/6 (delivering full capacity, C, in 6 hours)
Cycle Life:	50 cycles
Operating Temperature:	-2°C to 35°C
Shelf Life:	5 years

The technology will have been embodied in cells of two intermediate sizes (30- and 100-amp-hour) prior to the final 400-amp-hour cell development. This article discusses results obtained in sealed, multiplate 30-amp-hour size cells. The energy-density goal for the 30-amp-hour cell (65-watt-hours per pound) was less than that for the 100-amp-hour cell. In smaller cells, the ratio

of inert materials (containers, separators, bus bars, etc.) to reactive materials (chemicals) is greater, and consequently the energy density is less. Previous reports traced the development through fixtured cells[1] and 10-amp-hour size units[2] that were design precursors to the 30-amp-hour cells.

The electrochemical couple selected to meet our ultimate objective is lithium/cobalt oxide (Li/Li_xCoO_2). The discharge reaction of this cell involves the electrochemical oxidation reaction of a lithium (Li) anode to its dissolved ions and the electrochemical reduction of a lithiated cobalt oxide (Li_xCoO_2) cathode with the concurrent intercalation of lithium ions into that oxide. The cell reaction is:

$$(1-x)\, Li + Li_xCoO_2 \underset{\text{Charge}}{\overset{\text{Discharge}}{\rightleftharpoons}} Li_1CoO_2.$$
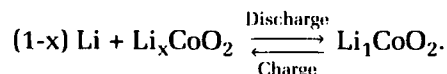
Cells whose cathodes cycle in the range $0.5 \leq x \leq 1$ display a nearly flat discharge curve with a midpoint voltage of 3.9 volts at the C/6 rate compared to 1.5 volts for AgO/Zn cells. Projections indicate[3] that 400-amp-hour cells operating in this range will meet program cycle life and energy density goals. With minor changes to the cathode, the stoichiometric range may be successfully extended[3] to values of $x < 0.5$ with a corresponding increase in energy density. Such studies are not addressed in the current program.

Cell Construction

The cells had a nominal 30-amp-hour capacity and were of a multiplate construction. The container, shown in Figure 1, was a 2.5-inch-diameter, 6-inch-high cylinder. The photograph also shows the two terminals (electrically isolated from the case by glass-to-metal seals), a safety vent designed to release at 360 psig, and

a tube used to fill the cell with electrolyte. After filling, the tube was closed off mechanically to establish a hermetic seal.

The electrolyte solution, prepared in a glove box under an argon atmosphere, consisted of 1.0 molar lithium hexafluoroarsenate (La Roche, Electrochemical Grade) and 0.4 molar lithium tetrafluoroborate (Foote Mineral Company, Electrochemical Grade) dissolved in methyl formate obtained from E.M. Science (Battery Grade made specially for Alliant Techsystems). Carbon dioxide was then passed through the solution at a pressure of 30 psig for at least 30 minutes to saturate it. Dissolved carbon dioxide raises the cycling efficiency of the lithium anode and avoids the need for excessive amounts of lithium metal.

Anodes were made from 0.008-inch-thick lithium foil (Li $\geq$ 99%, Foote Mineral Company) pressed onto both sides of a 316 Stainless Steel grid. The 0.027-inch-thick cathodes consisted of a blend of 85-weight-percent $LiCoO_2$ (Alfa Products), 10-weight-percent carbon black (Vulcan XC-72, Cabot Corporation), and 5-weight-percent Teflon obtained from Du Pont. It should be noted that the Li_xCoO_2 used to prepare the cathode was in the fully lithiated (discharged) state, i.e., $x = 1$. Therefore, after the cell was assembled and filled with electrolyte, it had to be charged prior to the first discharge. The cathode grid was made from Aluminum 1100. Microporous, high-density polyethylene (E003, 3M Company) was used for the 0.0012-inch-thick separator, which prevents a direct electrical short of anode to cathode. All anodes were individually heat sealed inside a two-layer separator envelope, while cathodes were sealed in a one-layer separator envelope. Thus, including one loose layer of separator, there was a total of four layers (0.0048 inch) between anode and cathode. The stack assembly is shown in Figure 2.

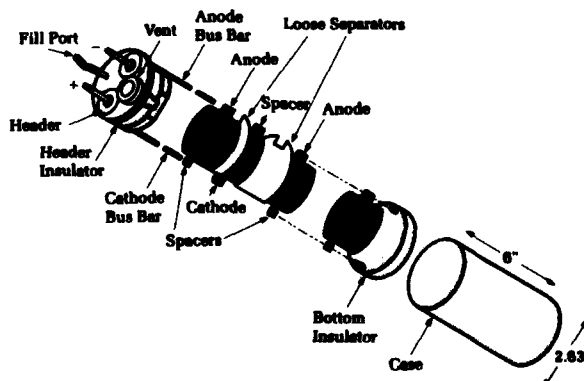To construct the cell stack, plates of opposite polarity (anodes and cathodes) were alternately

Figure 1. Rechargeable, 30-amp-hour lithium/cobalt oxide cell.

Figure 2. Cell stack assembly for rechargeable, 30-amp-hour lithium/cobalt oxide cell.

29

interleaved perpendicular to the axis of the cylinder. Bus bars connected the electrically paralleled plates of each polarity to the cell terminals. The bus bar and current collectors (grids) were made from Aluminum 1100 and Stainless Steel 316 for cathode and anode, respectively. Spacers were used to control cell stack compression and to provide electrical contact between the cell stack and the bus bar. Cells typically weighed 2.2 pounds and were designed to be cathode limited. The actual capacity of the cells when discharged from a cathode composition of $Li_{0.5}CoO_2$ to $LiCoO_2$ was 33 amp hours. The cathode material, with a total surface area of approximately 3600 cm^2, was distributed over 89 plates. The anode consisted of 88 plates as previously described and two half (end) anodes that had lithium foil on only one side (0.008-inch thick versus 0.016-inch thick).

Cell Testing

To assist in the evaluation of the lithium technology, commercial 30-amp-hour AgO/Zn cells (LR30) were purchased from Yardney Technical Products Inc. These cells (Figure 3) were 7.50" high x 2.01" wide x 1.04" deep and weighed 1.1 pounds.

Both lithium and silver oxide/zinc cells were evaluated for electrical performance at room temperature (22°C ± 2°C) and in temperature-controlled chambers set either at -2°C or 35°C. Cells were cycled (discharge, charge, etc.) using an automated battery cycler which discharged

them at constant current at the C/6 rate to a cutoff voltage of 3.0 volts for Li/Li_xCoO_2 or 1.1 volts for AgO/Zn cells. Cells were charged using constant current at the 10-hour rate (C/10). In the case of lithium cells, charging was terminated when the cathode composition was calculated to have fallen from $LiCoO_2$ to $Li_{0.5}CoO_2$ or when the cell voltage reached 4.3 volts, whichever occurred first. Silver oxide/zinc cell charging was terminated when the cell voltage reached 2.05 volts. The cycle at which the cell delivered less than 25-amp-hour (80% of the nominal capacity) was taken as the end of life.

A key objective of the test program was to evaluate the shelf life of Li/Li_xCoO_2 cells and compare it to that of the AgO/Zn technology. This was accomplished by allowing both types of cells to remain at open circuit (neither discharging nor charging) for three months, both at 22°C and 35°C. Two comparisons were made: one in which the cells were stored in their fully charged state and another where the cells were discharged prior to storage. After being stored for three months, the cells were cycled at 22°C, as described above, to assess any performance degradation caused by storage.

Cycling Performance

Figure 4 compares 20th cycle discharges (at the C/6 rate) for lithium and silver cells cycled at -2°C, 22°C, and 35°C. Li/Li_xCoO_2 cell performance was affected only slightly by temperature, and the cells maintained a flat, plateau voltage above 3.9 volts, while delivering over 30-amp-hours of capacity. In contrast, the AgO/Zn cell performance deteriorated sharply at the lower temperature (-2°C), delivering only 15 amp hours above 1 volt. Furthermore, the silver cells had poor voltage regulation and displayed two distinct voltage plateaus (1.85 and 1.5 volts at the higher temperatures).
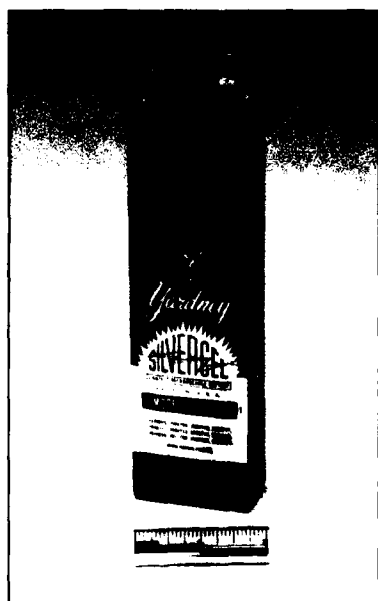

Figure 3. Rechargeable, 30-amp-hour silver oxide/zinc cell purchased from Yardney Technical Products (model LR30).
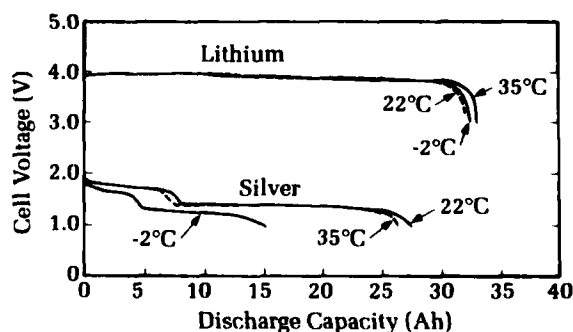

Figure 4. Discharge curves (20th cycle) for lithium/lithium cobalt oxide and silver oxide/zinc cells.

30

Table 1. Performance of 30-Amp-Hour Lithium/Cobalt Oxide Cells

Cell No.	Temp. (°C)	Cycles Achieved*	Average Energy Density (Wh/lb)
N6-CO-004	35	23	50
N6-CO-005	35	4	48
N6-CO-006	22	1	60
N6-CO-007	-2	37	62
N6-CO-008	-2	41	58
N6-CO-009	22	40	57
N6-CO-010	22	37	55
N6-CO-011	35	42	59
N6-CO-012	35	30	55
N6-CO-013	22	21	57
* Delivering more than 25 Ah.			

A summary of the cycling data for 30-amp-hour Li/Li$_x$CoO$_2$ cells is presented in Table 1. These cells did not achieve the 50 charge-discharge cycles demonstrated earlier with smaller cells (0.03, 2.5 and 10 Ah).[1,2] However, their average energy densities were similar. Detailed postmortem examinations conducted on cell components indicated that cells failed because of dendritic lithium shorts. During charge, plated lithium penetrated the separator and contacted the cathode. The resulting "soft shorts" formed internal shunts, causing the effective charging current to be less than nominal. This failure mode will probably be typical of fully developed cells.

Comparison of the performance of 30-amp-hour Li/Li$_x$CoO$_2$ cells with 30-amp-hour AgO/Zn showed that the higher voltage lithium system yielded greater energy density (Figure 5). Lithium cells also gave more charge-discharge cycles with almost 40 percent more energy density on a gravimetric basis. On
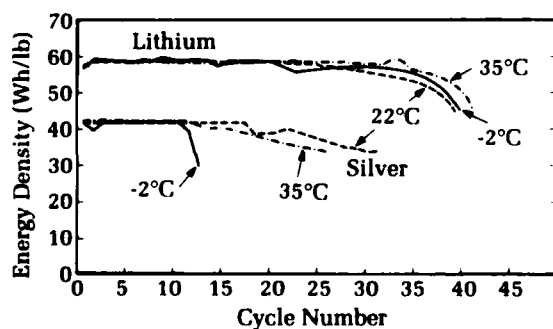
Figure 5. Comparison of energy density for lithium/lithium cobalt oxide and zinc/silver oxide cells as a function of cycle life.

a volumetric basis, lithium was approximately 50 percent more energy dense. Lithium's advantage was especially marked at -2°C, where Li/Li$_x$CoO$_2$ cycles four times longer than AgO/Zn. The 40-watt-hours per pound obtained from the silver cells is significantly less than the 63-watt-hours per pound cited by the manufacturer for the 10-hour discharge rate.[4]

Storage Performance

One of the problems associated with AgO/Zn technology is its limited storage life. Reports from the fleet indicate that a silver cell loses substantial capacity after only three months' storage in the charged state. This is borne out by results displayed in Figure 6, which compares the storability of the two electro-chemistries. No capacity was lost by either system after storage in the discharged state (curves A and C). However, after three months of charged storage, lithium and silver cells lost 35 percent and 60 percent, respectively, of initial capacity. Not only is this initial capacity loss greater for silver than for lithium, but even worse, silver oxide/zinc's capacity loss is essentially irreversible, i.e., it cannot be recovered by recharging. In contrast, lithium/cobalt oxide's cell capacity is fully recovered on recharge. Thus, Li/Li$_x$CoO$_2$ cells are far more storable, making the logistics of their use in the fleet much more attractive.

Safety

As with any newly emerging power source, safety must be demonstrated prior to service. In the case of lithium batteries, adoption by the
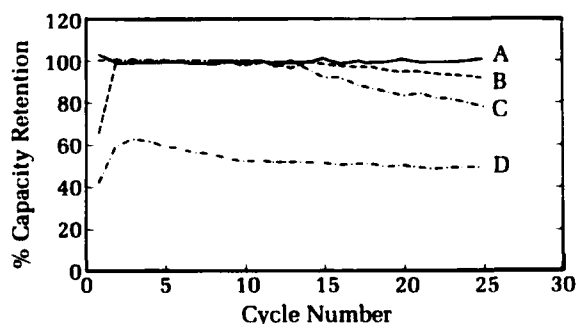
Figure 6. Effect of three-month storage at 35°C on the performance of lithium/cobalt oxide and silver oxide/zinc cells. Curves A and B refer to lithium cells stored in the discharge and charged state, respectively. Curves C and D refer to silver cells stored in the discharged and charged state, respectively.

31

fleet has been slow, primarily due to poor early designs, manufacturing flaws, and accidental misuse. Today, lithium batteries have found widespread use in the Navy in, for example, countermeasure and firing devices, missiles, exercise torpedoes, mines, transponders, and computers.

An understanding of lithium battery characteristics under all possible operational conditions is the key to the control of safety hazards. The battery can then be designed with safety devices such as pressure relief valves, fuses to protect against electrical and thermal overload, and diodes to prevent cell overdischarge or overcharge. The lithium/cobalt oxide system remains in the early stage of its development and has not been designed with such features. Consequently, it would be premature to conduct extensive safety evaluations, such as those required in NAVSEA Instruction 9310.1B.[5] A preliminary assessment (4 cells) of this technology, however, was conducted on AA- and D-size cells. In all cases, when cells were abused by heating, short-circuiting, or overcharging, they behaved safely. There was only one venting. It occurred when an AA cell was cycled 5 times, then in the charged state, heated to 110°C. The cell properly vented through a coined vent. No fire was observed. This work will be reported in greater detail at a future date.

Conclusions and Future Work

A high-energy-density electrochemical couple, lithium/cobalt oxide, was demonstrated in 30-amp-hour cells. Although the cells did not meet the 50-cycle goal, the program is viewed as a success. The higher voltage lithium system yielded energy densities 40 to 50 percent greater than silver cells. Lithium's cycle life was found to be superior to that of AgO/Zn, especially at low temperature (-2°C), where Li/Li_xCoO_2 cycles four times longer than AgO/Zn.

The next stage of the program is directed toward scaling up the technology to a size suitable for the SEAL delivery vehicle (SDV).

It is anticipated that the cell will be rectangular, as opposed to cylindrical, with a capacity between 400- and 700-amp-hours. This would allow a straightforward retrofit into existing vehicles, which are now powered by rectangular AgO/Zn cells. A preliminary design analysis indicated that development efforts should focus on the cathode. A substantial improvement in energy density could be realized if the cathode density were increased from 2.5 grams per cubic centimeter to 3.0 grams per cubic centimeter, the thickness from 0.027 inch to 0.080 inch, and the percentage of cobalt oxide in the cathode raised from 85 to 87. Such design changes could result in an SDV-sized cell with an energy density of 120-watt-hours per pound. A battery comprising these cells would double the SDV range.

Acknowledgments

References

1. Smith, P., et al., "The U.S. Navy's Lithium Rechargeable Battery Program Part I: Development of a Lithium Cobalt Oxide Prototype Cell," *Prog. Batt. & Solar Cells*, Vol. 9, pp. 229-237, 1990.

2. Smith, P., Chua, D. and James, S., "Development of a Lithium Rechargeable Battery for Underwater Vehicle Propulsion," *Naval Engineers Journal*, Vol. 103, No. 3, pp. 158-163, 1991.

3. Smith, P., Chua, D. and James, S., *Naval Engineers Journal*, Vol. 103, No. 4, "Authors' Reply to Comments" (on ref 2, above), p. 130, 1991.

4. Whittaker-Yardney Power Systems Brochure, *Rechargeable Silvercels*.

5. NAVSEA Instruction 9310-1B, "Naval Lithium Battery Safety Program," 13 Jun 1991.

The Authors

PATRICIA H. SMITH is Group Leader of the Battery Research and Development Group in the Electrochemistry Branch of the White Oak Detachment. She has 11 years' experience in exploring and extending electrochemical technology in order to bring safe, high energy lithium batteries into widespread naval use. Dr. Smith manages the High Energy Battery Project sponsored by the Office of Naval Technology. A major thrust of this project is the development of lithium batteries to propel naval underwater vehicles. Dr. Smith has authored numerous papers on lithium batteries and is currently Editor-in-Chief of the *High Energy Battery Newsletter*. She obtained her Ph.D. in inorganic chemistry at the University of Maryland in 1981.

STANLEY D. JAMES obtained his Ph.D. in physical chemistry of ion exchange membrane at the Imperial College of Science, London, in 1959. In 1967 he joined the White Oak Detachment and he is currently the Senior Technical Consultant to the White Oak Detachment's Battery R&D Group in the Electrochemistry Branch. Dr. James has authored 45 papers and is the Technical Editor of the Dahlgren Division's *High Energy Battery Newsletter*.

33

Effect of Alloy Composition on the Corrosion Characteristics of Tungsten Superalloys

A. N. Mansour and K. L. Vasanth

Tungsten superalloys prepared by liquid phase sintering are employed as the armor-piercing core of medium- to large-caliber kinetic energy ammunition and as preformed fragments in various antiaircraft and antimissile warheads. The technique of x-ray absorption fine structure (XAFS) spectroscopy described in this article allows identification of corrosion products, and hence permits design of superalloys strongly resistant to corrosive environments. Specifically, XAFS spectroscopy is used to determine the effect of composition on corrosion and to examine the electronic and atomic structure of corrosion products on two W-Ni-Fe alloys immersed in 3.5 weight percent NaCl solution (seawater equivalent). Analysis of the XAFS data indicates that the chemical and structural nature of Fe in the corrosion products of both alloys is similar to that of a highly structurally disordered form of α–Fe_2O_3. The chemistry and structure of Ni in the corroded alloys are similar to those of metallic Ni except for a small fraction (less than 20 percent), which is present in an oxidized form. Tungsten is the component of the alloy least affected by the corrosion process.

Introduction

Tungsten alloys, referred to as "superalloys" because of their high density and strength, are important engineering materials for numerous military and industrial applications.[1] In military applications, they are used as the armor-piercing core of medium- to large-caliber kinetic energy ammunition and as preformed fragments in various antiaircraft and antimissile warheads. Industrial applications include counterbalances, gyroscope rotors, and radiation shields. These alloys are prepared by liquid phase sintering in which tungsten particles are dissolved in a liquid solution of Ni-Fe, Ni-Cu, or Ni-Co.[2] The outcome of this process is a two-phase structure consisting of tungsten particles cemented together with an alloy containing a solid solution of W-Ni-Fe, W-Ni-Cu, or W-Ni-Co. The W in the solid solution is present in very small quantities compared to Fe, Ni, Cu, or Co.

The corrosion characteristics of tungsten alloys with various alloying elements have been studied by several authors. Andrew et al.[3] reported that a W 3.5 weight percent, Ni 2.5 weight percent Co alloy readily corrodes when exposed to air saturated with water vapor. Koger[4] observed that the corrosion rate for a W 3.5 weight percent, Ni 1.5 weight percent Fe alloy increased with an increase in pH. Vasanth et al.[5] and Vasanth and Dacres[6] reported on the polarization resistance measurements and pitting studies for five W-Ni-Fe alloys with varying compositions immersed in 3.5 weight percent sodium chloride (NaCl) solution. Based on immersion studies of these five alloys in

34

natural seawater, the authors reported a corrosion rate of less than 2 mils per year. However, the chemistry and structure of corrosion products have not previously been investigated.

XAFS spectroscopy is a powerful technique for investigating the chemistry and structure of materials and has been widely used in corrosion and electrochemical research.[7-9] X-ray absorption near-edge structure (XANES) spectroscopy is useful for valence state and site symmetry determinations. Extended x-ray absorption fine structure (EXAFS) spectroscopy, on the other hand, is useful for structural analysis. XAFS experiments can be performed under *ex situ* or *in situ* conditions, making the technique uniquely suited to corrosion and electrochemical investigations. The atomic specificity feature of XAFS spectroscopy renders the technique useful for studying alloys with many components since it permits determination of the local structure of individual components. The only exceptions are those alloys consisting of elements with closely overlapping x-ray absorption edges. The aim of the current investigation is to use XAFS spectroscopy to determine the effect of alloy composition on corrosion and examine the electronic and atomic structure of Fe, Ni, and W in the corrosion products of two W-Ni-Fe alloys immersed in 3.5 weight percent NaCl solution at ambient laboratory temperature and pressure.

Experiment

Two W-Ni-Fe alloys labeled K1 (98.5 W, 0.9 Ni, and 0.6 Fe wt%) and S1 (94.8 W, 3.4 Ni, and 1.9 Fe, wt%) were used in this investigation. Detailed analysis of the microstructure and composition of these alloys as determined by scanning electron microscopy and energy dispersive x-ray analysis was presented in earlier publications.[5,6] Samples in disc form, roughly 1.2 cm in diameter and 0.4 cm thick, were cut from the alloy material with a diamond disc saw. The specimens were wet polished with 320A, 400A, and 600A silicon carbide paper, rinsed with distilled H_2O, acetone degreased, and air dried. Corrosion was then induced by immersing the samples for 17 days in a glass beaker containing 3.5 weight percent NaCl solution (which mimics seawater) at ambient laboratory temperature and pressure.

XAFS spectral measurements were made on both control alloys (no induced corrosion) and corroded alloys. Spectra of the Fe K-edge (7112.0 eV) and Ni K-edge (8333.0 eV) were obtained in the fluorescence detection mode suitable for low elemental concentrations such as those of Ni and Fe.[10] Spectra of the W L_3-edge (10207.0 eV) were measured in both the fluorescence and total electron yield detection modes. The electron yield data are more surface sensitive than fluorescence data, and thus more useful for investigating thin films of corrosion products. The background component due to elastic and Compton scattering of the incident x-rays was minimized by use of an aluminum soller slits assembly and Mn, Co, and Cu filters, each with an effective thickness of three absorption lengths, for the Fe K-edge, Ni K-edge, and W L_3-edge fluorescence data, respectively. The XAFS data were collected from an analysis area of 12 mm by 1 mm. For fluorescence data, 63 percent of the Fe K-edge, Ni K-edge, and W L_3-edge signal originates from a depth of approximately 3.5 µm, 4.0 µm, and 3.6 µm, respectively. For the W L_3-edge total electron yield data, the escape depth for the resulting Auger electrons is estimated at approximately 300 Å.

Reference samples of pure Fe (5 µm thick), pure Ni (6 µm thick), α-Fe_2O_3, and NiO were also investigated to serve as standards for comparison purposes and subsequent data analysis. Samples of research-grade, high purity powders of α-Fe_2O_3 and NiO were prepared for the XAFS measurements by grinding the powder into fine particles. Small particles less than 20 µm in diameter were selected by sieving through a 20 µm size nylon screen. The fine particles were then deposited on Kapton tape and several layers were stacked to give a relatively uniform thickness appropriate for the XAFS measurements in the transmission mode. To ensure the reliability of measured EXAFS amplitudes, XAFS measurements were made with two thicknesses of each sample to check for spurious signals which might arise from the thickness effect. For α-Fe_2O_3, two and four layers giving a $\Delta\mu x$ of 0.53 and 1.00, respectively, and, for NiO, four and eight layers giving a $\Delta\mu x$ of 0.49 and 0.95, respectively, were investigated.

X-ray absorption measurements were performed on beamline X-11A at the National Synchrotron Light Source (NSLS) with an electron energy of 2.5 GeV and a stored current in the range of 110 to 220 mA.[11] Data were collected with a variable-exit, double-crystal monochromator using two flat Si(111) crystals. Harmonics were rejected by applying a 15 percent detuning at 500 eV above the Fe, Ni, and W x-ray absorption edge energies. The x-ray intensities were monitored using ionization chambers filled with nitrogen gas for both the incident and transmitted beams, krypton gas for the fluorescence signal, and helium gas for the total electron yield signal. Energy calibration for the Fe and Ni K-edge data of α-Fe_2O_3 and NiO oxide samples was monitored using Fe and Ni foils as reference samples and a third ion

35

chamber filled with nitrogen gas. All spectra presented here were measured at room temperature (298°K).

Results and Discussion

The normalized x-ray absorption fine structure data, $\mu(E)$, are extracted from the experimentally measured x-ray absorption spectra according to[12,13]

$$\mu(E) = \frac{\mu_o(E) - \mu_p(E)}{\mu_a(E_n)}, \qquad (1)$$

where E is the x-ray photon energy, μ_o is the experimentally measured x-ray absorption with $\mu_o x$ given by $\ln(I_0/I)$ for transmission data, I_f/I_0 for fluorescence data, and I_e/I_0 for electron yield data with I_0, I, I_f, and I_e being the incident, transmitted, fluorescence, and electron yield intensities, respectively, and x is the sample thickness. In determining $\mu_o x$, correction is made for the energy dependence of the incident x-ray intensity in the fluorescence and total electron yield measurements by using cross sections calculated with McMaster coefficients.[14] The pre-edge background absorption, μ_p, is determined from a quadratic fit to the data roughly 300 to 30 eV below the edge energy and then extrapolating over the entire range of the spectrum. The smoothly varying atomic absorption, $\mu_a(E)$, was determined by fitting the post edge data with cubic spline function. An energy-independent step normalization is applied by dividing with the value of the atom-

Description of XANES and EXAFS Spectroscopy

The attenuation of x-rays passing through material takes place via scattering with other electrons in the system, pair production, and the photoelectric effect. Scattering in which the energy of the scattered photon is modified from its initial energy is referred to as Compton scattering. Pair production corresponds to the simultaneous formation of a positron and an electron from a photon, which can only occur when the photon has an energy > 1.02 MeV and passes close to an atomic nucleus. Attenuation of x-rays in the vicinity of an x-ray absorption edge is mainly caused by the photoelectric effect. The photoelectric process takes place when the x-ray photon energy is equal to or greater than the binding energy of a core electron in an atom. In this process, the energy of the x-ray photon is absorbed by the core electron, which is then ejected to unoccupied states above the Fermi level. The occurrence of this process leads to a rapid increase in the x-ray absorption coefficient with increase in energy resulting in a structure referred to as the "x-ray absorption edge." The x-ray absorption edge jump, $\Delta\mu x$ (μ is x-ray absorption coefficient and x is sample thickness), is a quantitative measure of the strength of the absorption process measured as the difference in the absorption cross section above and below the edge energy. The x-ray absorption edge energy is characteristic of the element being investigated, as it represents the binding energy of the inner-shell electrons. In the energy range which extends from threshold up to 40 eV above the x-ray absorption edge energy, the structure is due to electronic transitions to unoccupied states and has been historically referred to as the "x-ray absorption near-edge structure (XANES)." For energies extending from 40 up to 1500 eV above the edge energy, an oscillatory fine structure referred to as the "extended x-ray absorption fine structure (EXAFS)" is observed. These EXAFS oscillations are due to the interference of the outgoing wave of the ejected photoelectron, with ingoing waves due to scattering by electrons of neighboring atoms. The outgoing and ingoing waves interfere constructively or destructively in a manner characteristic of the local atomic structure. Analysis of these oscillations provides information with regard to coordination number (number of atoms at a fixed distance) and bond length.

When a core level of an atom is ionized, such as by absorbing an x-ray photon (i.e., photoelectric effect), the atom can decay to a lower energy state through an electronic rearrangement. The energy difference between these two states of the atom will be released by emitting a fluorescence photon, in the radiative decay mode, or by emitting an Auger electron, in the nonradiative decay mode. In both cases, the energy of the emitted fluorescence photon or the Auger electron is characteristic of the parent atom. Since both the fluorescence yield and the Auger electron yield are proportional to the absorption cross section, measurements of the EXAFS oscillations can be achieved by measuring the fluorescence or the Auger electron yields. EXAFS measurements in the fluorescence mode increase the sensitivity of local structure determinations for atomic species that are present in small quantities as low as a few parts per million. EXAFS measurements in the electron yield mode provide surface sensitivity due to the smaller escape depth of electrons relative to photons.

36

ic absorption $\mu_a(E_n)$, where E_n is the normalization energy and is taken to be 100 eV above the edge energy.

The normalized XANES of the fluorescence Fe and Ni K-edges and the electron yield W L_3-edge data are shown in Figures 1, 2, and 3, respectively, where the normalized absorption coefficient is plotted as a function of photoelectron energy. Data of the Fe and Ni K-edges are plotted on the same scale with the upper spectra shifted vertically for clarity of presentation. Examination of the data in Figure 1 indicates that the XANES for Fe in the control alloys is distinct from that of metallic Fe with body-centered cubic lattice (BCC). The XANES of Fe in the control samples, in fact, is similar to the XANES of metallic Ni with face-centered cubic (FCC) lattice (shown in Figure 2), indicating the formation of an Fe-Ni solid solution with an FCC lattice. Inspection of the Fe K-edge XANES of control and corroded alloys reveals that the chemistry and structure of at least a fraction of Fe in both of the corroded alloys differ significantly from those of Fe in the control alloys. Comparison of the XANES for Fe in the corroded alloys with that of Fe_2O_3 indicates that a large fraction of Fe in the corroded alloys is present in an oxidized form of Fe. The oxidation state of the oxidized Fe in the corroded samples of both alloys is +3 (i.e., Fe^{+++}). From the analysis of the intensity of the shoulder at the onset of the edge, the fraction of Fe^{+++} is estimated at 0.72 in the S1 alloy and 0.47 in the K1 alloy (Table 1).

Figure 1. Normalized XANES data of the Fe K-edge.

Table 1. Summary of XANES and EXAFS Analysis

Alloy	% Oxidized Fe from Analysis of		% Oxidized Ni from Analysis of	
	XANES and	EXAFS	XANES and	EXAFS
K1	47	54	11	14
S1	72	68	18	17
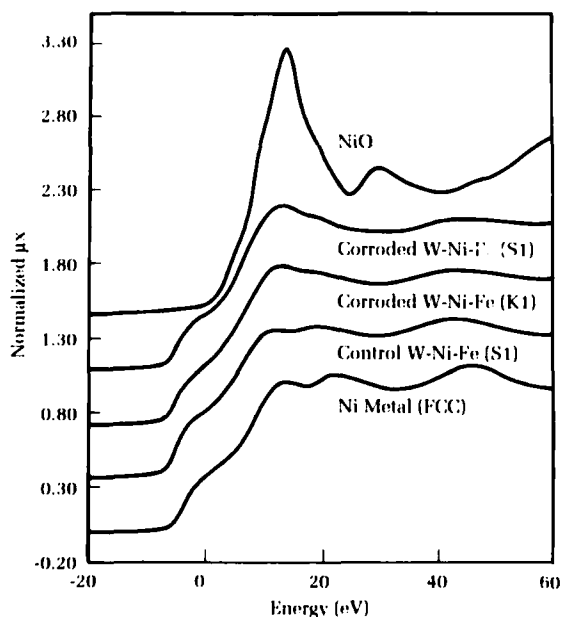
Figure 2. Normalized XANES data of the Ni K-edge.

Figure 3. Normalized XANES data of the W L_3-edge.

The Ni K-edge XANES data of control and corroded samples (Figure 2) indicates that Ni in the corroded samples is mainly metallic with only a small fraction of Ni in an oxidized state. From the analysis of the intensity of the shoulder at the onset of the edge, the fraction of oxidized Ni is estimated at 0.18 in the S1 alloy and 0.11 in the K1 alloy (Table 1).

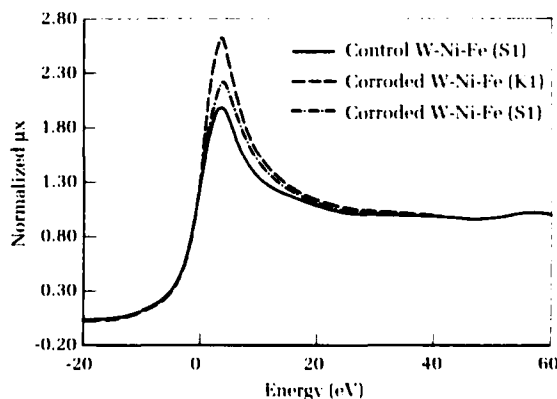The W L_3-edge XANES data of control and corroded samples (Figure 3) show prominent white lines, with the white-line intensity for the corroded samples of both alloys being greater than that of the control samples, indicating the presence of oxidized W. Furthermore, the intensity of the W L_3 edge white line for the K1 alloy is significantly greater than that of the S1 alloy, indicating that the fraction of oxidized W in the corroded K1 alloy is larger than that in the S1 alloy. This result is contrary to the fact that the fraction of both oxidized Fe and Ni is greater in the corroded S1 alloy relative to that of the corroded K1 alloy. Determination of the percent of oxidized W was not made due to lack of standards.

Next we turn our attention to the EXAFS portion of the XAFS region. The normalized EXAFS data, $\chi(k)$, are given by

$$\chi(k) = \left(\frac{\mu(k) - \mu_a(k)}{\mu_a(k_n)}\right)\left(\frac{\mu_m(k_n)}{\mu_m(k)}\right) . \qquad (2)$$

where k is the photoelectron wave number given by

$$k = \sqrt{2 \frac{m}{\hbar^2} (E - E_o)} . \qquad (3)$$

with E being the X-ray photon energy and E_o the edge energy. The function $\mu_m(k)$ represents the atomic absorption calculated with McMaster coefficients[14] which provides the energy-dependent normalization and k_n is the photoelectron wave number corresponding to the normalization energy E_n.

Figures 4 and 5 show a comparison of the normalized Fe and Ni K-edge EXAFS data, $\chi(k)$, respectively, of control and corroded samples of both alloys. The $\chi(k)$ data are plotted versus the photoelectron wave number after subtraction of the smooth background above the edge. The frequency and amplitude of the Fe EXAFS oscillation in the corroded samples are significantly different from those of Fe in the control samples of both alloys, indicating that the local structure of at least a fraction of Fe in the corroded samples is significantly altered from that in the control samples. The frequency and amplitude of the Ni oscillations in the corroded and control samples of both alloys are mainly similar, with only small variations in the low k region. Consequently, the local structure of

only a small fraction of Ni in the corroded samples of both alloys is altered from that of Ni in the control samples.

Comparisons of Fourier transforms (i.e., radial structure functions) of Fe and Ni $\chi(k)$ data for control and corroded S1 alloy are displayed in Figure 6. In addition, we have also displayed in Figure 6 the Fourier transforms data for bulk α-Fe$_2$O$_3$ and NiO oxides. These Fourier transforms display peaks corresponding to coordination spheres of the local structure. The amplitudes of the peaks are related to the coordination number and disorder in the material. The Fourier transforms are not phase corrected, and, hence, the peak positions are shifted to lower distances from the real crystallographic distances. The Fourier transform of Fe in the corroded alloy, when compared with the Fourier transform of Fe in the control alloy and α-Fe$_2$O$_3$, demonstrates (1) significant reduction

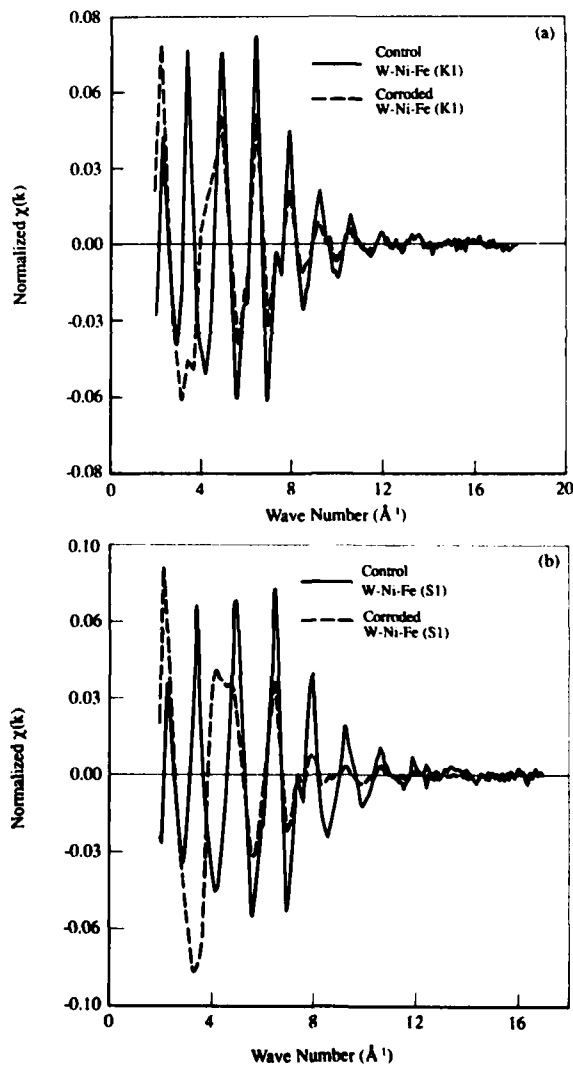
Figure 4. Normalized EXAFS data, χ(k), of the Fe K-edge for: (a) control and corroded samples of alloy K1; (b) control and corroded samples of alloy S1.

38
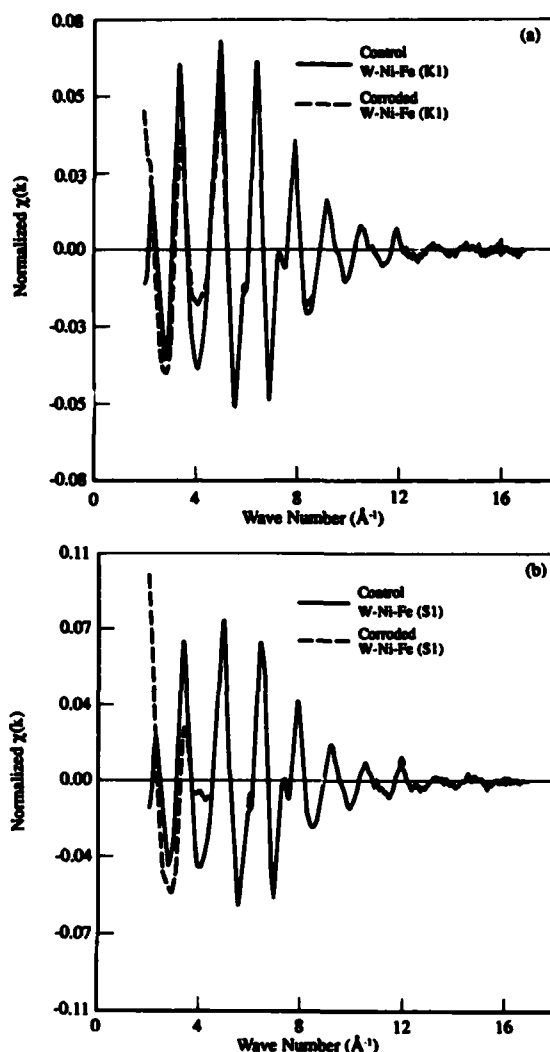
Figure 5. Normalized EXAFS data. $\chi(k)$, of the Ni K-edge for: (a) control and corroded samples of alloy K1: (b) control and corroded samples of alloy S1.

Figure 6. Fourier transforms comparisons: (a) of the Fe K-edge $\chi(k)$ over the k-range of 2.1-12.3 Å-1 for control and corroded alloy S1, and α-Fe_2O_3: (b) of the Ni K-edge $\chi(k)$ over the k-range of 2.1-13.0 Å-1 for control and corroded alloy S1, and NiO.

in the amplitude of metallic Fe in the corroded alloy relative to that of the control alloy. (2) the development of an oxide component similar to that of α-Fe_2O_3, and (3) that the significantly reduced amplitudes of higher coordination spheres of the oxide component in the corroded alloy relative to those in α-Fe_2O_3 indicate a highly structurally disordered form of α-Fe_2O_3. Comparisons of Ni data for the corroded alloy with Ni data for the control alloy and NiO demonstrate (1) a small reduction in the amplitude of the metallic Ni component, and (2) the development of a small oxide component.

In Figure 7, the Fourier transforms of Fe and Ni of the corroded S1 alloy are compared with those of the corroded K1 alloy. Examination of these data reveals that the fractions of oxidized Fe and Ni are greater in the S1 alloy relative to those of the K1 alloy. Based on the amplitudes

of the peaks corresponding to oxidized Fe and metallic Ni in the Fourier transform data of both alloys, it is estimated that the fractions of oxidized Fe are 0.68 and 0.54 for S1 and K1 alloys, respectively. The fractions of oxidized Ni are 0.14 and 0.17. These results compare favorably with results from XANES analysis (Table 1).

Analysis of W L_3 EXAFS data and their corresponding Fourier transforms of both alloys (not shown) reveals no significant changes in the chemistry and structure of W in the corroded alloys from those of the control alloys. The fact that the XANES data of the W L_3-edge indicate that some oxidized W is present in the corroded alloys is caused by the inherent sensitivity of the white-line intensity to small quantities

39

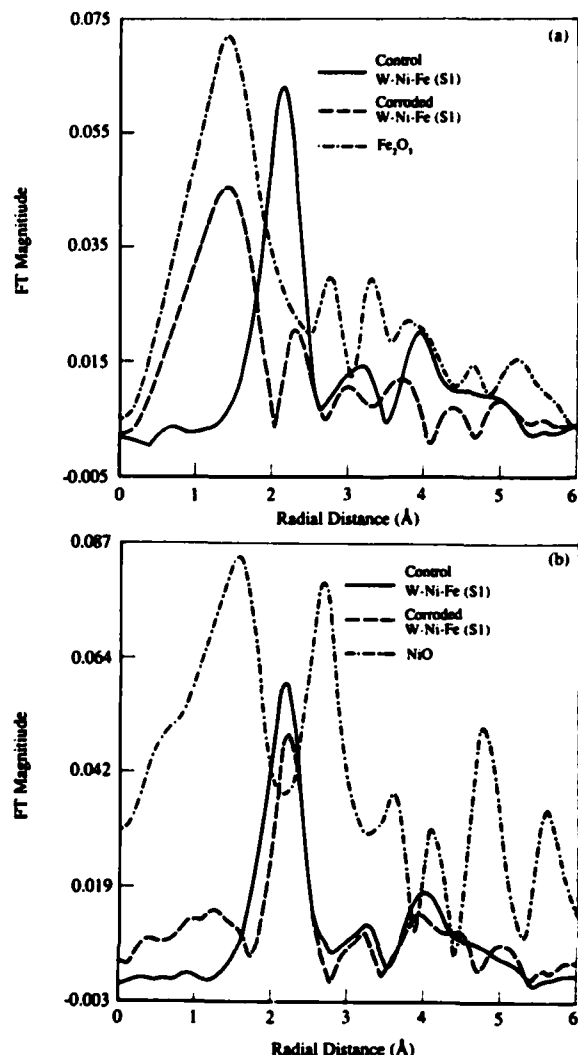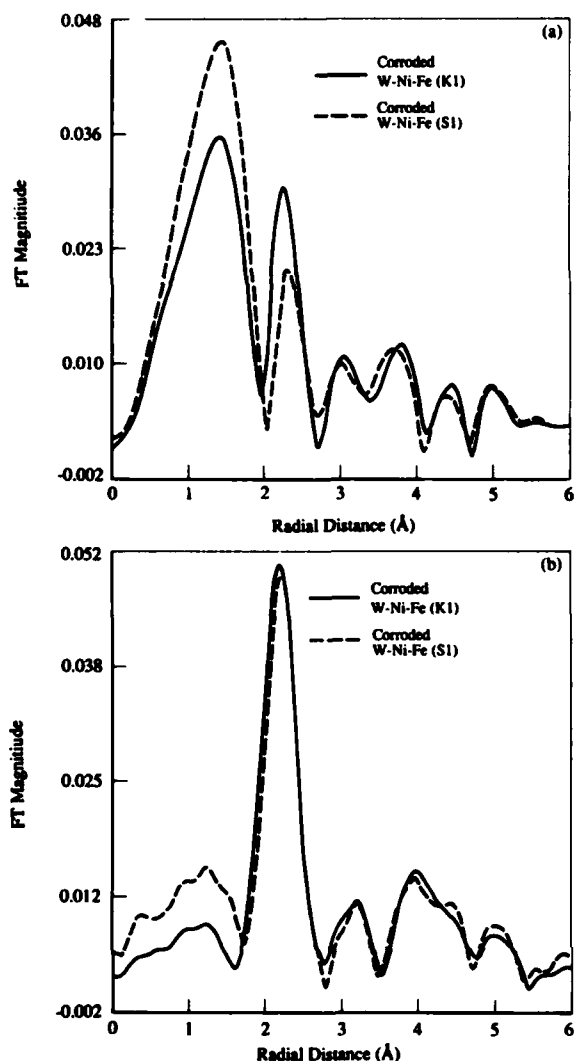**Figure 7.** Fourier transforms comparisons: (a) of the Fe K-edge $\chi(k)$ over the k-range of 2.1-12.3 $Å^{-1}$ for corroded K1 and S1 alloys; (b) of the Ni K-edge $\chi(k)$ over the k-range of 2.1-13.0 $Å^{-1}$ for corroded K1 and S1 alloys.

of oxidized species. Because the backscattering from W overwhelms that of oxygen, EXAFS is less sensitive than XANES for detecting oxidized W. The presence of oxidized W based on the analysis of XANES data is consistent with x-ray photoelectron spectroscopy results obtained in our laboratory.

Conclusions

Within the depth analyzed by XAFS spectroscopy, we conclude that (1) the chemical and structural nature of corrosion products on both alloys is similar to that of a highly structurally disordered form of α-Fe_2O_3, (2) the chemistry and structure of Ni in the corroded alloys remain unchanged from those in the control samples except for a small fraction (less

than 20 percent), which is present in an oxidized form, and (3) W is the alloy component least affected by the corrosion process.

References

1. Jones, P. N., "The Use of Tungsten in Armament Related Products," *Proc. Second International Tungsten Symposium,* San Francisco, CA, 1-5 Jun 1982, pp. 81-90.

2. Jones, D. J. and Munnery, P., "Production of Tungsten Alloy Penetration Radiation Shields," *Powder Metallurgy,* Vol. 10, No. 20, 1967, p. 156.

3. Andrew, J. F., Baker, M. T., and Heron, H. T., "Corrosion and Protection of Sintered Tungsten Alloy Ammunition Components," *Proc. Second Charlottesville Conference on High Density KE Penetrator Materials,* 1980.

4. Koger, J. W., "Corrosion of Tungsten-3.5 Nickel-1.5 Iron and its Constituent Phases in Aqueous Chloride Solutions," *Corrosion/75,* NACE, Paper No. 42, 1975.

5. Vasanth, K. L., Conrad, R., and Dacres, C. M., "Pitting Behavior of Tungsten Alloys in 3.5% NaCl Solution," *Proc. 11th International Corrosion Congress,* Florence, Italy, Vol. 5, 2-6 Apr 1990, p. 5.223.

6. Vasanth, K. L. and Dacres, C. M., "Corrosion of Tungsten Alloys in Marine Environments," *Proc. 1987 Tri-Service Conference on Corrosion,* W-PAFB, OH, AFWAL-TR-87-4139, Vol. II, 1987, p. 165.

7. Davenport, A. J., et al., "In situ X-Ray Absorption Study of Chromium Valency Changes in Passive Oxides on Sputtered AlCr Thin Films Under Electrochemical Control," *Electrochemical Society,* Vol. 138, 1991, p. 337.

8. Mansour, A. N., "Evidence for an Ag_4O_3 Phase of Silver Oxide," *J. Physical Chemistry,* Vol. 94, No. 2, 1990, p. 1006.

9. McBreen, J., O'Grady, W. E., and Pandya, K. I., "EXAFS: A New Tool for the Study of Battery and Fuel Cell Materials," *J. Power Sources,* Vol. 22, No. 4, 1988, p. 323.

10. Lytle, F. W., et al., "Measurement of Soft X-Ray Absorption Spectra with a Fluorescent Ion Chamber Detector," *Nuclear Instruments and Methods in Physics Research,* Vol. 226, 1984, p. 542.

11. Sayers, D. E., et al., "X-Ray Beam Line at the NSLS for X-Ray Absorption Studies in Material Science," *Nuclear Instruments and Methods in Physics Research,* Vol. 208, 1983, p. 631.

12. Sayers, D. E. and Bunker, B. A., "Data Analysis," *X-Ray Absorption, Principles, Applications, Techniques of EXAFS, SEXAFS And XANES,* D. C. Koningsberger, R. Prins, Ed., John Wiley & Sons, New York, NY, 1988, pp. 211-253.

40

13. Cook, J. W. and Sayers, D. E., "Criteria for Automatic X-Ray Absorption Fine Structure Background Removal," *J. Applied Physics*, Vol. 52, No. 8, 1981, p. 5024.
14. McMaster, W. H., et al., "Compilation of X-Ray Cross Sections," National Technical Information Service, Springfield, VA, 1969.

The Authors

A. N. MANSOUR joined the Weapons Research and Technology Department at the White Oak Detachment as a research physicist in October 1984. He received his Ph.D. in physics from the North Carolina State University (NCSU) in May 1983. He then joined NCSU as a research associate, investigating the effects of electronic and atomic structures on the catalytic activity of nanophase particles, using XANES and EXAFS synchrotron radiation experiments. In addition, he conducted research involving AES and XPS characterization of semiconductor thin films. At White Oak, Dr. Mansour conducted research which led to the discovery of a previously unknown phase of silver oxide resulting in the solution of an operational problem with silver oxide/zinc batteries and a new process for fabricating superior electrodes. Currently, he is performing synchrotron radiation research in the areas of high temperature superconductors, aluminum-rich amorphous alloys, corrosion, multilayered thin films, and thermoluminescent phosphor materials. Dr. Mansour is a member of both the American Physical and the Electrochemical Societies.

KUNIGAHALLI L. VASANTH is the senior research chemist in the Corrosion Technology Group at the White Oak Detachment, which he joined in 1985. He received his Ph.D. in chemistry from the University of Baroda, India. Dr. Vasanth worked as Professor and Head of the Department of Chemistry in PSG College of Technology, University of Madras, India. He worked as Associate Professor at the University of Lille, France (1976), and later carried out postdoctoral research work at Georgetown University, Washington, D.C. Before joining White Oak, he worked for several years at the Goddard Space Flight Center, Greenbelt, Maryland, performing research on nickel-cadmium batteries. His primary research interests are in the fields of corrosion prevention and control, and rechargeable secondary batteries. Under the leadership of Dr. Vasanth, the Corrosion Technology Group has provided several recommendations to control corrosion of the AEGIS combat systems, representing substantial cost savings to the Navy. His work has resulted in numerous publications.

Structures and Mechanical Properties of Centrifugally Cast SiC/Al Composites

A. P. Divecha, S. D. Karmarkar, M. N. Gungor, and A. H. Nakagawa

Metal matrix composites (MMCs) such as silicon carbide/ aluminum (SiC/Al) are in the forefront of advanced materials technology, with potential Navy application to the stable member in Trident II missiles, mines, torpedoes and their transducers, and shipboard antennae. Because powder metallurgy MMC fabrication techniques are expensive, the White Oak Detachment has developed an inexpensive MMC fabrication process known as centrifugal casting, using ingot metallurgy SiC/Al with superior fluidity. With samples fabricated by this method, we have characterized the structures and mechanical properties of SiC-A356 Al particulate-reinforced composites. The results demonstrated that a range of mechanical properties can be obtained as a function of microstructure, and that overall the strength and modulus of the composite layers were superior to those of the corresponding unreinforced Al layers.

Introduction

Compared to monolithic aluminum alloys, particulate-reinforced, aluminum-based composites offer a 10 to 25 percent increase in strength and a 30 to 80 percent increase in stiffness. Because these composites are stiffer than their monolithic counterparts, stiffness-limited components can be designed using reduced cross sections and attendant reductions in component weights.

Centrifugal casting offers an economical means of processing controlled composite structures, making it an attractive processing route for the production of particulate-reinforced tubes.[1-3] Rotation of the casting during solidification causes the components of the composite melt to segregate, and subsequently to solidify into well-defined, layered structures. This process can be controlled to drive the denser particles such as SiC toward the outer regions of the less dense Al matrix alloy. In this way, particulate loading can be increased in the outer layers of the tube, with concomitant increases of stiffness in this region. In addition, the centrifugally cast structures solidify in relatively short times, thereby improving production rates. Furthermore, the resultant structures are sounder than those of conventionally cast structures, thus producing better mechanical properties. Moreover, lightweight impurities and porosity can be driven toward the inner surface of the casting, where they can subsequently be machined away. Finally, since the castings do not have large risers (except at the inner surface, which effectively acts as a riser), the scrap rate is low compared to other foundry methods. This provides an added benefit by reducing the cost of raw materials for the already low-cost process.

Centrifugal casting processing of metal matrix composites was therefore investigated as a cost-effective, innovative means of producing high-integrity, high-stiffness structural tubes. This investigation demonstrated the use of centrifugal casting to produce controlled structures in SiC-A356 Al composites

42

on a laboratory scale. The structure and room temperature tension and compression properties of the samples produced were evaluated and correlated.

Experimental Work

Unreinforced A356 Al alloy and SiC particle-reinforced A356 Al alloy composites were used. The unreinforced Al alloy ingots were purchased from Belmont Metal Inc., Brooklyn, New York; the composite materials were procured from the Dural Aluminum Composites Corporation, San Diego, California.

Sample Fabrication

The samples, of 10 cm outside diameter (OD), 5 cm inside diameter (ID), and 13 cm long, were fabricated using a horizontal centrifugal casting machine and an experimental test matrix. The experimental test matrix was a statistical design of experiments to study centrifugal casting variables, which are not discussed in this article. Melting of materials was achieved in a resistance-heated furnace. The melt was then removed from the furnace and immediately poured into a rotating mold at a designated speed. The mold was rotated until solidification of the casting was complete. The mold was then arrested and the casting extracted for evaluation.

Structure Characterization

The macro- and microstructures of the cast samples were evaluated in the transverse and longitudinal directions of the castings. The macrostructures were revealed by grinding the samples with SiC particle-embedded papers (up to 600-grit size paper) with water lubrication in a semiautomatic polishing machine. Continued polishing with the diamond pastes (9, 6, and 1 μm diamond pastes) and an oil lubricant and etching with 5 percent hafnium solution revealed the material microstructures.

Three techniques quantified the extent of SiC particle segregation: wet chemical analysis, segregation ratio determination, and point-count technique. First, sample chips were drilled from the segregated layers. To determine the ratio of the SiC particulate to the alloy in the sample, the material chips were analyzed using a standard wet-chemical analysis procedure developed at the Dural Aluminum Composites Corporation. Second, by macroscopically observing the segregated layers of the casting, we measured the thicknesses of the SiC-depleted layer and the SiC-enriched layer.

We then defined a dimensionless "segregation ratio" term to express the extent of the SiC segregation on a comparative basis. The segregation ratio, S, an arbitrary definition, is given by

$$S = 1 - (R_m/R_c)^2. \qquad (1)$$

where R_m is the measured outer radius of the metal-rich layer, and R_c is the outer radius of the casting. The significance of this term is that as S decreases, the severity of the segregation increases. Distribution of the SiC particles was obtained as a function of radial distance by using a quantitative point-count technique developed by Hilliard and Cahn.[4]

Tension and Compression Testing

Flat tensile specimens were machined from the SiC-enriched layers of the cast samples parallel to the axial direction of the castings. Diamond tooling was used to machine the composite specimens. After machining, the specimens were heat treated to either the T6 condition or the T61 condition. Tension and compression tests were conducted at room temperature per ASTM D3552 and ASTM E9 in a Satec universal testing machine, model 30WBN. The tensile strain was measured with a 25.4-mm gauge length extensometer. Cylindrical compression specimens of 6.4 mm OD and 19 mm long were machined from the SiC-enriched layers of the cast samples in the axial direction. Compressive 0.2 percent offset yield strength and modulus were obtained with an extensometer of 12.7-mm gauge length. Due to the limitation imposed by the specimen geometry, deformation above the yield point was monitored by the load versus crosshead displacement output of the testing machine. The tension and compression test speeds were 0.042 cm/s. Two tests were conducted per material condition.

Results and Discussion

Casting Morphology

Figure 1 shows the typical cast samples of 10-volume-percent SiC-A356 Al. Although each specimen was produced with the different process variables, there are two distinct groups of samples. The four samples on the left-hand side of the picture were produced with a thermally conducting mold (graphite-coated steel mold). The four samples on the right-hand side were produced with a thermally insulating mold (alumina-coated steel mold).

43

Some of the readily observable characteristics of the samples shown are that those produced with the conducting mold have metallic, smooth, inhomogeneous surfaces. On the other hand, the samples produced with the insulating mold have rough, homogeneous surfaces.

The thermally conductive mold increases the rate of heat transfer from the casting to the mold. In this situation, due to relatively rapid heat removal from the castings, the surfaces of the castings contained traces of the rapidly solidified droplets and progressive traces of the molten metal flow. Therefore, the castings were produced with inhomogeneous surfaces because of enhanced heat transfer from the casting to the mold.

In the case of the insulating mold, however, the reduced heat transfer rate from the casting to the mold allows the molten metal to flow freely (i.e., without premature solidification) and cover the mold's inner surface completely before solidifying. Droplets that impinged on the mold ahead of the major flow of the liquid either did not solidify on contact or were remelted by the major flow of the molten metal. Therefore, the insulating mold produced homogeneous surfaces by reducing heat transfer rate from the casting to the mold. Further evidence

to support this mechanism will be presented following the materials macrostructure characterization section.

Macrostructure

The transverse macrostructures of the samples are shown in Figure 2 as a function of the initial composite composition and the mold thermal properties. Each of the macrostructures shows two layers: a segregated composite (SiC particle-rich) outer layer, and a metal inner layer. The two layers were separated by a well-defined interface. The thickness of the segregated layers in the samples produced with the conducting mold are greater than the corresponding samples produced with the insulating mold, i.e., more complete SiC particle segregation was produced in the latter case.

The longitudinal macrostructures of the samples produced with the two molds showed that the thickness of the segregated layer was more uniform in the insulating mold than in the conducting mold. Typical macrostructures of the two cases are shown in Figure 3. The darkness of the SiC particle segregated layer is proportional to the SiC concentration, i.e., the

Figure 1. The 10-volume-percent SiC/A356 Al composite cast samples (OD = 10 cm).
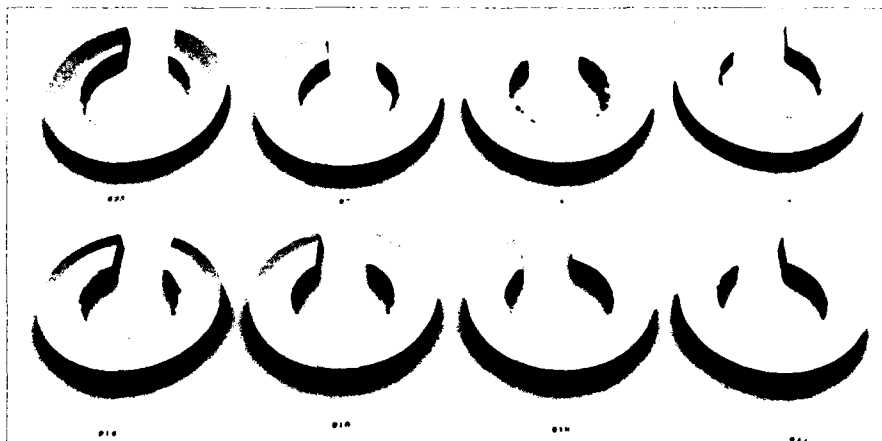
44

Figure 2. Macrostructures of the transverse sections of samples produced with the conducting mold (above) and the insulating mold (below) (OD = 10 cm).

darker the layer, the higher the SiC concentration. Figure 3 shows that the sample produced with the insulating mold has uniform contrast along the longitudinal and radial directions, whereas the corresponding conducting mold shows nonuniform contrast in the longitudinal and radial directions, an indication that the SiC distribution is more homogeneous in the former.

Modeling

A physical model based on the observations presented thus far is proposed as follows. Droplets form at the molten metal front as it enters the spinning mold. A thermally conducting mold does not retard heat transfer from the casting. Due to rapid heat removal through the mold, the droplets solidify instantly as they impinge on the mold surface. Then, as the molten metal front covers the inner surface of the mold (i.e., as it flows from the entrance of the mold to the far end), it solidifies progressively on contact with the mold surface, thus resulting in the flow traces observed on the casting surfaces (Figure 1) and in the internal structures (Figure 3). Because heat is removed from the progressive layers at such a fast rate, it does not remelt the droplets, and the droplets are covered by the progressively solidified layers. The conducting mold thus provides an inhomogeneous surface and internal structure by enhancing heat transfer from the casting at

Figure 3. Macrostructures of the longitudinal cross section of the samples produced using the conducting (above) and insulating (below) molds (length: 13 cm).

the mold/metal interface, causing local freezing before the entire inner surface of the mold has been covered by molten metal. This physical model is illustrated in Figure 4.

The insulating mold delays transfer of heat from the castings and allows the molten metal to flow freely (i.e., without premature solidification) and to cover the mold's inner surface. Any molten droplets that solidify ahead of the liquid flow are remelted as they are covered by the molten layer filling the mold. Once the mold's surface is covered by molten metal,
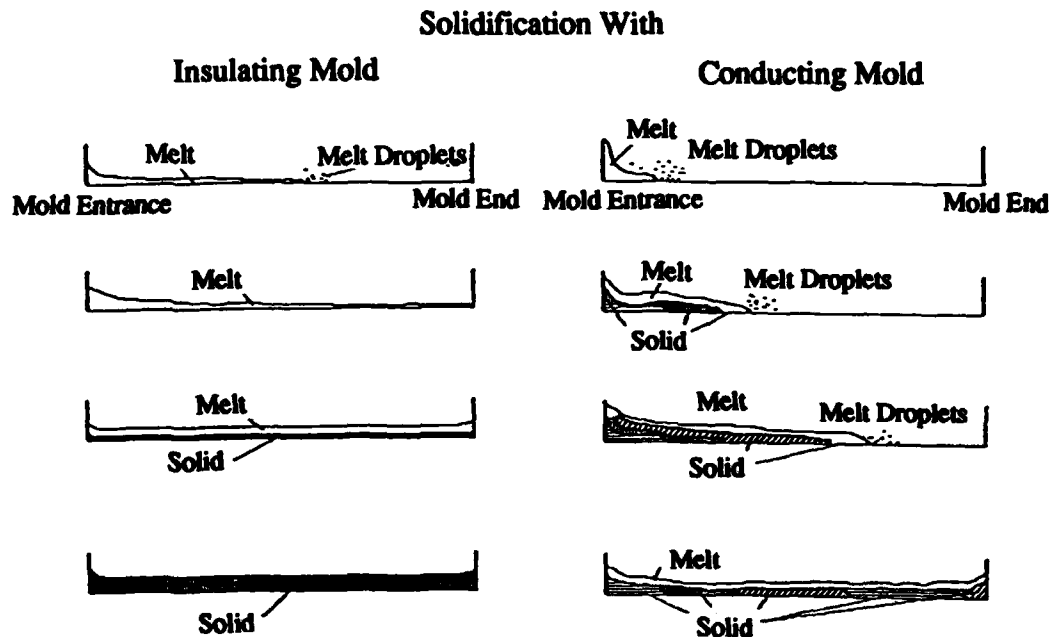
Solidification With

Insulating Mold

Conducting Mold

Figure 4. Physical models for centrifugal casting and solidification process as a function of mold thermal properties.

45

the solidification proceeds in the radial direction. The insulating mold thus provides a homogeneous surface and internal structure by delaying heat transfer from the casting at the mold/metal interface until the mold's inner surface has been covered by the molten metal. The physical model for this case is also illustrated in Figure 4.

Microstructures

Typical optical microstructures of the centrifugal castings are presented in Figures 5 and 6 for the conducting and insulating molds, respectively. In each figure, the transverse micrographs are shown as a function of radial distance. As expected, the SiC particles were distributed inhomogeneously in the microstructures in Figure 5, and more homogeneously in the microstructures in Figure 6. In both cases, the microstructure of the inner metal layer is predominately equiaxed dendrites. Typical Al-Si eutectic phase was located within the dendritic spaces. In the SiC-segregated regions the dendritic morphology is less obvious, particularly for the case of the insulating mold. More microporosity is observed to be associated with the SiC particles in the insulating mold.

SiC Segregation

Chemical Analysis. The results of the wet-chemical analysis are given in Table 1. The outer-layer SiC composition is plotted in Figure 7a, which shows two groups of data: those produced with the conducting mold and those produced with the insulating mold.

As listed in Table 1, the average SiC composition of the former samples was 11.9 volume percent, while that of the latter samples was 24.8 volume percent. Considering that the initial composition contained an average of 10-

Table 1. SiC Volume Percent Measured by Wet-Chemical Analysis – Initial Composition: 10-Volume-Percent SiC

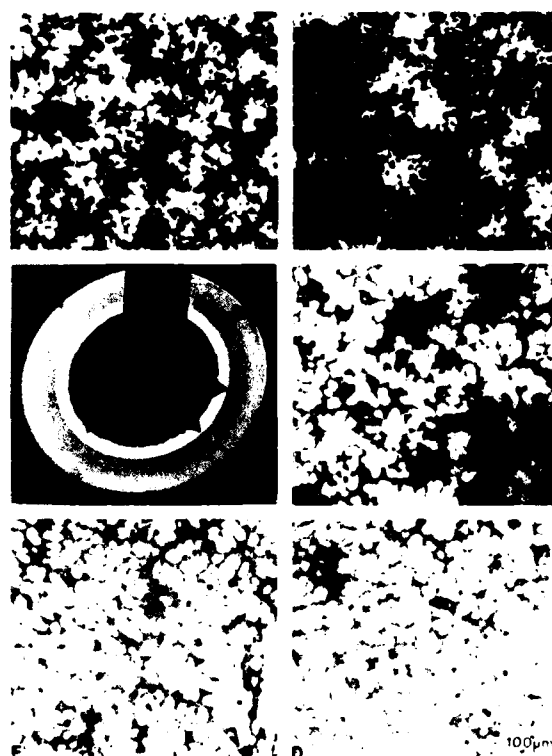| Specimen No.	Mold Type	SiC Vol% Outer Layer	SiC Vol% Inner Layer
10	Conducting	12.1	1.2
12	Conducting	11.2	1.2
7	Conducting	12.4	1.3
Average	Conducting	11.9 ± 0.6	1.2 ± 0.6
14	Insulating	23.9	0.3
18	Insulating	25.8	0.3
Average	Insulating	24.8 ± 1.3	0.3 ± 0

Figure 5. Microstructure of the sample produced using the 10-volume-percent SiC/A356 Al in the conducting mold.
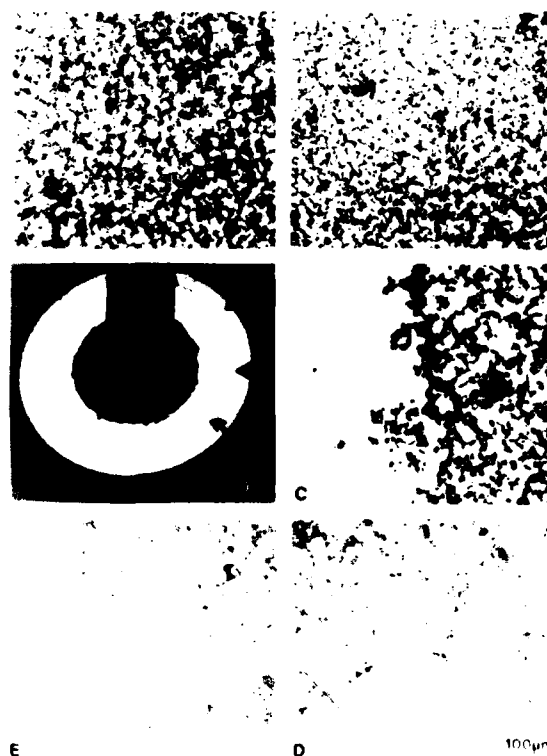

Figure 6. Microstructure of the sample produced using the 10-volume-percent SiC/A356 Al in the insulating mold.
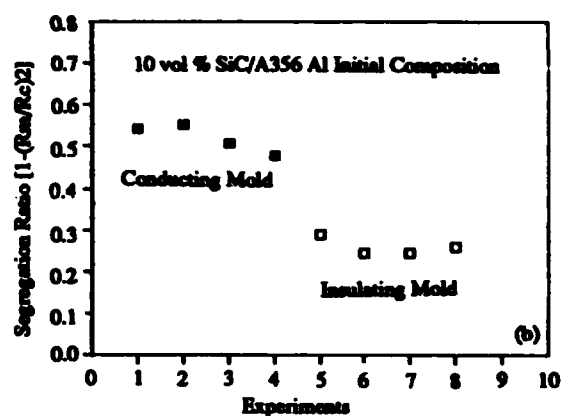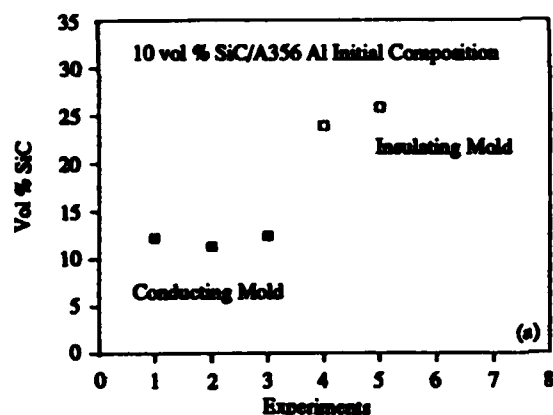
46

Figure 7. SiC segregation by wet-chemical analysis (a) and by segregation ratio measurement (b).

volume-percent SiC, the centrifugal casting process increased the SiC composition by factors of approximately 1.2 and 2.5, respectively.

Segregation Ratio. The segregation ratio measurements are given in Table 2, and the data are plotted in Figure 7b for the 10-volume-percent SiC initial composition. In an analogous manner to the previous chemical analysis results, the segregation ratio depended strongly on the mold type. The average segregation ratios of the samples produced with the 10-volume-percent SiC initial compositions were 0.52 and 0.25 for the conducting mold and insulating mold, respectively.

SiC Distribution. The results of the point-count experiments are shown in Figure 8 for two samples that were produced using the 10-volume-percent SiC initial composition, and the conducting and insulating molds. The volume-percent SiC data are plotted against radial distance. The average composition of the segregated regions was 25.6 volume percent and 11.2 volume percent SiC, respectively.

Table 2. Segregation Ratio Measurements – Initial Composition: 10-Volume-Percent SiC

Factorial Experiment No.	Specimen No.	Mold type	Segregation Ratio $1-(R_m/R_c)^2$
1	10	C	0.54
2	14	I	0.29
3	12	C	0.55
4	18	I	0.24
5	23	C	0.51
6	16	I	0.24
7	7	C	0.47
8	22	I	0.26

Average segregation ratio of "all C" = 0.52 ± 0.03
Average segregation ratio of "all I" = 0.25 ± 0.02
C = Conducting Mold   I = Insulating Mold

These data agree with the results of the wet-chemical analysis.

Tension and Compression Testing

The data for the tension and compression tests are given in Tables 3 and 4, for the A356 Al, 10-volume-percent SiC/A356 Al, and 20-volume-percent SiC/A356 Al samples. An analysis of the data as a function of the material microstructure is given as follows:

The only effect of the thermal properties of the molds on the tensile and compressive properties of the unreinforced A356 Al was that the tensile ductility was higher by a factor of two in the case of the insulating mold. However, in the case of the 10-volume-percent SiC initial composition, the composite samples produced with the insulating mold showed higher tensile yield strengths and compressive strengths, as shown in Figure 9. The average tensile yield strength values were of 215±14 MPa
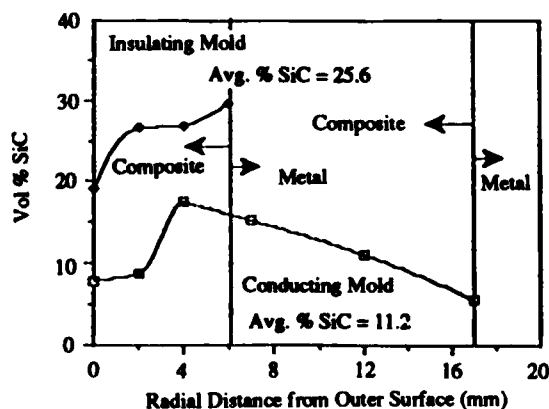
47

Figure 8. SiC volume-percent distribution as a function of radial distance for two samples produced with the conducting and insulating molds.

Table 3. Tensile Properties of A356 Al and SiC/A356 Al Composites

Specimen No.	Composition (Vol% SiC)	Material Condition	0.2% Offset Yield Strength (MPa)	Ultimate Tensile Strength (MPa)	Tensile Elongation (%)	Tensile Modulus (GPa)
6	0	C/T6	174 ± 0	255 ± 11	5.3 ± 1.7	70
6	0	C/Hip+T6	168 ± 6	280 ± 0	13.3 ± 1.8	73
17	0	I/T6	151 ± 12	259 ± 7	10.6 ± 1.1	64
17	0	I/Hip+T6	162 ± 3	276 ± 2	16.5 ± 2.1	80 ± 18
10	10	C/T6	221 ± 20	242 ± 4	0.6 ± 0.1	94 ± 7
10	10	C/Hip+T6	248 ± 0	256 ± 0	0.7 ± 0.4	94 ± 1
10	10	C/Hip±T61	182 ± 4	252 ± 48	2.2 ± 2.0	102 ± 14
14	10	I/T6	241 ± 5	255 ± 10	0.6 ± 0.1	91 ± 15
14	10	I/Hip+T6	274 ± 9	313 ± 17	0.7 ± 0.4	102 ± 23
14	10	I/Hip+T61	208 ± 2	246 ± 43	0.8 ± 0.3	98 ± 13
23	10	C/T6	212 ± 8	285 ± 4	3.2 ± 0.2	89 ±1
23	10	C/Hip+T6	219 ± 6	289 ± 20	2.4 ± 1.4	100 ± 25
23	10	C/Hip+T61	169 ± 1	244 ± 20	2.7 ± 1.9	94 ± 5
16	10	I/T6	255 ± 16	293 ± 2	0.8 ± 0.3	109 ±13
16	10	I/Hip+T6	268 ± 20	332 ± 16	1.2 ± 0.0	122 ± 5
16	10	I/Hip+T61	209 ± 16	255 ± 20	1.1 ± 0.8	104 ± 8
24	20	C/T6	279 ± 12	326 ± 6	0.9 ± 0.0	116 ± 30
26	20	I/T6	304 ± 26	330 ± 43	0.6 ± 0.1	129 ± 37
27	20	I/T6	310 ± 17	353 ± 14	0.7 ± 0.0	144 ± 12
29	20	I/T6	277 ± 3	316 ± 4	0.8 ± 0.0	121 ± 5

HIP: At 500 °C for 4 hours under 100 MPa Argon pressure
T6: Solution treatment at 537 °C in air for 4 hours, quench in water at 65 °C, age at 155 °C for 4 hours
T61: Same as T6 but age at 25 °C
C: Conducting mold
I: Insulating mold

(MegaPascal) and 254±15 MPa, respectively. Thus, there was an approximately 17 percent increase in tensile yield strength for the insulating mold over the conducting mold. Similarly, the compressive yield strengths of the 10-volume-percent SiC composition averaged about 226±10 MPa and 257±23 MPa for the conducting and insulating molds, respectively.

The effects of the composition on the tensile and compressive strengths are presented in Figure 10. The mean effect of composition on the tensile yield strength was determined by averaging the data points that fell into each individual composition group: 0-volume-percent SiC, 10-volume-percent SiC, and 20-volume-percent SiC. As the lines drawn in Figure 10 clearly show, the average tensile yield strength increased as the composition increased. The average yield strengths were 164±10 MPa, 242±24 MPa, and 292±18 MPa for the 0-volume-percent SiC, 10-volume-percent SiC, and 20-volume-percent SiC compositions, respectively. As in the case of the tensile

response, the compressive strength increased as the composition increased. As given in Tables 3 and 4, the tensile and compression moduli increased as the SiC composition increased. For example, the average tensile moduli calculated were 71.6±11 GPa (GigaPascal), 101.2±13.1 GPa and 127.5±20 GPa, for the 0-volume-percent SiC, 10-volume-percent SiC, and 20-volume-percent SiC, respectively. In all cases, the tensile elongation of the composites was on the order of 1 percent or less (Table 3). Note that the scatter in the data for the 0-volume-percent SiC composition was minimal, while the scatter in the data for the 10-volume-percent SiC and 20-volume-percent SiC compositions was much greater. This clearly indicates that the composite materials are much more sensitive to process variables than the unreinforced A356 Al.

The tensile properties and the compressive properties of the 10-volume-percent SiC initial composition were affected by the heat treatments. In general, the yield strengths were

48

Table 4. Compressive Properties of A356 Al and SiC/A356 Al Composites

| Specimen No.	Composition (Vol% SiC)	Material Condition	0.2% Offset Yield Strength (MPa)	Compressive Strength at 10% Deformation (MPa)	Compressive Strength at 20% Deformation (MPa)	Compressive Modulus (GPa)
6	0	C/T6	179 ± 12	356	456	78
6	0	C/Hip+T6	190 ± 3	353 ± 4	453 ± 7	79
17	0	I/T6	172 ± 3	334 ± 8	434 ± 11	72
17	0	I/Hip+T6	181 ± 3	353 ± 8	460 ± 11	71 ± 2
10	10	C/T6	220 ± 10	406 ± 31	489 ± 19	90
10	10	C/Hip+T6	259 ± 2	480 ± 2	535 ± 3	103 ± 14
10	10	C/Hip±T61	188 ± 6	426 ± 29	541	108 ± 16
14	10	I/T6	238 ± 2	459 ± 2	525 ± 5	117 ± 2
14	10	I/Hip+T6	288 ± 0	526 ± 4	578 ± 9	111 ± 4
14	10	I/Hip+T61	216 ± 8	494 ± 2	580 ± 2	97
23	10	C/T6	233 ± 5	439 ± 8	513 ± 3	96 ± 3
23	10	C/Hip+T6	248 ± 0	460 ± 9	533 ± 14	97 ± 13
23	10	C/Hip+T61	175 ± 12	409 ± 20	487 ± 48	101 ± 17
16	10	I/T6	277 + 4	515 ± 10	553 ± 9	112 ± 20
16	10	I/Hip+T6	282 ± 2	530 ± 2	587 ± 5	111 ± 11
16	10	I/T61	201 ± 10	462 ± 18	532 ± 18	117 ± 7
16	10	I/Hip+T61	223 ± 4	496 ± 1	571g:6	108 ±15
24	20	C/T6	298 ± 1	544 ± 2	—	13. ± 21
26	20	I/T6	343 ± 5	611 ± 16	635	132 ± 1
27	20	I/T6	324 ± 17	618 ± 2	618 ± 2	140 ± 33
29	20	I/T6	297 ± 5	540 ± 12	571	119 ± 12
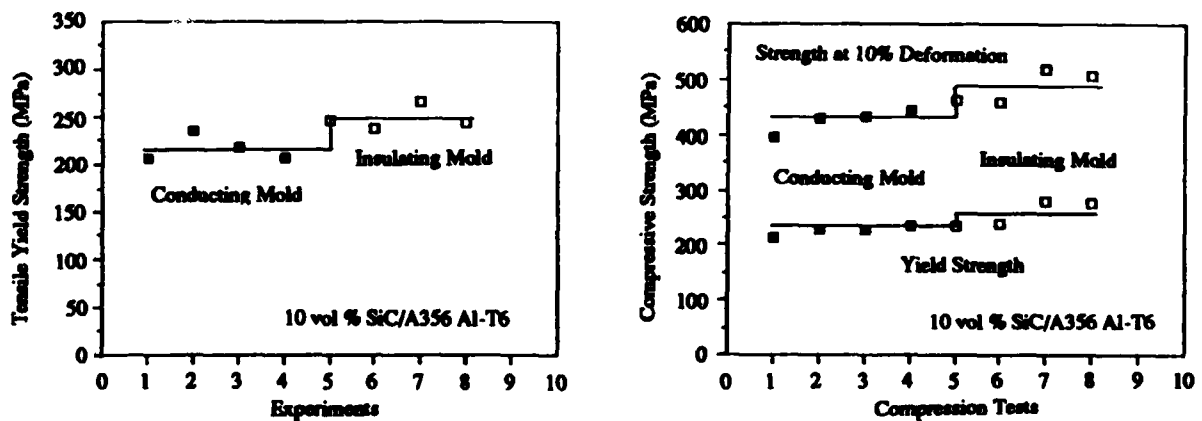
Figure 9. The effect of the mold properties on the tensile and compression properties.
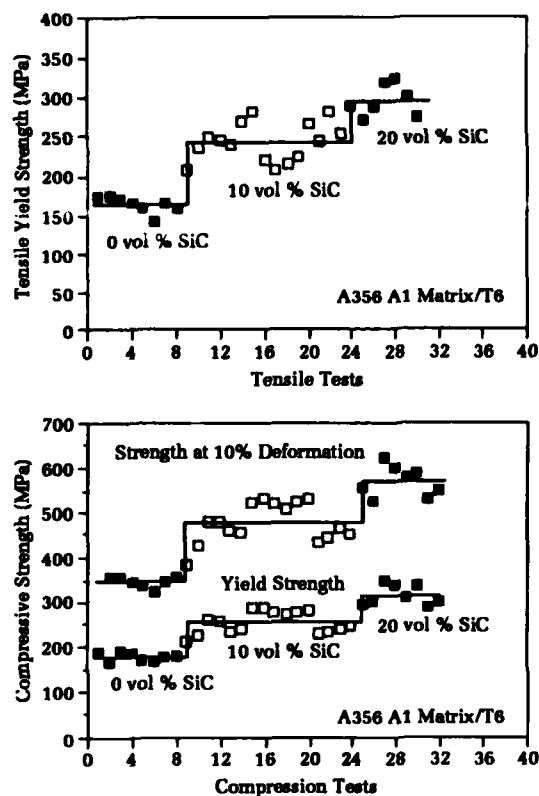
Figure 10. The effect of the composition on tensile and compression properties.

greater after the T6 treatment than after the T61 treatment. This result can be rationalized on the basis of matrix strengthening, i.e., the T6 treatment increases the strength of the matrix by the precipitation hardening.

In general terms, hot isostatic processing (HIP) improved the tensile and compressive strengths of all the materials. Its effect on the tensile and compressive moduli was, however, insignificant. HIP improved the tensile ductility of the unreinforced A356 by 50 to 100 percent (Table 3), though its effect on the tensile ductility of the composite materials was again insignificant. The increase in compressive strength, particularly for the composite specimens, can be attributed to a reduction in microporosity due to HIP. Absolute increases in properties were not very high due to the fact that the starting porosity levels were generally quite low (one percent or less).

All the composite tensile failures were typical of brittle failures, where the fracture generally occurred perpendicular to the testing direction. Unlike the unreinforced A356 Al, which failed in a very ductile manner, the composite materials' failures show no evidence of gross plasticity. Plastic deformation of the matrix did occur locally and could be observed on the fracture surfaces (Figure 11). The fracture surfaces of the composite materials also show

extensive particle fractures, evidenced by a strong SiC/Al interface. This in turn is consistent with the high tensile modulus data. Almost all specimens were free from the macroscopic defects (particle clusters, intermetallics, and the like) that are often observed in conventionally cast composites. The cleanliness of the fracture surfaces can be directly attributed to the well controlled microstructures produced by the centrifugal casting process. In
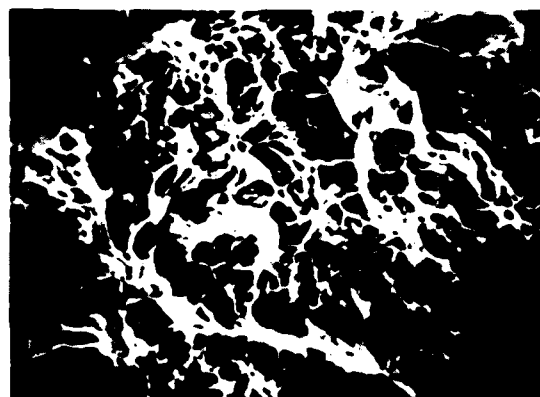
A356 Al
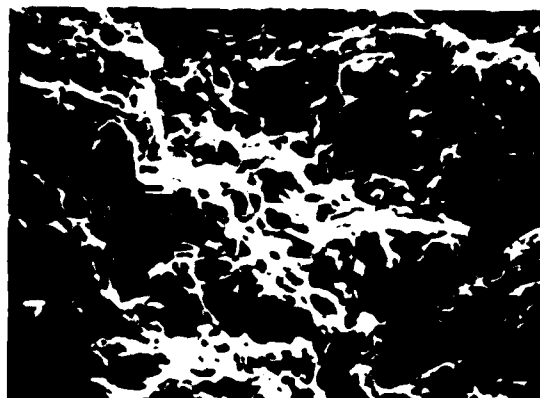
A356 Al-10 vol % SiC
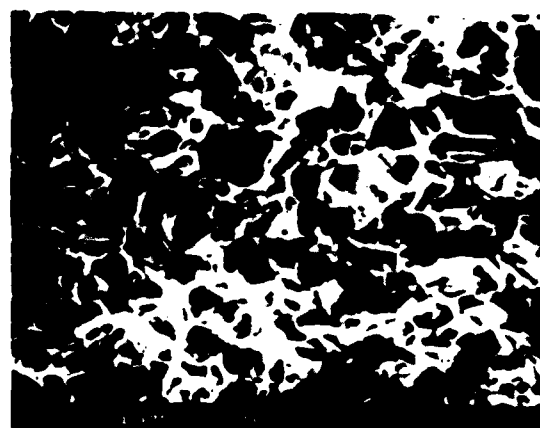
A356 Al-20 vol % SiC

Figure 11. Scanning electron microscopy micrographs of tensile fracture surfaces.

compression, the composite specimens failed in a manner typical of a brittle material. That is to say, the composite materials failed due to cracks that propagated in the directions of the maximum shear stresses in the specimen (approximately at a 45° angle to the axis of the specimens).

Summary

In summary, the mechanical properties of the centrifugally cast specimens were evaluated as a function of materials structures and processing. The results show that a range of properties can be attained by adjusting the structures through processing. Centrifugal casting is therefore a valuable means of engineering the desired structures and mechanical properties of metal-matrix composites. Overall results showed that the composite materials provided superior strength and modulus relative to the unreinforced aluminum, in both tension and compression loadings.

References

1. Karmarkar, S. D. and Divecha, A. P., "Centrifugal Casting of Composites," U.S. Patent No. 5,025,849, Jun 1991.
2. Karmarkar, S. D. and Divecha, A. P., "High Pressure Casting of Metal Matrix Composite Tubes," *Proc. Tenth Annual Discontinuously Reinforced MMC Working Group Meeting*, Park City, UT, 1987, pp. 165-190.
3. Lajoye, L. and Suery, M., "Modelling of Particle Segregation during Centrifugal Casting of Al-matrix Composites," *ASM Conf. Proc.*, Eds. S. G. Fishman and A. K. Dhingra, Chicago, IL, 1988, pp. 15-20.
4. Hilliard, J. E. and Cahn, J. W., "Evaluation of Procedures in Quantitative Metallography for Volume Fraction Analysis," *Trans. AIME*, 221, 1961, pp. 844-852.

The Authors

A. P. DIVECHA received a degree in chemistry from the University of Bombay in 1958 and a Master's degree in metallurgy from the University of Utah in 1962. In large part, Mr. Divecha has been involved in the synthesis and processing of metal-matrix composites (MMC) since 1963, with particular emphasis on the discontinuous SiC/Al system. He has also participated in the development of Navalite aluminum lithium alloys, and more recently in the processing of high-Tc superconductor wires. Mr. Divecha holds 14 patents, most of them concerning discontinuous MMCs. He is leader of the Advanced Materials Development Group of the Metallic Materials Branch at White Oak.

S. D. KARMARKAR received his B.S. in mechanical engineering from the University of Ranchi, Birla Institute of Technology, Ranchi, India in 1963 and his M.S. in metallurgy from Deutsche Technische Schule, Düsseldorf, West Germany in 1967. In 1969 he received a postgraduate diploma in operations research and industrial engineering from the University of Toronto, Ontario, Canada. He has more than 28 years of diversified industrial experience in various technical fields, tool and product design, material processing research and development, program planning and analysis, and product quality assurance and control. He joined White Oak in 1979 as a metallurgist and is currently responsible for planning and executing metal-matrix composites and low- and high-temperature superconductor research and development tasks. He is the author or coauthor of more than 40 technical papers and reports.

M. N. GUNGOR received his Sc.D. in materials engineering from MIT in 1986. He is currently a senior engineer at Westinghouse Science and Technology Center. He is a member of The Metallurgical Society, American Society of Metals International, and Materials Research Society. His research interests include processing, characterization, and implementation of advanced materials.

ALVIN H. NAKAGAWA received his Ph.D. in materials science from the University of California, Berkeley, in 1983. He is currently a senior design engineer at Westinghouse Electric Corporation Marine Division in Sunnyvale, California. While in the Advanced Materials Development Group, he was responsible for developing and applying advanced metallic, ceramic, and metal-matrix composite materials in advanced missile launchers and marine power and propulsion systems.

51

Processing of Tantalum to Achieve Optimum Metallurgy

J. B. Clark and R. K. Garrett, Jr

Tantalum, a high-density, high-melting-point metal, has numerous commercial applications including corrosion-resistant equipment for the chemical industry, heat shields for high-temperature furnaces, lamp filaments, and foil for capacitors. Potential commercial and military applications include liners for explosively formed projectiles and shaped-charge warheads. High ductility and formability are essential attributes for these applications. This article deals with the role of processing in controlling the preferred orientation of grains, or "recrystallization texture," to achieve optimum material performance. Orientation distribution function (ODF) analysis is used to characterize the influence of processing parameters on texture development in tantalum. The goal of this effort was to understand which parameters are critical in developing strong crystallographic textures while minimizing those textures that degrade formability. ODF analysis showed that processing variables strongly influenced the final recrystallized texture. From this research, a processing schedule was developed which produces tantalum with strong crystallographic orientations that enhance the deep-drawing process.

Introduction

Tantalum (Ta) is a high-density, high-melting-point metal with a body-centered cubic (bcc) crystal structure. With its high ductility, tantalum is normally processed into corrosion-resistant equipment for the chemical industry, heat shields for high-temperature furnaces, and foil for capacitor applications. It can be processed at room temperature into plates, rods, sheets, and thin foil. For these commercial applications, it has not been necessary to use the ODF analysis to determine preferred orientation of grains or "recrystallization texture," since formability has not been critical. Tantalum also has potential applications in military weapon systems. For example, high-density metals enhance the penetration performance of explosively formed projectiles (EFP) and shaped-charge warheads. Microstructure and crystallographic texture have a significant effect on performance of the liners of these weapons. Many researchers have investigated texture development for formability improvements in deep-drawing steel, but little work has been published on texture development in the case of refractory metals, especially tantalum.[1,2,3] Early work by Lankford et al.[1] on steels has shown that texture and microstructure strongly influence the ability of a metal to be deep drawn. In low-carbon, deep-drawing steels, researchers have shown that a fine grain size and a certain crystallographic texture significantly improves formability.[4] Since tantalum has the same bcc crystal structure as low-carbon steel, the plastic deformation and texture development on recrystallization should be similar.

Deformation and Recrystallization Textures

When a polycrystalline metal is plastically deformed, the lattice orientation in individual grains is altered toward a preferred orientation in which certain lattice directions are aligned with the principal directions of flow in the metal. The progress of reorientation is gradual; it is usually noticed by x-ray analysis only after the cross section of the metal has been reduced by a third or a half, but the process is not completed until the metal has received reductions of 90 percent or more. The nature of the preferred orientation, or "deformation texture," that is finally reached and the manner in which it is reached are characteristic of the metal and of the nature of the flow (the magnitude of the three principal strains).

Much attention has been given to the subject because of its relation to the properties of commercial products. A fine-grained metal in which the grains are oriented at random will possess identical properties in all directions (provided that there are no elongated inclusions, segregations, or boundaries), but a metal with a preferred orientation of grains will have directional properties, "anisotropy," which may be troublesome, as for example, in the deep drawing of sheet material. Orientations that are generated by the forming process are not as a rule returned to a random state by recovery, recrystallization and grain growth in subsequent annealing, but are altered to new orientations in the final annealing textures. This final annealing texture is called the "recrystallization texture." It is usually necessary to maintain careful control of both rolling and annealing operations in order to produce a sheet that flows uniformly in all directions during subsequent deep drawing. Preferred orientations are also of prime importance in the manufacture of metals used in commercial and military applications.

More recently, Emren et al. and Von Schlippenbach et al.[2,3] used ODF analysis to show that a correlation could be drawn between the presence of certain crystallographic textures and the ability of commercial steels to be deep drawn. In general, the {111}<110> and {111}<112> type textures improve deep-drawing properties, while the {100}<uvw> type textures degrade the deep-drawing properties. The researchers showed that pole figure analysis alone could not differentiate between the commercial steels with poor deep-drawing properties and those with better deep-drawing properties.

The ODF analysis is a powerful method developed to display the density of all the possible crystallographic orientations.[5] In the ODF analysis, all the possible crystallographic orientations are displayed using a cube, as shown in Figures 1 and 2. To understand the ODF, one locates the crystallographic plane using Figure 2A (valid for all PHI 1 sections where PHI, PHI 1, and PHI 2 are the three Euler angles) and then locates the possible crystallographic directions using a PHI 1 section similar to those shown in Figures 2B or 2C. The possible crystallographic directions vary for each of the PHI 1 sections, as indicated in Figures 2B and 2C. The ODFs in this paper show 10 horizontal slices through the ODF cube for PHI 1 from 0 to 90 degrees. Each slice is a plot of the x-ray density (contours) versus possible crystallographic orientations. Normally, cold-rolled bcc metals have the following ideal texture components

present: {001}<110>, {112}<110>, {111}<110>, and {111}<112>. These crystallographic orientations appear along two skeletal lines—the alpha fiber and the gamma fiber—as shown in Figure 1 of the ODF. In general, when bcc metals are annealed, the intensity of the {111}<110> and {111}<112> texture components increases while the intensity of the other texture components decreases.
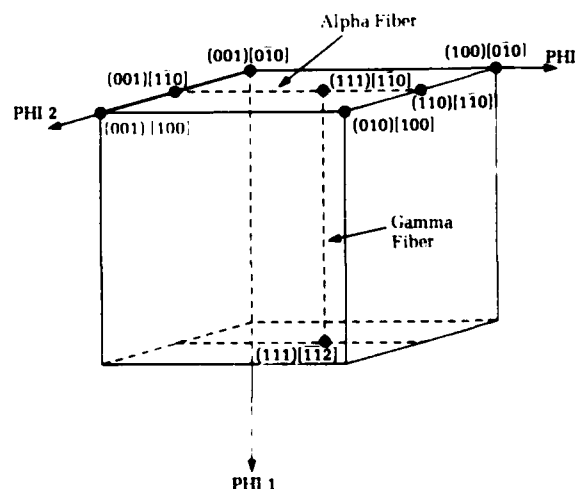
Figure 1. Representation of alpha and gamma fibers in the orientation distribution function.
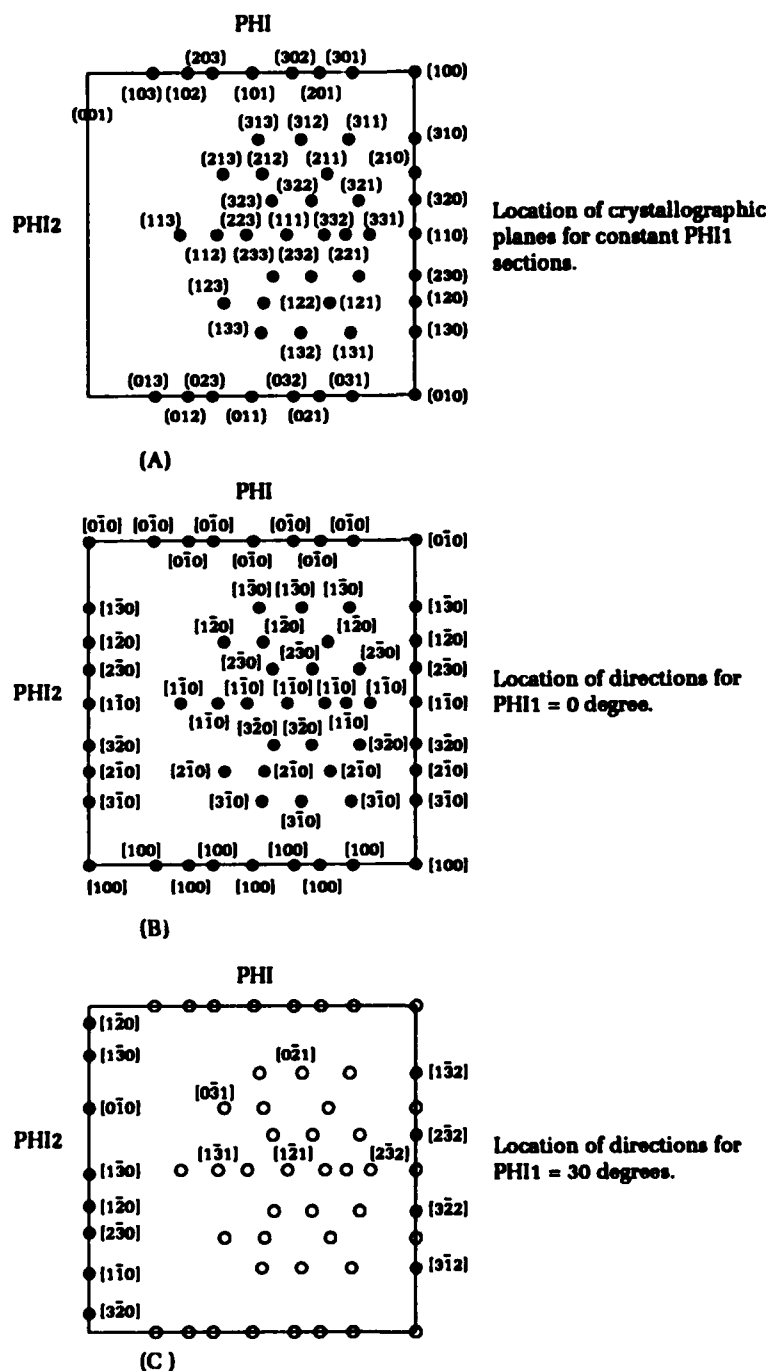
Figure 2. Location of the crystallographic planes and directions in the ODF. (A) Locations of the crystallographic planes, (B) locations of the crystallographic directions for PHI 1=0 degree, and (C) locations of the crystallographic directions for PHI 1=30 degrees.

A few researchers have investigated the texture development in commercially processed tantalum. C. Pokross showed that it was possible to obtain a fine grain size and a strong {111}<uvw> type texture in commercially processed high purity tantalum.[6] The authors have investigated the texture gradients that develop in commercially processed tantalum plates.[7] Severe texture gradients have been documented in some of these commercially processed tantalum plates. The goal of the current work is to further characterize the influence of processing variables, including the ingot breakdown process, rolling direction, and
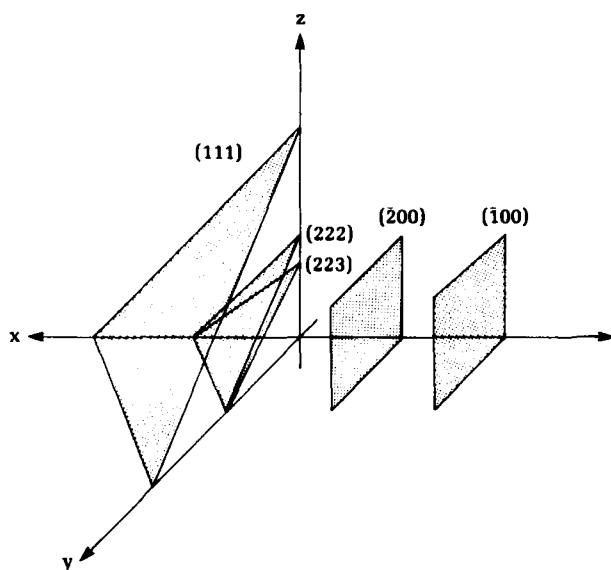
Notations for Faces of a Crystal and Directions

It is necessary to have a system of notation for the faces of a crystal, and for planes within a crystal or a space lattice, that will specify orientation without giving position in space. Miller indices are universally used for this purpose. These indices are based on the reciprocals of the intercepts of a plane with the three crystallographic axes (three edges of a unit cell). The intercepts are measured in terms of the dimensions of the unit cell, which are unit distances along the three axes. Thus, the plane cutting the axes in this figure has intercepts of 1,1,1 and therefore Miller indices (1/1,1/1,1/1) or just (111). The drawing shows some of the most important planes in relation to the unit cell, but it should be remembered that planes parallel to the crosshatched ones have the same indices.

Parentheses, (h,k,l), around the Miller indices signify a single plane or set of parallel planes. Curly braces signify planes of a form—those which are equivalent in the crystal. For a cubic crystal: {100} represents the (100) and (010) and (001) and ($\bar{1}$00) and (0$\bar{1}$0) and (00$\bar{1}$) planes, where the bar above a number indicates a negative index.

The indices of direction are derived as follows. Consider a point at the origin of the coordinates which must be moved in a given direction by means of motion parallel to the three crystal axes. Suppose the desired motion can be accomplished by going along the x-axis a distance u times the unit distance a, along the y axis a distance v times the unit distance b, and along the z axis a distance w times the unit distance c. In cubic crystals such as tantalum, all of the unit distances, a, b, and c are equal. If u,v,w are the smallest integers that will accomplish the desired motion, they are the indices of the direction and are written with square brackets, [uvw]. A full set of equivalent directions (direction of a form) are indicated by carets, <uvw>.

Adapted from *Elements of X-ray Diffraction*, 2nd Edition, by B.D. Cullity, Addison-Wesley Publishing Co.
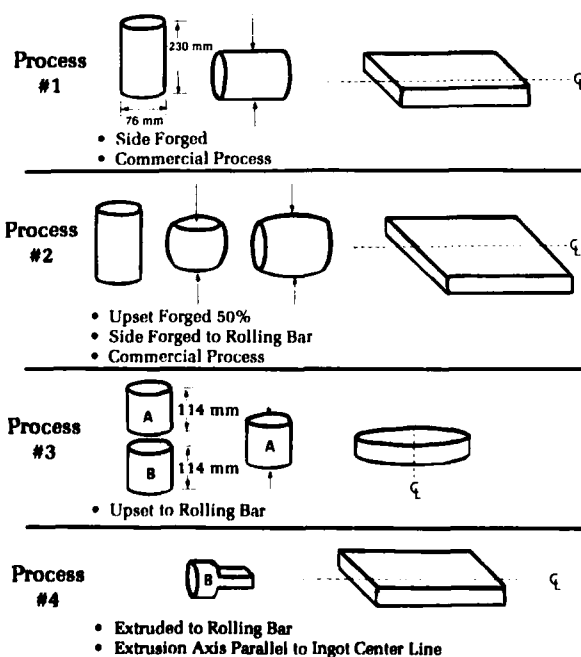
Figure 3. Schematic view of the four-ingot breakdown processes.

annealing conditions on the development of crystallographic texture in high-purity tantalum.

Material Processing Procedure

Initial Ingot Breakdown

Tantalum for this effort came from three 250-mm-long by 76-mm-diameter vacuum arc remelted (VAR) tantalum ingots, produced by Cabot Corporation. As-cast macrostructures were characterized by analyzing 25-mm-thick sections cut from each of the VAR ingots. Four different ingot breakdown processes produced the 32-mm-thick rolling bars, as shown in Figure 3. Two ingots were processed using steps that simulate current commercial practices. Process #1 included the side forging of the ingot into a rolling bar, which is similar to the commercial process employed at Cabot Corporation. In process #2, the ingot was upset forged 50 percent and then side forged into a

55

rolling bar. Process #2 is similar to the Fansteel process described by C. Pokross.[6]

The third ingot was sectioned into halves, each approximately 114 mm long, and processed using two novel techniques. In process #3, the half ingot was upset forged into a disk 32 mm thick and trimmed into a square for ease of rolling. Process #4 involved extruding the remaining half of the ingot parallel to the original ingot center line.

For processes #1, #2, and #3, forging of the VAR ingots occurred at temperatures less than 773°K. A temperature greater than 773°K had to be used in process #4. After the initial ingot breakdown, all four of the rolling bars had an annealing treatment at 1223°K for 3600 seconds.

Rolling Schedules and Annealing Temperatures

For part 1 of this work, all the plates had been processed in a similar manner, which included unidirectional rolling from the 32-mm-thick rolling bars down to a thickness of 4.6 mm. This provided a total reduction of 85 percent. For processes #1, #2, and #4, the tantalum was rolled parallel to the original ingot center line. For the complete upset process (process #3) the rolling direction was perpendicular to the ingot center line. After rolling, tantalum from each plate was annealed at temperatures of 1313°K, 1423°K, and 1533°K for 3600 seconds in a vacuum furnace.

In part 2, the tantalum was processed with an additional transverse rolling step, as shown in Figure 4. After the rolling bar anneal, processing consisted of rolling to a 50 percent reduction in thickness, turning the plate 90 degrees, and rolling to an additional reduction of 80 percent. The transverse rolling was perpendicular to the original ingot center line for processes #1, #2, and #4. The rolling bar from process #3 was not included in this transverse rolling study.

Metallography and Texture Evaluation

Metallography and texture specimens were prepared for each of the annealed specimens. For the annealed specimens, the Abrams three-circle method from ASTM E112 and optical micrographs were used for calculations of the grain size and the uniformity of the microstructure, respectively.[8] The surfaces of the texture specimens had been polished and chemically etched prior to x-ray analysis. A Siemens D500 Diffractometer equipped with a texture goniometer measured the x-ray intensities for each pole figure. The Schultz back reflection technique was used with molybdenum radia-

tion to record four pole figures: the (110), (200), (211), and (222) pole figures. X-ray intensity was recorded out to 85 degrees from the center. Intensity data were corrected using a random sample of hot isostatically pressed tantalum powder. Software supplied by Siemens with the x-ray texture system calculated the ODF. This software used data from the three most intense reflecting planes, (110), (200), and (211), to calculate the ODFs, using the spherical harmonics analysis method. There was no correction for the ghost peaks in the ODF. The notation used in the Siemens software uses Bunge's notation for the three
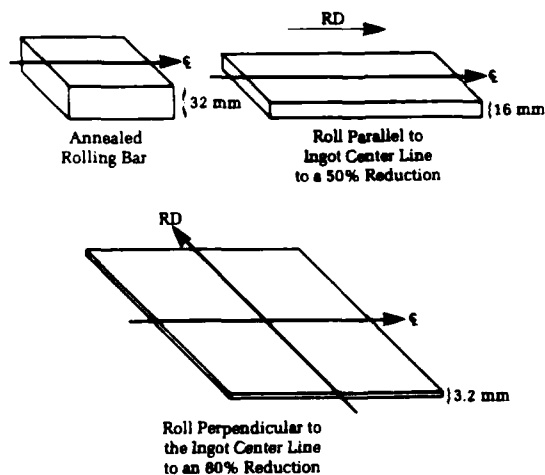

Figure 4. Schematic view of the transverse rolling process.

Figure 5. Transverse view of the macrostructure of the as-cast ingots.

Figure 6. Longitudinal view of the microstructure of the as-cast ingots.

Euler angles, i.e., PHI, PHI 1 and PHI 2.[5] For constant PHI 1=0 degree sections, shown in Figure 2, the {001}<010> orientations are located at the corners of the square, while the {111}<110> orientation is located at PHI 2 of 45 degrees and PHI of 54.7 degrees.

Microstructure and Texture Results

As-Cast Ingots

A view of the as-cast microstructure of the original VAR ingots shows large columnar grains that grew along the center line of the ingot. A photograph (Figure 5) of the grains at the end of the VAR ingot showed fairly large equiaxed grains. Figure 6 shows that the these grains had a large diameter of approximately 7 mm and grew along the length of the ingot. Other grains nucleated near the mold surfaces and grew toward the center.

Annealed Rolling Bars

All the rolling bars had a vacuum anneal at 1223°K for 3600 seconds to partially recrystallize the microstructure and break up the original as-cast grains. Figure 7 shows that the recrystallized microstructure depended strongly on the ingot breakdown process. For process #1, the rolling bar appeared essentially unrecrystallized by the 1223°K anneal. For the other processes, the microstructure showed a variety of grain sizes, some fine recrystallized grains, and some large grains remaining from the original ingot.

Unidirectionally Rolled and Annealed Tantalum

Table 1 lists the grain size results of the unidirectionally rolled and annealed plates. The lowest annealing temperature produced material that contained unrecrystallized bands in tantalum from all four processes. Optimum {111}<110> and {111}<112> orientations developed in plates from processes #1, #2, and #4 annealed at 1423°K. Plates processed by process #3 had optimum {111}<110> and {111}<112> orientations after annealing at a lower temperature of 1313°K, but the microstructure showed a small unrecrystallized band at midthickness. The highest annealing temperature produced what the authors decided were unacceptably large grains for most of the processes, and especially for processes #3 and #4, so the annealing temperature was reduced to 1473°K in part 2 of this work.

Table 1. Grain Size of the Annealed Tantalum (Microns)

Process #	Process	Annealing Temperature (K)		
		1313	1423	1533
1	Side Forged	65*	89*	116
2	Upset/Side	59*	66	82
3	Complete Upset	38*	78	218
4	Extruded	47*	83	244

* More than 5% unrecrystallized material
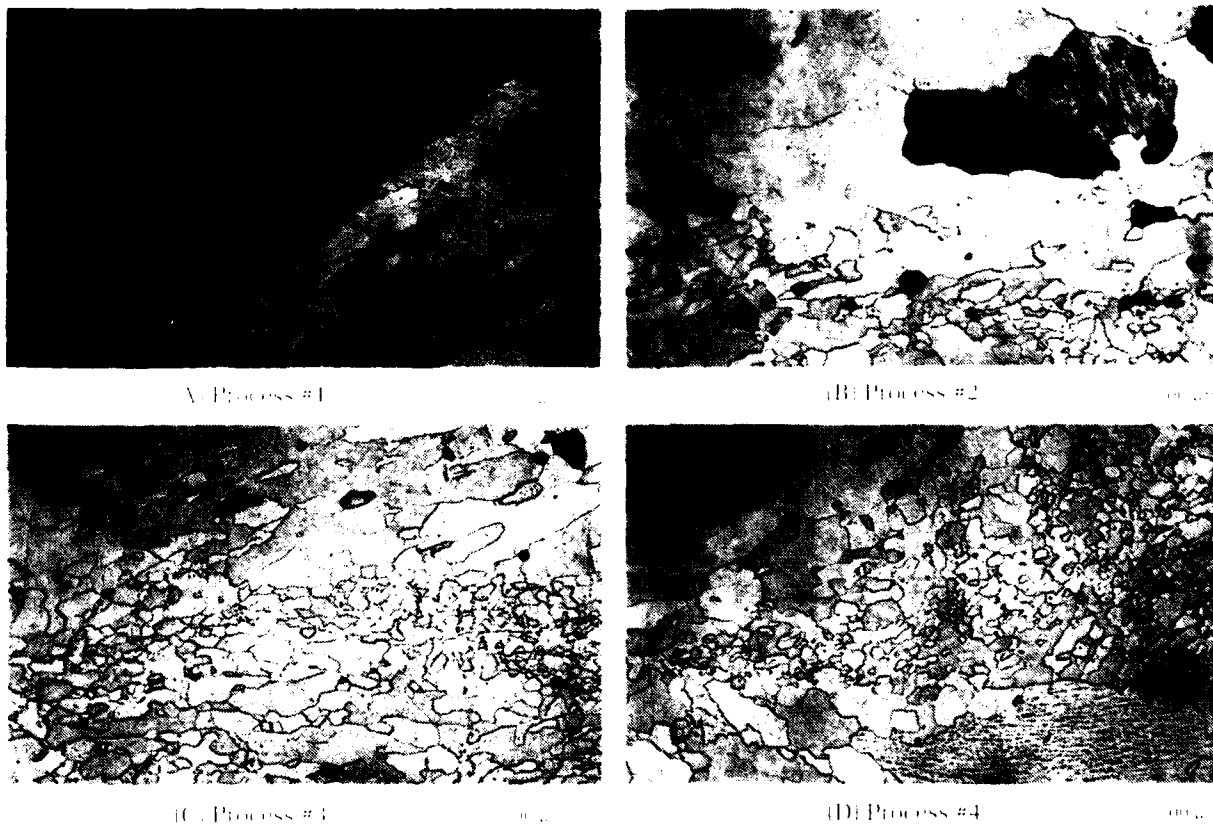
☐ Optimum {111}<UVW> texture components

57

Figure 7. Microstructures of the partially recrystalized rolling bars. (A) Process #1, (B) Process #2, (C) Process #3, and (D) Process #4
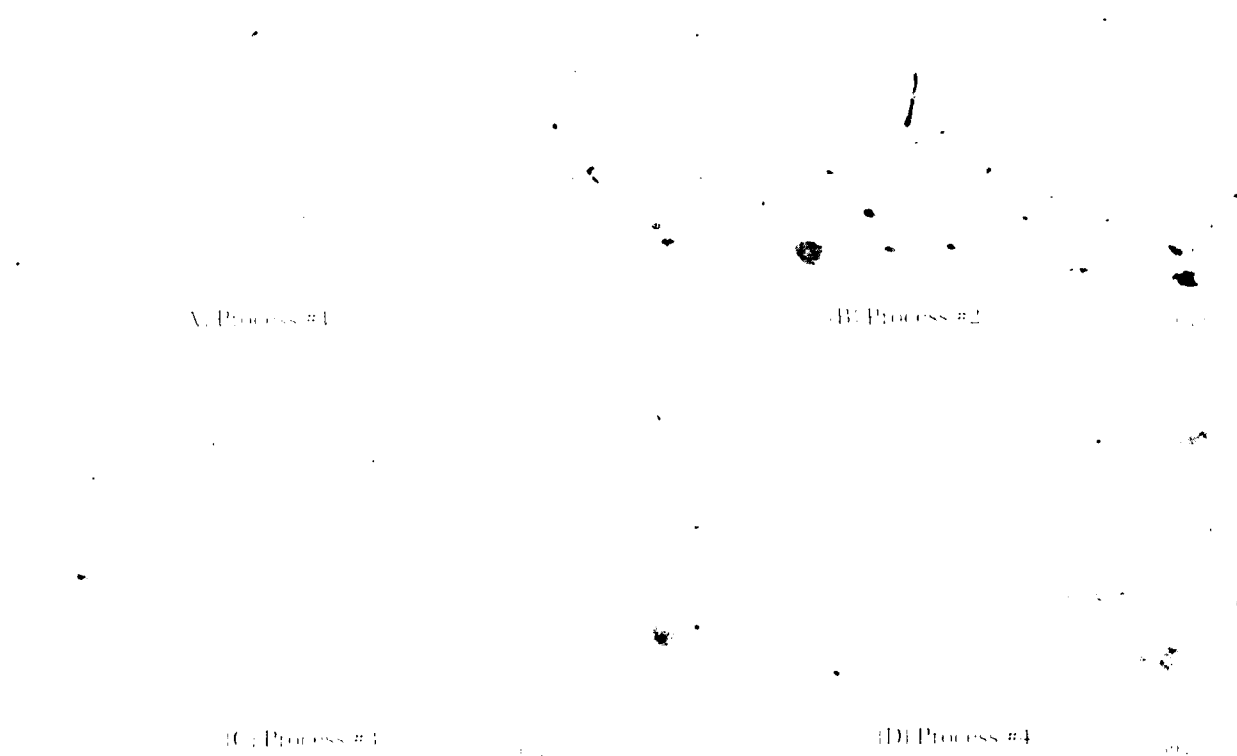
Figure 8. Microstructures of the plates annealed at the optimum annealing temperatures. (A) Process #1 at 1423 K, (B) Process #2 at 1423 K, (C) Process #3 at 1313 K, and (D) Process #4 at 1423 K.

Development of {111}<uvw> Textures

Photomicrographs of the plates, unidirectionally rolled and annealed at a temperature to produce an optimum {111}<uvw> type texture, are shown in Figure 8. Sections of the ODF for the four optimum annealing conditions are shown in Figure 9. The optimum temperature was selected as the one that provided the highest intensity for the {111}<110> orientation on the ODF and a low intensity for the {100}<110> orientation. The two commercial processes, #1 and #2, resulted in very similar mixed textures with both {111} and {100} type components. Process #1 actually exhibits a {114} component that essentially simulates the {100} type. The relative maximum intensities for the various components taken from the ODFs are listed in Table 2. Both processes #1 and #2 had the

Table 2. Texture Components for Unidirectionally Rolled and Annealed Plates

Process #	Process	Annealing Temp (K)	Maximum Intensity for Each Component {111}	{112}	{114}	{100}
1	Side Forged	1313	6	5	—	6
		1423	10	3	6	—
		1533	24	7	4	7
2	Upset/Side	1313	6	—	3	11
		1423	9	—	—	5
		1533	9	1	—	4
3	Complete Upset	1313	16	—	—	3
		1423	14	—	4	2
		1533	5	4	3	8
4	Extruded	1313	—	3	6	12
		1423	14	—	—	—
		1533	20	—	—	1

(A) Process #1
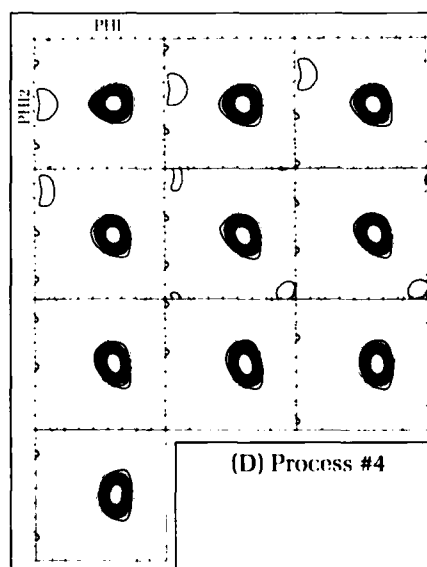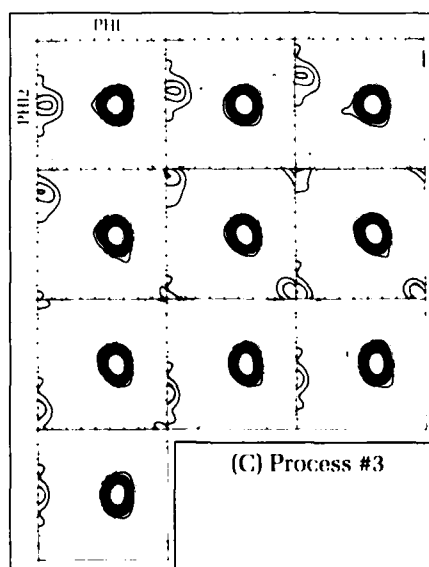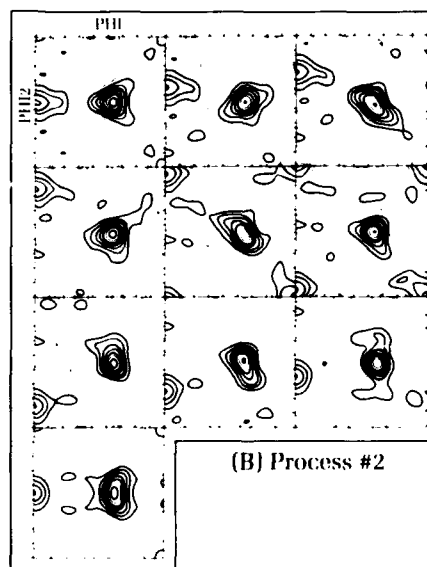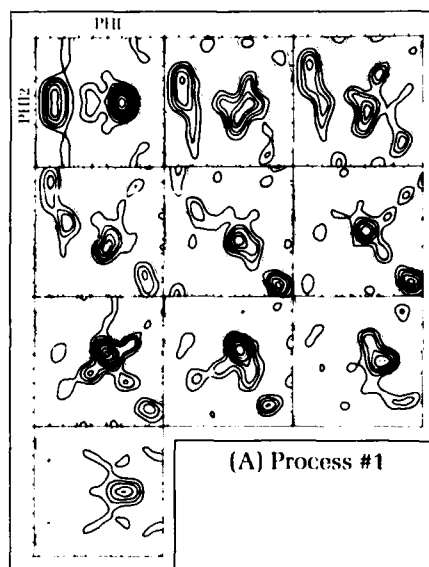
(B) Process #2

(C) Process #3

(D) Process #4

Figure 9. ODF sections for each plate after annealing. (A) Process #1 at 1423°K, (B) Process #2 at 1423°K, (C) Process #3 at 1313°K, and (D) Process #4 at 1423°K.
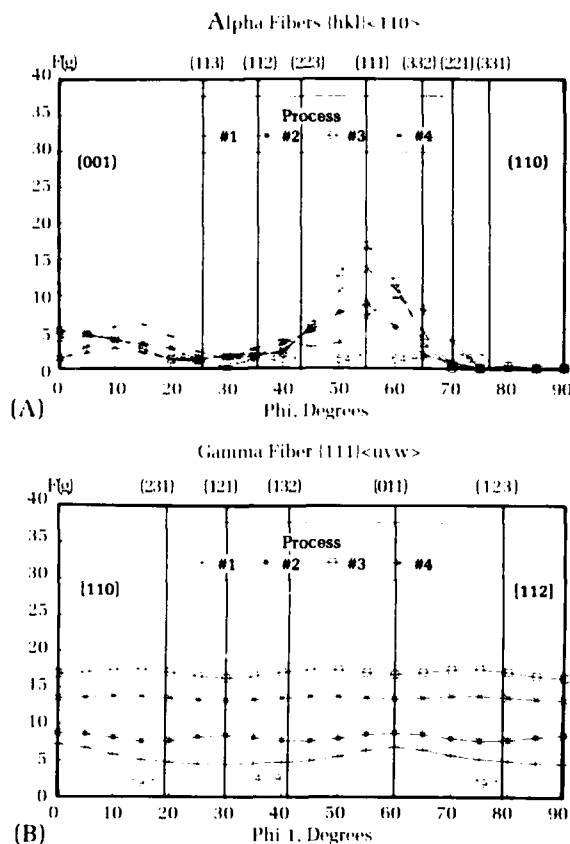
Alpha Fibers {hkl}<110>

(A) Phi, Degrees

Gamma Fiber {111}<uvw>

(B) Phi 1, Degrees

Figure 10. Alpha and gamma fibers from the anneal optimization study. (A) alpha and (B) gamma.

{111}<uvw> type texture as the strongest with an intensity of nine times random, as seen in Figure 10.

The remaining two processes resulted in very similar texture results to each other, with strong {111}<110> and {111}<112> orientations. The complete upset forging process (process #3) had mixed {111}<uvw> and {100}<uvw> type textures with the strongest {111}<110> peak of 16 times random. Plate from the extruded bar (process #4) had {111}<110> and {111}<112> texture components with no {100}<uvw> type texture components. The peak {111} intensity from the ODF was 14 times random.

Transverse Rolled and Annealed Tantalum

Additional transverse rolling did not change the recrystallized grain sizes from those of the unidirectionally rolled tantalum as shown in Table 3. For process #1, plate annealed at 1423°K had a grain size of 88 microns in the transverse rolled and annealed plate, while the unidirectionally rolled plate had an 89-micron grain size. The recrystallized grain size did not change significantly for the other processes.

Table 3. Grain Sizes for the Transverse Rolled and Annealed Plates (Microns)

Process #	Process	Annealing Temperature (K)		
		1313	1423	1473
1	Side Forged	74*	88	109
2	Upset/Side	42*	88	87
3	Complete Upset	Not Available		
4	Extruded	45	66	103

* More than 5% unrecrystallized material

Optimum annealing temperature

Table 4. Texture Components for the Transverse Rolled and Annealed Plates

Process #	Process	Annealing Temp (K)	Maximum Intensity for Each Component			
			{111}	{112}	{114}	{100}
1	Side Forged	1313	28	—	—	2
		1423	19	3	—	—
		1473	—	7	6	8
2	Upset/Side	1313	4	—	8	10
		1423	3	7	—	4
		1473	17	3	—	3
3	Complete Upset	Not Available				
4	Extruded	1313	5	—	3	3
		1423	6	—	2	5
		1473	15	2	—	6

Tantalum from processes #1 and #2 with the additional transverse rolling steps had stronger {111}<110> and {111}<112> textures, but transverse rolling weakened the {111}<uvw> type textures in the tantalum from process #4. After the additional transverse rolling process followed by annealing, plates from process #1 had a mixture of {111}<uvw> and {100}<uvw> orientations as listed in Table 4. The intensity of the {111}<011> component was strengthened by the additional transverse rolling steps to 28 times random while the {114} and {112} components were nonexistent. This texture was developed at the lowest annealing temperature of 1313°K. Annealing at higher temperatures degraded the texture. The texture of plates from process #2 also improved after the additional transverse rolling step. This plate had to be annealed at 1473°K to have dominant {111}<uvw> type textures.

Additional transverse rolling decreased the {111}<uvw> orientations in plates from process

60

#4, and it also increased the intensity of the {100}<uvw> orientations. The plate had to be annealed at the highest temperature in order to reduce the intensity of the {100}<uvw> texture components. Even at the highest annealing temperature, the ratio of the {111}<uvw> intensity to the {100}<uvw> intensity was only about 2 to 1. For both processes #2 and #4, the annealing temperature had to be raised to a higher temperature.

Development of {111}<uvw> Textures in Transverse Rolled and Annealed Tantalum

The optimum textures for the transverse rolled and annealed plates are highlighted in the boxes in Table 3. Figure 11 shows the microstructures of plates annealed at the optimum temperatures. Constant PHI1 sections from the ODF for the optimum temperatures are provided in Figure 12. For the plates processed with the additional transverse rolling step, process #1 gave the strongest {111}<uvw> type textures. For the other processes, #2 and #4, the plates had to be annealed at higher temperatures to strengthen the {111}<uvw> type textures. At these higher annealing temperatures, the plates from process #4 recrystallized to a large grain size. The alpha and gamma fibers for the three processes are shown in Figure 13.

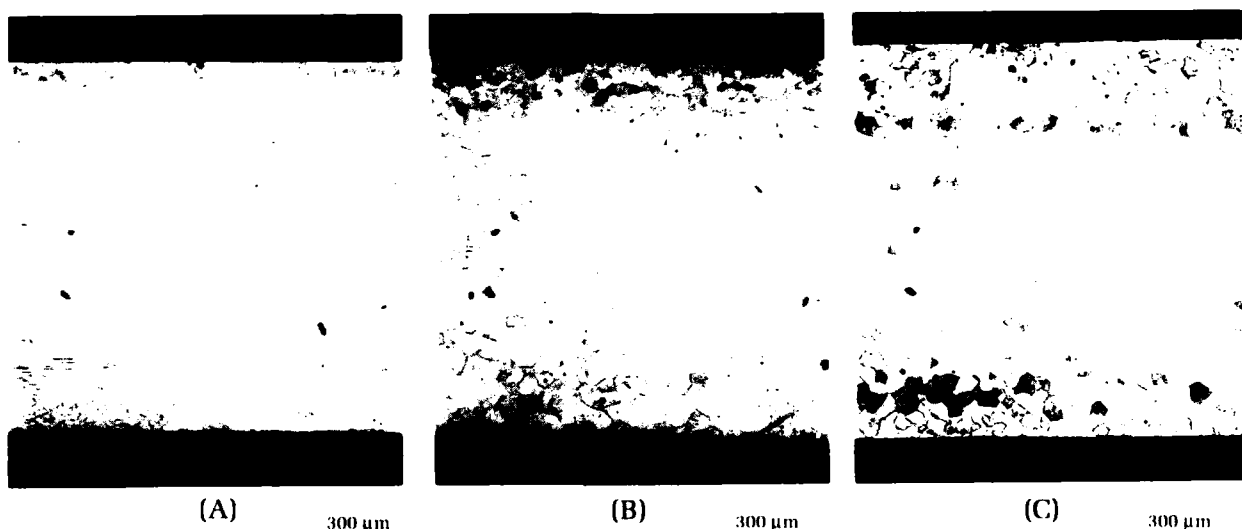(A)   300 µm   (B)   300 µm   (C)   300 µm

Figure 11. Microstructures of the transverse rolled and annealed plates. (A) Process #1 at 1313°K. (B) Process #2 at 1473°K, and (C) Process #4 at 1473°K.
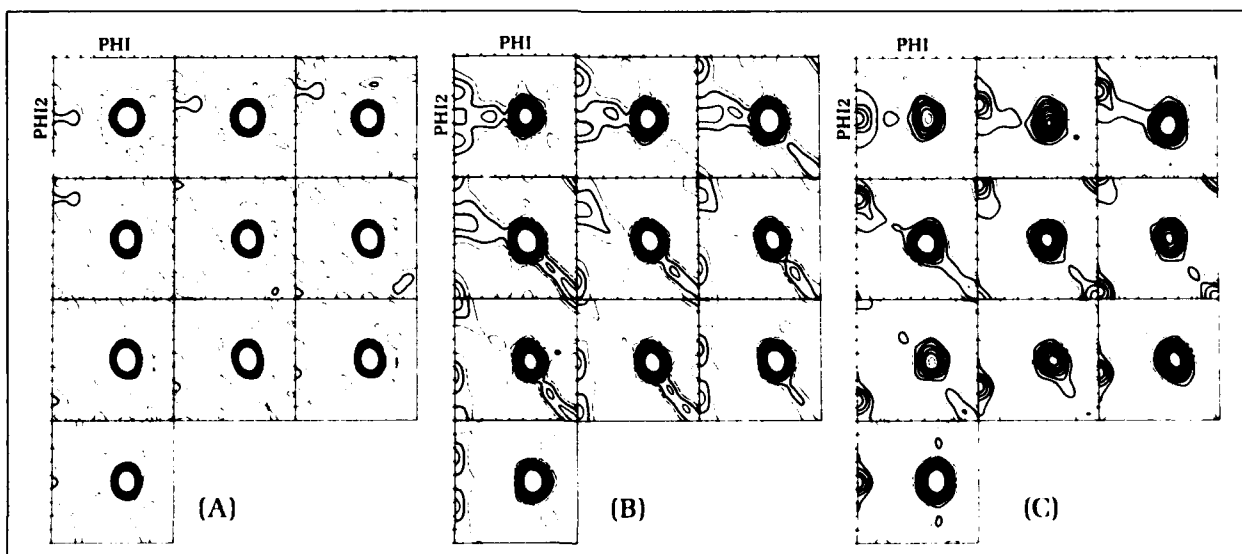

Figure 12. ODF sections for transverse rolled and annealed plates. (A) Process #1 at 1313°K. (B) Process #2 at 1473°K, and (C) Process #4 at 1473°K.

61

Discussion

The results of this study indicate that the ingot breakdown process greatly influenced the development of crystallographic texture in tantalum and the ability to recrystallize plate with strong {111}<110> and {111}<112> components. During the ingot breakdown process, the goal was to introduce work into the ingot to partially recrystallize the large as-cast columnar grains seen in Figure 6. In the side forging process, less cold work had been introduced in the axial direction (along the ingot center line) compared to the other rolling bars. The sum of the absolute value of the true strains along the ingot center line was only 0.15 compared to over 1.0 for the three other processes, as listed in Table 5. With the decreased level of cold work provided by the side forging process in this direction, the rolling bar did not recrystallize at 1223°K, while the rest of the rolling bars at least were partially recrystallized. With the 1323°K heat treatment, the rolling bar appeared to be partially recrystallized. By comparison, the 50 percent upset forged and side forged process bar had the highest level of true strain along the ingot center line, and it appeared to be almost completely recrystallized.

The influence of the original ingot breakdown process is also seen in the textures of the final annealed plates. Table 1 shows that after annealing at 1423°K, the plate from the side forged process was partially recrystallized, while plates from the three other processes were essentially fully recrystallized. Plates from the upset and side forged process had the finest grain size after annealing at both 1423°K and 1533°K, while the grain size of the plates from the other three processes were all larger. At a temperature of 1313°K, the plate processed by complete upset forging had the finest grain size. High strains introduced along the ingot

Table 5. True Strains Involved in the Ingot Breakdown Processes

Process #	Process	Axial Strain	Thickness Strain	Width Strain
1	Side Forged	0.15	0.875	0.47
2	Upset/Side	1.508	1.565	0.505
3	Complete Upset	1.28	0.64	0.64
4	Extruded	1.04	0.88	0.41

center line by forging assisted in the recrystallization process of the rolling bar by breaking up the original as-cast columnar grains, thereby nucleating finer randomly oriented grains for subsequent processing. Strain introduced by the side forging process did not add enough work to remove the original microstructure, and resulted in a strong {100}<uvw> type texture in the final plate.

The completely upset forged bar had the strongest {111}<uvw> type textures in the final recrystallized plate. Analysis of the cold-rolled texture of this plate showed a strong {100}<011> texture. For tantalum, the presence of the {100}<011> texture indicates a high level of cold work which aids in the recrystallization of a strong {111}<uvw> type texture.

The final grain size of the plates has been shown by previous studies on steel to depend strongly on the rolling bar grain size.[4] The original as-cast grains in the VAR ingots tended to be large, as shown in Figures 5 and 6. The rolling bar anneal temperature was chosen as the temperature at which the rolling bars had just started to recrystallize. Intermediate anneals during processing aid in reducing the final grain size of the plates and also in forming fine grains with the desired {111}<uvw> type
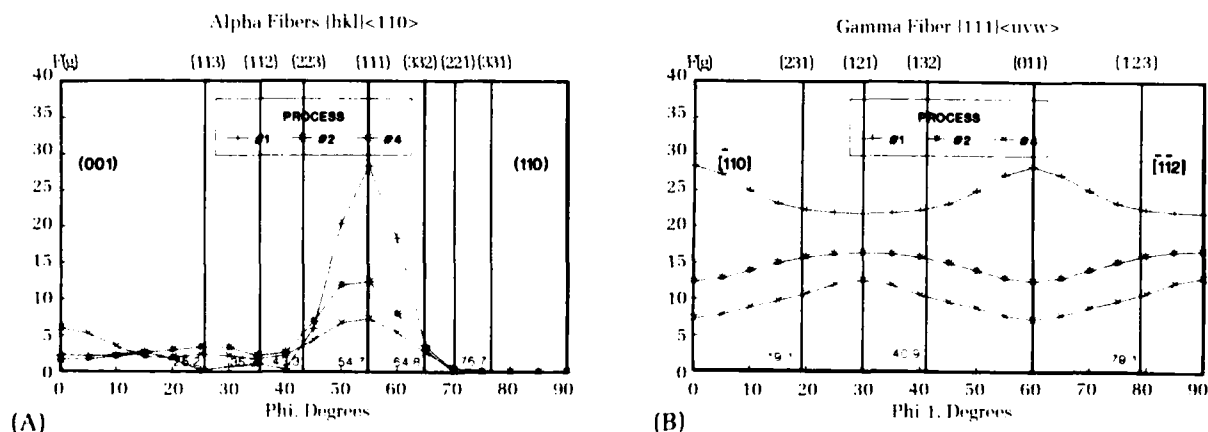
Figure 13. Alpha and gamma fibers for the transverse rolled and annealed plates. (A) alpha and (B) gamma.

Figure 14. Comparison of the alpha and gamma fibers. (A) Process #1. (B) Process #2, and (C) Process #4.

orientations. It appears that the partially recrystallized microstructure provides more grains with the correct orientations for the growth of the desired {111}<uvw> oriented grains. Formation of a strong {111}<uvw> type texture for steel depends strongly on the selected growth of the {111}<uvw> oriented grains from the cold-worked {112}<110> oriented grains.[3] A partially recrystallized rolling bar

evidently provides the ideal microstructure for the growth of {111}<uvw> oriented grains in the case of tantalum. If the rolling bar is not annealed, then there is a mixed texture with {111}<110> and {100}<011> orientations in the final annealed plates. Single crystal studies by Vandermeer and Snyder have shown that the {100}<uvw> oriented grains cold work less and recrystallize with a larger grain size.[9] By

63

comparison, the {111}<uvw> oriented grains cold work to a greater extent and recrystallize with a finer grain size. A high rolling bar annealing temperature would produce a large recrystallized grain size, which would also increase the final grain size of the plates. With a large grain size, fewer sites, i.e., grain boundaries, are available for dislocation generation and fewer grains with the desired {111}<uvw> orientations recrystallize.

Rolling parallel to the ingot center line for processes #1 and #2 did not reduce the {100}<uvw> texture components. Even after rolling to a reduction of 85 percent followed by annealing, the texture still consisted of mixed {111} and {100} type textures as shown by the alpha and gamma fibers in Figure 10. Side forged plate, process #1, had the weakest {111}<110> texture. It appears that upset forging along the ingot center line is necessary to recrystallize a plate with {111}<uvw> type textures.

Additional rolling transverse to the ingot center line tended to improve the textures in the final plates for processes #1 and #2, as shown by the alpha and gamma fibers in Figure 13. It did not improve the texture for the plate from process #4. The additional transverse rolling passes apparently are more effective in breaking up the coarse columnar type grains, which develop a strong {100}<001> texture in the annealed rolling bars. Figure 14 compares the alpha and gamma fibers for unidirectional rolling followed by annealing versus the results for the tantalum with additional transverse rolling steps followed by annealing. These results show that it is possible to obtain strong {111}<uvw> textures in both processes #1 and #2 using a transverse rolling step.

Conclusion

ODF analysis showed that tantalum processed by complete upset forging the ingot into a rolling bar provided recrystallized plate with strong {111}<110> and {111}<112> type textures and a fine grain size. Side forged plates had a detrimental {100}<001> texture in the rolling bar that could be removed only by subsequent rolling perpendicular to the ingot center line. The tantalum with strong {100}<uvw> orientations had to be annealed at higher temperatures for the microstructure to be fully recrystallized. Upset/side forging or extrusion of rolling bars produced plates with mixed {111}<uvw> and {100}<uvw> textures.

Rolling parallel to the ingot center line did not remove the {100}<001> orientations found in the annealed rolling bars. Transverse rolling perpendicular to the axis of the columnar grains was beneficial, breaking up the large

residual columnar microstructure. This processing resulted in the development of the desired {111}<112> and {111}<110> components in recrystallized tantalum.

It was possible to process tantalum ingots via different ingot breakdown methods and rolling schedules similar to the present commercial tantalum processes, producing plate with strong {111}<112> and {111}<110> texture components. This crystallographic texture, with no {100}<uvw> components, is highly desirable for both commercial deep-drawing applications and for potential military weapon systems.

References

1. Lankford, W. T., Snyder, S. C., and Bauscher, J. A., "Press Performance of Deep Drawing Sheets," *Trans. Am. Soc. Min. Engrs.*, Vol 42, 1950, pp. 1197-1232.
2. Emren, F., Von Schlippenbach, U., and Lucke, K., "Investigation of the Development of the Recrystallization Textures in Deep Drawing Steels by the ODF Analysis," *Acta Metall.*, Vol. 34, No. 11, 1986, pp. 2105-2117.
3. Von Schlippenbach, U., Emren, F., and Lucke, K., "Investigation of the Development of the Cold Rolling Texture in Deep Drawing Steels by ODF Analysis," *Acta Metall.*, Vol. 34, No. 7, 1986, pp. 1289-1301.
4. Hu, H., "Texture of Metals," *Texture*, Vol. 1, 1974, pp. 233-258.
5. Bunge, H. J. and Esling, C., *Quantitative Texture Analysis*, Pub. DMG Informationsgesellschaft, Germany, 1986, pp. 3-72.
6. Pokross, C., "Production of Tantalum Plate with Controlled Crystallographic Texture," Symp. on Tantalum Processing and Applications, 27 Feb to 3 Mar 1989, Las Vegas, NV.
7. Clark, J. B., et al., "Effect of Processing Variables on Texture and Texture Gradients in Tantalum," *Metall. Trans.*, Vol 22A, Sep 1991, pp. 2039-2048.
8. *Annual Book of ASTM Standards*, E 112-85, Vol 3.01, Pub. Amer. Soc. for Testing and Materials, Philadelphia, PA, 1987.
9. Vandermeer, R. A. and Snyder, W.B., Jr., "Recovery and Recrystallization in Rolled Tantalum Single Crystals," *Metall. Trans. A*, Vol. 10A, Aug 1979, pp. 1031-1043.

64

The Authors

JAMES B. CLARK received a B.E.S. degree in mechanics and materials science from the Johns Hopkins University in 1978, an M.S. in materials engineering from Rensselaer Polytechnic Institute, Troy, New York, in 1980, and a Ph.D. in materials science and engineering from the Johns Hopkins University in 1985. He has worked in the Materials Technology Branch (formerly the Metallic Materials Branch) for the past seven years investigating microstructural and texture development in refractory metals as well as developing advanced magnesium composites for missile and satellite applications. He is a member of the American Society for Materials International, the Metallurgical Society of the American Institute for Metallurgy and Petroleum Engineers, and the American Institute of Aeronautics and Astronautics.

ROBERT K. GARRETT, JR., received B.S. and M.S. degrees from Purdue University in 1981 and 1983, respectively. He has been with the White Oak Detachment since 1983. In the Research and Technology Department, he was lead engineer for several programs dealing with the relationships among metallurgy, processing, and performance of tantalum for ballistic applications. He successfully transitioned this reported texture technology to industry, where it has been used to develop current production processes. Before transferring to the Weapon Design Branch of the Weapons Systems Department, his work involved forged tungsten and molybdenum for ballistic applications and advanced corrosion-resistant aluminum alloys for weapon structures.

High-Power Magnetostrictive Materials

Arthur E. Clark

Research at the Naval Surface Warfare Center, Dahlgren Division, has demonstrated that certain lanthanide elements, e.g., terbium (Tb), dysprosium (Dy), and samarium (Sm), used individually or in compounds with iron, are excellent candidates for high-power magnetomechanical energy converting devices. The strong magnetomechanical coupling in these materials, plus their ruggedness and relative absence of failure mechanisms, make them attractive for many applications, such as smart structures, high-power sonar transducers, and active noise-canceling devices. In this article we review the magnetostrictive properties of two of these high-power magnetomechanical energy converting materials: (1) Tb_xDy_{1-x} alloys and (2) $Tb_xDy_{1-x}Fe_2$ (Terfenol-D) compounds $(0 \leq x \leq 1)$. These magnetostrictive materials have the capability of functioning under adverse environmental conditions, as well as the ability to generate large stresses and displacements at low frequencies.

Introduction

A magnetostrictive material is a magnetic material that changes dimensions when its magnetic state is changed, for example, when it is placed in a magnetic field. These changes are typically very small, generally only a few parts per million (ppm). Even so, magnetostrictive materials have been used in a wide variety of devices for many years, particularly when ruggedness and long lifetime are paramount. One important application of these materials of interest to the Navy is sonar transduction, where magnetic energy is converted into acoustic pulses for target recognition or communication. Another is active vibration cancellation and ship noise reduction. For all these applications, high-power capability relies on large, magnetically induced dimension changes (magnetostrictions).

The largest displacements achieved magnetically are the basal plane strains in the hexagonal lanthanides, Tb and Dy.[1,2] In these crystals, huge magnetostrictions ($\Delta\ell/\ell$, ~ 10^{-2}, where ℓ is the length of the crystal) derive from large anisotropic electric charge distributions of 4f electrons deep within these elements. When a magnetic field is applied, the coulomb interaction between these electrons and the lattice develops strong forces which can move heavy structures or emit strong acoustic signals. The lanthanides themselves, because of a low magnetic exchange interaction, are magnetic only at low temperatures (T < 240°K), thus their utility is generally restricted to temperatures below ~180°K. However, with the advent of recently developed high-temperature superconductors that can conduct electric currents without loss at temperatures as high as 100°K, they offer an efficient means of converting electric energy to strong forces at these temperatures. At 77°K (the boiling point of liquid nitrogen), magnetically induced strains reach 0.6 x 10^{-2}.

66

A number of attempts have been made to extend the temperature range of these large magnetostrictions to room temperature and above. Many failed. We have investigated the magnetic and magnetostrictive properties of: (1) lanthanide oxides, (2) rapidly solidified amorphous lanthanide containing alloys, and (3) intermetallic compounds of the lanthanides with the transition metals iron (Fe), cobalt (Co) and nickel (Ni). Lanthanide garnets such as $Dy_3Fe_5O_{12}$ exhibit large magnetostrictions only at low temperatures, even though their magnetic ordering temperatures are far above room temperature.[3] Rapidly solidified amorphous Tb-Fe and Dy-Fe alloys achieved maximum magnetostrictions at room temperatures of only $\sim500 \times 10^{-6}$.[4] In fact, large magnetostrictions at room temperatures ($\Delta l/l \sim 2 \times 10^{-3}$) were found to occur only in crystalline Tb-based and Sm-based iron compounds.[4,5] For example, in single crystal $TbFe_2$, the saturation magnetostriction along the crystallographic [111] direction, defined by $(3/2)\lambda_{111}$, equals 3.6×10^{-3} at room temperature.

High-Power Magnetomechanical Materials at Cryogenic Temperature

The low magnetic exchange interactions in Tb and Dy restrict their temperature range of high magnetostrictions to below $\sim220°K$ (Tb) and $\sim160°K$ (Dy). In this temperature region, because of a huge magnetic interaction that causes the magnetic moments to lie in the basal plane of these hexagonal elements, only the magnetostriction associated with this plane, commonly known as $\lambda^{\gamma,2}$, is attainable with magnetic fields (H) derived from ordinary drive coils (H < 2000 Oe). In addition, easy magnetization rotation and minimum hysteresis require a large basal plane magnetostriction to basal plane magnetic anisotropy ratio, defined by $\lambda^{\gamma,2}/K_6^6$. Thus, for optimum performance with easily obtained magnetic fields, a minimum in the basal plane magnetic anisotropy K_6^6 is required. Fortunately, the lanthanide elements Tb and Dy possess basal plane anisotropies of opposite signs. (In Tb, the basal plane b axis is easy; in Dy, the basal plane a axis is easy.) To determine the most desirable alloy for a given temperature, the magnetostriction and anisotropy were measured for Tb_xDy_{1-x} for x from 0 to 1.[6] The magnetostrictions ($\lambda^{\gamma,2}$) as a function of temperature are shown in Figure 1. Note that the values are very large and almost independent of x at the lowest temperatures. From magnetostriction measurements as a function of magnetic field, one can also deduce the basal plane anisotropy constant K_6^6 for each temperature. See Figure 2. (Here M_s is

the saturation value of the magnetization.) From these measurements, it is now possible to determine the desired values of x for each temperature. We find for $\sim 60°K$, x = .67; $\sim 100°K$, x = .5; $\sim 120°K$, x = .33; $\sim 135°K$, x = .17.

The magnetostrictions that can be obtained by applying a magnetic field to Tb_xDy_{1-x} sample rods at 77°K are shown in Figures 3 and 4. Figure 3 illustrates the magnetization and magnetostriction found for a b axis rod of $Tb_{.5}Dy_{.5}$ under typical loading conditions. Note the huge jump in magnetostriction of $\sim4.5 \times 10^{-3}$ at an applied magnetic field of less than 300 Oe. At 77°K, the b axis is magnetically hard, and rotation of the magnetization into the rod b axis and its accompanying magnetostriction occurs at higher fields. Clearly, the field dependence consists of three regions: (1) a low field region where the magnetization rotates from a direction (a axis) perpendicular to the rod axis to a direction near an easy axis, (2) a steep linear region where the magnetization "jumps" from
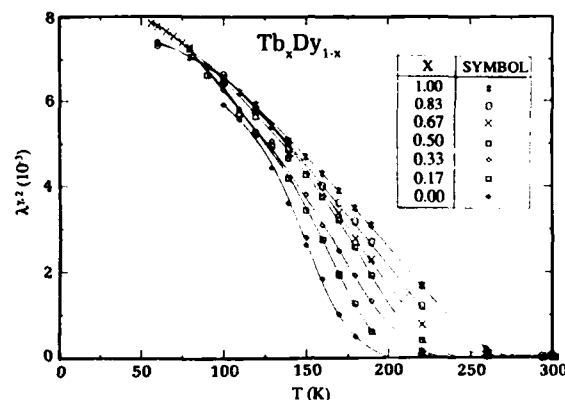

Figure 1. Magnetostriction, $\lambda^{\gamma,2}$, vs temperature for H = 20 kOe.
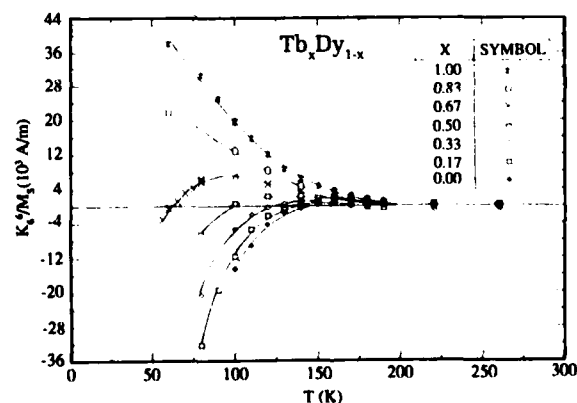

Figure 2. K_6^6/M_s vs temperature for H = 20 kOe, where K_6^6 is the basal plane magnetic anisotropy constant and M_s is the saturation value of the magnetization.
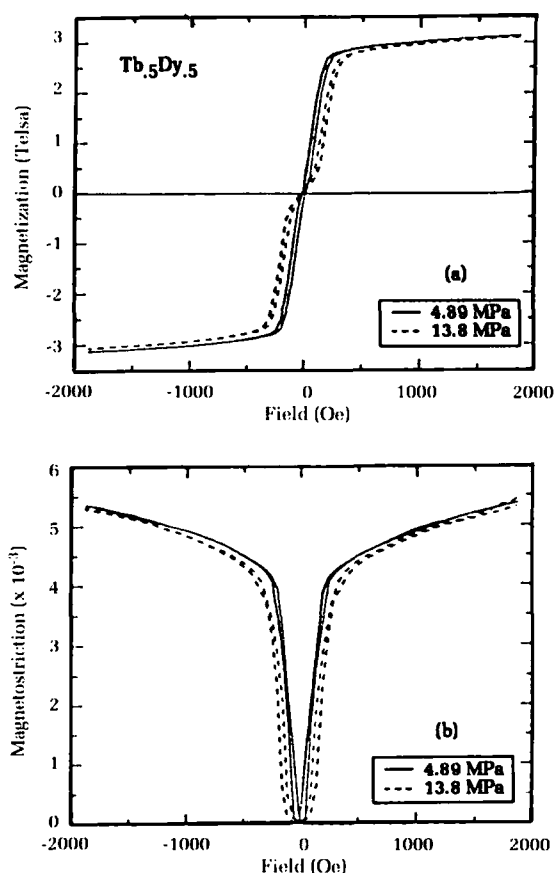
be obtained in the $TbFe_2$ (Terfenol) and $SmFe_2$ (Samfenol) based cubic compounds.[4] Numerous substitutions of lanthanides and 3d metals into the generic $TbFe_2$ and $SmFe_2$ compounds have been made to improve both magnetic and mechanical properties, such as hysteresis and ruggedness. By far the most common substitution is that of Dy for Tb in $TbFe_2$, which significantly reduces the lowest order cubic magnetic anisotropy constant K_1. As with the Tb_xDy_{1-x} alloys, a large magnetostriction/anisotropy ratio is important to ensure easy magnetization rotation and low hysteresis. And again, similar to the Tb_xDy_{1-x} alloys, this ratio can be maximized since in this cubic system of compounds, $K_1 < 0$ for $TbFe_2$, $K_1 > 0$ for $DyFe_2$, and the saturation magnetostriction is large and positive for both $TbFe_2$ and $DyFe_2$.[4] Magnetostriction/anisotropy ratio maximization (anisotropy compensation) occurs near room temperature for $Tb_xDy_{1-x}Fe_{2-y}$ (Terfenol-D) with $0.27 < x < 0.3$, $0 < y < 0.5$. Here $\Delta\ell/\ell = (3/2)\lambda_{111} = 2.4 \times 10^{-3}$.[5] In this section we describe some recent results and models for the high-power Terfenol-D

Figure 3. B-axis rod of $Tb_{.5}Dy_{.5}$ with applied stresses of 4.89 MegaPascals (MPa) and 13.8 MPa: (a) magnetization vs applied field and (b) magnetostriction vs applied field. Temperature = 77°K.

one easy direction to a second easy direction closer to the rod axis, and (3) a region of slow approach to saturation as the magnetization approaches the hard b axis. In Figure 4 we depict the magnetization and magnetostriction for $Tb_{.6}Dy_{.4}$ at 77°K. Here $K_6^6 \cong 0$ and the desired full magnetostriction of ~6.5 x 10^{-3} is observed. The magnetization curve for this sample is distinctly different from that of Figure 3. In this alloy, the magnetization process is essentially rotational, with saturation occurring at relatively low magnetic fields. These figures provide two examples of the kind of design data needed for high-power devices at temperatures accessible with the newly emerging high-temperature superconductors.

High-Power Terfenol-D Alloys Near Room Temperature

Above temperatures of ~180°K, the magnetostrictions of the lanthanide elements fall rapidly, so higher values of magnetostrictions must
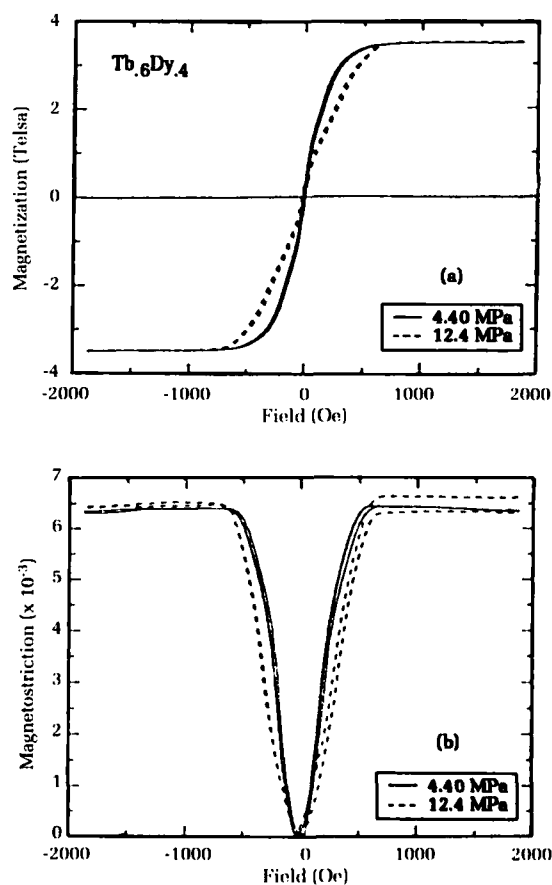
Figure 4. A-axis rod of $Tb_{.6}Dy_{.4}$ with applied stresses of 4.4 MPa and 12.4 MPa: (a) magnetization vs applied field and (b) magnetostriction vs applied field. Temperature = 77°K.

alloys with x ~ 0.3. Samarium compounds, which are difficult to prepare and yield negative displacements, will not be discussed further in this paper.

The highly magnetostrictive $Tb_xDy_{1-x}Fe_{2-y}$ alloy grows most easily along a crystallographic [112] direction in long, thin dendritic plates. This growth direction is not a principal direction in the cubic system and, unfortunately, the magnetostrictive behavior is very complex.[7] A further complexity occurs because the dendrites are twinned. These growth habits, plus a large $\lambda_{111}/\lambda_{100}$ magnetostriction ratio,[4] strongly influence the magnetic field, temperature, and stress dependencies of the magnetostriction.[8] At temperatures far below room temperature (T < magnetic anisotropy compensation temperature), we find the (nearly nonmagnetostrictive) <100> axes magnetically easy. Relatively small magnetostrictions are found. At temperatures near room temperature and above (T > magnetic anisotropy compensation temperature), the highly magnetostrictive <111> axes are magnetically easy, and magnetization jumping can occur between one easy [111] direction and a second [111] easy direction close to the rod axis. Huge changes in sample length accompany these jumps (similar to those in the low temperature $Tb_{.5}Dy_{.5}$ alloy). During the jump, a large amount of internally stored magnetic energy is abruptly converted to elastic energy, which can do extensive work against externally applied stresses.

High-power lanthanide-iron alloys are now marketed worldwide by many suppliers from whom representative magnetostrictive curves and magnetomechanical properties are available. In the following, we report data for Terfenol-D taken from magnetostrictive rods supplied by Edge Technologies, Inc., Ames, Iowa. The "turning-on" of the magnetostriction with increasing temperature is shown in Figure 5. At -50°C, far below the anisotropy compensation temperature for this alloy, a conventional magnetization curve is observed, accompanied by a small magnetostriction. The primary magnetization process is found to proceed by the movement of walls between magnetic domains with antiparallel magnetizations (180-degree domain wall motion), followed by some magnetization rotation away from the nonmagnetostrictive <100> axes toward the <111> axes. From -50°C to -10°C, the magnetostriction gradually increases. At -10°C, $K_1 \cong 0$. At this temperature and above, with the compressive stress of 13.3 MegaPascals (MPa) providing a transverse easy direction, the magnetization lies along the magnetostrictive [111] direction perpendicular to the rod axis for zero applied field. As the magnetic field is increased, a small increase in length is

observed until at a critical field, H_{cr}, a rapid increase in length occurs with increasing field ($\Delta\ell/\ell > 10^{-3}$). A still further increase in length occurs at greater fields. At 0°C and above, the <111> directions are sufficiently easy to cause the magnetization to jump between two <111> directions as the magnetic field is changed. For 20°C < T < 80°C, the break in the magnetostriction and magnetization curves at H_{cr} is even more distinct (Figures 5 and 6). At these higher
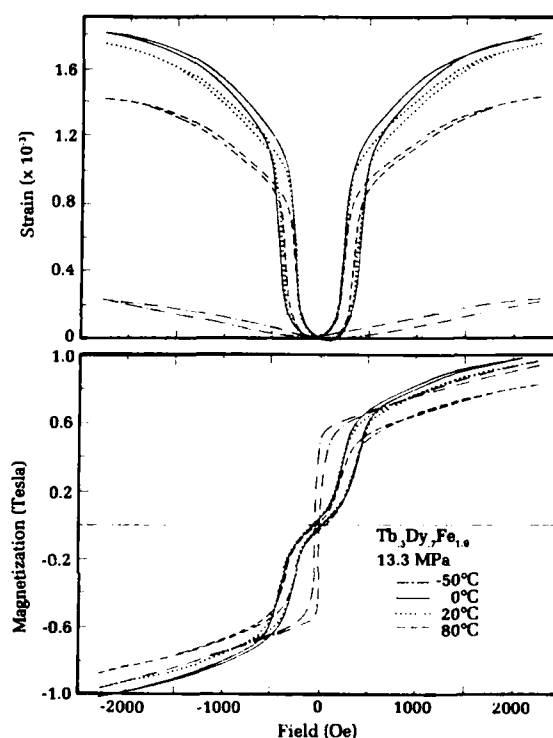

Figure 5. Magnetostriction and magnetization curves of $Tb_3Dy_7Fe_{1.9}$ as a function of temperature with a compressive stress of 13.3 MPa.

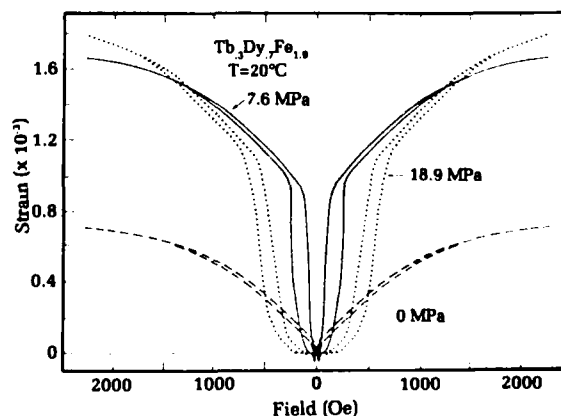**Figure 6.** Magnetostriction of $Tb_3Dy_7Fe_{1.9}$ at 20°C with compressive stresses of 0, 7.6, and 18.9 MPa.

69

temperatures. K_1 is more negative and the barrier between the <111> directions is higher. The slowly decreasing value of magnetostriction with increasing temperature for 20°C < T < 80°C is due to the decrease in the saturation magnetostriction with temperature. In summary, at temperatures above 0°C both the magnetization and magnetostriction consist of three distinct regions: (1) a very low field region where there is little magnetization and magnetostriction, (2) the important magnetization jumping region in which the magnetic moment jumps between two directions which have widely different magnetostrictions, and (3) a final magnetization rotation region where the magnetic moment rotates toward the [112] rod axis. Substantial magnetostrictions also occur in the high field region.

Magnetostriction and magnetization curves, similar to those depicted in Figure 6, are observed for all compressive stresses, σ > 7 MPa. As the compressive load is increased above 7 MPa, however, a larger external field is required to produce the greater work done by expansion against the stress. This is illustrated in Figure 6 for σ = 7.6 MPa and 18.9 MPa. At very low applied stresses (σ < 5 MPa), internal stresses developed during the growth process dominate the external stress and prevent the H = 0 state from being the minimum magnetostriction state (one in which all magnetic domains point in the transverse direction). Figure 6 shows that for zero applied stress there is no magnetization jumping. In this case the magnetization process proceeds by 180-degree domain wall motion at low field, followed by magnetization rotation at high fields. For σ = 0, only this latter process gives rise to magnetostriction. At 20°C approximately 5 MPa to 7 MPa is required to achieve 70.5-degree wall motion and magnetostriction jumping.

Typical temperature dependencies of the magnetostrictions are summarized in Figure 7 for σ = 7.6 MPa and 18.9 MPa and for applied fields of 250 Oe, 500 Oe, 1000 Oe, and 2000 Oe. Note that the onset of the magnetostrictive state (<111> easy) occurs near -10°C in $Tb_xDy_{1-x}Fe_{1.9}$ with x = 0.3. For x < 0.3, this onset moves to higher temperatures; for x > 0.3, this onset moves to lower temperatures. Thus, the peak in the temperature dependence of the magnetostriction can be adjusted by varying x.[9] An important characteristic of twinned, single-crystal Terfenol-D is the large increase in length at low applied fields. Magnetostrictions ~800 ppm exist at 250 Oe for σ = 7.6 MPa, and ~600 ppm at 500 Oe with σ = 18.9 MPa. Large magnetostrictive bars of Terfenol-D for high-power acoustic transducers were characterized by Moffet, et al.[10] for operating stresses up to 30 MPa and fields up to 800 Oe. Hybrid transducers utilizing Terfenol-D and conventional

piezoceramic materials in a unified structure are described by Butler, et al.[11]

A simple, two-dimensional model of the magnetization process in Terfenol-D is depicted in Figure 8. Here at H = 0 (and with pressure sufficient to populate only the [111] direction perpendicular to the rod axis), a single domain exists which traverses the dendrites. As the field is first increased, the magnetic moments remain close to the perpendicular [111] direction (Figure 8a) until the magnetic energy is sufficient to exceed the magnetocrystalline anisotropy energy barrier and perform the work required against the compressive load. At low
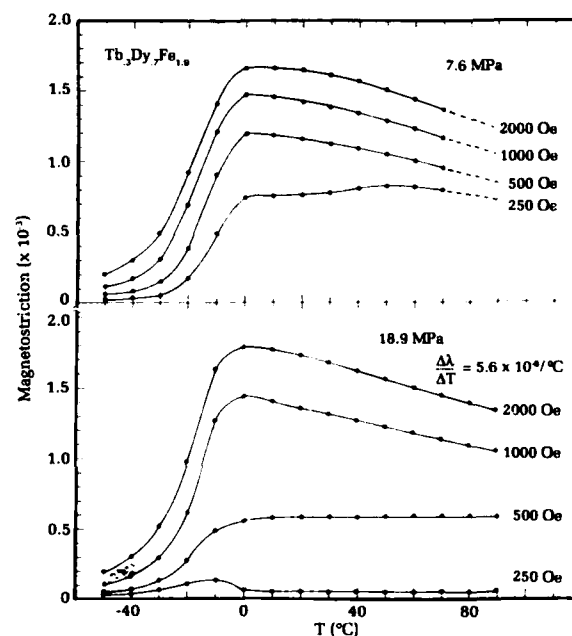

Figure 7. Magnetostriction of Terfenol-D vs temperature for compressive stresses of 7.6 and 18.9 MPa.
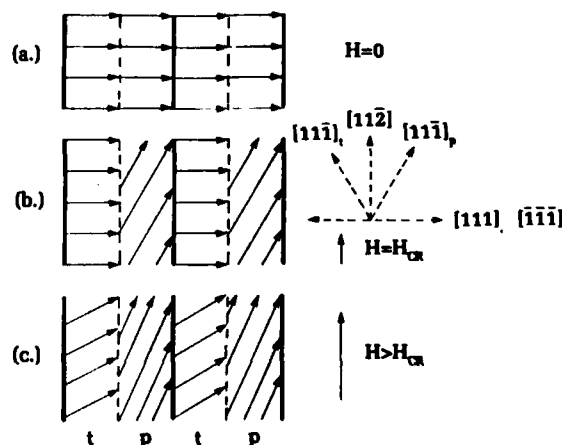

Figure 8. Model of the magnetization process for [112] twinned Terfenol-D single crystal.

fields, only a small magnetostriction results. At the critical magnetic field, H_{cr}, the magnetization of one twin jumps to a new direction close to the [111] direction, which is 19.5 degrees from the [112] rod axis, while the magnetization of the other twin remains close to the perpendicular [111] direction (Figure 8b). With further increase in magnetic field, final rotation of both twins toward the [112] direction occurs (Figure 8c).

The application of this model to the data of Figure 6 predicts that the strain which occurs with magnetization jumping, $\Delta\lambda$, is given approximately by 1/2 of the saturation magnetostriction. For measurements along [112] and rotation from [111] perpendicular to the rod axis to [111] 19.5 degrees from the rod axis, the saturation magnetostriction is given by $(4/3)\lambda_{111}$. Thus the strain in the twinned samples is predicted to be $\Delta\lambda = \Delta\lambda_p/2 + \Delta\lambda_t/2 = (2/3)\lambda_{111} + 0 = 1067$ ppm. (Here equal volumes of parent (p) to twin (t) are assumed, and $\lambda_{111} = 1600$ ppm.[4]) This calculated value is very close to the observed value of ~1000 ppm. Similarly, the magnetization jump (ΔM) is approximately given by $(M_s/2)\sin 70.5° = $ ~0.5 T, where the saturation magnetization M_s is taken to be 1.05 T. This also is in good agreement with an observed value of ΔM ~ 0.58 T. At higher compressive loads, the magnetostriction and magnetization jumps become slightly smaller since the angle change is less than 70.5 degrees.

It is interesting to compare the work done against the compressive load to the magnetic energy supplied by the magnetic field. For pressures of 7.6 MPa, 13.3 MPa, 18.9 MPa and 24.5 MPa, critical fields, H_{cr}, were 295 Oe, 500 Oe, 705 Oe, and 1000 Oe, respectively. Figure 9 shows the fraction of the magnetic energy, E_{mag} (M·H) converted to mechanical energy or work, W ($\sigma\cdot\Delta\lambda$) during the magnetization jumping process. (The additional work done during the final rotation process is not included in the figure.) As the compressive load is increased, a larger fraction of the magnetic energy is converted to work. Because of magnetization jumping, only a moderate triggering magnetic field is required to transfer the energy between the magnetic state and the mechanical state. The size of this field depends upon the magnetic hysteresis. The sample used in this experiment required ~100 Oe to trigger the jump. If a bias magnetic field (H_b) is introduced and the magnetic energy is given by the triggering magnetic energy, M·(H - H_b), rather than by M·H, the ratio of work done against the stress to the magnetic energy supplied, W/E_{mag}, can become far greater than unity.

Using this magnetization jumping mechanism for samples with lower hysteresis, larger amounts of energy can be transferred from the internal magnetic state to the external mechanical state by a small triggering magnetic field. The strain discontinuities for twinned [112] samples of Terfenol-D are limited to ~1000 ppm at room temperature. In [112] untwinned samples these discontinuities are predicted to increase to ~2000 ppm, and in single crystal, $TbFe_2$ jumps up to ~3500 ppm would occur. Thus, further substantial increases are possible in performance of high-power transducers, vibration isolators, and actuators, as well as rapid solid-state mechanical switches. An "inchworm" or "magnetostriction" motor developed from these materials would be highly efficient.

Magnetomechanical Materials at High Temperature

In the region above room temperature, the magnetostrictions of both $TbFe_2$ and $Tb_{.27}Dy_{.73}Fe_2$ slowly decrease to zero as the temperature is raised. Figure 10 illustrates the magnetostriction resulting from a 90-degree rotation of the magnetization in a field of 9 kOe.[12] In this study, the samples were not composed of perfectly aligned, twinned dendrites. Because of the magnetocrystalline anisotropy, the magnetostriction is not saturated at the lower temperatures, particularly in $TbFe_2$. Substantial magnetostrictions (> 10^{-3}) persist as high as 150°C in $Tb_{.27}Dy_{.73}Fe_2$ and 250°C in $TbFe_2$. At these high temperatures, the magnetic anisotropy is small and saturation is attained at low applied fields.
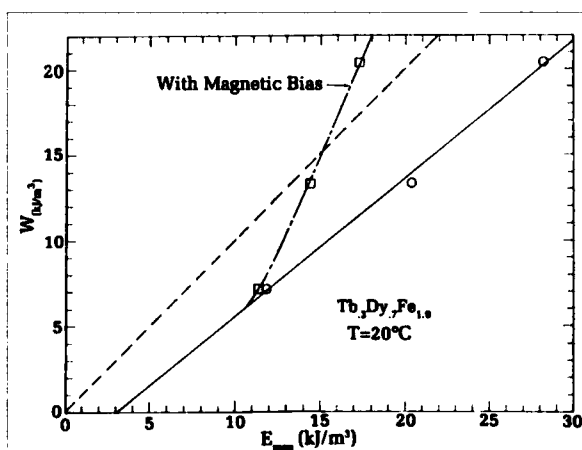

Figure 9. Magnetic energy, E_{mag} (M·H) converted to Work, W ($\Delta\lambda\cdot\sigma$) during the magnetization process. The dashed line represents lossless conversion.
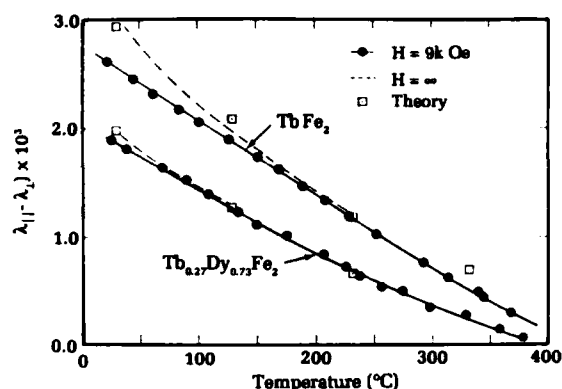
71

Figure 10. Magnetostriction of $TbFe_2$ and $Tb_{.27}Dy_{.73}Fe_2$ at high temperatures.

Conclusions and Applications

Two classes of high-power magnetostrictive materials have been developed at White Oak. Alloys of Tb and Dy have achieved huge strains at temperatures up to 100°K. Intermetallic compounds containing Tb, Dy, and Fe have produced strains of 1000 ppm at temperatures up to 250°C. A large number of magneto-mechanical transducers and actuators utilizing these materials have been designed and manu-factured. See, for example, Butler,[13] Kvarnsjo,[14] and Claeyssen[15] for design details. Structures with infinite stiffness, as well as structures that are extremely soft, can clearly be fabricated with highly magnetostrictive materials. Because of the large saturation mag-netostriction and the large blocking forces of the lanthanides, structures designed to be infi-nitely rigid can withstand strong impulses, and structures designed to be soft can isolate vibra-tions at very low frequencies. Additionally, variable frequency resonators with large fre-quency spans are possible.[4] Structures using composite magnetostrictive/piezoelectric mate-rials have already produced unconventional nonreciprocal sonar performance, with large front-to-back power outputs.[11]

Acknowledgments

References

1. Rhyne, J. J. and Legvold, S., "Magnetostriction of Tb Single Crystals," *Phys. Rev.* 138, A507, 1965.
2. Clark, A. E., DeSavage, B. F., and Bozorth, R. M., "Anomalous Thermal Expansion and Magnetostriction of Single-Crystal Dysprosium," *Phys. Rev.* 138, A216, 1965.
3. Clark, A. E., Rhyne, J. J., and Callen, E., "Magnetostric-tion of Dilute Dysprosium Iron and of Gadolinium Iron Garnets," *J. Appl. Phys.* 39, 573, 1968.
4. Clark, A. E., *Ferromagnetic Materials*, Vol. 1, ed. E. P. Wohlfarth, North Holland Publ. Co., Chap. 7, 1980, p. 531.
5. Clark, A. E. and Belson, H. S., "Giant Room Tempera-ture Magnetostrictions in $TbFe_2$ and $DyFe_2$," *Phys. Rev. B.* 5, 3642, 1972.
6. Spano, M. L., Clark, A. E., and Wun-Fogle, M., "Magnetostriction of Dy-Rich Tb_xDy_{1-x} Single Crystals," *IEEE Trans. on Magnetics* 25, 3794, 1989.
7. Teter, J. P., Clark, A. E., and McMasters, O. D., "Aniso-tropic Magnetostriction in $Tb_{.27}Dy_{.73}Fe_{1.95}$," *J. Appl. Phys.* 61, 3787, 1986.
8. Clark, A. E., Teter, J. P., and McMasters, O. D., "Mag-netostriction 'Jumps' in Twinned $Tb_{0.3}Dy_{0.7}Fe_{1.9}$," *J. Appl. Phys.* 63, 3910, 1988.
9. Clark, A. E., Teter, J. P., and Wun-Fogle, M., "Anisotropy Compensation and Magnetostriction in $Tb_xDy_{1-x}(Fe_{1-y} T_y)_{1.9}$ (T = Co, Mn)," *J. Appl. Phys.* 69, 5771, 1991.
10. Moffett, M. B., et. al., "Characterization of Terfenol-D for Magnetostrictive Transducers," *J. Acoust. Soc. Am.* 89, 1448, 1991. See also: Moffett, M. B., Powers, J. M., and Clark, A. E., "Comparison of Terfenol-D and PZT-4 Power Limitations," *J. Acoust. Soc. Am.* 90, 1184, 1991.
11. Butler, J. L., Butler, S. C., and Clark, A. E., "Unidirectional Magnetostrictive/Piezoelectric Hybrid Transducer," *J. Acoust. Soc. Am.* 88, 7, 1990.
12. Clark, A. E., and Crowder, D. N., "High Temperature Magnetostriction of $TbFe_2$ and $Tb_{.27}Dy_{.73}Fe_2$," *IEEE Trans. on Magnetics* MAG-21, 1945, 1985.
13. Butler, J. L., "Applications for the Design of Etrema Terfenol-D Magnetostrictive Transducers," Edge Technologies, Inc. 306 South 16 St., Ames, IA, 1988.
14. Kvarnsjo, L., "Principles and Tools for Design of Mag-netomechanical Devices Based on Giant Magnetostric-tive Materials," Royal Institute of Technology, Dept. of Plant Engineering, S-10044, Stockholm, Sweden.
15. Claeyssen, F. and Boucher, D., "Design of Lanthanide Magnetostrictive Sonar Projectors," *Proc. Defense Technologies Conference*, Paris, France, 1991, p. 1059.

72

The Author

ARTHUR E. CLARK, a senior scientist in the Sensors Technology Branch, holds a B.S. degree in physics and electronics from the University of Scranton (1954), M.S. in physics from the University of Delaware (1957), and a Ph.D in physics from the Catholic University of America (1960). He is a Navy Distinguished Scientist and has been head of the magnetics group at White Oak for 18 years. Since receiving his Ph.D., he has been engaged in research on the elastic and magnetic properties of solids, particularly on the magnetostrictive properties of rare earth ions in metals and insulators. He is noted for his development of Terfenol (rare earth-iron alloy), which exhibits huge magnetostriction values, thereby opening up a host of new magnetomechanical devices. He is also recognized for the development of near unity magnetomechanical coupling in amorphous alloys, and has been cited for performing the critical research leading to a new class of high-energy-product permanent magnets. Dr. Clark has published over 100 papers and has delivered invited lectures in most countries of the industrialized world. He holds patents in the areas of magnetic refrigeration, magnetostrictive materials, and magnetomechanical transduction.

73

Molecular Beam Epitaxy of Insulators and Semiconductors on Si-Based Substrates

T. K. Chu, F. Santiago, and C. A. Huber

The growth of high quality, single-crystalline materials on top of each other (heteroepitaxy) is a subject of intense interest in the electronic and opto-electronic industries. By combining the desirable properties of various materials in heteroepitaxial structures, many innovative devices have been developed and commercialized in recent years. Our objective here is to investigate the physical and chemical processes involved in the epitaxial growth of semiconductors and insulators on standard electronic-grade silicon (Si) wafers. It is motivated by the potential for sensor integration and for monolithic devices. Both are of interest to Navy system development. For this work, the molecular beam epitaxy method is used with in situ surface analysis techniques under ultrahigh vacuum, contamination-free conditions. Results are presented for an insulator, barium fluoride (BaF$_2$), and a semiconductor, lead telluride (PbTe). From these results, it is projected that alloy semiconductors of the mercury cadmium telluride (HgCdTe) system can also be grown epitaxially on Si. Such epitaxies would have positive impact on the Navy infrared focal-plane array technology by allowing on-chip integration of the detector with the signal-processing circuitry.

Introduction

Molecular beam epitaxy (MBE) technology is the most advanced among those used for semiconductor material processing. Materials can be fabricated on a layer-by-layer basis on an atomic scale, under ultrahigh vacuum, ultraclean conditions. This is achieved through stringent control of both the vacuum environment and the evaporation of the source materials. An advantage of the Dahlgren Division's facility is our capability to monitor *in situ* the MBE growth by x-ray photoelectron (XPS), ultraviolet, Auger and reflection high-energy electron diffraction (RHEED) spectroscopies. This capability has led to very exciting discoveries in the growth of both insulators and compound semiconductors on Si substrates.

In this investigation, the majority of the surface analysis was done with XPS and RHEED. XPS is also known as electron spectroscopy for chemical analysis,[1] which involves the photoelectric effect when a specimen is exposed to soft x-rays. The electrons thus emitted are energy analyzed. The kinetic energy of the electron is given by:

$$KE = h\nu - BE - \phi, \tag{1}$$

74

where BE is the binding energy of the atomic core level (designated by the quantum numbers of the Bohr atom, such as Ba $3d_{5/2}$, etc.) from which the photoelectron is emitted; $h\nu$ is the x-ray photon energy; and ϕ is the work function of the electron-energy analyzer. From the energy distribution of the photoelectrons, one can obtain element identification and chemical information by comparing a chosen core level with that of either the pure element or a known compound.

A problem commonly encountered in this analysis is that shifts can also be due to charging on insulating surfaces. Fortunately, in this work the thicknesses of the films studied were small enough that only very slight charging was found. Moreover, in the instances when charge was present, the shift due to charging and shifts due to changes in chemical state could be distinguished. Charging causes a small displacement of the entire photoelectron spectrum. This displacement is dependent on sample thickness. Changes in chemical state, on the other hand, induce relative energy shifts that are thickness independent. Thus, energy shifts due to chemical changes were easily identified in our experiments.

In the RHEED technique, the diffraction of an electron beam at a low incident angle is displayed on a phosphor screen. Long-range order of the irradiated specimen is manifested by well defined lines. This technique is an *in situ*, real-time monitor of the crystallinity of the deposited films. Information on the crystal structure can also be extracted from analysis of the diffraction pattern. This analysis, however, was not carried out in great detail in the current investigation.

Recently, the growth of fluorides on silicon had been investigated by various researchers. This interest arises due to the excellent dielectric properties of these insulators, which are desirable for micro-electronic circuitry. Efforts had been focused mostly on calcium fluoride (CaF_2)[2-4] because of its good lattice match with silicon. Fluorides are also transparent in the mid- to long-infrared spectrum. In addition, their lattice constants match quite closely those of infrared detector semiconductors. Fluoride crystals, especially barium fluoride (BaF_2), are therefore useful as substrates for the epitaxial growth of these semiconductors. Examples include the IV-VI semiconductors (compounds of Group IV and Group VI elements) such as lead telluride (PbTe), lead tin telluride (PbSnTe), and lead selenide (PbSe).[5-7] Unfortunately, high quality, large-area single crystalline substrates of fluoride compounds suitable for epitaxial film growth are difficult to produce, and in fact are unavailable commercially. As a consequence, epitaxial fluoride films on large-area Si wafers are highly desirable. Zogg et al.[8] concentrated on heteroepitaxy of BaF_2/CaF_2 on [111]-oriented silicon substrates, where the CaF_2 layer served as a buffer between the highly mismatched BaF_2 and Si. Infrared detectors covering both the 3 μm to 5 μm and the 8 μm to 12 μm atmospheric windows had been demonstrated.

More recently, Asano et al.[9,10] and Schowalter and co-workers[2,4] showed that BaF_2 tends to grow in the [111] orientation regardless of the Si orientation, and that growth in any other direction was very difficult to achieve. This was attributed to the strong dipole interactions across the (111) fluoride plane. We have confirmed that large area, single crystalline [111]-oriented BaF_2 films can be grown directly on silicon of either the [111] or the [100] orientation.[11] These BaF_2 films were also used as substrates for the growth of the IV-VI semiconductors.[12] From a simple atomic stacking model, it was difficult to understand how a single crystalline material with a lattice constant so much larger can grow on an Si lattice (6.20 Å vs 5.43 Å). On the other hand, a buffer material at the Si surface can bridge the lattice mismatch between Si and BaF_2 and facilitate crystalline growth of the latter.

As will be shown, our investigations by XPS strongly suggest the latter scenario, where a Ba-Si compound is formed via a chemical reaction at the interface between the Si and the fluoride. Furthermore, by controlling the BaF_2 flux and the substrate temperature, a predominantly Ba-Si buffer layer can be formed on the Si. The thickness of this buffer layer is estimated to be on the order of 10 Å. Although the nature of the Ba-Si layer has not been fully characterized, the potential of the Ba-Si/Si structure as a substrate for the deposition of semiconductors with large lattice constants has been explored. We report here also the very promising results on the growth of PbTe on Ba-Si/Si substrates.

XPS analysis of the deposition of PbTe on Ba-Si/Si also shows evidence of a chemical reaction at the PbTe/Ba-Si interface. The analysis suggests that a Ba-Te compound is formed. Together with those of the BaF_2/Si interface, these results have important general implications for the understanding of the chemistry and physics at the interface between a substrate and a deposited material.

Results of these investigations suggest also that the heteroepitaxial growth of the II-VI compounds (such as cadmium telluride, CdTe, which has a lattice constant close to that of PbTe) on the Ba-Si/Si may be highly likely. The successful growth of large area CdTe films will impact on the manufacturing cost of the HgCdTe infrared focal plane arrays, which is the technology of choice for Navy search and

75

track systems. It could also make monolithic infrared focal plane arrays, with full integration to Si electronics, a real possibility.
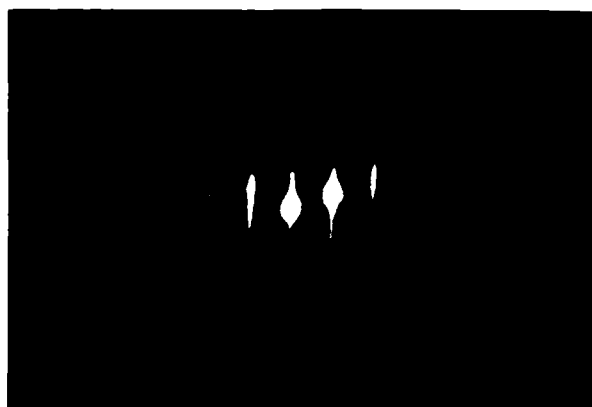

Figure 1. RHEED pattern of a BaF$_2$ film grown on a [111]Si substrate.

Barium Fluoride Film

Film Growth

BaF$_2$ films were grown on 3-inch-diameter Si wafers, either [100]- or [111]-oriented. In the current experiments, we were not able to detect any difference between films grown on the [111]- or the [100]-oriented wafers. The chamber used was a Vacuum Generator (VG) Model VG80M, designed for the growth of Si thin films. The residual pressure was less than $4 \cdot 10^{-11}$ mbar. The source material was single-crystal BaF$_2$, crushed into roughly 1 mm^3 pellets. This material was sublimated from a Knudsen effusion cell (K-cell) at a temperature of 1050°C. The shuttered orifice of the cell was ~0.2 m from the substrate. The substrate was situated in a horizontal, downward facing position, and was rotated at about 0.5 revolution per second. Prior to the fluoride deposition, the standard commercial Si wafer was heat-cleaned at 1000°C. During deposition, the incident flux was approximately $2 \cdot 10^{-10}$ mbar, or equivalently, a molecular beam on the order of two to three monolayers per minute. The background pressure in the chamber was $8 \cdot 10^{-11}$ mbar during deposition. The substrate temperature was about 750°C. This temperature was read by a thermocouple at the substrate holder. Surface temperature measurements with an optical pyrometer indicated that the actual substrate temperature was probably 700°C to 710°C. This is the lowest temperature at which high-quality epitaxial films can be made. At the flux given above, a deposition time of about one hour is needed to yield good quality BaF$_2$ surface layers. Several series of films were also grown using deposition times of 1, 2, 5, 10, and

20 minutes. These films were deposited for the purpose of chemical analysis and also for tracking the development of the deposited material. After growth, the samples were cooled naturally to room temperature, which took approximately 60 minutes. When necessary, the samples were transferred from the growth chamber to an analysis chamber through vacuum interlocks. The samples were exposed to pressures no greater than $1.5 \cdot 10^{-10}$ mbar during the transfer. Figure 1 shows the RHEED pattern of a BaF$_2$ film grown on a [111]Si substrate. A parallel streak pattern, indicative of good two-dimensional growth, is displayed.

Damage by X-rays

A problem with using XPS to analyze fluoride compounds is that the x-rays can decompose the samples. Fortunately, a product of the decomposition is gaseous fluorine, which can escape from the surface. Thus it is convenient to monitor the decomposition by tracking the diminishing fluorine signal, and at the same time the emergence of a signal from the metallic species. Using these indicators, we have established that it took six hours of exposure to the radiation emitted by the x-ray source in our instrument to yield a 15 percent decomposition on the BaF$_2$.[11] Figure 2 shows the evidence for such decomposition from the XPS signals for the Ba 3d$_{5/2}$ and the Ba 3d$_{3/2}$ levels for exposure times up to 20 hours. In subsequent XPS analyses, we maintained a constant total x-ray exposure time of 20 minutes for all samples, in order to limit the damage to less than 1 percent, and in order that our findings from these analyses on the interface chemistry were not substantially affected by the decomposition. In addition, we were also able to identify the part of the signal due to damage, since the damaged materials showed chemical shifts different from the results reported here.
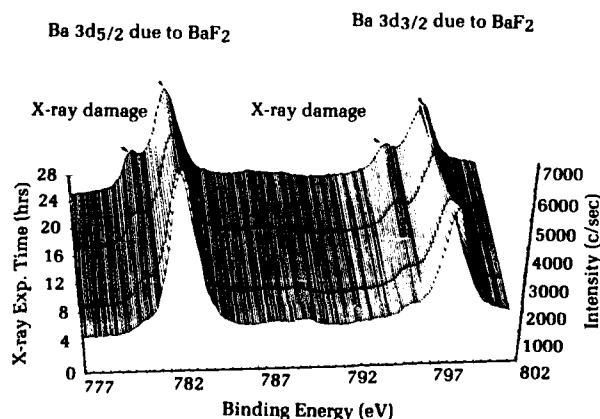

Figure 2. XPS spectrum of the Ba 3d$_{5/2}$, 3d$_{3/2}$ levels showing the effects of damage by x-ray exposure in the analysis chamber.

Barium Fluoride Signature

In order to establish a basis for comparison and for quantitative analyses of results on the deposited films, the characteristic signature of a pure BaF_2 compound has to be established. However, because BaF_2 is a good insulator, there was a large differential charging when bulk BaF_2 samples were examined. Thus, the XPS spectrum of pure BaF_2 is not accessible. Consequently, the XPS spectrum of BaF_2 was chosen as that from a deposited film with deposition times long enough that: (1) only one Ba chemical species was observed (i.e., when the Ba signal is stable), (2) no Si was detected, and (3) an F/Ba ratio of 2:0 was attained. These requirements are satisfied easily by films of 60-minute deposition time. Even though we did not establish the exact thickness of such a BaF_2 layer, we believe that the above criteria are sufficient for the purpose of identifying BaF_2. An additional consideration is that, for this duration, more than 60 molecular layers of BaF_2 would have impinged on the surface. Even assuming a low sticking coefficient of only 10 percent, the BaF_2 film should have at least six molecular layers. This is larger than the three molecular layers for a similar compound, CaF_2 (as determined by Olmstead et al.[13]), to acquire a bulk character on an Si surface. It should be mentioned here that the Ba $3d_{5/2}$ peak observed on this "bulk BaF_2" film can be represented by a Gaussian profile centered at 783.4 eV with a full width at half maximum (FWHM) of 0.90 eV. This peak will be used for numerical analyses of other XPS spectra, details of which are given below.

Interface Chemical Reaction

The surface analysis in this work was done in a VG analysis chamber equipped with a computer-controlled Model CLAM-100 electron energy analyzer and a dual-anode Mg/Al x-ray source. For the BaF_2-Si analysis, the radiation used was the Mg $K\alpha_{1,2}$ emission with a combined FWHM of 0.82 eV. The source was run at 15 kV with an emission current of 20 mA. The electron energy analyzer was operated in the constant-pass-energy mode (i.e., collecting electrons within a constant energy spread), with a pass energy of 5.0 V and a resolution of 0.1 eV. The pressure inside the analysis chamber was never greater than $2 \cdot 10^{-10}$ mbar. The films were analyzed within an hour after they were deposited, even though storage in the chambers for periods up to two months resulted in no detectable change in the chemical composition of the surface.

In the wide-scan XPS spectra of BaF_2 films on Si, only Ba, F, and Si peaks were present. Detailed examinations of the spectra revealed no contaminants. Figure 3 Curve (a) shows the wide-scan XPS spectrum of a film with 60 minutes of BaF_2 deposition. In this spectrum, the Ba and the fluorine signal are clearly displayed while the Si is completely masked by the BaF_2 film. Curve (b) is included in this figure for convenience and will be discussed later.

Detailed analysis of the surface was facilitated via the Ba $3d_{5/2}$ level. This was chosen because of its high intensity and good separation from other atomic levels of the spectrum. Figure 4 displays four spectra of this level (together with the Ba $3d_{3/2}$ level, which behaves similarly) from a set of specimens with

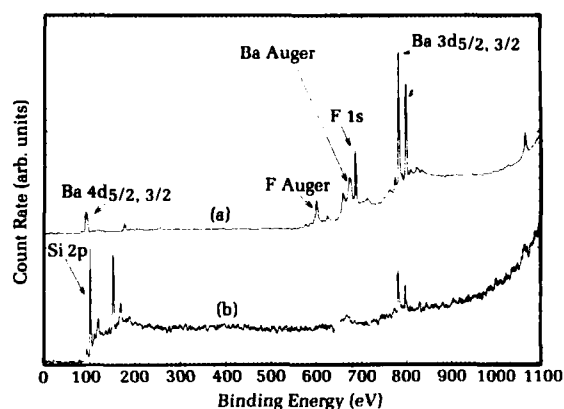**Figure 3.** The wide-scan XPS spectrum of (a) a BaF_2 film deposited on a [100]Si substrate at 750°C for 60 minutes, and (b) the same film after being heated at 750°C for 2 hours in the growth chamber.
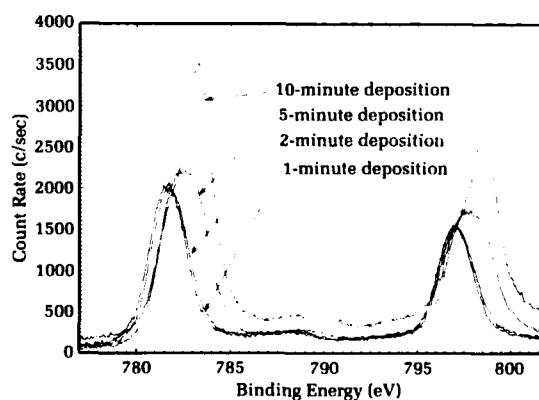
Figure 4. Superposition of the Ba $3d_{5/2}$ (left) and the $3d_{3/2}$ (right) spectra for four deposition times. This figure shows evidence for the existence of a chemical gradient normal to the substrate surface.

77

different deposition times. It is clear that the binding energy increased as the deposition time increased — shifting in fact toward that of the bulk BaF$_2$ discussed earlier. Notice that the spectra became sharper (smaller FWHM) at longer deposition times. This indicates that the film initially formed on the Si surface by the BaF$_2$ deposition comprises a mixture of chemical states that became more sharply defined as deposition time increased. This is seen from the spectrum of the film of 10-minute deposition, where the sharp peaks with humps on the low-energy side are displayed. (The position of the main 3d$_{5/2}$ peak is 783.3 eV, practically the same as that for the bulk BaF$_2$ film.) The humps on the low-energy side of the peaks are indications of the existence of an additional state or states.

Attempts to identify the chemical state(s) included heat treating the deposited films. Curve (b) of Figure 3 shows a result of such treatment. It is clear that after heating for two hours at the deposition temperature, the fluorine signal is gone. This implies that the BaF$_2$ film is being converted to a different compound at this temperature, one which contains Ba and Si only. This will be discussed in detail in the following section.

Barium Silicide Film

Evolution of Surface Chemistry

As mentioned above, epitaxial [111]-oriented films of BaF$_2$ have been reported to grow successfully both on [100]- and [111]-oriented Si substrates despite large disparities in both lattice spacing and crystal orientation. The mechanism involved was not fully understood at the time. For these earlier growth studies, the deposition rates were in the vicinity of 1 μm/hr. These rates were more than a thousand times higher than used in this study. We surmised that their high growth rates tend to mask the interaction at the Si surface. In the current investigation, we were able to track the growth of films, especially during the first few monolayers of deposition, by reducing the BaF$_2$ flux drastically.

In the previous section, we demonstrated that the surface chemical reaction between the Si substrate and the deposited BaF$_2$ resulted in a surface layer made up of a mixture of BaF$_2$ and at least one other compound, not yet identified. Further evidence is provided by the result of a shorter heat treatment (i.e., less than the two hours used for the specimen of Curve (b) in Figure 3). Figure 5 shows the Ba 3d$_{5/2}$ and 3d$_{3/2}$ spectra of a film of five-minute deposition, and those of the same film after being heated at the deposition temperature for 45 minutes. It is obvious that the treatment

resulted in a reduction of the magnitude of the signal, partially due to the re-evaporation of the deposited BaF$_2$. It is also obvious that the peaks became sharper and shifted toward lower energies. In fact, the positions of these peaks remained essentially the same upon further heating at the same temperature, demonstrating that this as-yet-unidentified chemical can exist in a stable state. Even though we cannot establish the composition of this chemical state, we believe it involves the elements Ba and Si only, since fluorine is no longer present after heat treatment at this temperature, as shown by Curve (b) in Figure 3. This conclusion is also supported by the concurrent shift in the XPS spectrum of the Si 2p$_{3/2,1/2}$ level (the Si 2p$_{3/2}$ and 2p$_{1/2}$ levels are unresolved, hence the combined designation) to a lower energy, shown in Figure 6. This shift is consistent with the interpretation of the formation of a Ba-Si bond, similar to the Ca-Si bond reported by Olmstead et al.[13] For lack of a better name, we refer to this chemical as a barium silicide, or Ba-Si. The Ba
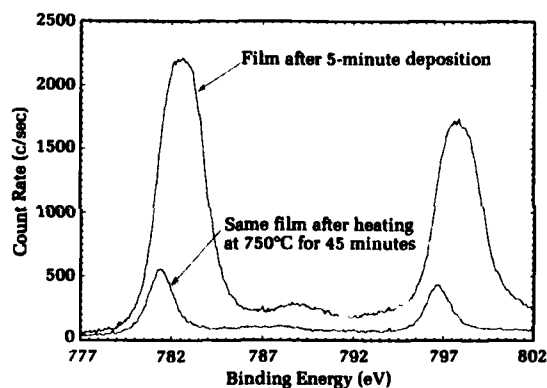

Figure 5. The change in the Ba 3d$_{5/2}$ (left) and 3d$_{3/2}$ spectra after heating a film of 5-minute deposition at the deposition temperature of 750°C.
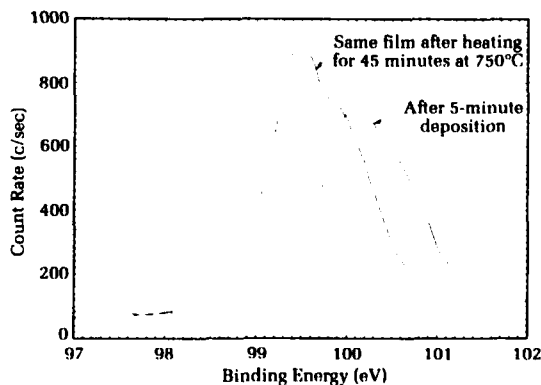

Figure 6. Spectra of the Si 2p$_{3/2,1/2}$ level for the same specimen as Figure 5.
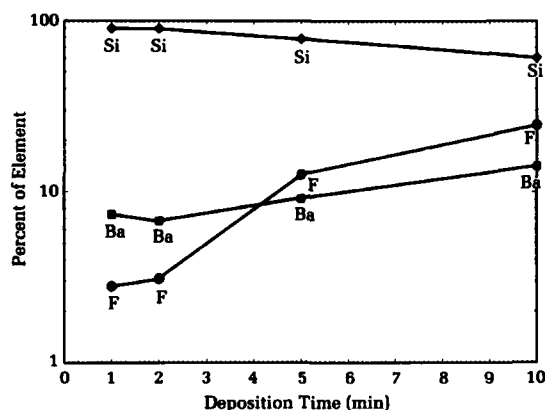
Figure 7. Profile of elemental composition as function of deposition time.
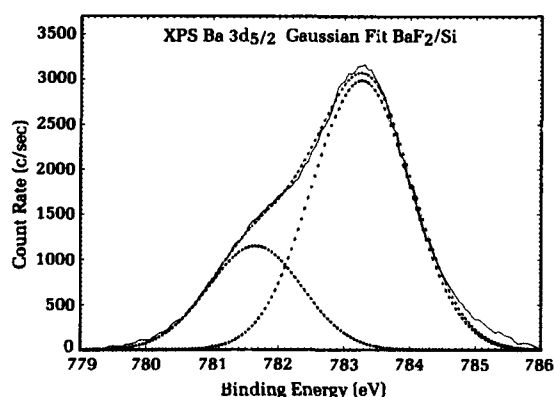

Figure 8. Fit to the Ba $3d_{5/2}$ spectrum of a film of 10-minute deposition, using the two component Gaussians specified in the text.

$3d_{5/2}$ peak of this state can be represented by a Gaussian profile at 781.46 eV with an FWHM of 0.85 eV.

Once the stable characteristic of the Ba-Si state is established, the character of a deposited film can be described by a combination of the BaF_2 and the Ba-Si states. The relative abundance of these two states varies with the deposition time. At shorter times, the deposited film is composed of both BaF_2 and Ba-Si. As deposition time increases, the top surface of the specimen becomes dominated by pure BaF_2. This is supported by an atomic concentration analysis using the method of Scofield cross sections.[1] The result is shown in Figure 7. It is seen that the ratio of F to Ba goes from about 1/4 at 1-minute deposition to 3/2 at 10-minute deposition. After 60 minutes of deposition, the ratio was found to be two.

Further support for the evolution of the surface chemistry can be obtained by numerical analysis of the XPS data. For example, the $Ba3d_{5/2}$ spectra for films of deposition times

larger than 10 minutes could be fitted, to within the experimental uncertainty of 0.1 eV, with the two Gaussians mentioned above: (1) one pertaining to the BaF_2 state at 783.4 eV with an FWHM of 0.90 eV and (2) one to the Ba-Si state at 781.46 eV with an FWHM of 0.85 eV. Figures 8 and 9 show the excellent fits for films of 10- and 20-minute deposition times, respectively. It is important to mention that the only adjustable parameters in these fits were the magnitudes of the two component Gaussians. These fits strongly support the conclusion that the deposited BaF_2 layer undergoes a chemical reaction, resulting in a mixture of the BaF_2 state and a Ba-Si state. It should be emphasized again that this interfacial chemistry is independent of substrate orientation; these results were identical for both [111]- and [100]-oriented silicon substrates.

Preparation of the Ba-Si Buffer

The existence of definitive and distinct BaF_2 and Ba-Si states points to the premise that a Ba-Si layer provides a buffer for the growth of the BaF_2 on the Si surface. This is supported by the results of a film grown in two stages. First, a deposition of BaF_2 was carried out for five minutes. The film was cooled down to room temperature and reheated to 750°C. Then an additional deposition of five minutes was carried out. Figure 10 shows the XPS spectrum of this two-layer film. For comparison, the spectrum of a film with a 10-minute continuous deposition is also shown. The clearly distinguishable double peaks displayed by the two-layer film attest further to the existence of two distinct chemical states. Furthermore, a simple superposition of this figure and Figure 8 reveals that the positions of the peaks for the two-layer
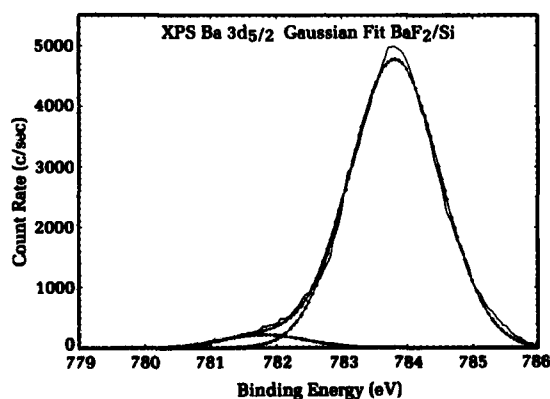

Figure 9. Gaussian fit to the Ba $3d_{5/2}$ spectrum of film of 20-minute deposition. The spectrum is shifted toward a higher energy due to the effect of charging.
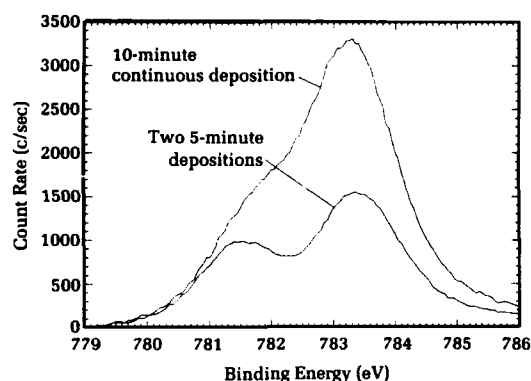
79

Figure 10. The Ba $3d_{5/2}$ spectra of a film with two 5-minute depositions interrupted by cooling down from and heating up again to the deposition temperature, and a film with a continuous 10-minute deposition.

film, to within the experimental uncertainty of 0.1 eV, are the same as those of the two Gaussian components for the film of 10-minute deposition. Therefore, it can be inferred that the Ba-Si interfacial compound actually exists as a separate and somewhat distinct layer. This layer then serves as a buffer for the subsequent growth of epitaxial BaF_2. Also, this buffer layer is stable during the heating and cooling cycle.

A further test of this premise was carried out by first annealing a deposited film and heating it at 750°C until its surface displayed only the "silicide" characteristics. Then a BaF_2 deposition was done at 550°C. The resultant film was not as uniform as the BaF_2 films grown at 750°C; but large areas with excellent film quality were found as determined by the clean RHEED pattern with well defined lines exhibiting only faint hints of rings. Subsequently, some effort was spent on the preparation of this buffer for investigating its potential for the growth of other materials. The following is a description of a procedure by which an Si substrate with a thin Ba-Si buffer layer was made.

This procedure essentially consisted of depositing a layer of BaF_2 and then heat treating the wafers *in situ*. The important indicator is the surface chemistry, which was monitored with XPS analysis. The Ba-Si was considered satisfactory when there were no further shifts in the Ba and the Si XPS spectra. This should also be accompanied by the absence of any fluorine signal.

80 RHEED measurements on this buffer surface showed distinct streaks. However, the patterns were very complex, suggesting a complex crystal structure. In addition, since the Ba-Si layer was very thin, it is likely that interference from the underlying Si wafer also affected the

diffraction pattern. A detailed analysis of the RHEED pattern is beyond the scope of the present investigation, and was not carried out.

Lead Telluride Film

Deposition

The PbTe was deposited in another growth chamber (VG80H). The wafers were standard 3-inch-diameter commercial Si stock, with a Ba-Si buffer prepared by the method described above. The base pressure of the chamber was $<2 \cdot 10^{-11}$ mbar before the substrates and the K-cells were heated. During growth, the pressure of the chamber was $\sim 1 \cdot 10^{-8}$ mbar. A RHEED gun was used to monitor *in situ* the crystal quality of the layers being grown. The substrate temperature of the PbTe films was usually $\sim 450°C$. Since the pressure during transfer of the substrate from the VG80M chamber was less than $2 \cdot 10^{-10}$ mbar, no outgassing was carried out before PbTe deposition. The growth rate was ~ 0.3 μm per hour. A flux of atomic Te from a cracker cell was used to compensate for the slight dissociation of the PbTe molecules. This is a commonly adopted procedure for the MBE growth of the Te-containing IV-VI compounds. This Te flux is three orders of magnitude lower than the PbTe flux. The substrate was rotated at ~ 0.5 revolution per second during growth. For investigation of the surface chemistry, growths at other substrate temperatures were conducted, usually between 400°C and 500°C.

PbTe/Ba-Si Interface Analysis

XPS analysis was again done with a VG Model CLAM-100 electron energy analyzer using the Al Kα line for excitation. The electron energy analyzer was used in the constant-pass-energy mode with a pass energy of 10.0 V and a resolution limit of 1.06 eV. Figure 11 shows a wide-scan spectrum after a 3-minute deposition at 500°C. For comparison, a scan of the Ba-Si surface is included. It is clear that Te is present at the surface, as are Ba and Si. The thickness of this surface layer could not be determined; it is very likely that the coverage was on the order of one monolayer. Qualitatively, it can be established that the position of the Te $3d_{5/2}$ level was higher than that of the Te $3d_{5/2}$ level found in bulk PbTe. Shifts in the Ba and Si levels relative to those on the Ba-Si surface were also observed. Only an extremely low Pb signal was observed, indicating that there was very little PbTe deposited. This is consistent with our observation that PbTe

grows at progressively lower rates as the temperature approaches 500°C. It is likely that the PbTe molecules have largely decomposed at 500°C, and Te is left behind. It is important to note that during deposition, the atomic Te flux was three orders of magnitude lower than the PbTe flux, and is not considered responsible for the observed Te signal. The Te from the PbTe decomposition then reacted with either the Ba or the Si on the Ba-Si surface, as shifts in the Ba and the Si levels were also observed at the same time.

Even though we cannot determine the exact chemical nature of this Te compound from the result of the 500°C deposition, we believe that it represents a stable surface state. This is supported by XPS analysis of depositions at lower temperatures; in general, chemical shifts at the interface between PbTe and Ba-Si were also
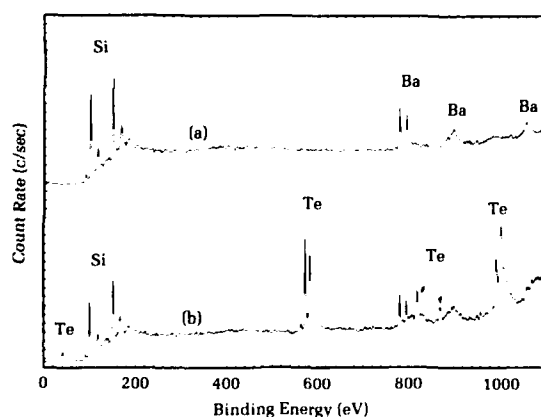

Figure 11. The wide-scan spectra of (a) a Ba-Si surface and (b) the same surface after a 3-minute PbTe deposition at 500°C.
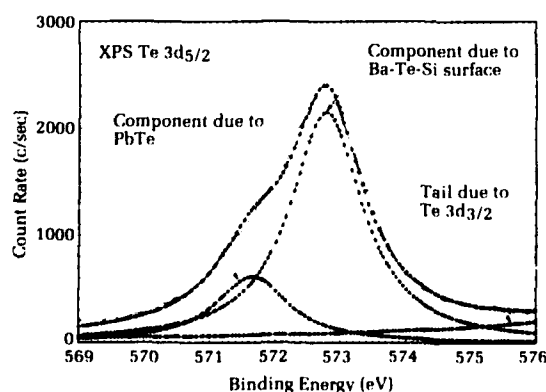
Figure 12. The Te $3d_{5/2}$ spectrum of a film of one-minute PbTe deposition at 450 C. The two main Lorentzian profiles for fitting the data are shown. Also shown is the low-energy tail of the Te $3d_{3/2}$ level, which is included to account for the high-energy side of the $3d_{5/2}$ peak.

observed at deposition temperatures below 500°C. For example, at 450°C, the Te $3d_{5/2}$ peak position shifted toward lower energy with deposition time. At certain combinations of deposition temperature and time, two distinct peaks could be seen.

In order to establish a basis for quantitative analysis of the XPS spectra, we took the Te $3d_{5/2}$ spectrum of a film of three-minute deposition at 500°C as representative of the interfacial Te state. (It should be pointed out that for this deposition time of three minutes, the Pb signal was still absent.) This spectrum turned out to fit a Lorentzian profile at a mean energy of 572.78 eV with an FWHM of 1.28 eV. We also took the Te $3d_{5/2}$ spectrum of a thick ($\approx$ 1 μm) PbTe film as representative of a true PbTe state, which could be fitted to a Lorentzian at a mean energy of 571.82 eV with an FWHM of 1.28 eV. The Te $3d_{5/2}$ spectrum of films of other deposition conditions can then be fitted to a combination of these two Lorentzians. An example, the spectrum for a film deposited at 450°C for one minute, is given in Figure 12. The good quality of these numerical fits to the XPS spectra suggest that, similar to the case of BaF$_2$ on Si, chemical reaction takes place at the PbTe/Ba-Si interface. At higher temperatures (~500°C), PbTe was decomposed, with Te forming a compound with either Ba or Si. At lower temperatures, the growth of the PbTe layer was preceded by the formation of this compound, similar to the case of the Ba-Si layer on the Si substrate for growth of BaF$_2$. We have not been able to identify this interfacial compound from the current results. That this compound was formed at lower temperatures might be pivotal in the heteroepitaxial growth of PbTe on Si surfaces. A possible candidate for this interfacial compound is BaTe, which has the same sodium chloride (NaCl) structure that PbTe has, and is therefore amenable to PbTe growth.

Figure 13. Photographs of PbTe films grown on bare Si (left) and Ba-Si/Si substrates.

It should be mentioned that an attempt to grow PbTe on Si directly without a Ba-Si layer resulted in a granular film, as shown on the left in Figure 13; this PbTe film may be compared

81

with one grown on a Ba-Si/Si substrate, seen on the right. The film grown directly on Si peeled off quite readily from the Si wafer even before it was taken out of the growth chamber. This poor adherence of PbTe to the Si surface seems to preclude the possibility of an Si-Te compound. Other candidates may include more complex chemicals involving all three elements, Ba, Si, and Te.

RHEED and X-ray diffraction

In situ RHEED was used to monitor the crystal quality of the PbTe films. X-ray diffraction measurements were also carried out after film deposition and XPS analysis. The PbTe films demonstrated good crystal quality, as shown in Figure 14 where the x-ray diffraction spectra of two films grown on Ba-Si/Si substrates of different Si orientations are displayed. Notice that the (100) series of peaks are present on both films irrespective of the Si substrate orientation, and that no (111) peaks are evident.

The RHEED patterns also attest to the good long-range ordering of the PbTe films; an example is given in Figure 15.
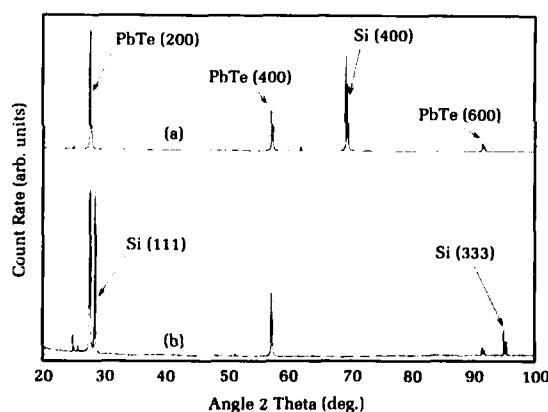

Figure 14. X-ray diffraction for the Cu Kα lines of two PbTe films on (a) Ba-Si/Si(100) and (b) Ba-Si/Si(111) substrates.

Discussion

We have demonstrated that in the MBE deposition of BaF$_2$ on Si, the BaF$_2$ molecules react with the Si surface and establish a Ba-Si bond at the interface. The fact that the XPS spectrum of a film of prolonged heating can be fitted with a single Gaussian, and that the spectra of other films can be fitted to a combination of this Gaussian and one attributable to BaF$_2$, leads to the conclusion that this interfacial bond results in a single Ba-Si compound instead of a mixture of silicides. A search of the

literature[14] reveals several possible candidates for the silicide. However, stoichiometric analysis on the XPS data for a Ba-Si surface, such as that after prolonged heating, yielded an Si/Ba ratio as high as 70:1. This value is much too large for any known silicide. It is obvious that a definitive conclusion on the nature of this Ba-Si compound requires further investigation.

Previously, Olmstead et al.[13] observed Si(111) surface reconstruction during the deposition of a similar material, CaF$_2$. In addition, they detected bonding between the Si and both the Ca and the F atoms. Upon prolonged heating, both Ca and F were lost, returning the Si surface to a clean state. This loss of Ca was contrary to the present result that a stable Ba-Si state resulted from a BaF$_2$/Ba-Si/Si structure upon heat treatment. This may be attributable to a different chemistry at a CaF$_2$/Si interface than at a BaF$_2$/Si interface. On the other hand, even though Si surface reconstruction might have also occurred during BaF$_2$ deposition, it is unlikely to have been responsible for the epitaxial growth of BaF$_2$ on Si. This is evident from the fact that [111]BaF$_2$ growth is independent of Si substrate orientation. (Furthermore, the Si(100) surface should have no reconstruction.) Thus, the interfacial buffer model discussed in the previous section is favored.

The thickness of the Ba-Si buffer cannot be established directly from the current results. Similar studies of CaF$_2$ on Si growth by Himpsel et al.[15] showed that at a thickness of 14 Å, the bulk characteristic of CaF$_2$ was established. Our result on the two-layer film (Figure 10) showed that the Ba-Si signal was of the same magnitude as the BaF$_2$ signal, and the BaF$_2$ signal had the same character as a bulk film (i.e., its spectrum is centered at the same energy as that of the bulk BaF$_2$ film, 781.3 eV). Therefore, it may be inferred that the thickness of the Ba-Si layer is on the order of 10 Å. At this thickness, the Ba-Si compound should

Figure 15. RHEED pattern of a PbTe film on a Ba-Si/Si(100) substrate.

have bulk-like behavior. This is substantiated by the observation that the peak of this Ba-Si component occurs at 783.4 eV, which is the same as for the film after prolonged heating (Figure 3). The truly surprising result is that single crystals of both BaF_2 and PbTe can be grown on this Ba-Si buffer.

The deposition of a single crystalline material on a dissimilar substrate depends to a large extent on the lattice match between the two materials. A notable exception is the IV-VI family of compounds for which high quality (in terms of carrier mobility and crystallinity) materials can be grown successfully on substrates as disparate as NaCl and BaF_2. It may be argued that the IV-VI semiconductors are mechanically soft so that a "self-buffer," highly strained and defective, may exist at the interface between the substrate and the semiconductor. Another exception is the direct growth of [111]BaF_2 on both [100]- and [111]-oriented Si, which may be facilitated by dipoles on a truncated surface.[2] Nonetheless, results of this work and the observation by others of BaSe formation on the BaF_2 surface during the liquid phase epitaxy growth of PbSe[16] and after exposure to Se vapor[17] strongly suggest that interfacial chemical reaction is an important factor to be considered.

Our results also suggest that competition between the atomic species at the interfaces may be important, such as the competition for the Ba between the Si and the F at the BaF_2/Si interface. In the case of the PbTe/Ba-Si interface, there is also apparent competition between either the Ba or the Si for the Te. The character of the interfacial layer and the quality of the top layer subsequently formed are affected by this competition. This is attested to by the difference between the two films depicted in Figure 13.

The beneficial effect of an interfacial chemical layer was demonstrated by the surprising resistance of the PbTe/Ba-Si/Si heterostructure to thermal shock. A wafer with this heterostructure was subjected to severe thermal cycling: heating on a hot plate at 250°C and then immediate immersion in a liquid nitrogen bath. Even after 20 cycles, the film did not show any visible peeling or cracking. In addition, x-ray diffraction measurements showed practically no difference in the spectra (peak positions and FWHMs) before and after these 20 cycles.[18]

One final observation of these growth studies on the Ba-Si buffer is that the growth directions for both BaF_2 and PbTe are also the directions in which the interatomic distances have the longest projections. This relationship between the growth direction and the interatomic distance may provide guidance in understanding nucleation and bonding between dissimilar materials.

Conclusion

The results obtained in this work suggest that more materials can be deposited on silicon than previously envisioned. We have demonstrated that large-area, single-crystalline films, with lattice constants larger than that of Si by more than ~0.8 Å, can be deposited on Si surfaces. This is of obvious technological importance, as one can now envision a large variety of materials that may be fabricated on silicon wafers, thus enabling the integration of other semiconductor technologies with that of Si. The results also suggest that, by making use of solid-phase reactions at interfaces, films of other metal silicides can be made by the deposition of reactive compounds instead of the pure metals, as is commonly done. Possibilities include the transition metal silicides, such as $NiSi_2$ and $CoSi_2$, which are of interest to the electronic industry. Another silicide of interest is Mg_2Si, which is a potential substrate material for infrared semiconductors because of its large (~6.5 Å) lattice constant.

The truly unexpected result of this investigation is that the Ba-Si buffer layer can facilitate the epitaxial growth of both an insulator such as BaF_2 and a semiconductor such as PbTe on standard Si wafers. It may be argued, as was done above for this particular case, that the Ba provides the chemical "link" between the Si surface and the deposited layers. If this chemical link picture is appropriate, then the current results suggest a vast potential for heteroepitaxy between materials that can react with a third material to form compounds that can serve as beneficial interfacial layers. It may be argued further that such reactions can occur only under an ultrahigh vacuum environment. Under such a contamination-free condition, the possible interference and competition from the ubiquitous oxygen, and perhaps from other reactants, may no longer be operative.

Irrespective of the true reason for its success, we have demonstrated that a new artificially structured material consisting of a thin Ba-Si compound on top of an Si wafer can be a very desirable substrate for the growth of single crystalline PbTe films. Since PbTe and its alloys with SnTe form a complete material system for infrared detectors, this discovery implies a promising potential for infrared detector focal-plane-array technology. For example,

83

advantage can now be taken of production methods designed for large-area Si wafers. More important, a truly monolithic array with full integration of the detectors and the signal processing circuitry on a single chip is now a possibility.

The infrared technology based on HgCdTe, which is the technology adopted in Department of Defense (DoD) systems, is at an advanced stage of development. In this technology, bulk CdTe crystals are usually used as substrates for the HgCdTe alloys. Large-area CdTe substrates are expensive and cannot be truly integrated with Si. It is therefore advisable to explore the feasibility of the growth of CdTe on the Ba-Si/Si substrates. Even though the zinc blende structure of CdTe is different from the NaCl lattice of PbTe, its lattice constant is only 0.3 percent larger than that of PbTe. In addition, it is not inconceivable that an interfacial chemistry involving the elements Ba, Si, Cd, and Te may also be operative at the interface. Thus, the deposition of single-crystalline CdTe and other II-VI compounds and alloys on the Ba-Si/Si substrates is a distinct possibility. Based on the discussion given above, CdTe should grow in the [111] direction on Ba-Si/Si substrates. Since the (111) surface of CdTe is desirable for detector fabrication, the successful growth of CdTe should have an important impact on infrared technology for Navy as well as DoD applications. Such studies have been initiated.

Acknowledgments

References

1. Feldman, L. G. and Mayer, J. W., *Fundamentals of Surface and Thin Film Analysis*, Elsevier, New York, 1986.
2. Taylor, A. P., et al., "Substrate Engineering with Fluoride Buffer Layer on Silicon," *MRS Proc.* 220, 537, 1991.
3. Schowalter, L. J. and Fathauer, R. W., "MBE Growth of Epitaxial Calcium Fluoride on Silicon," *MRS Proc. 54*, 285, 1986.
4. Schowalter, L. J. and Fathauer, R. W., "Growth and Characterization of Single Crystal Insulator on Silicon," *CRC Crit. Rev. Sol. State and Mat. Sci. 15*(4), 367, 1989.
5. Carver, G. P., et al., "Dependence of the Amplitude of Transverse Magnetoresistance Oscillations in n-PbTe on Film Thickness," *Solid State Comm. 30*, 461, 1979.
6. Lopez-Otero, A., "Hot Wall Epitaxy," *Thin Solid Films 49*, 3, 1978.
7. Holloway, H. and Walpole, J. N., "MBE Techniques for IV-VI Optoelectronic Devices," *Prog. Crystal Growth Charact. 2*, 49, 1979.
8. Zogg, H., Vogt, W., and Melchior, H., "Growth and Applications of Heteroepitaxial Narrow Gap IV-VI Infrared Detectors on Silicon," *SPIE Proc. 587*, 170, 1985.
9. Asano, T. and Ishiwara, H., "Epitaxial Growth of Group-IIa-Fluorides/Silicon Heterostructures," in *Layered Structure Interface Kinetics*, U. S.-Japan Seminar Solid Phase Epitaxy Interface Kinetics, 1983, Ed., S. Furukawa, KTK Publ., Tokyo, Japan, 1985.
10. Asano, T., Ishiwara, H., and Kaifu, N., "Heteroepitaxial Growth of Group-IIa-Fluoride Films on Si Substrates," *Jpn. J. Appl. Phys. 22*, 1474, 1983.
11. Santiago, F., "Epitaxial Deposition Mechanism of Barium Fluoride on Single Crystal Silicon Substrate Using Molecular Beam Epitaxy," Ph.D. Thesis, the American University, 1992.
12. Chu, T. K., et al., "Growth of PbSSe on Heteroepitaxial BaF_2/Si Substrates," *MRS Proc. 221*, 483, 1991.
13. Olmstead, M. A., et al., "Initial Formation of the Interface Between a Polar Insulator and a Nonpolar Semiconductor: CaF_2 on Si (111)," *J. Vac. Sci. Technol. B4*, 1123, 1986.
14. Hansen, M. and Anderko, K., *Constitution of Binary Alloys*, McGraw-Hill Co., Inc., New York, 1958.
15. Himpsel, F. J., et al., "Structure and Bonding at the CaF_2/Si(111) Interface," *Appl. Phys. Lett. 48*, 596, 1988.
16. McCann, P. J., "The Role of Substrate Surface Reactions in Hetero-epitaxy of Lead Selenide (PbSe) on Barium Fluoride," *MRS Proc. 221* 289, 1991.
17. McCann, P. J. and Fonstad, C. G., "Auger Electron Microscopy Analysis of Barium Fluoride Surface Exposed to Selenium Vapor," *J. Electron. Mater. 20*, 915, 1991.
18. Santiago, F., Chu, T. K., and Huber, C. A., "Interface Chemistry of BaF_2 on Si Grown Using MBE," submitted to *J. Vac. Sci. Technol.*

The Authors

TAK KIN CHU came to White Oak in March 1980 as a research physicist in the Research and Technology Department, where he has specialized in solid-state opto-electronic materials and devices. He holds a B.S. degree in physics from the Chinese University of Hong Kong and a Ph.D. in physics from Dartmouth College. His postgraduate training was in low-temperature physics and superfluidity. Prior to joining the White Oak Detachment, his professional activities included thermal and electronic transport and mechanical properties of solids at cryogenic and elevated temperatures.

CARMEN HUBER received her Ph.D. in physics from Brown University in 1983. She was a professor at the University of Puerto Rico from 1983 to 1989 and a Science Fellow at the Bunting Institute of Radcliffe College in 1990-91. She joined the Research and Technology Department at the White Oak Detachment in 1991. Her experimental research involves optical spectroscopy techniques applied to semiconductor thin films and nanocomposites.

FRANCISCO SANTIAGO came to White Oak in January 1980. His specialization is in the growth of semiconductor thin films using MBE and surface/interface characterization of such films using surface analytical techniques. In May 1987 he joined the Semiconductor Group headed by Dr. T. K. Chu. Under the sponsorship of the Dahlgren Division's long-term training program, Dr. Santiago earned an M.S. in physics from the University of Maryland. Portions of the work described in this article were done by F. Santiago as partial fulfillment for the requirements of a Ph.D. degree in physics at the American University, awarded in January 1993.

Active Thermal Control With Liquid Crystal Heat Valves

J. W. Rish, III, and C. N. Pham

A liquid crystal heat valve (LCHV) is a device that utilizes the
convective flow instabilities induced by the interaction of an ac
electric field with certain nematic liquid crystals to enhance the
flow of heat between two boundaries. The thermal transport char-
acteristics of the LCHV are governed primarily by the amplitude
and frequency of the applied field, the thermophysical and electri-
cal properties of the liquid crystal at operating temperature, and
the concentration of impurity ions in the liquid crystal. Initial
investigations made use of the liquid crystal [p-methoxybenzili-
dene p-(n-butyl) aniline] or MBBA. Subsequent studies utilized the
liquid crystals TN-3252 and TN-6459, since these compounds have
greater chemical stability and a wider range of operating tempera-
tures than does MBBA. A conducting salt material, ZLI-235, was
used as a dopant. Thermal conductivity of liquid crystal increased
significantly after doping. The LCHV is being developed for use in
insulated diving suits to reduce heat stress and to increase mission
duration for divers in the cold water environment.

Introduction

Diver thermal protection is a subject of continuous concern to the U.S.
Navy. An endless assortment of missions and mission variants requires divers
to be able to function in underwater environments with temperatures ranging
from 29°F to 85°F. Standard thermal protective gear for non-surface-supplied
divers on underwater breathing apparatus includes a variety of neoprene wet
suits and several different types of dry suits. Very cold water missions gener-
ally require thermal protection in the form of dry suits with thinsulate under-
garments. The thinsulate undergarments can be obtained in several weights
(heavier weights are associated with increased insulation value), and the
undergarments are selected on the basis of estimated mission duration, water
temperature, and diver experience. Mission durations vary from several min-
utes to several hours, and work levels range from light to heavy.

Many of the longer missions dictate that the divers endure long periods of
dormancy and then engage in relatively strenuous activity for short periods of
time. In these situations the divers are subject to physiological stress on both
ends of the thermal scale. In very cold water, the inactive diver is in danger of
hypothermia unless equipped with adequate thermal insulation. However,
once the diver becomes active, the heavy insulation required to keep warm
while at rest can cause the diver to overheat. In some instances, divers have
been reported to flood their dry suits, with dire consequences.

One way to mitigate the heat load/environmental adaptability limitations of
a standard insulation configuration in cold environments is to insulate a diver
sufficiently for periods of inaction, and to provide an outlet (valve) for excess

86

heat during periods of heavy work. This approach effectively creates a "variable thermal conductivity" or "variable-k" insulation that will protect a diver against overheating, but will maintain near-optimum temperature during low-load situations. Heat pipes and phase-change materials (PCMs) are two conventional ways to approach this problem, but each approach has limitations, depending on the application.

The LCHV is a novel technology that has the potential to accomplish the variable-k objective in situations where heat pipes and PCMs may not be practical. This study examines the feasibility of using liquid crystal heat valves for applications involving active thermal control for divers in cold water environments where both hypothermia and hyperthermia present problems. The LCHV capitalizes on the electromagnetic and viscoelastic properties of liquid crystals to selectively augment the flow of heat between two surfaces. Nematic liquid crystals that have nematic-isotropic (N-I) transition temperatures well above the operating temperature of a system are the preferred active materials. An active LCHV consists of a nematic liquid crystal in a chemically neutral container sandwiched between two electrodes, as shown in Figure 1. The basis of operation is the electrohydrodynamic (EHD) motion that is induced in nematic liquid crystals with small negative dielectric anisotropy, $\Delta\varepsilon = \varepsilon_{\parallel} - \varepsilon_{\perp} < 0$, and positive electrical conductivity anisotropy, $\Delta\sigma = \sigma_{\parallel} - \sigma_{\perp} > 0$, when an ac electric field is applied between the electrodes. If a temperature gradient exists across the heat valve, the induced EHD motion or flow in the liquid crystal substantially increases the effective heat transfer between the hot and cold boundaries. When the field is turned off, the flow ceases and the LCHV becomes a thermal insulator.
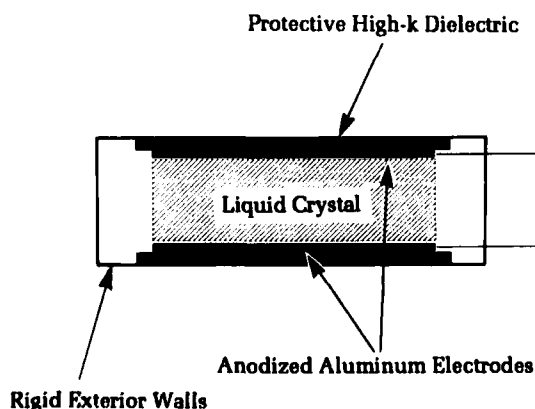

Figure 1. Liquid crystal heat valve configuration.

A number of material properties affect the performance of LCHVs. Among these are vis-

cosity, intrinsic thermal conductivity, electrical conductivity/resistivity, dielectric anisotropy, and nematic range. For example, the selection of a material with a slight negative dielectric anisotropy ensures that the device can be placed in its most insulating mode (the molecules' preferred orientation is with the long axis perpendicular to the E-field) by realignment of the molecules. Chemical stability for long periods of time is also important.

The subject of this paper is the experimental determination of the heat transfer characteristics of two liquid crystals currently under consideration for LCHV applications. The experimental results are compared to earlier results using the liquid crystal [p-methoxybenzilidene p-(n-butyl)aniline], MBBA.[1,2] The two liquid crystals were selected from a number of commercially available options based on their low viscosity, dielectric anisotropy, and chemical stability. They should be near-optimum for LCHV applications in the temperature range of interest (-2°C to 40°C).

Background

The potential use of a liquid crystal device for active thermal control was first proposed in the early 1980s by Carr.[3,4] Carr used a simple experiment in which a bulk sample of the liquid crystal MBBA was placed under a temperature gradient between two electrodes. A substantial increase in heat transfer between the hot and cold boundaries took place when a dc field was applied. Carr's observations indicated that the heat transfer enhancement was field-dependent and suggested an E^2 relationship. A follow-up paper by Hwalek and Carr[5] provided quantitative measurements on MBBA in a dc field that showed a factor of 25 increase in heat transfer and suggested that a factor of 100 increase might be possible.

The most plausible physical mechanism for the EHD motion in the liquid crystal that enables the operation of the liquid crystal heat valve is the Carr-Helfrich model.[6] According to this model, the anisotropy of electrical conductivity in the liquid crystal and the presence of ionic impurities give rise to the formation of space charges when an ac electric field is applied. The charges separate and the field exerts forces on the charges, which then transmit these forces to the liquid crystal molecules. The molecules are thus forced into motion, but because of their alignment, the motion tends to occur as a shear flow along planes parallel to the long axis of the molecules. Flow cells ultimately form that are internally bounded by "defects" or "walls" normal to the planes of the electrodes. Below some critical frequency, the

87

motion of the space charges can follow the field. In thin cells (d ≤ 100μm) and relatively low field strengths, the flows form striated patterns known as Williams domains. At frequencies greater than the critical frequency, the space charges cannot follow the field, and the motion is associated with angular oscillations of the molecules. In thick cells (bulk samples) and high field strengths, the EHD motion actually becomes turbulent, and the characterizations developed for thin cells may not be directly applicable.

More recent experimental work[1,2] used the liquid crystal MBBA as the active medium to obtain more detailed information on the heat transfer characteristics of room-temperature nematics. Those results showed the heat transfer enhancement could be expressed in terms of an "effective" thermal conductivity, k_a, of the liquid crystal. This effective thermal conductivity is a function of the electrical conductivity (governed by the concentration of impurity ions), the strength of the applied field, the frequency of the applied field, viscosity, and temperature. For all other parameters fixed, k_a increased linearly with the square of the applied voltage. The results also showed that there is an optimum operating frequency, i.e., a frequency at which the measured "effective" thermal conductivity is a maximum. The optimum frequency was found to decrease with temperature, indicating that viscosity affects performance.

The liquid crystal MBBA was used in the above study because it was the only room-temperature nematic with well-documented thermophysical properties; however, it is not an appropriate choice for a functional device, since it is a Schiff's base material, and thus subject to hydrolysis reactions.[7] A more stable liquid crystal material is needed for an operational LCHV.

Liquid Crystal Selection

Liquid crystal heat valves for cold-water diving applications require low-viscosity liquid crystals with a slightly negative dielectric anisotropy and a nematic range T_{N-N} between -10°C and 50°C. Low viscosity translates into lower friction losses and higher overall efficiency. Furthermore, the liquid crystal should have good long-term chemical stability characteristics. Specific conductivity of the materials is not an overriding concern, since dopants can be added to adjust this parameter to the desired level. The purity of the material is of considerable importance, however, because contaminants tend to alter dramatically the specific conductivity of these materials in an unpredictable fashion.

A goal of the current study was to identify suitable liquid crystals for heat valve applications, and to determine the heat transport characteristics of these substances. A survey of the marketing literature produced several candidate liquid crystals from which a selection was made for experimental evaluation. These materials are primarily produced and blended for the display industry, and have been subjected to extensive life-time testing. Two mixtures produced by the Roche Liquid Crystal Division, TN-6459 and TN-3252, were deemed to be the most likely candidates for the LCHV. Both of these materials are in the nematic phase at room-temperature, with melting points below -10°C and N-I transition points above 50°C. The "average" room-temperature viscosities reported for these two mixtures were 14.2 cP (TN-6459)[8] and 21 cP (TN-3252),[9] which is roughly comparable to that of MBBA. Thermal conductivities for these materials were not reported.

Experimental Methods

Thermal performance characterizations on the candidate liquid crystals were effected with the same instrumentation used in the earlier studies on MBBA.[1,2] The device used to measure the effective or "apparent" thermal conductivity k_a is essentially a cut-bar apparatus with two ceramic (alumina silicate) columns of known thermal conductivity (54.7×10^{-4} cal/(cm-sec-°C)). These 20-cm-long columns were embedded in heavy aluminum blocks, referred to as interfaces, which served as constant temperature heat sources or sinks. Type-T thermocouples were placed at regularly spaced intervals to measure the temperature profiles on each column. The distance between adjacent thermocouples was reduced on the portions of each column near the sample area to improve accuracy of the calculated heat transfer. Temperature control in the upper and lower interfaces was achieved by constant temperature fluid circulators. Channels within the aluminum blocks allowed the fluid to circulate through the interface, maintaining the desired temperature. The circulators are capable of sustaining set-point temperature to within ±0.02°C. Hoses connecting the circulators and interfaces were insulated to minimize heat loss or gain.

The liquid crystal sample container, illustrated in Figure 2, was constructed of a thin (approximately 0.071-cm wall thickness) cylindrical Teflon shell with an inner diameter of 1.588 cm. Sapphire disks were used to cap the ends of the shell, and a layer of thermal grease with thermal conductivity $k_g = 55 \times 10^{-4}$ cal/(cm-sec-°C) was placed on each disk, followed by a
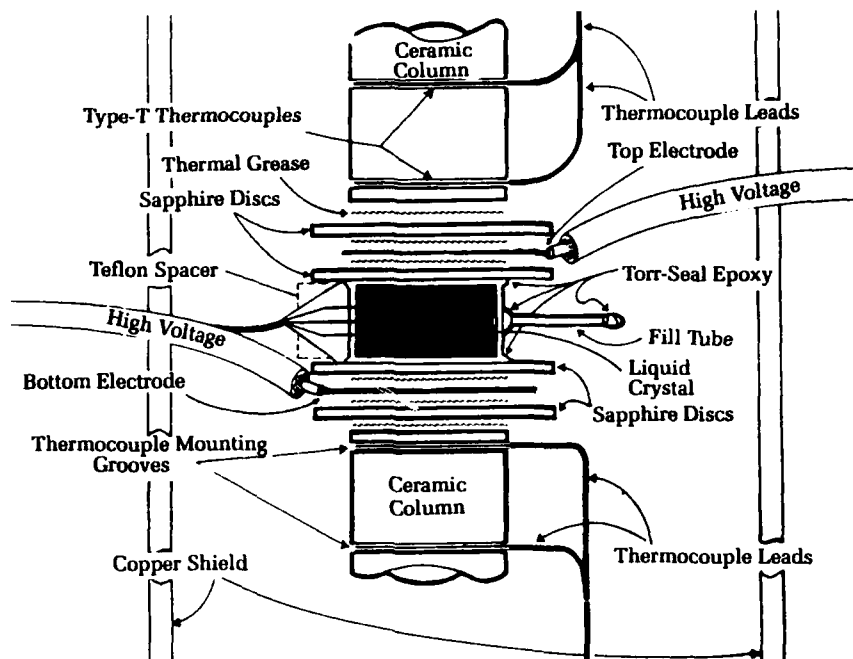
88

Figure 2. Expanded view of the liquid crystal sample geometry.

copper electrode, another layer of grease, and a second sapphire disk. These sapphire disks are 0.056-cm thick with a diameter of 2.223 cm. The thermal conductivity of these disks in the axial direction is $k_{sa} = 800\times10^{-4}$ cal/ (cm-sec-°C). The electrodes were 1.9 cm in diameter and 0.018-cm thick. The exposed gap between the two sapphire disks surrounding each electrode was sealed in order to minimize the chance of arcing.

Liquid crystal was transferred to the sample container through a small tube in one side of the Teflon cylinder. The transfer was executed in a vacuum oven at a temperature of 50°C where the liquid crystal was placed under vacuum for several hours (usually overnight) to ensure that residual moisture was removed. Upon insertion, the upper column and circulator were lowered onto the sample, and the column-sample alignment was carefully checked. Thermal contact was maintained by allowing the lower column/sample to support part of the weight of the upper column/interface. Three type-T copper-constantan thermocouples were mounted on the sample just prior to insertion to measure local temperatures, and a single type-T thermocouple was mounted on the inside rim of each of the two sapphire end caps. A two-layer thermal shield made of thin sheet copper was placed around the columns and sample and attached to the upper and lower constant-temperature interfaces. The purpose of this shield was to maintain approximately the same thermal gradient as that imposed across the columns and sample, thus reducing heat loss/gain by radiation and natur-

al convection. A large temperature-controlled stainless steel vacuum bell-jar with a polished interior was placed around the entire assembly to isolate, insofar as possible, the sample and measurement device from the room thermal environment.

An HP model 3852A data acquisition unit (DAC) was used to monitor all thermocouples and thermistors, and the experiment was completely automated by coupling the DAC, circulators, and other instruments via an IEEE-488 interface bus to a Hewlett Packard 9000 series computer. The voltage drop across the liquid crystal was provided by a home-grown, high-voltage amplifier (HVA) capable of providing a gain of almost 200:1. A Hewlett Packard function generator with an output voltage amplitude range of 0 to 10 volts acted as a sinusoidal driver to the HVA; thus, the system was capable of producing a total voltage drop of almost 20 kV across the two electrodes. The DAC was programmed to query the thermocouples at regular time intervals, and the reported thermocouple readings represent an integrated average of 590 independent samples.

The effective thermal conductivity of the liquid crystals was determined from the measured temperature drop across the sample and the heat transferred at the upper and lower faces of the sample. The heat transfer at these interfaces was computed from the temperature profiles measured on the upper and lower columns immediately adjacent to the sample, assuming one-dimensional, steady-state heat transfer. The sample was always heated from the top to minimize free convection, so the difference

89

between the heat transferred into the top face and out of the bottom face of the sample represents the sum of the internal heat generated by the liquid crystal and any environmental interactions that might have occurred during the course of an experiment. The expression used to compute the effective thermal conductivity is

$$k_a = -\frac{1}{2A_{lc}}(q_u+q_l)\frac{\Delta Y_{lc}}{\Delta T_{lc}} - k_{cyl}\left(\frac{A_{cyl}}{A_{lc}}\right) : \Delta T_{lc} \neq 0 \quad (1)$$

where ΔY_{lc} is the lengthwise dimension of the sample, ΔT_{lc} is the measured temperature drop across the sample, q_u is the heat transfer to the upper face, q_l is the heat transferred out of the lower face, and k_{cyl} is the thermal conductivity of the Teflon shell. (The sign convention adopted in the analysis dictates that q_u and q_l are negative in the presence of a positive temperature gradient ($\Delta T_{lc} > 0$), and ideally $|q_l| > |q_u|$ when there is internal heat generation.) The areas A_{lc} and A_{cyl} are the cross-sectional areas of the liquid crystal and the Teflon shell normal to the direction of the flow of heat. The heat generated by the liquid crystal is given by

$$\dot{q} = \frac{q_u - q_l}{A_{lc}\,\Delta Y_{lc}}. \quad (2)$$

The volumetric heat source term in Equation 2 does not account for environmental interaction, so the total heat generated, Q_d, is obtained by evaluating Equation 2 at both field and no-field conditions, taking the difference and multiplying by the liquid volume to yield

$$Q_d = (\dot{q}_f - \dot{q}_o)\,A_{lc}\,\Delta Y_{lc}. \quad (3)$$

where the subscripts f and 0 designate the field and no-field conditions, respectively.

Results And Discussion

A series of experiments was run to evaluate the thermal transport characteristics of TN-6459 and TN-3252 as a function of voltage, frequency, temperature, and ionic concentration. These measurements were made at two sample midpoint temperatures, 31°C and 15°C. Applied voltages ranged from 0 kV to 15 kV, and the range of frequencies for the measurements was 0 Hz to 600 Hz. The ionic concentration in each mixture was adjusted by incremental doping with a conducting solution, designated ZLI-235, produced by Merck Industries.

The first step in the process was to determine the performance of the individual mixtures as a function of frequency at a selected voltage, temperature, and ionic concentration. This serves to determine the optimum operating frequency of the mixture for a reference set of conditions. The optimum frequency is strongly coupled to the viscosity of the mixture. It is also associated with the existence of an ionic double layer that acts to shield the liquid crystal from the full impact of the applied voltage.[10]

Figure 3 presents plots of the normalized thermal conductivity of TN-6459 and TN-3252 as a function of frequency at an applied voltage of 8.5 kV and at a temperature of 31°C. Data for MBBA is also plotted as a reference. The doping level for TN-6459 was 0.3 percent and for TN-3252 it was 0.1 percent. The plot clearly depicts the existence of an optimum operating frequency for each of the mixtures. TN-6459 and TN-3252 both have peak values at relatively low frequencies, and TN-3252 exhibits a relatively sharp peak at a frequency of approximately 30 Hz. The optimum operating frequency of MBBA is in the vicinity of 100 Hz, and it exhibits a very broad operating range. TN-6459, which has the lowest viscosity of any of the mixtures, has the lowest optimum operating frequency and the best performance. The lower viscosity mixtures allow the flow cells to form more rapidly, and larger flow cells are formed, i.e., higher flow velocities and greater heat transfer enhancement potential. Thus, the tendency is for the optimum operating frequency to correlate with viscosity. But while TN-6459 exhibits the best performance, it is noted for the moment that it has a higher level of doping than TN-3252.

Figure 4 presents data similar to that shown in Figure 3, with the exception that the doping levels were different, and the sample midpoint temperature for these runs was 15°C. The increased viscosity associated with the reduced temperature acted to degrade dramatically the heat transfer performance of the liquid crystals, especially that of MBBA. Optimum operating frequencies were also reduced. Once this effect was noted, it was later discovered that the performance could be adjusted to accommodate a particular temperature range by adjusting the doping of the materials, as shown in Figure 5.

Figure 5 shows the results obtained for eight doping levels ranging from 0.1 percent to 0.4 percent by volume that were evaluated to determine the effect of ionic concentration on performance at 31°C and 15°C. The maximum thermal conductivity of each sample at an applied voltage of 8.5 kV was used to make the comparison. The results indicate the existence of optimum doping levels for each mixture at the two operating temperatures. At doping levels
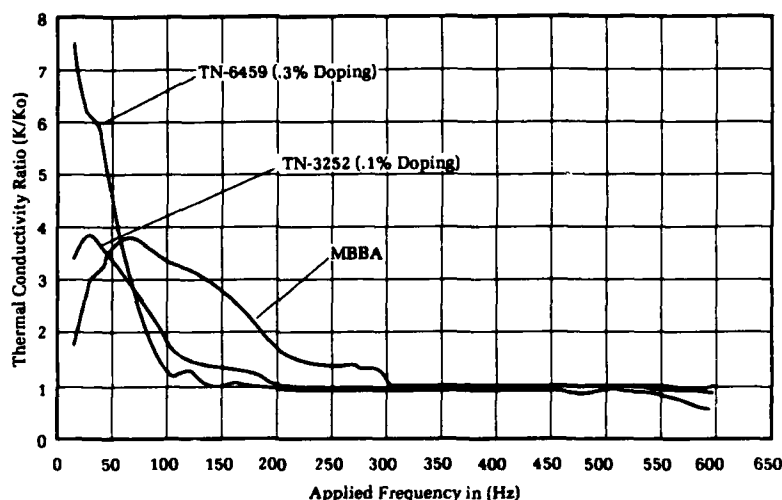
90

Figure 3. Thermal conductivity ratio as a function of frequency at 31°C.

Figure 4. Thermal conductivity ratio as a function of frequency at 15°C.
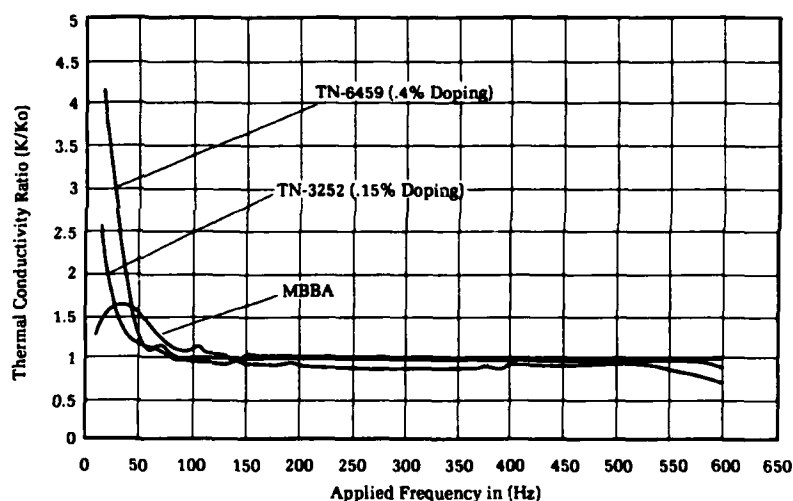
beyond the optimum, the excess ions serve only to increase the Joule heating within the sample, and the performance of the mixture is reduced.

Figure 6 shows the relative thermal performance of each mixture as a function of voltage at the optimum operating frequency for each mixture and an operating temperature of 31°C. The optimum doping levels for each mixture at this temperature were used to make the comparison. The results show that the optimum performance of TN-3252 is roughly comparable to that of MBBA, whereas the optimum performance of TN-6459 is roughly three times greater at an applied voltage of 14 kV. The data also show TN-3252 to be well behaved, i.e., the data exhibit the same general E^2 dependence on the applied voltage as that exhibited by MBBA.

The data for TN-6459 did not show the same smooth increase.

Summary

There are several items that should be noted if liquid crystal heat valves are to be effectively developed for practical applications. First and foremost is the process of selecting and optimizing a mixture for a given application. The coupling between the anisotropic characteristics, viscosity, operating temperature, electrical conductivity (joule heating), and the concentration of ions in the material must all be carefully evaluated. The highest thermal conductivity at a given temperature will generally be achieved

91
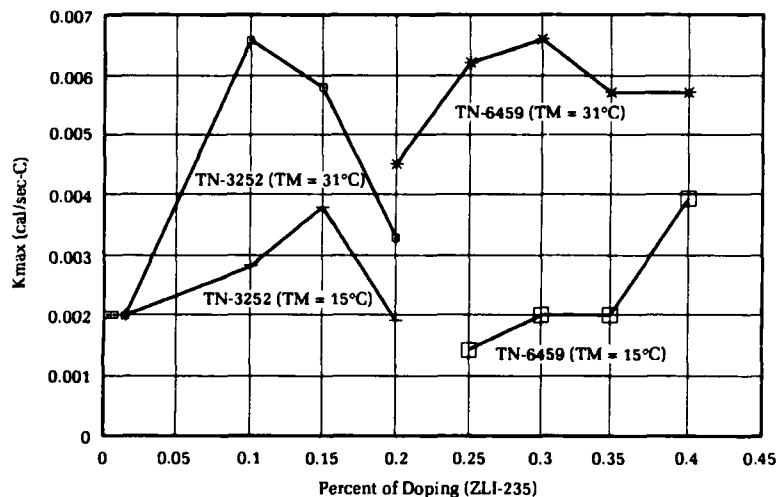
Figure 5. Influence of doping on maximum thermal conductivity of TN-6459 and TN-3252 at 15°C and 31°C.

Figure 6. Thermal conductivity ratio as a function of applied voltage at 31°C.
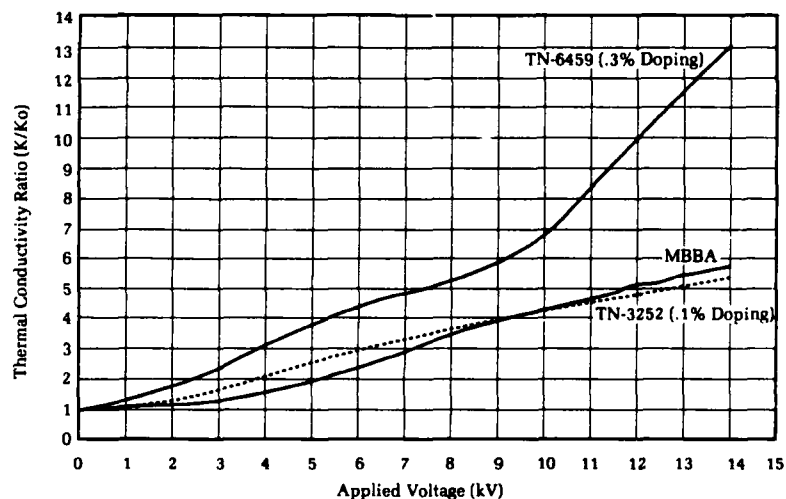
by selecting a material that has the lowest viscosity. However, if operation over a temperature range is important, it might be more beneficial to select material on the basis of its viscosity-temperature curve. Performance of the mixtures can be adjusted somewhat by doping the materials to change their electrical conductivity. The two mixtures that were studied here had good performance characteristics and were both chemically stable.

The thermal conductivity of liquid crystal increased significantly after doping. LCHVs can be used in insulated diving suits to reduce heat stress and to increase mission duration fₙ divers in the cold water environment. Similar liquid devices may also find applications in

optical data processing as an electrically addressed optical light modulator for spectrum analysis, image correlation, radar, and spread-spectrum signal processing.[11]

Acknowledgments

92

References

1. Biggers, R. R., Rish, J. W., III, and Henderson, G. L., "Influence of Electric Fields on Heat Transfer Through Thermotropic Liquid Crystals," *Developments in Theoretical and Applied Mechanics*, Vol. XIV, Proc. of the 14th Southeastern Conf. on Theoretical and Applied Mech., S. Y. Wang, et al., Eds., School of Engineering, Univ. of Mississippi, University, MS, 1988, pp. 454-461.

2. Biggers, R. R., Rish, J. W., III, and Fuller, R., "Heat Transport Through MBBA Due to Induced Electrohydrodynamic Motion," accepted for publication in *Mol. Cryst. Liq. Cryst.*

3. Carr, E. F., "Regulation of Heat Transfer Using Liquid Crystals in the Presence of Electric Fields," *Mol. Cryst. Liq. Cryst.*, Vol. 92 (Letters), 1983, pp. 165-170.

4. Carr, E. F., "A Heat Switch Using Liquid Crystals in the Presence of Electric Fields," *Mol. Cryst. Liq. Cryst.*, Vol. 111, 1984, pp. 161-170.

5. Hwalek, J. and Carr, E. F., "A Liquid Crystal 'Heat Switch,'" *Heat Trans. Engr.*, Vol. 8, No. 1, 1987, pp. 36-39.

6. Parker, J. H. and Carr, E. F., "Anomalous Alignment and Domains in a Nematic Liquid Crystal," *J. Chem. Phys.*, Vol. 55, No. 4, 15 Aug 1971, pp. 1846-1850.

7. Rodelez, E., Diguet, D., and Durand, G., "Dielectric and Resistivity Measurements on Room Temperature Nematic MBBA," *Mol. Cryst. Liq. Cryst.*, Vol. 15, 1971, pp. 183-188.

8. Manufacturer's Data Sheet for TN-6459, Roche Liquid Crystals.

9. Manufacturer's Data Sheet for TN-3252, Roche Liquid Crystals.

10. Sprokel, G. J., "Resistivity, Permittivity and the Electrode Space Charge of Nematic Liquid Crystals," *Mol. Cryst. Liq. Cryst.*, Vol. 22, 1973, pp. 249-260.

11. Efron, U., et al., "Silicon Liquid Crystal Light Valves: Status and Issues," *Optical Engineering*, Vol. 22, No 6, 1983, pp. 682-686.

The Authors

JEFF W. RISH, III, attended the University of Mississippi where he received B.S.C.E. and B.S.M.E. degrees in 1977 and 1978, respectively. He completed his M.S. (1983) in fluid-structure interactions in unsteady flows and did his Ph.D. (1985) work on coupled conduction and radiative energy transfer in fibrous insulations. He joined the Materials Science Branch at the Naval Coastal Systems Center (now Coastal Systems Station, CSS) as a mechanical engineer in 1986. While at CSS he performed research in thermoacoustics and liquid crystal heat transfer. Dr. Rish is presently a research engineer in the Wright Laboratory Air Base Systems Branch, operating location at Tyndall AFB, Florida. His current research interests are in the area of jet heat and blast effects on operating surfaces and nondestructive evaluation. His work has resulted in numerous publications.

CHUONG N. PHAM received a B.S. in mechanical engineering from Widener College in 1980 and an M.S. in mechanical engineering from the University of Houston in 1984. His thesis addressed the acoustic signature to detect cracks on tubular members. He joined the Materials Science Branch at the Coastal Systems Station in 1984. His current research involves measuring the thermal conductivity of liquid crystals, designing a liquid crystal heat valve, and using a two-dimensional heat transfer model to predict the behavior of liquid crystal heat valves. This work has led to numerous publications and several patents.

Nanophase Aluminum for Potential Applications to Improved Explosives

B. C. Beard, C. S. Coffey, and R. A. Brizzolara

Nanophase materials technology is an exciting, rapidly growing area of research and application in the quest for new, higher performance materials. Every area of materials endeavor...metals, ceramics, and thin films...is touched by the advances in this field. This article describes a new approach to the use of metal fuels in energetic materials, coupling recent advances in nanophase (NP) materials processing with the well known performance enhancement of metals in propellants and explosives. An apparatus was assembled and procedures perfected for the generation of nano-size aluminum (Al) particles. NP Al metal particles were created by the gas condensation method under a flowing argon (Ar) atmosphere at 10^{-2} torr. Al particles on the order of 50 nanometers were prepared and characterized. Reaction of the nano-sized metal particles with ammonium perchlorate was evaluated using the Ballistic Impact Chamber method pioneered at the White Oak Detachment. The rate of initiation of the Al reaction was found to be faster and more sustained for the NP form of Al when compared to more conventional sized (44 μm) Al particles. This research could lead to the development of more energetic explosives for underwater applications.

Introduction

Recent developments in the fabrication and processing of nano-crystalline materials have demonstrated the potential for significant impact on Navy systems that require novel materials.[1] Due to the extremely fine particle size, modification from the elemental state is readily accomplished for the production of oxide, carbide, or nitride-coated particles that can be consolidated to nearly 100 percent density. Ceramics represents only one area of potential application. Mixed metal phases (or their oxides) can be generated, leading to alloys unattainable through conventional metallurgical techniques. Catalysts, magnetic materials, optical materials, and semiconductors can be created with nanometer particle sizes under the proper conditions.

Generation of NP materials has been attained through several methods. Generally, atoms or clusters emitted from the bulk (by thermal, optical, sputtering, or high potential excitation) have their highly excited internal modes quenched by interaction with a high backing pressure of gas in the synthesis chamber. Collisional energy losses with the high-pressure (>10^{-2} torr) gas molecules quench the high energy of the particles that could cause them to coalesce. A liquid nitrogen (LN_2) cooled target block condenses the metal particles from the gas phase, collecting them for use. Inert gases are used for

94

metal particle formation. Oxides, nitrides, and carbides may all be created by proper selection of the blanketing gas used during the condensation process.

NP Al was chosen to illustrate NP technology for Navy use. Al is a common high-energy fuel in propellant and explosive formulations. In conventional blast explosives, however, the energy release of Al converting to Al_2O_3 is late in the reaction process, minimizing its contribution to the blast. More rapid reactions of NP Al in blast explosives could move the Al energy release closer to the detonation front, resulting in an increase in pressure. Underwater explosives exploit Al in the hopes of its complete conversion to oxide through the consumption of oxygen from the water. Increased surface area of the metal would enhance the likelihood of complete oxidation and release of energy. Initially NP Al was thought to be pyrophoric and was suggested as a fuel-air blast agent. It has since been demonstrated that NP Al is not spontaneously pyrophoric. Its use as a blast agent may still be possible if it is formulated with an appropriate initiating explosive.

The particular system employed for the demonstrations of NP Al as an energetic ingredient is the reaction between ammonium perchlorate and NP Al. It is hoped that through the increased intimacy of contact and/or higher surface area afforded by the NP Al, increased energy release rates and complete consumption of the Al will result.

Apparatus

We assembled the apparatus (Figure 1) from high-vacuum hardware available in our laboratory and made several modifications. The unit is based upon a 50-liter/second turbomolecular pump. A main vacuum isolation valve separates the pump from the evaporator. A butterfly valve adjacent to the isolation valve controls gas flow when NP materials are made. The evaporation chamber is a 5-way, 2.75-inch, ConFlat cross. Pumping is from the top, and the evaporator current feedthrough flange is mounted on a nipple attached to the bottom of the cross. Vapor-phase Al generated from a resistively heated tantalum boat was found to operate better than the tungsten filament used initially. The V-shaped tantalum boat can accommodate 40 mg of Al wire for each deposition. A high-current Variac connected to a 5x step-down transformer supplies the power, with full voltage ~20V. A gas admission is controlled by an ultra-high-vacuum variable

leak valve attached to the evaporator nipple, with flow entrance below the evaporator. A pressurized bottle of research-grade Ar provides the gas source. Chamber pressure is monitored by a cold-cathode vacuum gauge capable of measuring the chamber pressure within the range of 10^{-2} to 10^{-9} torr.

The following were the typical deposition conditions: chamber base pressure ~1×10^{-7} torr; flowing Ar pressure $\geq 10^{-2}$ torr; sample cooled with flowing LN_2 for $\geq$15 min.; Variac was taken to 21 percent, whereupon the tantalum boat glowed a bright orange-yellow; and deposition was in two stages of 1.5 minutes each, separated by ~3 minutes to allow the substrate to cool. LN_2 flow through the copper pipes of the coldfinger (Figure 2) was continuous during the deposition. Estimations of the substrate's surface temperature were obtained from an alumel-chromel thermocouple exposed to the radiant glow of the evaporator boat. This was not a measurement of the target's true surface temperature, but did prove to be a valuable guide for minimizing radiation effects on the target. Measured temperature during a deposition under the conditions noted above was approximately 300°C. Again, this was the temperature of a freestanding thermocouple junction, not the continuously cooled target surface.

We determined the actual cooling rate of the sample substrate by the flowing LN_2 by attaching a thermocouple onto a nickel foil, which in turn was attached to the coldfinger. This measurement determined that after 10 minutes the target temperature leveled off at about -120°C.

Results

Direct Al Deposition Onto Ammonium Perchlorate Crystals

We produced the first samples in the chamber without the capability of monitoring the pressure or maintaining consistent flow of argon. Ammonium perchlorate (AP) crystal fragments mounted with double-sided tape onto the coldfinger were used as deposition substrates in the early runs. Metallic, "mirror-like" films were obtained in these runs. From the preparation of these samples, a number of lessons were learned. First, the radiant heating at the surface of the target was sufficient to melt the tape. Second, proper pressure control and monitoring were necessary to deposit NP material.

95
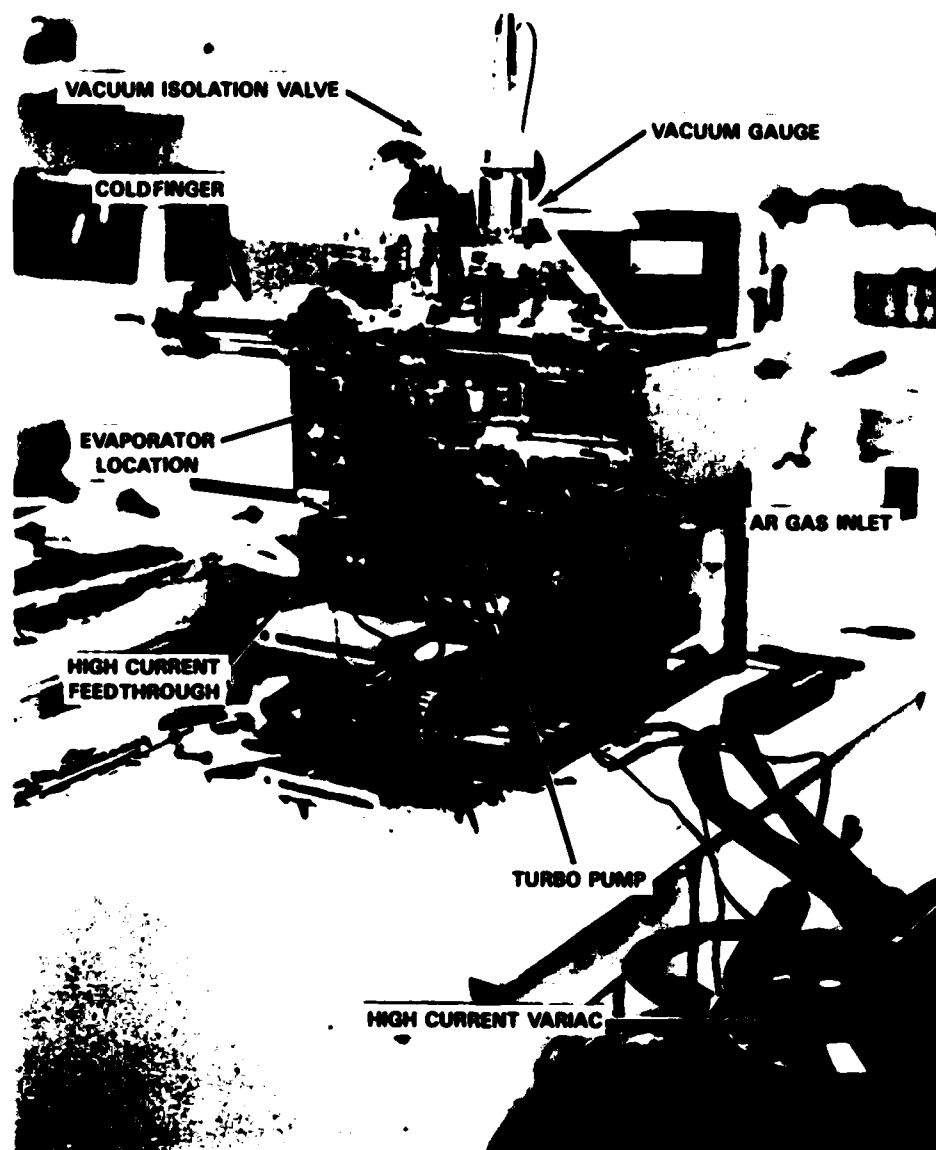
Figure 1. Nanophase deposition chamber.

There was a question as to whether a direct Al-to-AP interface would react. X-ray photoelectron spectroscopy (XPS) combined with noble gas ion etching was performed to evaluate the chemistry of the Al layer at the surface and at its interface with the AP crystal. Sputter depth profile results indicate a thin oxide on the surface of the evaporated film and an oxide layer at the Al/AP interface approximately one-third the thickness of the Al layer. The film thickness was determined to be ~250Å by scanning electron microscopy (SEM) analysis. This result indicates reaction between Al and AP, leading to the formation of an oxide. This is not a clean result, however, because the high temperature attained at the surface of the crystal due to radiant heating must have been sufficient to decompose AP, creating sufficient

oxygen pressure above the surface of the AP to result in the appreciable Al oxidation.

Nanophase Al Preparation

Upon incorporation of the cold-cathode gauge (Figure 1), the chamber pressure could be accurately monitored. The overnight base pressure of the deposition chamber after some leaks were repaired was found to be 2×10^{-7} torr.

With the ability to determine and control the pressure of argon gas in the chamber, conditions leading to the formation of NP Al could be achieved. NP Al was deposited on a set of AP crystal fragments, nickel foil, and a silicon wafer. SEM analysis of an NP Al film deposited on nickel foil determined the layer to

96
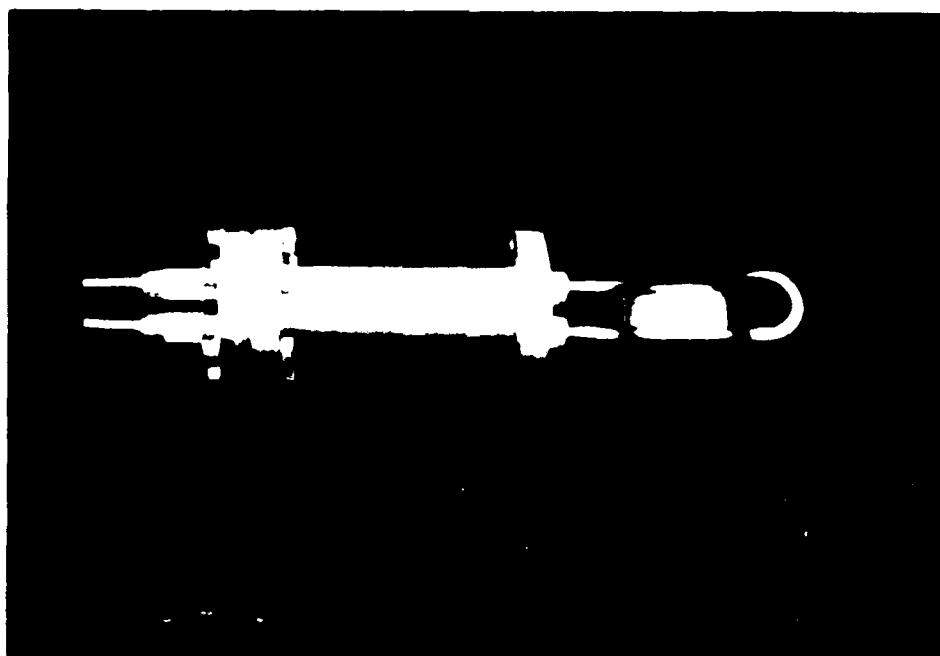
Figure 2. Coldfinger upon which deposition substrates were fixed.

be ~ 1.5 μm thick (Figure 3). This layer comprised two successive layers resulting from the two-stage deposition procedure employed in laying down the film. Features within these layers suggest a columnar growth of the film, with each column on the order of 50 nanometers wide.

Scanning tunneling microscopy (STM)[3] of the NP Al deposits on nickel foil achieved only marginal success. The rapid development of even a thin oxide (~1 nanometer) presents a sufficiently insulating barrier to the STM to make tunneling impossible. As an alternative approach, gold deposits were produced under similar conditions as the NP Al for STM

evaluation. Images from this material indicated a cluster size of from 10 to 20 nanometers (Figure 4). While this result is encouraging for truly NP material, results on gold are not directly relatable to the Al work.

Visually, the NP films appeared black or grey, completely obscuring the substrate below. The darkened nature of the films evidently arises from the altered electronic structure of the fine Al particles. This observation, together with the fine feature size of the films observed by SEM and STM, were taken as an indication of the formation of a nominally 50-nanometer NP Al material.

Glossary

Noble Gas Ion Etching. A method whereby noble gas atoms (i.e., Ar) are ionized and accelerated to several kilovolts of energy, then directed to a materials surface. The resulting "sputtering" process removes material on an atomic scale as a function of the etching time.

Scanning Electron Microscope (SEM). A microscope in which a beam of electrons is made to scan the surface of a sample. The spatial distribution of intensity of the secondary electrons thus emitted forms an image of the surface.

Scanning Tunneling Microscope (STM). A microscope in which electrons tunnel between the sample surface and a very sharp metal tip held approximately 1 nanometer away from the surface. As the tip is scanned over the surface, the tunnel current is measured as a function of tip position. This generates an image of the surface. The STM is the highest resolution surface imaging technique available; it has the capability to resolve individual atoms on certain materials.

Sputter Depth Profile. A procedure in which the sample surface is repeatedly sputtered to remove layers of material. After each sputtering stage, surface analysis is performed to assess the changes in surface composition with respect to depth.

X-ray Photoelectron Spectroscopy (XPS). A surface analytical technique providing elemental and chemical information of the uppermost 5 to 10 nanometers of a material. X-rays are employed to excite photoelectrons from the sample surface. The characteristic energy of these photoelectrons is unique to the element and its chemical state.

97

Nanophase Al On Powdered AP

To increase the contact between AP and Al, powdered AP rather than crystal fragments was used as a deposition substrate. The powder was mounted to nickel foil with double-sided tape. The AP-coated foil was held to the coldfinger by carbon paste, which provided the vacuum-stable, thermally conducting adhesive needed for this work. Measurement of the weight of AP and Al was difficult to achieve. A "witness" foil of nickel was placed adjacent to the AP sample to determine the amount of Al being deposited. Weight of the nickel was taken then, and again following the NP Al deposition.

XPS analysis of an NP deposition blank revealed the presence of chlorine in both the perchlorate and chloride chemical states.[3] This result indicates the dissociation of the AP at the surface during the deposition procedure. Apparently the radiant energy heating of the source is sufficient both to volatilize and to decompose AP, as suggested above. As a result, the Al films deposited in the presence of AP are not pure Al, and they are highly oxidized from the oxygen arising from the decomposed AP. A blank nickel foil was mounted to serve as a means of measuring the weight of the deposited Al. In one case, the weight increase was 0.0003 g. Taking the area of the nickel substrate for the deposition to be 0.6 cm^2, the layer thickness turns out to be approximately 1.8 µm, in very good agreement with the SEM result.

Preparation Of Nanophase Al Powder

To avoid the difficulty of thermal degradation of the AP, formation of NP Al onto a metal substrate was employed. The coldfinger was modified by the addition of a large tantalum plate, 1.25 inches x 2.5 inches, held in place by
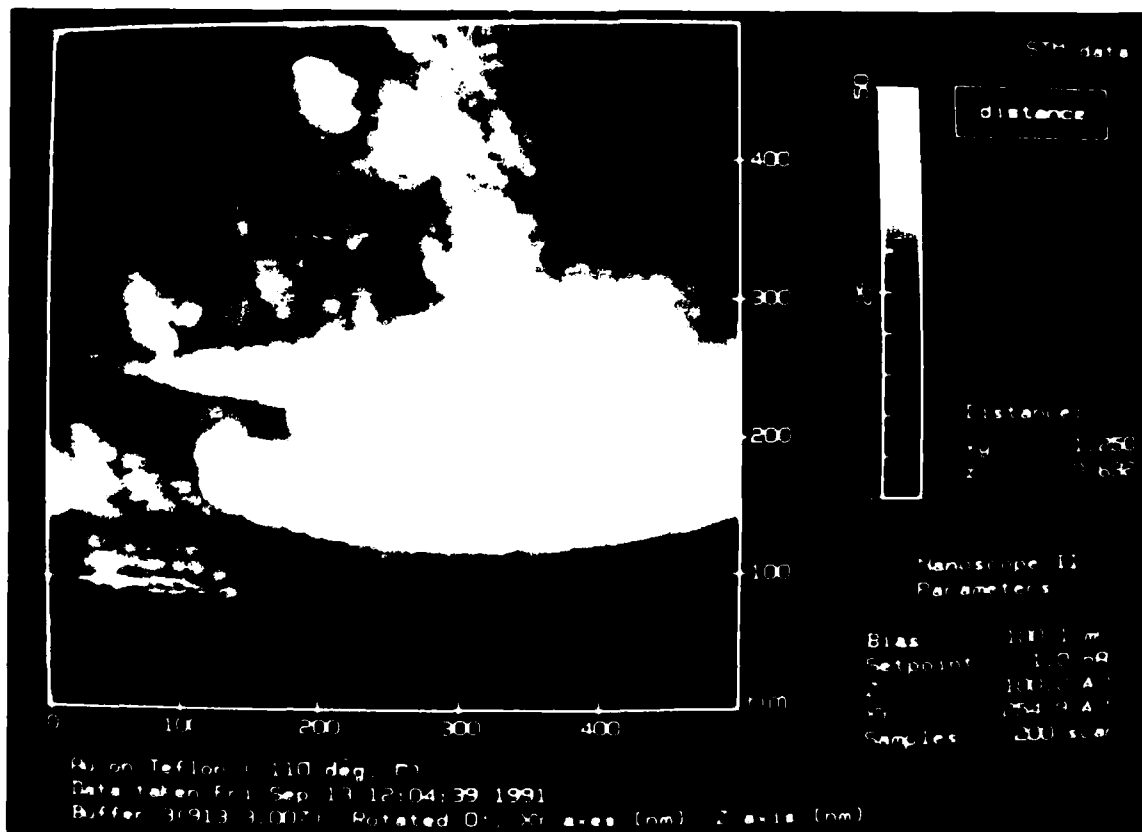

Figure 3. SEM micrograph of nanophase Al layer deposition on nickel foil.

Figure 4. STM image of an NP gold (Au) deposit on Teflon.

98

wires wrapped around both the plate and the copper coldfinger cooling pipes. The deposited film was scraped from the surface of the tantalum foil for analysis and testing. Determination of the average oxide thickness on the NP particles was made by XPS. The ratio of the metallic Al peak intensity to that of the assumed continuous oxide overlayer was used for the calculation (Figure 5). The average oxide thickness on this material was found to be ~4.2 nanometers following 24 hours exposure at 70°C, 60 percent relative humidity. Bromine was observed as a very minute contaminant, the source of which is unknown. The -325 mesh (44 μm), fine-particle size Al used for comparison in the BIC tests had an average oxide thickness of ~4.7 nm.

Ballistic Impact Chamber Tests

Ballistic Impact Chamber (BIC) tests were run to assess the differences in sensitivity and burning rate of AP/Al versus AP/NP Al. In this instrumented impact test the drop height and weight are fixed, the sample size is held close to 35 mg, and all tests are run on #180-grit sandpaper (Figure 6). The advance in this test relative to previous impact tests is the real-time record collection of the pressure output of the sample during the impact-induced burn.[4] A transducer measures the pressure within the enclosed striker volume. The increased pressure works on a pellet accelerated down a nine-inch barrel. Knowing the volume and measuring the pressure allows for the calculation of the energy output by the material. In addition, since the pressure is measured during the

impacting event, the initiation rate of burn can be determined.

In this particular work, the initial rate of burn and the time delay to ignition are of critical interest. If the NP Al is behaving as a more active fuel, its combustion should be more facile and complete. Due to the difficulties in obtaining a reproducible ratio of the AP to Al in these samples, the BIC energy output results are not particularly meaningful. Several different sets of samples were tested, including control AP both in powdered and single crystal form; single crystal AP with metal Al metal layer deposits; and powdered AP mixed with both -325 mesh Al powder and NP Al. The data of most relevance are the set of experiments for AP powder; AP powder mixed with -325 mesh Al; and AP powder mixed with NP Al. In Table 1 the result of most critical interest is the time delay to ignition, Δt. This result demonstrates that the AP/NP Al reaction initiates more rapidly than the other two samples, suggesting that the NP Al can interact more readily than the larger -325 mesh Al powdered material. Curves from the BIC tests of AP, AP with -325 mesh Al, and AP with NP Al are shown in Figure 7. Pure AP shows a slow, featureless growth in pressure followed by a long pressure decay due to continued burning. AP in the presence of Al demonstrates an earlier low-level reaction leading to a major build-up of pressure. In this region a difference was noted between the two types of Al. As indicated in the table, NP Al initiates faster and maintains a greater reaction rate after the initial onset. This difference is thought to reflect the greater ease of initiation of the NP Al particles relative to the much larger 44-μm
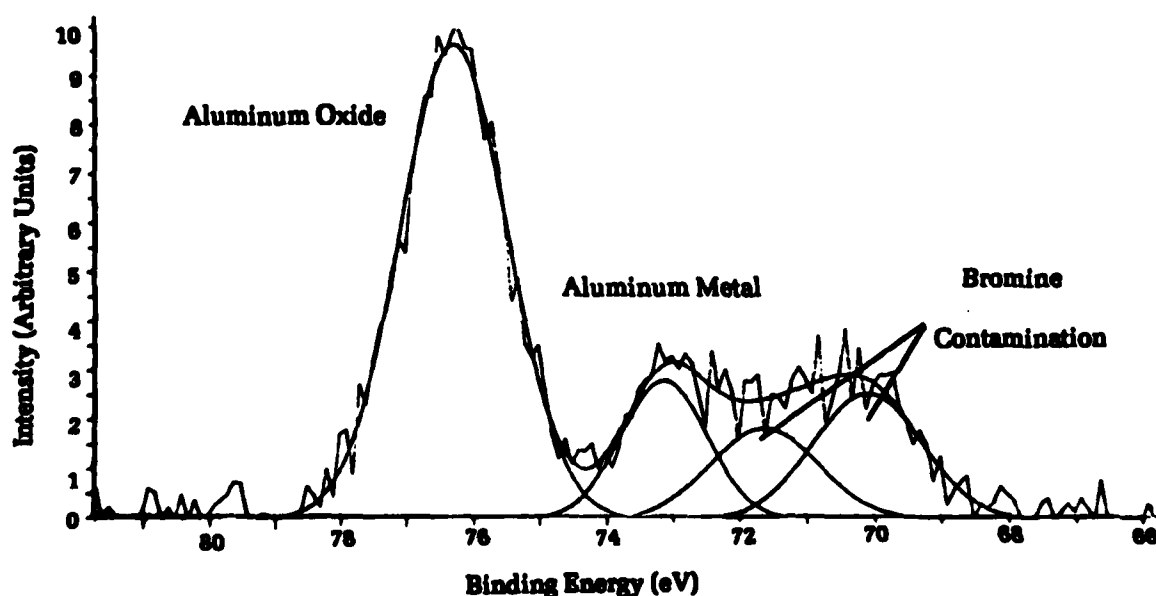

Figure 5. Al(2p) photoelectron spectrum of NP Al scraped from the target after deposition.

99

material. It appears that once initiated, the burning rates are approximately equal, indicating the chemical reaction rate limit of AP with Al.

Summary

NP Al particles have been fabricated by the gas consolidation method for use as a high-energy, high-burning-rate fuel for propellant and explosive applications. Experimental evidence has demonstrated the particle size of the NP materials to be on the order of 50 nanometers, an order of magnitude smaller than the smallest material currently employed in energetic formulations. Despite initial expectations that the NP Al would be pyrophoric, the material was found to be air stable and to develop an oxide layer of only 4.2 nanometers after 24 hours of exposure to atmosphere.

BIC test results suggest an accelerated initiation of Al combustion when the material is in the NP form. This shortened ignition delay holds out the promise of Al oxidation reaction initiating at the detonation front.

Although these results are most encouraging, additional experiments are required to substantiate the conclusions drawn from this limited study. One to two grams of commercially available NP Al would permit thorough characterization of the material, more controlled BIC testing, and shock initiation studies. The material for these experiments would be formulated into a highly solids-loaded binder/AP/NP Al explosive. Documented, reproducible demonstration of the enhanced reactivity in such a system under shock and impact conditions would provide the data needed to transition the NP Al materials into new, high-performance formulations.

Table 1. BIC Test Results: Burn Rate and Energy Output

Sample	dP/dt (psi/µs)	Δt (µs)	P_{av} (psi)	E (J)	E/gm (J/gm)
AP powder	28.63	208.6	162.2	4.7	126.0
AP powder mixed with -325 mesh Al	9.35	155.9	196.4	5.7	152.1
AP powder mixed with NP Al	8.73	140.8	195.4	5.63	158.0

Figure 6. Schematic diagram of the Ballistic Impact Chamber apparatus.

100
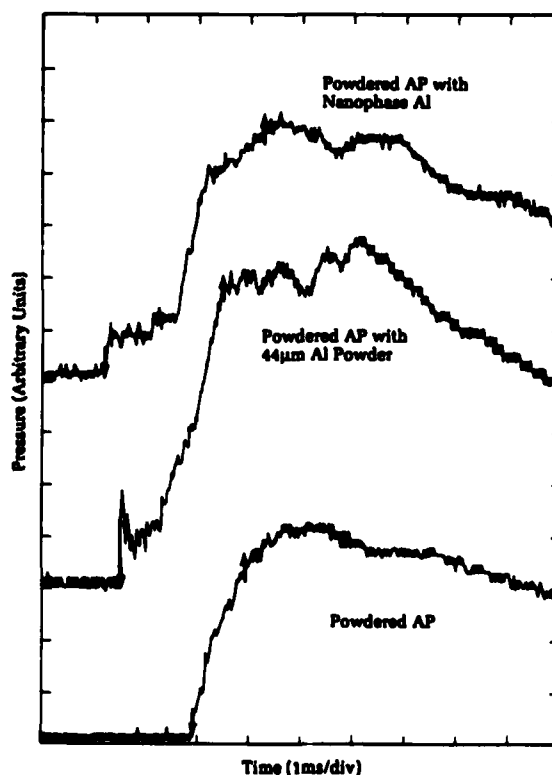
Figure 7. Ballistic Impact Chamber test results.

Acknowledgments

References

1   Andres, R. P., et al., "Research Opportunities on Clusters and Cluster-Assembled Materials – A Department of Energy, Council on Materials Science Panel Report," *Materials Research*, 4(3), 1989, p. 704.
2   Binnig, G., et al., "Surface Studies by Scanning Tunneling Microscopy," *Phys. Rev. Lett.*, 49(1), 1982, p. 57.
3   Sharma, J. and Beard, B. C., "Fundamentals of X-Ray Photoelectron Spectroscopy (XPS) and its Applications to Explosives and Propellants,"*Chemistry and Physics of Energetic Materials*, Ed. S. N. Bulusu, NATO ASI series C, Kluwer Academic Publishers, Boston, c. 1990, Vol. 309, p. 569.
4   Coffey, C. S., DeVost, V. F., and Woody, D. L., "Towards Developing the Capability to Predict the Hazard Response of Energetic Materials Subjected to Impact," *Proc. Ninth Symposium (International) on Detonation*, OCNR-113291-7, 1991, p. 1243.

The Authors

BRUCE C. BEARD is a research chemist in the Surface Evaluation Facility at the White Oak Detachment, Silver Spring, Maryland. He began his studies at Millersville State College, Millersville, Pennsylvania, receiving a B.S. in chemistry. Graduate studies were performed at Lehigh University, Bethlehem, Pennsylvania, where an M.S. in chemistry and a Ph.D. in physical chemistry were earned. His graduate work was in the area of ultrahigh vacuum surface analytical techniques under the direction of Dr. G. W. Simmons. Dr. Beard's thesis research addressed the inherent acid-base chemistry of the hydrated oxide layer present on the surface of iron and titanium metals. He continued his research during a two-year postdoctoral fellowship at Lawrence Berkeley Laboratory, where his studies addressed the preparation and characterization of novel supported platinum alloy fuel cell catalysts. Dr. Beard's major effort during the past 6 years has been the application of surface-specific analytical techniques to the elucidation of the physical and chemical sources of ignition of energetic materials.

CHARLES S. COFFEY received his B.S. in electrical engineering from the Massachusetts Institute of Technology and his Ph.D. in physics from the University of Arizona. He joined the White Oak Detachment in 1976, where he has worked in the Detonation Physics Branch. Currently, his professional interests are in the areas of the initiation of chemical reaction in explosives and propellants by shock or impact, and in the energy localization-molecular excitation processes that occur in crystalline solids during rapid deformation.

ROBERT A. BRIZZOLARA is a research physicist in the Surface Evaluation Facility of the White Oak Detachment. He received his B.A. (1981), M.S. (1984), and Ph.D. (1987) degrees from the University of Delaware. He performed graduate research under the direction of Professor C. B. Cooper in the area of ion bombardment of surfaces and mechanisms of sputtered neutral cluster ejection. In 1988, he was awarded a National Research Council Cooperative Research Associateship at the Naval Research Laboratory in Washington, D.C. There he performed research concerning sensor applications of the scanning tunneling microscope. Dr. Brizzolara joined the staff at White Oak in 1990. His research interests include molecular electronics, the fabrication of nanomolecular structures using the STM, the study of surfaces and adsorbates using scanning probe microscopies, and sensor applications of the STM. Dr. Brizzolara is a member of the American Physical Society and the American Vacuum Society.

101

Molecular-Level Study of Insensitive and Energetic Layered and Intercalated Materials

Richard D. Bardo

An important goal of the detonation physics and chemistry community is to develop explosives with high-performance capabilities, yet sufficiently low sensitivities for advanced, invulnerable Navy warheads. The traditional ways of developing increasingly energetic explosives have led to an increase in shock and impact sensitivities, thereby exacerbating the problems associated with warhead performance and decreased safety. It is, therefore, of practical and theoretical importance to design, from molecular-level considerations, polycrystalline explosive systems that clearly exhibit directional sensitivity and initiation properties, while also approaching the insensitivity of homogeneous or single-crystal explosives. In the current work, theoretical studies indicate that such systems may be constructed from special materials such as high-quality pyrolytic, layered, hexagonal boron nitride (BN) crystals. These studies are part of a White Oak Detachment program concerned with the design of high-performance explosive crystals, the directional shock sensitivity properties of which are identified with specific crystal axes.

Introduction

The design and construction of advanced, invulnerable Navy warheads involve the selection of explosives which have not only high performance capabilities, but also sufficiently low sensitivities to shock or impact. While new energetic compounds with ever-improving fragment acceleration and blast pressure continue to be synthesized, these same explosives often show a concomitant increase in sensitivity. Because the traditional "trial and error" methods used in the scale-up of the new materials from laboratory-to-warhead test conditions continue to show conflicting performance and sensitivity results, it would be of practical and theoretical importance to be able to design, from the ground up, a highly energetic explosive system that clearly exhibits the needed insensitivity and performance at all stages of development. Therefore, the purpose of this article is to indicate the feasibility of such a program by exploiting the current understanding of the molecular-level processes governing the behavior of energetic materials at high pressures and temperatures.

102

Benchmark experiments exist which show profound differences in the way homogeneous and heterogeneous explosives initiate under shock. In the case of sustained shock-pulse initiation of homogeneous liquid nitromethane (NM),[1] which is free of discontinuities of any kind, fast reaction appears to begin close to the driver-plate interface after an induction time of about 10^{-6} seconds. No light is emitted directly behind the initiating shock, which at 60 kbar propagates 8 mm before initiation begins at the interface. The absence of light emission indicates no appreciable excitation of electronic states with lifetimes $\leq 10^{-6}$ seconds. Similar behavior is observed in molten trinitrotoluene[1] as well as in single crystals of pentaerythritol tetranitrate (PETN),[1] cyclotrimethylene trinitramine,[2] and cyclo-tetramethylene tetranitramine.[2] On the other hand, sustained shock-pulse initiation of heterogeneous NM containing air and oxygen bubbles and of polycrystalline solid explosives gives rise to initiation close to the initiating shock, with negligible induction times.[1] In all these materials, sensitivity is a function of the defect structure and heterogeneous nature of the medium.

More recently, directional shock sensitivity has been discovered in single crystals of PETN by Dick et al.,[3] who showed that, in the chosen geometry, initiation is difficult to achieve along the crystal direction of greatest slip. Although existing crystals of shock-insensitive, "graphitic" triaminotrinitrobenzene (TATB) are too small to be reliably studied with the techniques used for PETN (crystal size of 1 cm), it is expected that larger specimens would show similar, but more pronounced behavior. In PETN, all three orthogonal directions have van der Waals bonding, whereas the layered structure of TATB has such bonding only in one direction and strong intralayer hydrogen bonding.[4] Other explosives with similarly pronounced slip systems would be expected to show directional sensitivity properties as well. It should be emphasized that while the above research pertains to the structure of single crystals, an understanding of the effects of polycrystalline interactions is crucial in the final analysis of shock sensitivity. Toward this goal, van der Steen et al.[5] have, for example, determined that crystalline shapes significantly affect sensitivity.

This article introduces a White Oak program, currently under way, involving the design of high-performance explosive crystals that clearly exhibit directional-shock sensitivity properties along specific crystal axes, and yet clearly approach the insensitivity of homogeneous explosives along the other

axes. Such materials are being constructed from layered pyrolytic BN crystals.

Intercalation of BN

Intercalation compounds are formed by insertion of a guest chemical species—an intercalate—between layers in a host material. Because of its simple structure, high quality pyrolytic graphite is most often the preferred choice of host lattice for purposes of enhancing its electrical conductivity and chemical reactivity.[6] Another simple lattice is pyrolytic BN, the crystal structure of which is closely related to that of graphite and built of hexagonal layers of the same kind, but, as depicted in Figure 1, arranged so that atoms of one layer lie vertically above those in the layers below.
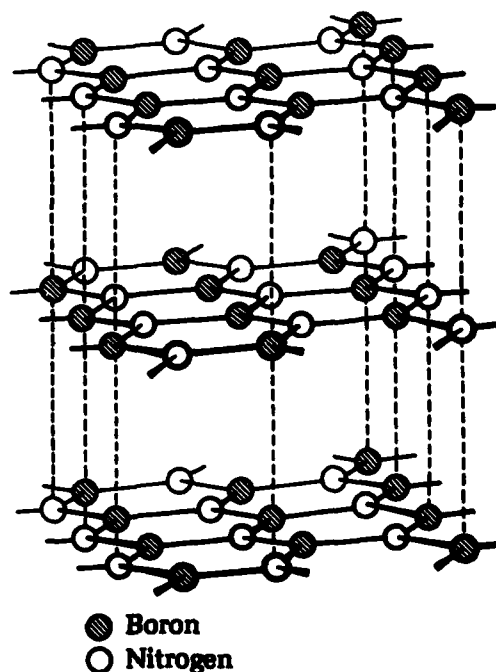
⦾ Boron
○ Nitrogen

Figure 1. Crystal structure of boron nitride, BN.

Although each layer in graphite or BN is one of the most stable structures in nature, intercalation of crystals with various oxidizing agents can yield explosive systems with the desired properties. In the case of BN, highly energetic reactions are possible with formation of B_2O_3 (ΔH_f = -303 kcal/mol). Under ordinary laboratory conditions, the molecules of intercalant enter the host crystal by exploiting the weak binding energy (1.5 kcal/mol or 0.065 eV) between the layers and increasing the interlayer spacing.[6]

103

Intercalation proceeds by charge transfer from the host BN layers to the oxidizer molecules, causing bonding within the layers of intercalate. This intercalate-intercalate bonding is generally much stronger than the intercalate-host bonding, resulting in a large thermal expansion of the intercalate layer relative to that of the host layer, which exhibits almost no thermal expansion. For the oxidizer or acceptor compounds, the intercalate layer becomes negatively charged by extracting electrons predominantly from the host-bounding layers. Thus, these host layers have a high concentration of holes, causing the Fermi level to fall and the corresponding cylindrical Fermi surface to shrink.

It is interesting to note here that intercalation of "graphitic" TATB would likely produce a much less stable structure, since the transfer of charge would be small and localized in the vicinity of the carbon rings. As a consequence, the intercalate-intercalate bonding would be weaker than that found in the extended structures with uniform bonding in the host layers.

While ordinary doping procedures give random distributions of guest species, inter-calation produces a highly ordered structure. The resulting process of staging gives a mechanism for controlled variation of the physical properties of the compounds. Stage m compounds have m graphite or BN layers between successive layers of intercalate. For maximum intercalation, m = 1, and the theoretical maximum density (TMD) of the crystal falls in the range $2.30 \leq \text{TMD} \leq 2.80$ g/cm^3 for the simple molecular intercalates. In this case, the host and intercalate layers alternate so that the structure is uniform and homogeneous. In the case of planar NO_3, stacking of the BN and NO_3 layers at TMD = 2.50 g/cm^3 gives the arrangement shown in Figure 2. For higher staging (i.e., lower intercalation), high-resolution electron microscope imaging shows a range of m values, as depicted in Figure 3 for the $FeCl_3$ intercalation of graphite.[7]

Since slip in the layered materials must occur without breakage of the B-N bonds, basal dislocations must be present to allow deformation of the hexagons.[8] For stage 1 compounds, maximum slip along the glide planes of dislocations is possible, since the Burgers vectors corresponding to the active
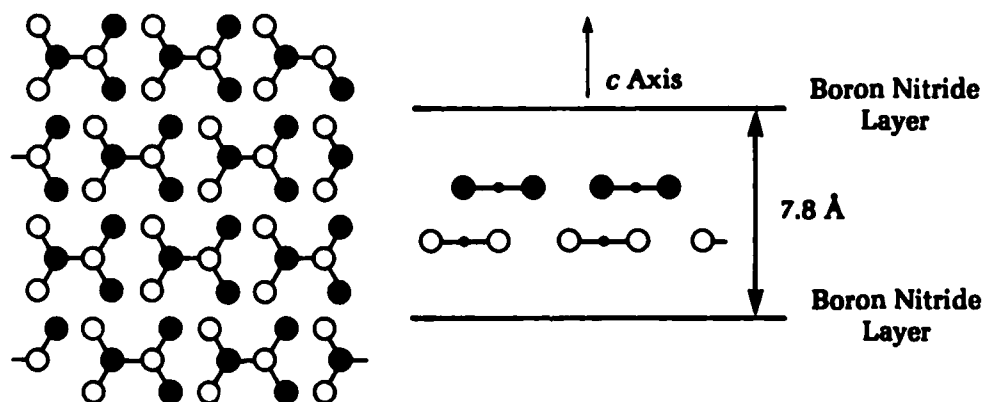
Figure 2. Possible double layer for planar NO_3 intercalated between BN layers. Side view shows NO_3 layers parallel to the BN layers. Eclipsed oxygen atoms are shown as closed circles in the top layer and as open circles in the bottom layer. Top view of double layer is displayed at left. Stage 1 formula is $(BN)_2NO_3$.
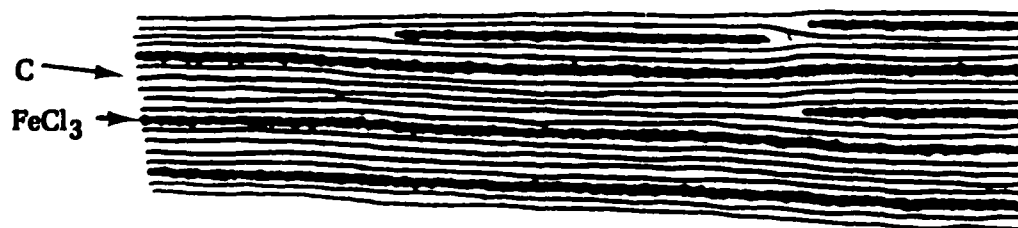
Figure 3. Schematic drawing of high-resolution electron microscope image of $FeCl_3$-graphite, showing interpenetration of differently staged regions.[7]

104

SOME CONCEPTS IN PLASTIC DEFORMATION

Dislocation: The boundary between slipped and unslipped regions of a crystal. This boundary is also a line imperfection or singularity which propagates through the crystal, enabling slip to occur at low values of critical shear stress. The crystal is highly strained near the dislocation.

Burgers vector: The dislocation-displacement vector $\vec{b}$ which determines the strength and direction of propagation of the dislocation and slip. The strain energy is a function of b^2. In layered crystals such as graphite and BN, a perfect dislocation becomes an extended dislocation during deformation by splitting in'o two partial dislocations separated and bound together by a stacking fault. From the Frank dissociation rule,[8] the strain energy is lowered by formation of the two partials, since $b^2 > b_1{}^2 + b_2{}^2$. Deformation of hexagonally stacked graphite, for example, produces stacking faults corresponding to graphite layers having rhombohedral stacking. The shock-pressure processing of rhombohedral graphite is known to increase greatly the yield of hexagonal diamond.

Shear Acoustic Modes: Long wavelength vibrations (corresponding to phonons of low frequency ω and wave-vector $\vec{k}$ of the centers-of-mass of atoms and molecules. They are preferentially excited by shock waves. An improved mathematical description of plastic deformation is attained when fluctuations of the Burgers vector $\vec{\delta b}$ are expanded in terms of the components b_k corresponding to the excited modes, $\vec{\delta b} = \sum \vec{b}_k e^{i\vec{k}\cdot\vec{r}}$.

basal dislocations of the layers are parallel to the basal plane.[8] In this case, there is minimal slip perpendicular to the basal plane. These dislocations, which split into two partials, have associated with them shear, acoustic modes which are soft (low frequency ω). For stages m > 1, regions or galleries of intercalate species are formed between adjacent host layers, resulting in strain of the graphite or BN

layers. These galleries are depicted in Figure 3. As shown in Figure 4 for graphite, the presence of a layer of intercalate causes the two adjacent host layers to undergo relative shear to bring them into eclipsed stacking. The presence of a dislocation at a boundary of a gallery has, then, a Burgers vector with basal and perpendicular components.[8] The presence of the latter component corresponds to an edge dislocation, allowing slip also to occur perpendicular to the basal plane.
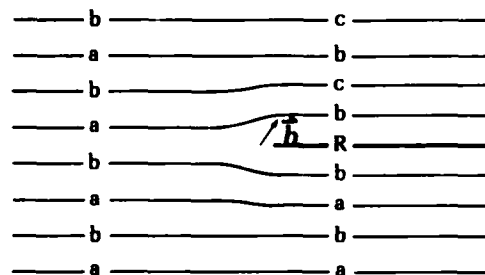
Figure 4. Burgers vector $\vec{b}$ corresponding to a boundary dislocation in intercalated graphite.[8]

Times to Ignition in Shocked, Intercalated BN

A theory[9,10] has been developed by the author which provides a formal framework and guide for the analysis of shock ignition in layered materials. This theory describes the interrelationship among bimolecular chemical reactions and processes for vibrational energy transfer between the crystal lattice and its molecules. Chemical reaction occurs only after sufficient energy is transferred for activation of the molecules. In many cases, this is the slow or rate-determining step, the characteristic time t_{pv} given by

$$t_{pv} = \hbar \sqrt{\rho_a \rho_o}. \qquad (1)$$

where h, ρ_a, and ρ_o are, respectively, Planck's constant and the densities-of-state for the acoustic and optical lattice modes. As indicated in earlier work,[9,10] ρ_a and ρ_o may be calculated from the general expression

$$\rho = \left(\frac{2}{\pi n}\right)^{1/2} \frac{(1 - 1/12n)\lambda}{h\langle v\rangle(1 + \eta)}\left[\left(1 + \frac{\eta}{2}\right)\left(1 + \frac{2}{\eta}\right)^{\eta/2}\right]^{\eta} \qquad (2a)$$

105

where n is the number of vibrational degrees of freedom, $\langle v \rangle$ is the average of the n frequencies vi, and λ and η are defined by the equations

$$\lambda^{-1} = \prod_i (v_i/\langle v \rangle).$$
(2b)

$$\eta = E/E_0.$$
(2c)

In Equation (2c), E is the internal energy interval and E_0 is the zero-point energy. Equations (2a) through (2c) apply to both harmonic and anharmonic vibrations.

Calculation of the energy transfer times t_{pv} indicates the important role of slip in the initiation of PETN, as interpreted earlier by Dick et al.[3] Since excitation of the higher-energy optical modes of the lattice is crucial to ignition,[9,10] preferential excitation of the long wavelength acoustic modes corresponding to slip can, by Equation (1), give times t_{pv} which are too slow for the given dimensions of the explosive.

The importance of t_{pv} may be seen in context with other processes occurring in the system which also have characteristic times. These processes and their corresponding rate coefficients pertain to (1) energy transfer from the host lattice into the intercalation molecules $k_{pv} = t_{pv}^{-1}$, (2) energy transfer from the molecules back into the host lattice k_{vp}, and (3) bimolecular reaction k_b between host and intercalate, which combine to give the total rate coefficient[9,10]

$$k_{tot} = k_{pv} k_b/(k_{vp} + k_b).$$
(3)

If most of the shock energy is dissipated into the low-frequency acoustic vibrations corresponding to the direction of greatest slip, little reaction is generated, so that $k_{vp} \gg k_b$ in Equation (3). If, then, $k_{tot}^{-1} > t_r$ where t_r is the time for arrival of rarefaction waves, any reaction is quenched and no ignition is possible, since reduction of the shock pressure P_s below a critical value inhibits the important bimolecular reactions. For the single 1 cm PETN crystals used in Dick et al., calculation shows that $k_{tot}^{-1} \cong 10^{-5}$ seconds for $10 \leq P_s \leq 80$ kbar, and $t_r \cong 10^{-6}$ seconds for shocks along crystal direction $\langle 100 \rangle$. (The designations $\langle 100 \rangle$, $\langle 010 \rangle$, or $\langle 001 \rangle$ indicate the directions of shock propagation and uniaxial compression parallel to, respectively, the a-axis, b-axis, or c-axis of the crystal.) On the other hand, if $k_{tot}^{-1} \leq t_r$ ($t_{tot} > t_r$), ignition is possible. This is the case for orientation $\langle 001 \rangle$ where slip is minimized

and $k_b \gg k_{vp}$, so that $k_{tot}^{-1} = t_{pv}$. Here, calculation shows that $k_{tot}^{-1} < 10^{-10}$ seconds for $10 \leq P_s \leq 80$ kbar. These results for PETN are portrayed in Figure 5. It is emphasized here
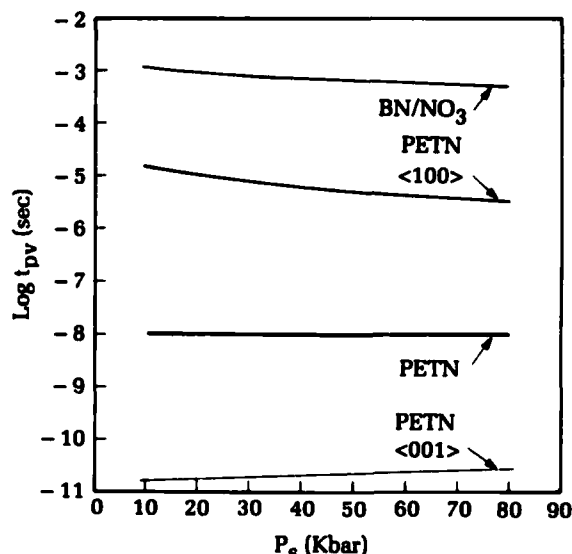
Figure 5. Comparison of shock-pressure dependence of t_{pv} for acoustic and optical modes along various crystal directions in BN/NO$_3$ and PETN. The curve labeled PETN corresponds to the geometric mean of the densities-of-state, Equation (1), for directions $\langle 001 \rangle$ and $\langle 100 \rangle$. The upper two curves for BN/NO$_3$ and PETN pertain to maximum slip.

that the slow, rate-determining step identified with t_{pv} ultimately determines the ability of the explosive to ignite at certain critical pressures and temperatures.

For initiation to occur in layered crystals, planar shocks must be directed along the c-axis of the unit cell or at small angles with it, as indicated in Figure 6. At some critical shock pressure P_{cs}, excitation of the initiating optical modes along the c-axis results in bimolecular reaction between the host and intercalate layers, and $t_{pv} < t_r$. For the BN/NO$_3$ system depicted in Figure 2, an estimate of t_{pv} is readily obtained from Equations (1) and (2) if the following reasonable assumptions are made: (1) initiation along the c-axis is effectively one-dimensional and (2) $P_{cs} \approx 130$ kbar, which approximates the known minimal pressure required to cause significant distortion of the BN or graphite planes to form the cubic structures.[11] It is assumed here that the lower bound to the optical-mode quantum $\hbar\omega$ along the c-axis of BN is about 70 cm^{-1}, which is

106

the value for high-quality graphite.[12] Also, the ratio $\lambda \cong 1$ in Equation (2b) and $E \cong 5 \times 10^9$ ergs/g at $P_{cs} = 130$ kbar,[13] so that in Equation (2c), $\eta \cong 14.3$, since $E_0 \cong 35$ cm^{-1}. The number of atoms per unit cell in the BN/NO$_3$ structure at stage 1 is 10, and the corresponding number of optical modes n for the one-dimensional problem is 9. Substitution of all these values into Equation (2a) gives, then, $\rho_0 \le 1.2 \times 10^{24}$/erg. Accordingly, since n = 1 for the acoustic mode along the c-axis, substitution of the remaining parameters above into Equation (2a) gives $\rho_a \le 7.8 \times 10^{13}$/erg. Thus, from Equation (1), $t_{pv} \le 10^{-8}$ seconds, which is much shorter than $t_r \cong 10^{-6}$ seconds for centimeter-scale crystals.

The effects of sustained shocks of $P_{cs} = 130$ kbar at increasing angles from the c-axis are, to good approximation, two-dimensional in the crystal, corresponding to slip of the host and intercalate planes past each other because of the relatively weak host/intercalate interaction under shock conditions. In this case, n = 2 and 18 for the acoustic and optical modes, respectively. Substitution of these values, as well as those given above for hω, λ, and η, into Equation (2a) gives $\rho_a \le 1.1 \times 10^{15}$/erg and $\rho_0 \le 4.7 \times 10^{15}$/erg, and from Equation (1), $t_{pv} \le 0.02$ second. Here then, $t_{pv} \gg t_r$ and initiation is unlikely. For lower pressures, additional calculations indicate that $t_{pv} \approx 10^{-3}$ seconds in the range of

$10 \le P_{cs} \le 80$ kbar. In Figure 5, these times are seen to be longer than those for PETN, indicating the much greater insensitivity of BN/NO$_3$ crystals of comparable size.

A similar analysis of TATB, the planar molecules of which form a graphitic structure, is expected to yield times in the range $10^{-5} \le t_{pv} \le 10^{-3}$. This is a result of the rigidity (r) of the slip planes for the shock pressures indicated, where r has the order PETN < TATB < BN/NO$_3$.

Summary

The important criteria for optimal directional sensitivity in intercalated, layered BN materials are that (1) they must be stage 1 or close to it; (2) the interplanar activation energies for reaction between BN and the intercalate layers must be less than those for reaction within each intercalate layer; and (3) the important interlayer reactions must be bimolecular and exothermic. Criterion (1) addresses the requirement of minimal slip along the crystal axis perpendicular to the basal plane. In this case, $t_{pv \parallel} \gg t_{pv \perp}$, for the parallel and perpendicular directions. Criterion (2) addresses the need to eliminate or minimize reaction in the intercalate layer as a result of energy transfer from the gliding host layers caused by shocks not normal to the basal

Direction of Shock

↑ C

Basal Plane of Crystal Structure

Oriented Intercalated Crystals

b

a

All of Oxidizer is Intracrystalline

Intercrystalline Ignition Unlikely Since Reaction Occurs Between Host Lattice and Oxidizer
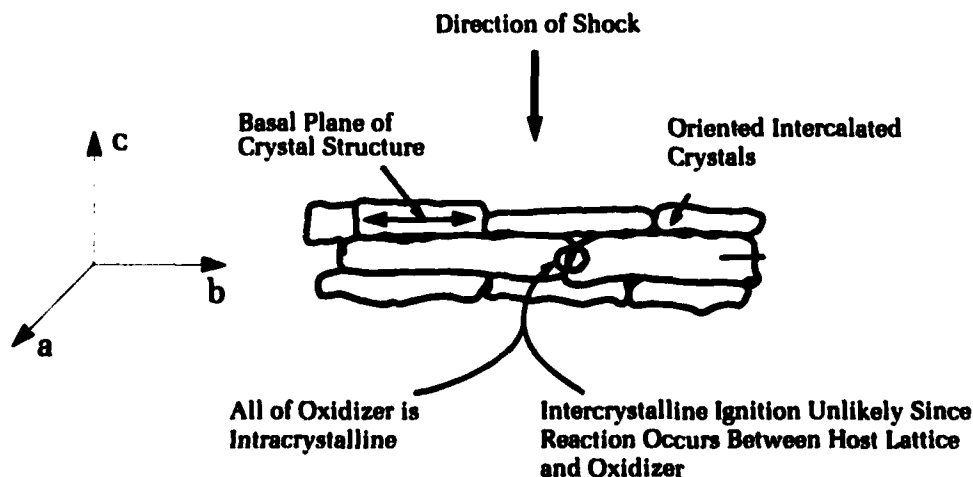
107

Figure 6. Directional initiation of layered and intercalated polycrystalline explosives.

plane. This requires the careful selection of intercalate. Various oxidizing agents are currently being studied at White Oak. Criterion (3) guarantees that the reactions will occur in times which are short compared to arrival of rarefaction waves caused by shocks. These reactions occur with activation energies that are much lower than those in unimolecular processes. The rates of these reactions given by k_b can be sufficiently fast at the pressures and temperatures of interest in detonations,[9,10] so that "initiating" energy transfer from the BN lattice into the intercalate molecules is the slow step. Together, these criteria help to guarantee that the most likely direction of shock initiation is normal or near-normal to the basal plane.

Figure 6 indicates schematically how directional sensitivity of single crystals may be retained with careful layering of the crystallites during scale-up. The retention of this important property is realizable, because the oxidizer is internal to the crystallites, so that sensitizing intercrystalline reactive "hot spots" are unlikely to develop in the short times required for shock initiation.

Acknowledgment

References

1. Campbell, A. W., Davis, W. C., and Travis, J. R., "Shock Initiation of Detonation in Liquid Explosives," *Phys. Fluids*, Vol. 4, 1961, pp. 498-510.

2. Campbell, A. W. and Travis, J. R., "The Shock Desensitization of PBX-9404 and Composition B-3," *Proc. of the Eighth Symp. (International) on Detonation*, NSWC MP 86-194, 15-19 Aug 1985, pp. 1057-1068.

3. Dick, J. J., et al., "Shock Response of Pentaerythritol Tetranitrate Single Crystals," *J. Appl. Phys.*, Vol. 70, 1991, pp. 3572-3587.

4. Cady, H. B. and Larson, A. C., "The Crystal Structure of TATB," *Acta Cryst.*, Vol. 18, 1965, pp. 485-496.

5. van der Steen, A. C., Verbeek, H. J., and Meulenbrugge, J. J., "Influence of RDX Crystal Shape on the Shock Sensitivity of PBX's," *Proc. of the Ninth Symp. (International) on Detonation*, Vol. 1, OCNR 113291-7, 28 Aug-1 Sep 1989, pp. 83-88.

6. Bartlett, N. and McQuillan, B. W., "Graphite Chemistry," M. S. Whittingham, and A. J. Jacobson (eds.), *Intercalation Chemistry*, Academic Press, New York, 1982, Ch. 2.

7. Thomas, J. M., et al., "Direct Imaging of a Graphite Intercalate: Evidence of Interpenetration of 'Stages' in Graphite: Ferric Chloride," *Mat. Res. Bull.*, Vol. 15, 1980, pp. 671-676.

8. Amelinckx, S., Delavignette, P., and Heerschap, M., "Dislocations and Stacking Faults in Graphite," P. L. Walker, Jr. (Ed.), *Chemistry and Physics of Carbon*, Vol. 1, 1965, Ch. 1.

9. Bardo, R. D., "Theoretical Calculations of Rate-determining Steps for Ignition of Shocked Condensed Nitromethane," *Int. J. Quantum Chem.*, Vol. S20, 1986, pp. 455-469.

10. Bardo, R. D., "The Lattice Density of States Concept and Its Role in Determining the Shock Sensitivity of PETN and Nitromethane," *Proc. of the Ninth Symp. (International) on Detonation*, Vol. 1, OCNR 113291-7, 28 Aug-1 Sep 1989, pp. 235-245.

11. Coleburn, N. L. and Forbes, J. W., "Irreversible Transformation of Hexagonal Boron Nitride by Shock Compression," *J. Chem. Phys.*, Vol. 48, 1968, pp. 555-559.

12. Green, J. F., Bolsaitis, P., and Spain, I. L., "Pressure Dependence of c-axis Elastic Parameters of Oriented Graphite," *J. Phys. Chem. Solids*, Vol. 34, 1973, pp. 1927-1937.

13. Rice, M. H., McQueen, R. G., and Walsh, J. M., "Compression of Solids by Strong Shock Waves," F. Seitz and D. Turnbull (Eds.), *Solid State Physics*, Academic Press Inc., New York, 1958, pp. 1-63.

The Author

RICHARD D. BARDO received a Ph.D. degree in theoretical chemistry in 1973 from Iowa State University at Ames, in conjunction with the Ames Laboratory, U.S. Department of Energy. After postdoctoral research at the University of California, Irvine, he joined the Detonation Physics Branch at White Oak in 1977. He has been active in several areas of physics and chemistry, including reaction-rate theory at high pressures and temperatures, electronic structure of molecular solids at high pressure, and properties of metastable organic and inorganic semiconductors and superconductors. He has published over 40 papers in these and other areas. He was a science and technology agent and principal investigator for the SDIO/IST program, "High-Pressure Metastable Materials." His current research interests include the design of a new class of insensitive and powerful layered, intercalated explosives, the development of equations-of-state for high-T_c superconductors, and the theory of flux pinning at twin boundaries and crystal interfaces in high-T_c superconductors. He received the Center's Independent Research Excellence Award in 1987. He is a member of Sigma Xi, Phi Lambda Upsilon, and the American Physical Society.

Electromagnetic Nondestructive Evaluation of Carbon-Carbon Composites

John M. Liu and Susan N. Vernon

Carbon-carbon composites are used in naval strategic weapon systems, and their capability to retain excellent mechanical properties and dimensional stability in hostile environments makes them prime candidate materials for future space structures. However, development of the design, processing, and proof-testing of these structures is complex and costly. Therefore, increasing demands have been placed on nondestructive evaluation techniques that may identify anomalies early in the materials processing and fabrication stages. This article reports on electromagnetic nondestructive evaluation techniques developed in the Materials Evaluation Branch that have been demonstrated to be effective in verifying the properties of composites manufactured by proprietary processes.

Introduction

Among lightweight materials suitable for future aerospace applications is a type of carbon-carbon composite being developed at the Dahlgren Division's White Oak Detachment. These composites can have elastic stiffness comparable to steel and mass density less than that of aluminum. The manufacturing processes for carbon-carbon composites, used for missile nose tips and exit cones of rocket nozzles, must be substantially modified to achieve such properties.

Items fabricated successfully thus far include tubes, panels, and cones. Some examples of these items are shown in Figure 1. The wall thickness of the tubes and the cone was typically 0.030 inch; tube lengths were 12 inches; panels ranged in thickness from 0.030 to 0.125 inch.

When suitably coated for protection against the oxidative, thermal, and radiative environment existing in space, the tubes are potentially useful for structural and thermal management purposes. The heat treatment, which determines the graphitization process, must be controlled to allow the mechanical and thermal properties to reach the design values.

In the thin-walled carbon-carbon cone typically used in rocket nozzles, the small cylindrical attachment section has the same number of fiber tows as the much larger cone section. Consequently, in the region joining these two sections, both fiber density and matrix density tend to be nonuniform. Because this region also suffers the highest thermal stresses during rocket firing, it is important to verify its material state.

As the manufacturing process for the more advanced composites is still evolving, nondestructive material evaluation techniques are needed to provide

Figure 1. Carbon-carbon composite articles studied in this work.

property screening. This screening offers many benefits: it increases the efficiency of conventional property testing; it provides a measure of consistency of materials from different manufacturers; and it provides early detection of the effects of changing processing conditions.

Commercial nondestructive evaluation of composites is based primarily on ultrasonics and radiography; electromagnetic techniques historically have been restricted to the detection of surface and near-surface flaws in metal components. We have extended this technology to the characterization of advanced composite materials.[1-5] The information made available by electromagnetic techniques complements that provided by the more traditional technologies.

This article reports on application of the technology to the characterization of carbon-carbon composites. The work was motivated by expectations that electrical transport properties reflect the extent of the graphitization process in the reinforcing fibers which, in turn, control the mechanical and thermal properties of the material. In addition, we have demonstrated that our technique is capable of both characterizing the stacking sequence in a composite laminate and detecting macroscopic porosity localized in the regions of large curvature change in a composite cone.

Principles of Electromagnetic Nondestructive Evaluation

The principles of our technique are based on the excitation of eddy currents in an electrical conductor when a "probe" carrying radio-frequency (rf) current is placed on the conductor. Typically, a probe consists of a multiturn coil of wire. We place the coil in a ferrite cup core to concentrate the electromagnetic field.

Single or multiple probes constituting transmitting and receiving devices can be used for obtaining the signal associated with the effects of the material on the rf magnetic field. In the work reported here, a single probe was used.

Characteristics of the material were extracted through analysis of the changes in probe impedance as a function of frequency. The impedance changes with the electromagnetic flux linking the probe as a result of the secondary magnetic field associated with the eddy currents induced in the material.

Some basic features of the impedance of the probe with and without the presence of the material are illustrated in Figure 2a for frequencies ranging from 125 kHz to 8000 kHz. A normalized impedance diagram of the same data is shown in Figure 2b, together with the definition of the liftoff angle (Θ). Vernon has shown that there is a special relationship between this liftoff angle and the material resistivity,[6,7] allowing the latter to be determined in isotropic conductors.
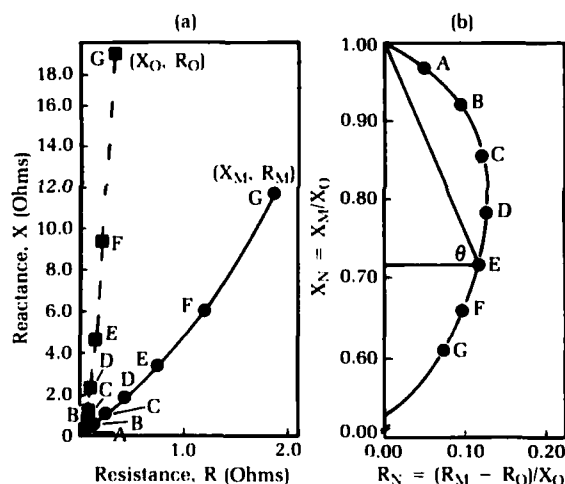
Figure 2. (a) Reactive and resistive components of the impedance of a 0.44-inch O.D. eddy current probe in air (dashed lines) and on a carbon-carbon composite (resistivity of 842 $\mu\Omega$cm). The frequencies in kilohertz are: A, 125; B, 250; C, 500; D, 1000; E, 2000; F, 4000; and G, 8000. (b) Normalized impedance diagram for data in (a).

The attenuation of the electromagnetic field inside a conductor is generally expressed by the concept of a "skin depth." This is defined by

$$\delta = 1.98 \, (\rho/f)^{1/2},$$

where skin depth, δ, is in inches, resistivity, ρ, is in $\mu\Omega$cm, and frequency, f, is in hertz.

111

Numerical values of δ for a number of metals and carbon-carbon composites are shown in Table 1 for the frequency ranges commonly available in our measurement system.

It is noted that except for the thickest of the carbon-carbon panels, the skin depth is usually greater than the composite thickness.

Approaches to Electromagnetic Nondestructive Evaluation

The extension of electromagnetic non-destructive testing technology from metals to carbon-carbon composites requires a recognition of the difference in material anomalies of concern in the two classes of materials. These are listed in Table 2. As a consequence of these differences, our approach to the evaluation of carbon-carbon composites is quite different from the conventional practice on homogeneous metals.

The approach is based on measurement of the absolute components of the probe impedance. As in metals, this impedance is affected by the resistivity of the material and the measurement frequency which, together, determine skin depth; and by the ratios of the probe radius and the material thickness to the skin depth. In addition, the anisotropy of the eddy current flow, the weak coupling between the incident electromagnetic field and the composite of high resistivity, and the surface curvature of the tubes and cone are all issues of concern.

In the past several years, significant advances have been made in the design of eddy current probes for the characterization of

Table 1. Values for Skin Depth in Metals and Carbon-Carbon Composites

Material	Resistivity (μΩcm)	Skin Depth (inch) (40 kHz)	(400 kHz)	(4000 kHz)
Aluminum	4	0.020	0.006	0.002
304-stainless steel	70	0.083	0.026	0.008
Titanium 6-Al-4V	171	0.129	0.041	0.013
Isotropic Carbon-Carbon	842	0.287	0.091	0.029
Carbon-Carbon P100/A240 (Along Fibers)	250	0.157	0.050	0.016
Carbon-Carbon P100/A240 (Transverse to Fibers)	2600	0.505	0.160	0.050

Table 2. Material Conditions and Anomalies of Concern Amenable to Electromagnetic Nondestructive Evaluation in Metals and in Carbon-Carbon Composites

Metals	Composites
Surface Cracks	Composition
Cracks Emanating from Bolt Holes	Homogeneity of Properties and Density
Heat Treatment Effects	Architecture
Coating Thickness	Delamination
Subsurface Corrosion	Voids
Alloy Composition	Porosity
	Processing Effects on Properties
	Fiber Alignment
	Fiber Wrinkles

112

composites.[8-10] Some of these probes are shown in Figure 3. Recently, probe geometry has been developed[11] approximating a pair of line sources embedded in ferrite cores to improve coupling and shielding. Special construction to conform to curved surfaces has also been achieved. Through a combination of data correlation and theoretical analysis, these probes have been shown to allow the determination of anisotropic electrical resistivities in composites. The resistivity determination method, based on measurement of the frequency dependence of the probe impedance, follows Vernon's technique developed for isotropic materials. In thin carbon-carbon composites of high resistivity, the skin depth is usually greater than the material thickness, requiring detailed consideration of material thickness effects in our measurements. In the next section, we present some examples of successful applications of our techniques.

Orientation Dependence of Resistivity

Since the microstructure of fibers in a carbon-carbon composite is highly graphitic, the electrical resistivity is generally aniso-tropic; it is much lower in the fiber direction than transverse to this direction. In Figure 4 electrical resistivity is shown as a function of the angle between the fiber direction and the eddy current path in a uniaxial composite panel with P100 fibers in A240 pitch matrix. The resistivity in the fiber direction is about a tenth of that transverse to this direction. In addition, the orientation dependence is

reasonably well described by the expected behavior of a second-order tensor.

Carbon-Carbon Composite Laminates

Composites are usually designed to have useful properties in more than one direction. For this purpose, uniaxially reinforced layers are fabricated into laminates with fiber directions distributed from one layer to another. For these laminates, it is important to assess properties one layer at a time. Because the depth of penetration of the electromagnetic field can be controlled by changing the frequency, our techniques allow for the evaluation of electrical resistivity and its anisotropy as a function of the stacking sequence in a laminate.

An example of such an application is shown in Figure 5 for a stack of two carbon-carbon layers of P100/A240 carbon-carbon composite in which the fiber direction of the top layer is orthogonal to that of the bottom layer. It is seen that at low frequency both the top and bottom layers interacted with the electromagnetic field, exhibiting an apparent 4-fold symmetric resistivity for the laminate as a whole. On the other hand, when the frequency was such that

Figure 3. Examples of White Oak-designed eddy current probes for nondestructive evaluation of carbon-carbon composites. The larger one is a ferrite-core probe approximating two line sources. In the smaller one, the coil windings are opposing each other for differential measurements.
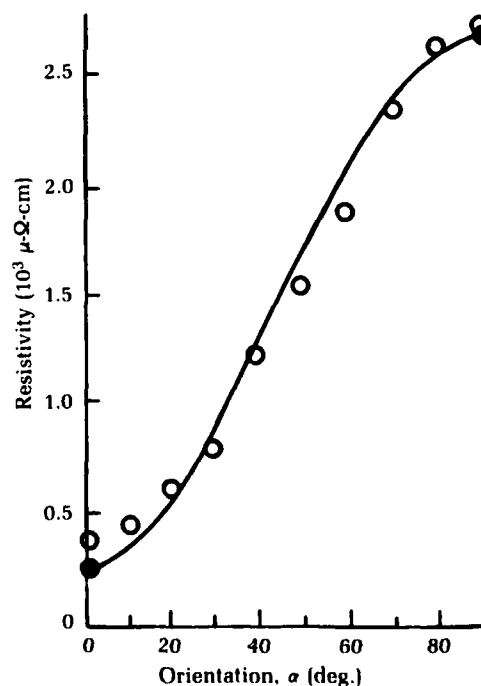

Figure 4. Variations of electrical resistivity as the direction of eddy current flow changes from the fiber direction ($\propto$ = 0) to the transverse direction ($\propto$ = 90); o = measured data. The continuous curve shows the expected variation of a second-order tensor, based on dc contact measurements at $\propto$ = 0 and $\propto$ = 90.
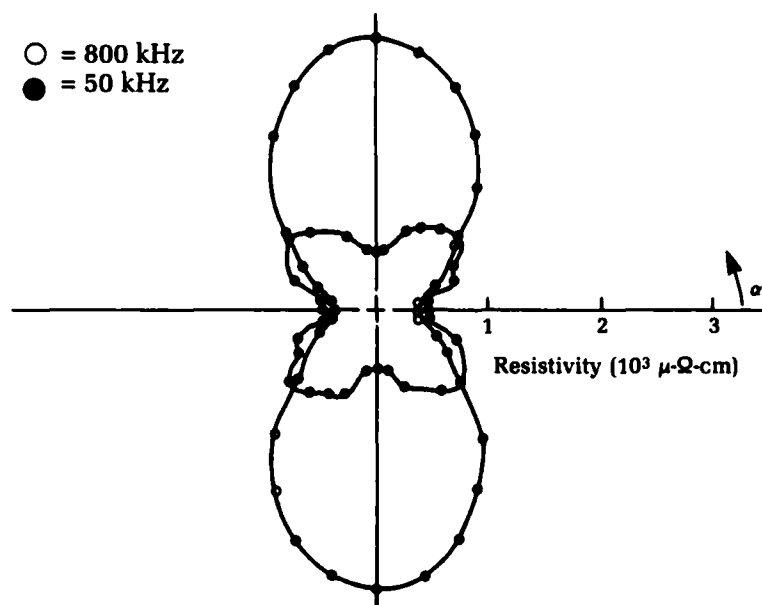
113

Figure 5. Polar plot of the variations of electrical resistivity in a two-layer, P100/A240 carbon-carbon composite laminate, as the direction of the input electric field varies on the surface of the laminate. The fiber directions in the top layer and the bottom layer are at $\propto = 0$ and $\propto = 90$, respectively.

only the top layer interacted with the input field, a 2-fold symmetric pattern characteristic of a uniaxially reinforced top layer was observed.

When more than two layers are present, inversion schemes capable of a unique determination of the resistivities in each layer are as yet unavailable. The extension of previous methods for the inversion of eddy current data in homogeneous, isotropic metals[12-14] to composites, taking into account the three-dimensional electromagnetic interactions,[15-17] remains an area of active research that should provide further insight into the solution of this problem in the future.

Carbon-Carbon Exit Cone

Lightweight, high temperature resistant exit cones can be fabricated by a technology similar to that used for tubes. As mentioned above, it is important to detect nonuniform areas, which tend to be present in the region joining the cylindrical and conical sections. While immersion ultrasound is useful for the evaluation of a cone, ultrasonic evaluation for these regions would be difficult as a result of the refraction of the ultrasonic beam associated with the rapidly changing surface curvature. Eddy-current-based techniques offer several

advantages: no liquid couplant is required; and construction of eddy current probes in conformity with complex surface geometry, in contrast to its ultrasonic counterpart, is easier.

Figure 6 shows the change in electrical resistivity around the circumference in the region of largest surface curvature between the cylindrical and the conical sections of the cone shown in Figure 1. Two independent series of measurements resulted in the data represented by the symbols □ and O. They show a consistent pattern of resistivity variation of up to 10 percent along the circumference in this part of the cone. Areas of high resistivity appear to be caused by nonuniform fiber density and matrix infiltration that occur during the manufacturing process. Research is continuing on the construction of polarization-sensitive, differential probes and the supporting theoretical analysis in order to separate the effects of the fibers and the matrix.

Thin-walled Carbon-Carbon Tubes

In order to achieve the required mechanical stiffness and thermal conductivity for satellite structural application, we subject carbon-carbon tubes to heat treatment at high temperature. Rapid verification for the maturity of this heat treatment process is provided by testing
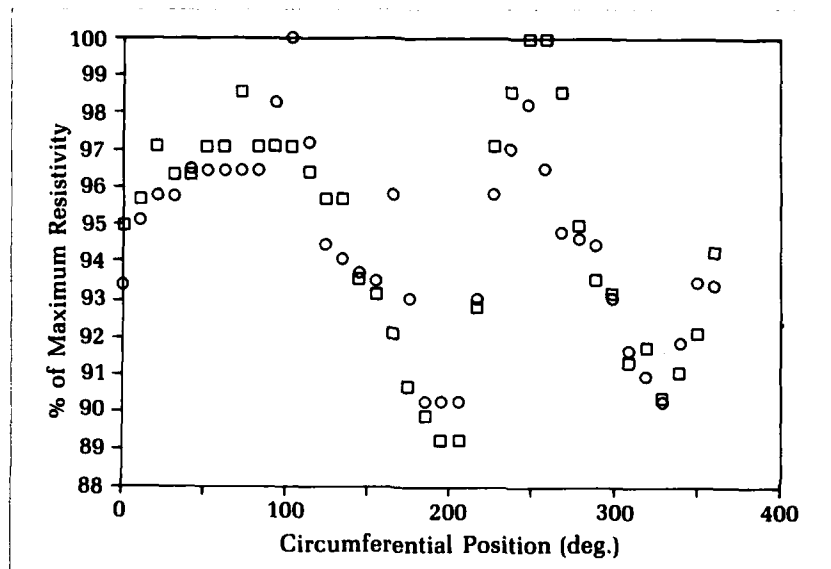
114

Figure 6. Variation in the electrical resistivity around the circumference in the highly curved regions between the cylindrical top section and the conical base in the thin-wall carbon-carbon cone shown in Figure 1.

Table 3. Axial Electrical Resistivity and Young Modulus in Carbon-Carbon Tubes at Two Different Heat Treatment Temperatures

Heat Treatment Conditions	Electrical Resistivity (micro-Ohm-cm)	Elastic Modulus (MSI) (Compression)	(Tension)
100C Below Requirement	1281.5 ± 7	30.1 ± 1.3	29.8 ± 1.9
Required Temperature	939.4 ± 9	33.0 ± 1.7	33.9 ± 1.8

for the axial electrical resistivity of these tubes, since the degree of graphitization in the fibers progresses with the heat treatment temperature and heating time.

Table 3 shows the results for two sets of tubes. One set was heat treated at the required temperature. The other was heat treated at 100 degrees C below that temperature for the same amount of time.

It is seen that the resistivities changed by 20 percent as a result of the difference in heat treatment temperature. Table 3 also includes the results of mechanical testing (performed at Southern Research Institute, Birmingham, Alabama), showing the corresponding increases in the Young Modulus in tension and in compression for the tubes heat treated at the higher temperature. Our techniques should be useful for detecting departures from proper heat treatment time and temperature, as well as for assessing potential variations in the material state from one part of a tube to another.

Summary

Several applications of electromagnetic nondestructive evaluation technology, developed at White Oak for thin-walled carbon-carbon composites, are reported in this article. Through a combination of probe design for anisotropic conductors and theoretical modeling, we have succeeded in extending eddy current testing technology for characterizing the heat treatment states of carbon-carbon tubes, for detecting porosity in regions of large surface curvature, and for characterizing the stacking sequence in laminates. Correlation between the mechanical stiffness properties and the eddy current testing results is very good. Further development of this technology is continuing at White Oak for future DoD and NASA applications.

115

Acknowledgments

References

1. Liu, J. M. and Vernon, S. N., "Electrical Conductivity in Heat Treated Aluminum Alloys Reinforced with Discontinuous SiC Whiskers," *Review of Progress in Quantitative Nondestructive Evaluation*, Vol. 5B, Ed. D. O. Thompson and D. E. Chimenti, Plenum Press, New York, 1986, pp. 1171-1178.

2. Liu, J. M. and Vernon, S. N., "Multi-frequency Eddy Current Techniques for Inhomogeneous Metallic Materials," *Nondestructive Testing Communications*, Vol. 2, 1986, pp. 141-153.

3. Warren, J. M., Vernon, S. N., and Gammell, P. M., "Ultrasonic and Eddy Current Inspection of a Thick Wall Graphite Epoxy Cylinder," *Proc. Sixteenth Symp. on Nondestructive Evaluation*, Ed. D. W. Moore and G. Matzkanin, Nondestructive Evaluation Testing Information Analysis Center, Southwest Research Institute, San Antonio, TX, 1987, pp. 132-138.

4. Vernon, S. N., "Parametric Eddy Current Defect Depth Model and its Application to Graphite Epoxy," *NDT International*, Vol. 22, No. 3, 1989, pp. 139-148.

5. Vernon, S. N., "Eddy Current Inspection of Carbon Fibre Reinforced Composites," *Proc. International Conf. on European Advances in Nondestructive Testing*, Toulouse, France, 1989, pp. 271-285.

6. Vernon, S. N., "Single-Sided Eddy Current Method to Measure Electrical Resistivity," *Materials Evaluation*, Vol. 46, No. 12, 1988, pp. 1581-1587.

7. Vernon, S. N. and Gammell, P. M., Patent #4922201: "Eddy Current Method for Measuring Electrical Resistivity and Device for Providing Accurate Phase Selection," 1 May 1990.

8. Vernon, S. N. and Lane, Stephen, "Eddy Current Device to Inspect Filament-Wound Composites," SIR-H879, 1 Jan 1991.

9. Vernon, S. N. and Gammell, P. M., "Optimization of Eddy Current Probes for NDE of Carbon Fiber Composites," *Proc. Fifteenth Symp. on Nondestructive Evaluation*, Ed. D. W. Moore and G. A. Matzkanin, Southwest Research Institute, San Antonio, TX, 1986, pp. 287-291.

10. Vernon, S. N., "The Universal Impedance Diagram of the Ferrite Pot Core Eddy Current Transducer," *IEEE Transactions on Magnetics*, Vol. 25, No. 3, 1989, pp. 2639-2645.

11. Vernon, S. N. and Liu, J. M., "Eddy Current Probe Design for Anisotropic Composites," *Materials Evaluation*, Vol. 50, No. 1, 1992, pp. 36-41.

12. Sabbagh, H. A. and Sabbagh, L. D., *Inversion of Eddy-Current Data and the Reconstruction of Flaws Using Multifrequencies*, AI/TR-1/83, Sabbagh Associates (formerly Analytics, Inc.) Bloomington, IN, April 1983.

13. Kahn, A. H., et al., "Determination of Electrical Conductivity Profiles from Frequency-sweep Eddy Current Measurement," *Review of Progress in Quantitative Nondestructive Evaluation*, Vol. 5B, Ed. D. O. Thompson and D. E. Chimenti, Plenum Press, New York, 1986, pp. 1383-1391.

14. Fillion, G. and Bussiere, J. F., "Eddy Current Profiling of Magnetic Coercivity in Layered Ferromagnetic Materials," *Research in Nondestructive Evaluation*, Vol. 2, 1990, pp. 97-117.

15. Sabbagh, H. A., Sabbagh, L. D., and Robert, T. M., *An Eddy Current Model for Three-Dimensional Nondestructive Evaluation of Advanced Composites*, NSWC TR 85-304, Jul 1985.

16. Sabbagh, H. A., et al., "Inversion of Eddy-Current Data and the Reconstruction of Three-Dimensional Flaws," *IEEE Transactions on Magnetics*, Vol. 26, No. 2, 1990, pp. 626-629.

17. Burke, S. K., "Eddy Current Induction in a Uniaxially Anisotropic Plate," *J. Applied Physics*, Vol. 68, No. 7, 1990, pp. 3080-3090.

116

The Authors

JOHN M. LIU is a group leader in the Materials Evaluation Branch at the White Oak Detachment, specializing in research and development of ultrasonic, electromagnetic, and thermal techniques for the nondestructive characterization of material properties in composites, ceramics, and metals used in current and future Navy systems. He received a B.S. in physics from St. Vincent College in 1966 and a Ph.D. in mechanics and materials science from the Johns Hopkins University in 1973. He held research and teaching positions at the State University of New York prior to joining White Oak in 1983. His recent projects include the development of novel techniques for the evaluation and validation of EHF antenna radomes, ceramic composite missile radomes, composites for space applications, and composites for Navy ship mast applications.

SUSAN N. VERNON received a B.A. in physics from Goucher College, Baltimore, Maryland, and an M.S. in metallurgy from Massachusetts Institute of Technology. Prior to joining the White Oak Detachment in 1982, she worked at Bell Laboratories, Murray Hill, New Jersey, and in the Electronic Materials Development Branch at the MIT Lincoln Laboratory. At White Oak, she has concentrated on the development of electromagnetic nondestructive methods for the inspection of advanced composite materials. She has been awarded several patents in this field, both on data interpretation and probe design.

117

Experimental Protective Coatings Exposed to Space Environment Aboard Atlantis

John V. Foltz

The White Oak Detachment submitted 27 specimens for space flight STS-46 exposure on the space shuttle. The samples included various carbide, oxide, phosphate coatings under development to protect structural and thermal management components from the atomic oxygen present in low-earth orbits, structural carbon-carbon composite material, and a space mirror made of foam metal-matrix composite. The samples returned from the orbital exposure are currently being analyzed to determine the degree of reactivity with the space environment.

Introduction

In July 1992, the space shuttle program launched STS-46 on an eight-day mission. The flight was intended to accomplish a number of objectives. A retrievable platform carrying various experiments was to be placed in orbit. This platform, called EURECA, would be brought back by another shuttle in 1993. The feasibility of deploying a satellite on a tether was to be explored. A number of cargo bay and middeck payloads, to be activated by the astronauts, were on the manifest.

The White Oak Detachment participated in the STS-46 mission. One of the cargo bay payloads was an experiment in which samples of various materials would be exposed to the space environment and returned to the ground for postflight analyses of their reaction. Motivated by a need to develop coatings to protect spacecraft components made of advanced composite materials against the atmosphere of low earth-orbit, the White Oak Detachment submitted test samples for this experiment. The returned samples are currently undergoing analyses. This article provides background information about the shuttle flight and documents the materials exposed in our investigations.

Background

The Problem

Materials are affected by the thin upper atmosphere. Many polymers and some metals that returned from the first shuttle flights exhibited significant changes in surface properties attributed to the orbital environment. Susceptibility to atomic oxygen seemed the most plausible explanation for the effects observed.

Early satellite measurements had revealed that the neutral oxygen atom is the predominant species in the upper atmosphere (200 km to 600 km), formed

118

at these altitudes through the dissociation of O_2 by ultraviolet radiation. Atomic oxygen in the ground state, $O(^3P)$, is a strong oxidizing agent. Oxidizing effects from laboratory experiments with atomic oxygen were reported in the literature well before the first shuttle flight.[1]

Concentration of oxygen atoms is low at altitudes above 200 km, but a spacecraft suffers a significant incident flux by virtue of its orbital speed. The flux may be estimated from the atomic oxygen density[2] and the vehicle speed, typically 8 km/sec. Table 1 gives some representative numbers for two altitudes. The fluence, or total number of particles impacting a unit area over an extended exposure, is the time-integrated flux. The collision energy of the atom with the spacecraft is 5 eV.

Table 1. Atomic Oxygen Flux versus Altitude

Altitude (km)	Density (atoms cm^{-3})	Flux (atoms cm^{-2} sec^{-1})
200	5×10^9	4×10^{15}
600	5×10^6	4×10^{12}

Atomic oxygen density from Reference 2.

Previous Flight Experiments

In the early 1980s, NASA began developing flight experiments to address the atomic oxygen problem. The approach was to use the shuttle to convey samples to the space environment, where they would be exposed in a known manner and then returned to Earth for postflight analyses. The experiments, known as EOIM, or Evaluation of Oxygen Interactions with Materials, were characterized by exposures of short duration, typically lasting about 40 hours. In the mid-1980s, NASA also developed the LDEF, or Long Duration Exposure Facility, to provide information about the effects of much longer exposures. The LDEF was a retrievable platform on which samples were mounted, placed in orbit by one shuttle, and recovered months later by another.

In the 1980s, two flights occurred in the EOIM series. EOIM-1 and EOIM-2 evaluations were performed on the fifth (STS-5) and eighth (STS-8) shuttle missions. The results of the EOIM investigations provide much of the current information regarding reactivities of materials with atomic oxygen in the low-earth-orbit environment.[2] STS-5 carried about 60 samples and STS-8 over 300. Diagnostic investigations ranging from mass change and surface morphology to surface-chemistry changes were

conducted on the exposed surfaces after the flights. Although the exposure times were comparable for both missions, a difference in flight altitudes (300 km for STS-5 compared to 225 km for STS-8) resulted in total accumulated fluences of 1.0×10^{20} and 3.5×10^{20} for STS-5 and STS-8, respectively. Surface recession (or thickness loss) for reactive materials, as determined from change in mass of the specimens, was found to be proportional to the fluence. Qualitatively, the findings are:[2] (1) organics (materials containing only carbon, hydrogen, oxygen, or nitrogen) have high reaction rates; (2) perfluorinated and silicone polymers are more stable than the organics by at least a factor of 50; (3) macroscopically, metals, except for osmium and silver, are stable.

The LDEF was placed into orbit in April 1984. Originally intended to be one year, the exposure actually lasted for almost six years. LDEF contained 57 experiments with over 200 principal investigators and more than 10,000 test samples. While many LDEF studies are still in progress, results to date have given valuable information on long-term performance in orbit and resulted in lessons learned.[3]

Details Of Current Flight Experiment

The EOIM-3 experiment was conducted on the 49th overall flight of the space shuttle program as part of the STS-46 mission, summarized in Table 2. Launch and landing were at the Kennedy Space Center in Florida. The director of EOIM-3 is L. J. Leger of the Johnson Space Center. Sample spaces were allocated to the various NASA agencies, the Department of Defense (with the lead laboratory being The Aerospace Corporation), the University of Alabama in Huntsville, the European Space

Table 2. STS-46 Mission Summary

Flight Date:	31 Jul 1992 – 8 Aug 1992
Orbiter:	Atlantis (Twelfth Flight)
Mission Duration:	8 Days
Miles Traveled:	3.5 Million
Orbits of Earth:	126
Orbits:	230 nm x 230 nm (EURECA*)
	160 nm x 160 nm (TSS**)
	124 nm x 124 nm (EOIM-3)
Crew:	Loren J. Shriver (Commander)
	Andrew M. Allen (Pilot)
	Claude Nicollier
	Marsha S. Irvins
	Jeffrey A. Hoffman
	Franklin R. Chang-Diaz
	Franco Malerba

* European Retrievable Carrier Platform
** Tethered Satellite System

119

Agency, Canada, and Japan. Overall, more than 1100 samples were submitted. White Oak, the only Navy laboratory to participate, did so under the auspices of The Aerospace Corporation.

White Oak investigators need to know the reaction rates of certain candidate materials for protective coating systems. Samples consisted of flat substrates on which experimental coatings were deposited. The list of coatings and substrates is given in Table 3. Two materials were tested as monolithic discs.

The substrates were of AXF-5Q polycrystalline graphite made by Poco Graphite, Inc., carbon-carbon composite material (C-C) made by Kaiser Aerotech, or silicon carbide aluminum metal-matrix composite material made by Advanced Composite Materials Corporation. Polycrystalline graphite was chosen as a substrate for basic research materials because it is inexpensive, readily polished, and has a low thermal expansion coefficient similar to the coatings placed on it. Carbon-carbon composite is being developed for spacecraft applications and is representative of an engineering

structural material. Carbon-based materials in general will require an undercoat for atomic oxygen protection and an overcoat for thermal control. The metal matrix composite substrate is actually a prototype space mirror, consisting of a foam SiC/Al core with a face sheet of optical grade SiC/Al.

The samples were fabricated in the form of small discs 1/2 inch in diameter. The fixture that holds samples during the space exposure is shown in Figure 1. Control samples were fabricated for comparison with exposed materials. When the sample size permitted, two samples of each material were flown in the same fixture: the evaluation sample flown face up and exposed to the oxygen stream, and the flight-control sample mounted face down in the tray. The thickness of the SiC/Al mirror prohibited a flight control sample for this material.

All samples were photographed and weighed before assembly into the flight trays. Figure 2 shows a sample being loaded. Fully loaded, ambient temperature tray no. 12 held 82 samples from White Oak and Aerospace Corporation. The assembled tray and all associated hardware were placed in a vacuum chamber on a table maintained at 65°C and outgassed for 72 hours. Three trays were designed with heaters to hold samples in orbit isothermally at 60°C, 120°C, or 200°C in order to assess the

Table 3. White Oak Samples on Ambient Temperature Tray Number 12

Coating	Undercoat	Substrate
TiC	—	POCO
VC	—	POCO
TIB2	—	POCO
TiC	—	POCO
—	—	NiAl
NiBe	—	POCO
Ti2Be17	—	POCO
V	—	POCO
Cr	—	POCO
Si-SiC*	—	C-C
Rh	Si-SiC*	C-C
SiO2	Si-SiC*	C-C
Al2O3	Si-SiC*	C-C
—	—	C-C
ZrP2O7	—	C-C
SiO2	ZrP2O7	C-C
SiP2O7	—	C-C
SiO2	SiP2O7	C-C
AlPO4	—	C-C
SiO2	AlPO4	C-C
Ni	—	SiC/Al

* Si-SiC is a co-deposited material.

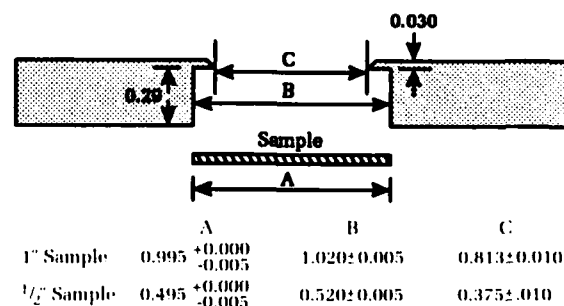|	A	B	C
1" Sample	0.995 +0.000 -0.005	1.020±0.005	0.813±0.010
1/2" Sample	0.495 +0.000 -0.005	0.520±0.005	0.375±0.010

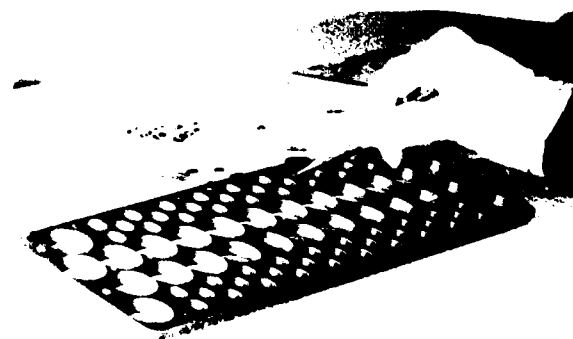**Figure 1.** Dimensions of sample holder on carrier tray.

Figure 2. Sample carrier tray No.12 (unloaded). (Photo courtesy of The Aerospace Corporation.)

120

effect of temperature on material reaction rates. TiC and VC coating samples were exposed on each of the three elevated temperature trays. Flight control samples were not used.

The EOIM-3 qualification hardware is shown in Figure 3 mounted on a table for a vibration test. Fifteen ambient temperature trays (sans specimens) are in the foreground. The three elevated-temperature trays are visible at the top of the assembly on the right-hand side. The flight hardware, a duplicate of this assembly, is mounted on a truss support structure located in the aft region of the orbiter cargo bay (Figure 4). This arrangement is intended to minimize reflection of the incoming atomic oxygen flux and position samples for direct impingement.

In previous flight experiments, calculations based on models of the Earth's atmosphere were used to estimate atomic oxygen flux during the exposure period, leading to an uncertainty in fluence on the order of 15 to 20 percent. Reaction rate determinations from EOIM-3 are expected to be more accurate than those yielded by earlier flight evaluations due to the use of an ion-neutral mass spectrometer to measure the incoming atomic oxygen atom flux *in situ*. In Figure 3, the mass spectrometer is on the left.
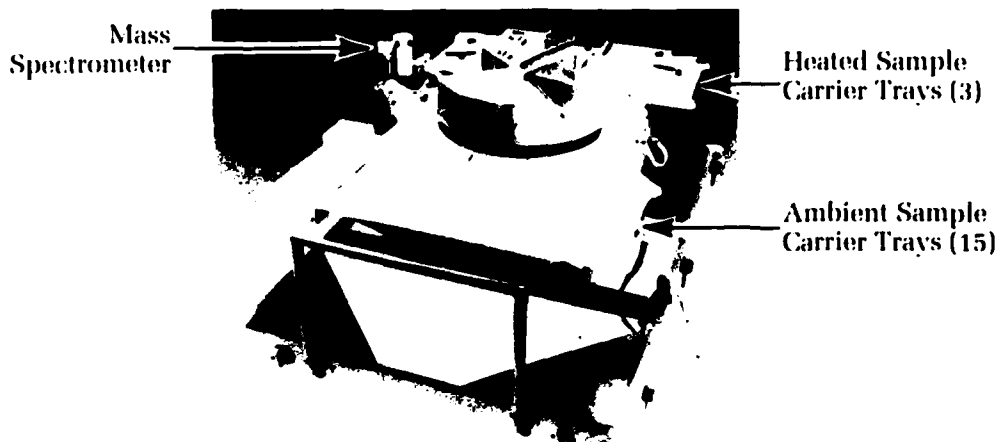

Mass Spectrometer

Heated Sample Carrier Trays (3)

Ambient Sample Carrier Trays (15)

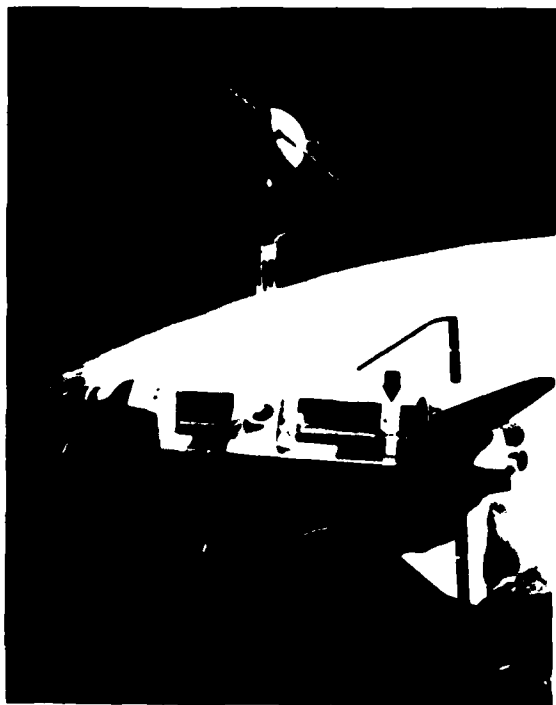**Figure 3.** Qualification test setup for EOIM-3. (Photo courtesy of NASA.)

Figure 4. Location of EOIM-3 on shuttle is shown by arrow. (Photo courtesy of NASA.)

Results

A high percentage of the STS-46 secondary payloads successfully accomplished their purpose. The EURECA retrievable platform was placed in orbit. Attempts to deploy the Tethered Satellite System were not fully successful due to a problem with the tether reel mechanism. The crew was able to cast the satellite out to only a small fraction of the intended length. The EOIM-3 experiment was executed largely as intended, although the start was delayed. The experiment was initiated by Atlantis' crew on the sixth day of flight. The shuttle was lowered to an altitude of 230 km and oriented nose-to-earth with the cargo bay facing into the velocity vector. The cargo bay doors were opened and the samples were exposed for 42 hours. The exposure provided a calculated atomic oxygen fluence of 1.99×10^{20} atoms/cm^2, based on values of solar activity predicted before the flight. Results of the mass spectrometer measurements were not available at this writing.

121

After return to earth, the samples were unloaded and the trays distributed to the principal investigators. This process took approximately three weeks. Preliminary postflight analyses of all DOD samples were conducted at The Aerospace Corporation. Initially, all samples were photographed, dessicated, and weighed. Scanning electron microscopy observations were recorded.

Photographs of four samples taken postflight are shown in Figure 5. The experimental sample and the flight control sample are presented together for comparison. The test results confirm that the baseline carbon-carbon composite was, as expected, susceptible to atomic oxygen attack. Etching of the uncoated composite is clearly visible in Figure 5a as a darkened ring inside the area protected by the flange that held the sample in place. Overall, eight of the other twenty test samples on the ambient tray exhibited obvious effects of exposure to the space environment in a visual examination. Figure 5b, c, and d shows the results for three of the test coatings.
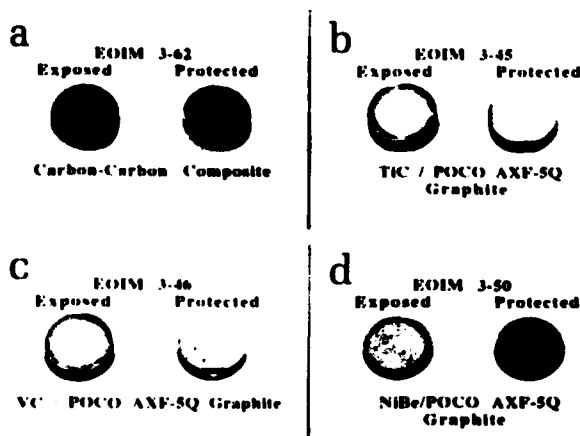

Figure 5. Four samples exposed to the space environment. (Photo courtesy of The Aerospace Corporation.)

Future Work

The samples were returned to White Oak in early 1993, and detailed in-house analyses are in progress. Microscopy (electron or optical) will be the initial diagnostic tool. Other analytical methods such as x-ray photoelectron spectroscopy, Rutherford backscattering spectrometry, or atomic force microscopy will be employed as appropriate. Integrated scattering and diffuse reflectance measurement techniques are useful in characterizing the space mirror, which was intitially polished to a specular finish.

Summary

The White Oak Detachment submitted 27 samples for a materials science experiment aboard the space shuttle on mission STS-46. These samples are being evaluated as protective coating materials by determining their reactivity with the low-earth-orbit atmosphere in a space flight exposure. The space flight exposure has been successfully accomplished and the samples returned to earth for analyses. Preliminary results indicate that some of the materials reacted significantly with the space environment. The ultimate goal is to determine how materials deteriorate so they can be designed for longer survival in space.

Acknowledgments

122

References

1. Hansen, R. H., et al., "Effect of Atomic Oxygen on Polymers," *J. Polym. Sci.*, A3, 1965, pp. 2205-2214.
2. Leger, Lubert J. and Visentine, James T., "A Consideration of Atomic Oxygen Interactions with the Space Station," *J. Spacecraft*, 23, No.5, 1986, pp. 505-511.
3. Stuckey, Wayne K., "Lessons Learned from the Long Duration Exposure Facility," to be published in *Proc. 14th Aerospace Testing Seminar*, Mar 1993.

The Author

JOHN V. FOLTZ received a bachelor's degree in physics from Gettysburg College in 1961, and M.Sc. (1963) and Ph.D. (1966) degrees in physics from Pennsylvania State University. Since then he has worked at the Naval Surface Warfare Center, Dahlgren and White Oak, primarily on projects involving carbon-carbon and metal-matrix materials. He has experience in failure analysis, optics, and composites. He is currently in the Weapon Materials Division.

Ion-Beam Materials Analysis And Modification

David J. Land, Jack L. Price, Donald G. Simons, Noel A. Guardala, and Stanley H. Stern

An ion beam impinging on the surface of a solid material proves to be a powerful tool for the modification and nondestructive analysis of the surface layers of the material. By observing the energy spectrum of the scattered particle, or the products emitted from nuclear or atomic reactions, information concerning the composition and stoichiometry of the target can be deduced as a function of near-surface-layer thicknesses. Several systems which have been studied at White Oak are discussed in this article. As an example of ion-beam analysis, layers of quarter-wavelength zinc sulfide and aluminum oxide designed by the Naval Air Warfare Center, China Lake, California and proposed for use as mirror coatings in the advanced beam control system were characterized to confirm the layer thicknesses and desired stoichiometry. The aluminum oxide layer was found to have 50 percent bulk density, thereby indicating susceptibility to damage. As an application of ion-beam modification, recently initiated studies indicate the potential for bulk diamonds to be recrystallized following the ion implantation of energetic carbon.

Introduction

The development of increasingly sophisticated and advanced materials for both macroscopic and microscopic applications continues at a fast pace. For many applications, the use of a positively charged ion beam plays a significant role in two distinct ways. Ions having energies from several thousand to many million electron volts can be injected into the surface layers of materials to produce altered material properties or desired electronic characteristics. This implantation can be done in a very controlled way, since the behavior of these energetic ions in materials is fairly well understood. In addition, the use of energetic ion beams impinging on material surface layers serves as the basis of several very important analysis techniques. Through the observation of the energy spectrum of the scattered particles or of the products of atomic and/or nuclear reaction processes, information related to the stoichiometry and composition of these layers can be inferred.

In this article we describe some of our efforts related to materials modification and analysis through the use of ion-beam interactions. Initial work was done with the Division's 2.5-MeV Van de Graaff Accelerator, but more recently with the 3-Million-Volt Positive-Ion Tandem Accelerator, which replaced it in 1990. The Van de Graaff Accelerator was constructed 45 years ago and had been in continuous use since 1962. A brief characterization of the interaction of ion beams with materials is presented in the next section in order to illustrate its relation to ion-beam modification and analysis. A discussion of the

124

analysis techniques is also given. An account of several selected studies performed over the past few years follows in subsequent sections. A final section summarizes the overall thrust of this effort.

Interaction of Particles With Matter

When an energetic projectile impacts a target, it interacts in many different ways with the atoms of the target. The projectile can scatter from the atom as a whole; it can cause excitation of the target electrons as well as its own electrons in processes involving electron capture and loss; and the projectile nucleus can interact directly with the nucleus of the target atom, resulting in nuclear reactions. A specific process occurs only rarely. Certain of these processes that are particularly useful in material analysis are discussed below. In a general sense, however, one can identify two classes of processes that occur continuously and result in energy loss or slowing down of the projectile.

A projectile having a velocity much greater than the velocity of the target electrons loses most of its energy through the excitation (and ionization) of the electrons of the target atoms. The projectile travels through the target in nearly a straight line. As the projectile slows, a second interaction becomes effective: the projectile scatters from the target atom as a whole through some effective interatomic potential. Initially, at the higher velocities, it undergoes many small angle scatterings, causing small deviations from the straight-line trajectory and resulting in small energy losses. But at lower velocities many close collisions involving large-angle scatterings and large energy losses from target atoms take place, with the projectile finally coming to rest. The ability of the target to slow a projectile is termed stopping power. In most applications, the stopping power is separated between that caused by electronic excitation (termed electronic stopping) and that caused by the scattering from the target atom as a whole (termed nuclear stopping). The two interactions are usually combined additively. If the stopping power of a target material for a given projectile is known, then the range of the projectile can be calculated with the help of suitable transport theory.

Use of Ion Beams for Materials Modification

The ability to implant a given ion into a solid sample to a desired depth forms the basis for the use of ion beams for material modification. The introduction of foreign or dopant atoms can alter the local physical or chemical properties of the target. Thus, suitably chosen

projectiles giving rise to known desirable electronic or material characteristics are implanted in the target. A series of implants at suitably chosen energies can be employed to develop tailored implant profiles. It should be clear that the ability to implant ions at a desired depth in the target depends critically on knowledge of the stopping power. This field of research has been very active for many years and there has been significant experimental and theoretical effort in this area at White Oak.[1,2,3]

One of the earliest and still one of the most important applications of ion implantation is the formation within the target of one or more p- or n-type layers as appropriate for the purpose of fabricating an electronic device. The earliest transistors were developed through the use of diffusion techniques to introduce dopant atoms into the semiconductor. However, these techniques lack the precise control over the position of the dopant layer that is required by the microdevices of today. Ion implantation allows for the required precision.

Another general application of ion implantation concerns the alteration of the surface of a material to yield higher resistance to wear, scratching, or corrosion. To consider some specific illustrations,[4] the corrosion resistance of palladium-implanted titanium was shown to increase by three orders of magnitude over unimplanted samples. As another example, nitrogen-implanted alloy parts used as artificial hip joints promise improvement in lifetimes with increases up to a factor of four hundred. Also, the use of nitrogen atom implants has been shown to produce tools having a longer useful lifetime because of reduced wear. Steel surfaces implanted with titanium and carbon have yielded coefficients of friction about half those of unimplanted surfaces. These are but a few instances that illustrate the benefits of ion implantation for both commercial and potential military applications.

Use of Ion Beams for Materials Analysis

As discussed above, as a projectile traverses a target many different interactions with the constituents of the target, both atomic and nuclear, elastic and inelastic, take place. Among the atomic interactions, two specific kinds of events lead to highly useful material analysis techniques: backward-angle scattering and the production of atomic inner-shell vacancies. In addition, certain purely nuclear interactions are effective for analysis. An important advantage in employing a beam of heavy ions for analysis is that background radiation levels are usually low, in contrast to what would be obtained from an electron beam. In addition, the fact that high-velocity heavy ions move in

125

straight-line trajectories provides considerable simplification to the analysis.

While the majority of elastic scattering events at high projectile velocity produce no change in direction of the projectile, occasionally the projectile will approach the nucleus closely enough to lead to a violent scattering in the backward direction. These events form the basis of Rutherford backscattering spectrometry (RBS), for which protons or helium (He) nuclei are most frequently chosen for projectiles. This scattering is like a billiard ball collision: a scattered projectile has more energy if it scatters from a heavier target atom than from a lighter one. Thus, from the measurement of the energy spectrum of the scattered particles, knowledge of the composition and stoichiometry of the target material as a function of depth can be inferred. Since the violent collisions that give rise to scattering in the backward direction are rare, the observed event is most likely a single scattering, thus simplifying the analysis. The basic analysis tool is a computer code which produces a simulated spectrum based upon an assumed stoichiometry. By comparing the simulated and measured spectra and by adjusting the input parameters for the simulation, the stoichiometry of near-surface layers can be inferred. In constructing this spectrum, a knowledge of the stopping power of the target is paramount. The basic atomic interaction in this process is Rutherford scattering of the projectile nucleus from the target. This process is well understood and can be calculated quantitatively, although in some specific situations the potential from the atomic electrons can influence the process.

A second technique stems from the observation of the energy spectrum of the x-rays that are produced when the projectile knocks out an electron from an inner shell of a target atom. When such a vacancy is created, the atom can de-excite by emitting an electron or an x-ray. The energy of either is quite specific to the target atom in question. While both are observed, it is generally easier to obtain a clean x-ray spectrum. In order to determine stoichiometry quantitatively in this method, precise knowledge of the x-ray production rates is required. This rate is closely associated with the ion-induced, inner-shell vacancy-production cross section. We have also conducted intensive experimental and theoretical research in this area.[5,6,7] The combination of this technique, called particle-induced x-ray emission (PIXE), with RBS serves as a powerful method of determining the atomic species composition and depth distribution from the first 50 to 100 Angstroms to 1 or 2 micrometers. Note that both of these techniques are generally nondestructive in that the target sample remains at least materially unscathed and is available for further investigation.

Some Specific Studies

The investigations mentioned above deal with issues of a basic scientific nature. However, the primary goal of this overall program is to use available techniques in pursuit of solutions to Navy and other problems that arise in the materials community. In this section, we discuss several such studies involving thin-film layers used as sputter standards, mirror coatings, and superconductors.

Characterization of Sputter Standards

It was explained above that a projectile traversing a solid material at low energy (low velocity) undergoes many large-angle scatterings. If a solid is bombarded by projectiles at low energy, then these scattering events occur near the surface and there is the possibility that either the projectile itself or one of the recoiling target atoms will knock other target atoms out of the material. This process is termed sputtering. Surface erosion by sputtering is routinely used for a variety of materials analyses and preparation methods. For example, compositional depth profiles can be determined by surface analysis techniques such as Auger electron spectroscopy or by secondary ion mass spectroscopy in combination with progressive surface layer removal by sputtering. Thin surface layers are often prepared by using sputter deposition sources when techniques such as vacuum vapor deposition are not suitable. However, depth profiling may be strongly influenced by the atomic collisions that occur during the sputtering process. Effects such as preferential sputtering, projectile implantation, recoil implantation, and atomic mixing all contribute to uncertainties in analysis results. In surface layer preparation, ion-beam energies and currents must be selected to produce the desired etching or deposition rate needed. In all these applications, sputtering rates must be known for proper instrument calibration. Thus, there exists a need in the scientific community for standard reference materials (SRM) for sputter depth calibration.

This problem was addressed in a collaborative effort with the National Bureau of Standards (NBS) (now National Institute of Standards and Technology) in which NBS prepared the targets and performed sputtering analyses and White Oak characterized the samples using RBS. RBS was chosen as the analysis technique since it is essentially nondestructive for the type of targets studied and it requires no calibration standards. Multilayered structures were prepared by alternately sputter depositing *in situ* layers of approximately 60 nm each of chromium (Cr) and nickel (Ni) for a total of nine layers, with Cr forming the

outermost layer. Figure 1a shows the schematics of a four-layer Cr/Ni system and the layer components which contribute to an RBS spectrum. The RBS spectrum obtained with an incident 2.0-MeV 4He beam scattered at a laboratory angle of 165° from a nine-layer structure is shown in Figure 1b. Since the energy of the He scattered from the first layer of Cr is almost the same as the energy from the first layer of Ni (second film layer), and so forth, the nine-layer structure resolves itself into a five-peaked RBS spectrum. RBS measurements were made on three samples randomly selected from each of three prepared batches for a total of nine samples. These studies show that the standard deviation in the film thickness of like films within any given batch and from batch to batch is less than 3 percent. As a result of these RBS studies and companion Auger studies conducted at NBS,[8] the Cr/Ni structures were offered as an SRM by NBS to the scientific community.[9]

Space-Based Mirrors

A joint study with the Naval Air Warfare Center, China Lake, was undertaken to determine the effect of high-energy ion bombardment
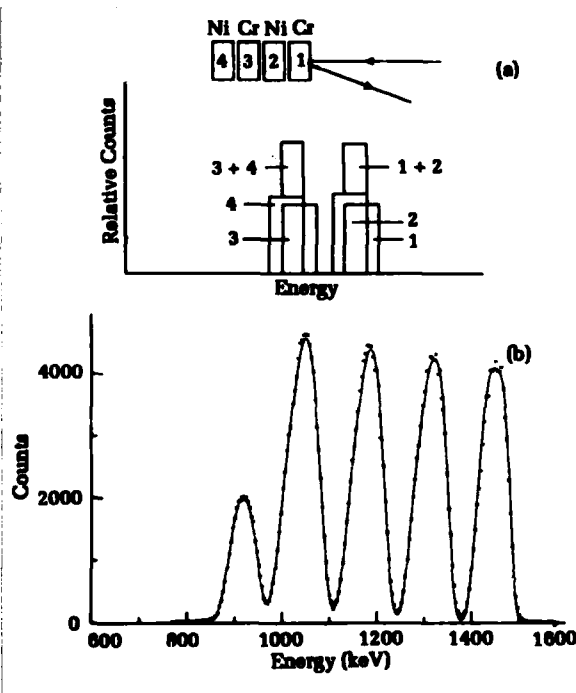

Figure 1. Schematics of a four-layer Cr/Ni structure and the components of the corresponding Rutherford backscatter spectrum (a). Typical Rutherford backscatter spectrum of 2 MeV ^{4}He scattered from a multilayered Cr/Ni structure. Xs indicate the measured spectrum, and the solid curve is that obtained from the computer simulation code (b).

on the reflectivity of multilayered, highly reflecting mirrors proposed for the advanced beam control system (ABCS). This high reflectivity is achieved, in part, by coating the mirror surface with paired quarter-wave layers. Each pair consists of a quarter-wave compound with a high index of refraction and a quarter-wave compound with a low index of refraction. Since the spacecraft containing the ABCS system is designed to be viable over a period of five years in a space environment, it is important to consider the effects on the mirror coatings which might result from radiation the space vehicle would encounter at the proposed operational altitudes. Ion-beam radiations and ion-beam materials analysis were conducted using the 2.5-MeV Van de Graaff Accelerator Facility. Mirror structures studied consisted of quarter-wave layers of zinc sulfide (ZnS) and aluminum oxide (Al_2O_3) on a substrate with layers of chromium oxide (Cr_2O_3), silver (Ag), and Cr on Ultra Low Expansion (ULE) glass. A schematic of the mirror structure along with the expected thicknesses is shown in Figure 2. These mirrors were irradiated with protons at energies and fluences that simulate the five-year space environment the mirror would be expected to encounter. Optical evaluation and response to exposure to high energy laser radiations on the proton-irradiated mirrors by China Lake show that the effects of the proton irradiation were negligible.[10] Figure 3 shows the RBS spectrum obtained by scattering 2-MeV ^{4}He at a lab angle of 150°. In the figure, the dots represent the experimental points, and the solid line is the result of a simulated spectrum in which the layer thickness, constituent elements, and their atomic concentrations are adjusted to give a "best fit" to the experimental spectrum. The energy contributions to the spectrum from the components of the target mirror are shown on the figure. The RBS spectra also show no effects from the space environment simulation. However, the measurements do show that the film density of the Al_2O_3 is about 50 percent of the bulk density. This lower value is not too surprising if the layer is amorphous, but could indicate that these mirrors might undergo surface damage should they
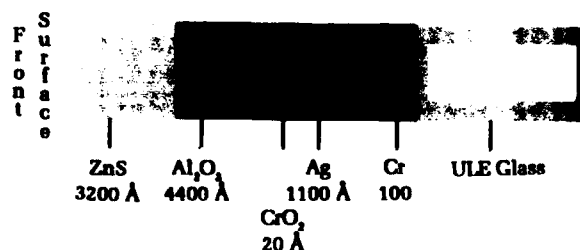

Figure 2. Space mirror structure for quarter-wave layers of ZnS and Al_2O_3 on reflecting substrate.
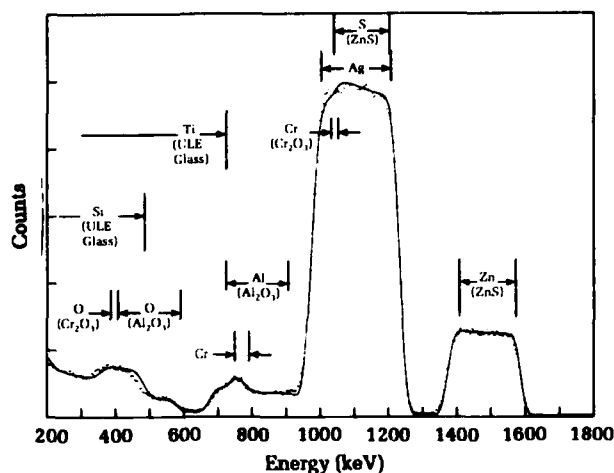
127

Figure 3. RBS spectrum of 2-MeV ^{4}He scattered from a multicoated ABCS mirror structure shown in Figure 2. The dots are the experimental points and the solid curve the simulated spectrum generated by varying the elemental concentrations and the layer thicknesses to obtain a "best fit" to the experimental values. The contributions of the various elements in the mirror target to the energy spectrum are shown.

encounter mechanically stressed conditions. In addition, it was determined that the Ag layer is nearly twice as thick as originally thought.

Diamond Recrystallization

Diamond and diamond-like films are one of the most important new areas of materials research to emerge in the last few decades. These films have great potential for use as hard, transparent surface coatings with excellent heat conductivity, making them ideal as protective coatings for various structures. In addition, the manufacture of substitutional doped n- or p-type semiconducting diamond or diamond films will make it possible to fabricate high-speed electronics with high thermal conductivity. The properties of these materials will revolutionize the thermal management of sophisticated electronics, especially in space applications where this need is a particular problem. In addition, the inherent hardness of carbon-based materials to radiation damage makes diamond electronics useful for space and nuclear environments.

One of the major obstacles for semiconductor application is the development of a process for substitutional doping of the diamond to obtain the proper electrical characteristics. This process must either fabricate this material without damaging the diamond or recrystallize the damaged diamond through an appropriate annealing technique. Fundamental studies

have been initiated to study this recrystallization problem.

Natural type II-A diamond, a very rare type which is practically free of nitrogen and is transparent to ultraviolet above 225 nm,[11] is implanted with carbon (introducing no impurities) at a high energy to form an amorphous carbon layer deep under the diamond surface. Optical transmission scans as a function of particle fluence were measured. The results indicate that the transmission is increasingly reduced with increasing fluence throughout the entire ultraviolet-visible-infrared optical region.
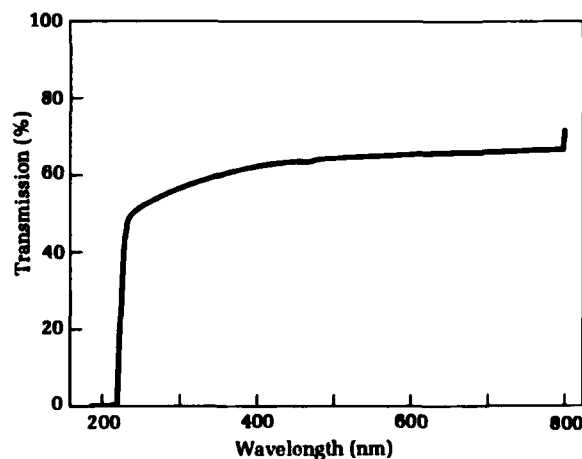
Figure 4a. Typical optical transmission scan for an unimplanted natural type II-A diamond chip, showing near uniform transmission through the UV-visible-IR region. The sharp cutoff at 225 nm is characteristic of type II-A natural diamond.

Figure 4b. Optical transmission as a function of wavelength for a carbon-ion implanted diamond (fluence of 1×10^{16} atoms/cm^2) before and after thermal annealing at 1000°C for 30 minutes. Note the restoration of the transmission at longer wavelengths with virtually no restoration for the shorter wavelengths.

128

Figure 4a shows a typical scan for an unimplanted diamond chip. The characteristic cut-off at 225 nm is seen clearly. Thermal annealing of the samples at constant temperature does not restore the diamo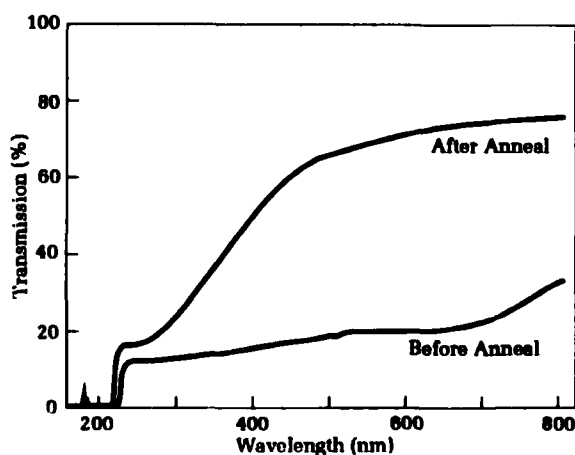nd to its original transmission characteristics, especially in the shorter wavelengths, and hence the diamond is not properly recrystallized. However, in Figure 4b, it is obvious that there is some restoration at the longer optical wavelengths. A program is currently under way to pursue this problem further with other annealing methods such as pulsed-laser or energetic electrons.

Thin-Film, High-Temperature Superconductors

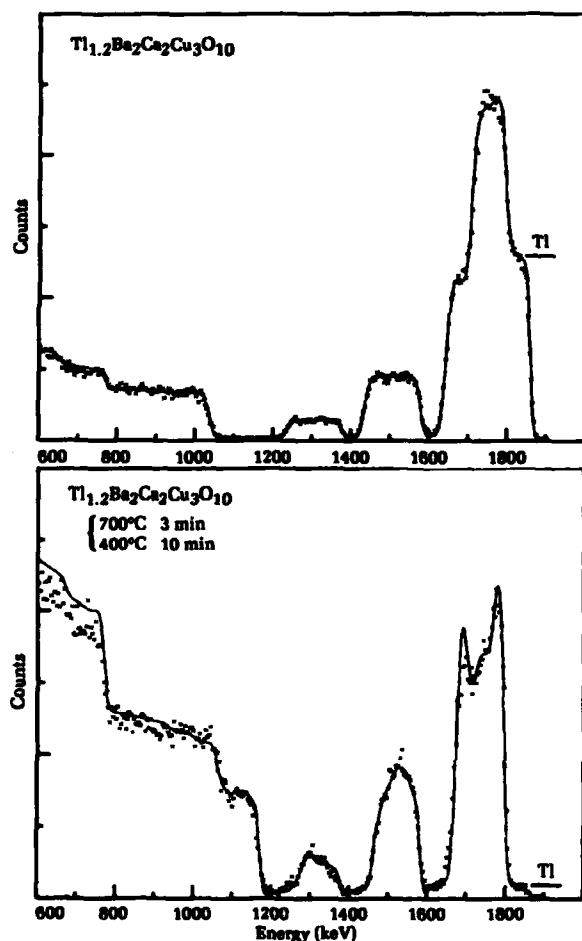In a collaborative study with the U.S. Army Research Laboratory in Adelphi, Maryland, the fabrication (consisting of deposition and annealing) of thin-film high T_c superconductors was studied. One series of studies concentrated on the process of utilizing an eximer laser to ablate bulk thallium-barium-calcium-copper-oxide ($Tl_{1.2}Ba_2Ca_2Cu_3O_{10}$) superconducting material onto a silicon substrate and the subsequent thermal annealing to activate the film. Results of the RBS and PIXE analysis indicated surprising thermal effects. Figure 5 shows two RBS spectra obtained for an "as deposited" and a "thermally annealed" sample of a $Tl_{1.2}Ba_2Ca_2Cu_3O_{10}$ film. It can be seen that, while the "as deposited" film is highly uniform, the spectrum for the annealed film indicates a substantial loss of thallium (highly undesirable for safety and electronic concerns) and a significant segregation of the remaining barium, copper, and calcium. A study was then initiated to examine the possibility of annealing the film on the substrate while deposition was taking place. The substrates were heated and the films examined to determine the relationship between substrate temperature and film stoichiometry. Figure 6 presents the results of this investigation, indicating that the optimum substrate temperature for laser ablation deposition to obtain stoichiometric conditions from a thallium-rich bulk target is near 450°C. While this material is inherently unstable and therefore not amenable to this type of processing, additional work on yttrium-barium-copper-oxide (YBa_2Cu_3O) and samarium-barium-copper-oxide ($SmBa_2Cu_3O$) indicated more positive results and helped establish laser ablation as a viable technique for stoichiometric deposition of high-T_c superconductor films.[12]

Figure 5. RBS spectra for an "as deposited" (top) and a "thermally annealed" (bottom) sample of a $Tl_{1.2}Ba_2Ca_2Cu_3O_{10}$ superconducting film. The "as deposited" film is highly uniform, while the annealed film is not uniform and shows a substantial loss of thallium, as indicated by the sharply reduced level in the spectrum.
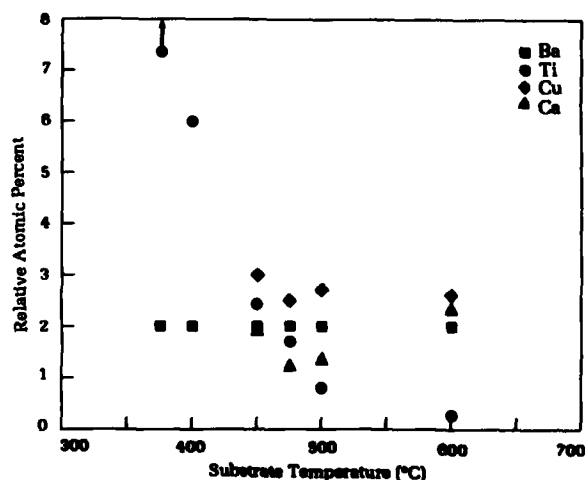
Figure 6. *In situ* substrate temperature dependence of the stoichiometry of $Tl_2Ba_2Cu_3Ca_2O_{10}$ thin superconducting film fabricated from a Tl rich bulk target. Optimum temperature is 450°C. All data are normalized to the barium atomic percent.

Summary

The foregoing discussion gives an overview of the use of ion-beam materials analysis and modification and presents several examples of their use for materials problems of potential interest for naval applications. It is hoped that these examples are illustrative of the broad capability of these techniques available at White Oak and their potential power for future investigations. Perhaps the most exciting studies today are those involving diamond and diamond-like films, because of the highly desirable and promising characteristics of this material. However, detailed results concerning the composition and stoichiometry of the superconducting candidate materials and the Cr/Ni SRM typify the usefulness of ion beam techniques.

Acknowledgments

References

1. Land, D. J. and Brennan, J. G., "Electronic Stopping Powers of Low-Velocity Ions: Ions C-Xe, Targets H-Xe," *Atomic Data and Nuclear Data Tables*, Vol. 23, No. 3, 1979.

2. Land, D. J., et al., "Z_2 and Energy Dependence of Range Distributions and Stopping Powers for Nitrogen Ions in Solids," *Physical Review A*, Vol. 22, 1980, pp. 68-75.

3. Price, J. L., et al., "Stopping Powers for 400 to 2400 keV N Ions in He and Ar," *Nuclear Instruments and Methods*, Vol. B56/57, 1991, pp. 348-350.

4. Picraux, S. T., "Ion Implantation Metallurgy," *Physics Today*, Vol. 37, 1984, pp. 38-44.

5. Simons, D. G., et al., "K-Shell Ionization Cross Sections for Targets from Z=21 to Z=47 Induced by He Ions and by Protons in the Energy Range 0.2-2.5 MeV/u," *Physical Review A*, Vol. 39, 1989, pp. 3884-3889.

6. Simons, D. G., et al., "Impact-Parameter Dependence of Inner-Shell Ionization Cross Sections Induced by Protons and He Ions in the Energy Range 0.4-2.0 MeV/u," *Physical Review A*, Vol. 42, 1990, pp. 1324-1330.

7. Land, D. J., "Time-Dependent Distortion in Calculations of K-Shell Ionization for Incident Protons and Helium and Lithium Ions," *Physical Review A*, Vol. 44, 1991, pp. 274-290.

8. Simons, D. G., et al., "Rutherford Backscatter Analysis of Multi-Layered Cr-Ni Structures," *Nuclear Instruments and Methods*, Vol. 218, 1983, pp. 585-587.

9. NBS Certificate, SRM 2135, "Ni/Cr Thin-Film Depth Profile Standard," 1985.

10. Decker, D. L. and Fogdall, L. B., "Simulated Natural Space Radiation: Testing of Multilayer Dielectric Mirrors for 2.7 Micron Applications," presentation at the *High Power Laser Optical Components Topical Meeting*, Boulder, Colorado, 21-22 October 1991.

11. Bachmann, P. K. and Messier, R., "Emerging Technology of Diamond Thin Films," *Chemical and Engineering News*, May 15, 1989.

12. Neifeld, R. A., et al., "Systematics of Thin Films Formed by Eximer Laser Ablation of $SmBa_2Cu_3O_7$," *Applied Physics Letters*, Vol. 53, 1988, pp. 703-706.

The Authors

DAVID J. LAND received a B. S. degree from Boston College in 1959 and a Ph.D. degree in 1966 from Brown University, both in physics. At White Oak since 1966, he initially performed research in the fields of elementary particle physics and quantum mechanical scattering theory. Since 1973 he has worked as a theoretical physicist with the Ion-Beam Materials Physics Group. Other programs with which he has been associated include REVMAT (Reentry Vehicle Materials), HEL (High-Energy Laser), and IRST (Infrared Search and Tracking). Currently, he is performing basic and applied research in the areas of atomic collision physics and ion-beam materials modification and analysis, and working in support of programs associated with the Division's new 3-MV Positive-Ion Tandem Accelerator. He is a member of the American Physical Society and the Optical Society of America and serves as referee for several professional journals.

JACK L. PRICE attended Norwich University where, in 1976, he graduated *cum laude* with B.S. degrees in mathematics and physics. In 1978, he received an M.S. degree from the University of Kansas in space-plasma physics. After working as a radiation protection specialist for the state of Kansas, he returned to school and earned a Ph.D. from North Texas State University in 1986 with a specialty in accelerator-based atomic collision physics. He was then appointed as an Office of Naval Technology postdoctoral research fellow at the Naval Surface Warfare Center and collaborated with the Ion-Beam Materials Physics Group in investigations of charged-particle induced ionization and the application of heavy ion beams to materials modification and analysis. In June 1987, he became a permanent full-time research physicist at White Oak, and he is the facility manager for the new Positive-Ion Accelerator Facility. In 1990 he received the Young Professional of the Year Award. He is an adjunct faculty member at Montgomery College in Germantown, Maryland.

130

DONALD G. SIMONS received his B.S. degree in 1951, M.S. degree in 1954, and Ph.D. degree in nuclear physics in 1964, all from the University of Maryland. He started working at White Oak in 1951 as a research physicist. Dr. Simons was instrumental in the procurement of both the 2.5-MV Van de Graaff Accelerator and the current 3-MV Tandem Positive-Ion Accelerator. Before retiring from White Oak in 1987, he was the group leader of the Atomic Collisions Physics Research Group and played an important role in directing the research efforts of that group to ion-beam materials analysis and modification. Dr. Simons received the Navy's Meritorious Civilian Service award in 1985. He is presently at White Oak on an IPA agreement with The Catholic University of America, where he is employed as a research professor.

NOEL A. GUARDALA is a research chemist in the Radiation Science and Technology Branch at White Oak. His main research areas are the experimental and theoretical study of ion-atom collisions, ion-beam analysis of advanced novel materials through the use of both nuclear and atomic excitation techniques, ion-beam modifications of materials, measuring the stopping powers of projectiles, and electron emission studies using x-rays produced at the National Synchrotron Light Source, located at Brookhaven National Laboratory. Dr. Guardala received his B.S. in chemistry from Brooklyn College in 1974 and his Ph.D. from the City University of New York in nuclear chemistry in 1989. He was a research associate in the Physics Department of Stanford University and, during the same time period, was a guest scientist at Lawrence Berkeley Laboratory. Prior to his present position, he was a visiting scholar in the Center for Materials Research at Stanford University.

STANLEY H. STERN received his undergraduate education at Rutgers University, where he received his B.S. degree with High Honors in 1972. He was granted his M.S. in physics in 1975 and his Ph.D. in physics in 1982 at New York University. Following a one-year position as an associate research scientist at New York University, he joined White Oak in 1983 and entered the Charged Particle Beam Program to perform basic and applied research concerning the physics of intense high-energy electron beams and their use as directed-energy weapon systems. More recently, he became a member of the Ion-Beam Materials Physics Group and performed basic and applied research at the new Positive-Ion Accelerator Facility in programs involving the stopping power of matter and characteristics of phosphor materials for thermoluminescent dosimeters. In January 1992, he took a position involving the design and testing of health physics instrumentation at the Food and Drug Administration.

Microbiologically Influenced Corrosion Of Copper Alloys

J. M. Jones-Meehan, B. J. Little, P. A. Wagner and R. I. Ray

Copper (Cu) and nickel (Ni) alloys such as CDA 706 and Monel 400 are used in military and commercial applications because of good corrosion resistance combined with mechanical workability, excellent electrical and thermal conductivity, and resistance to macrofouling. This article describes case histories of microbiologically influenced corrosion (MIC) in a CDA 706 seawater piping system after approximately one year of seawater service and of Monel 400 tubing after exposure to estuarine water for six months. Pits developed under surface deposits of mixed bacterial communities that contained 10^4-10^5 sulfate-reducing bacteria (SRB). The observed corrosion was attributed to a combination of differential aeration cells; c large cathode, small anode surface area; concentration of chlorides; development of acidity within the pits; and the specific reactions of the base metals with sulfides produced by the SRB. Chlorine and sulfur appear to have reacted selectively with the iron and nickel in the alloys. Nickel had been selectively removed from the pitted areas, leaving a copper-rich, spongy pit interior. The environmental scanning electron microscope (ESEM) offered a nondestructive method for imaging wet biofilms on surfaces taken directly from liquid medium without any sample preparation. Anaerobic, copper-tolerant bacterium (isolated from a Cu-containing marine coating) produced large amounts of extracellular polymer that had metal-binding ability. Biofilms of this microbe resulted in a fivefold increase in the corrosion rate of Cu metal. The corrosion appeared to be uniform with no localized attack. The data obtained from these studies provides a more accurate image of biofilms, including the amount of polymer-bound metals in biofilms and MIC on copper-containing surfaces.

Introduction

Copper and nickel alloys have a long history of successful application in the marine environment. Copper alloys are frequently used for seawater piping systems and heat exchangers due to good corrosion resistance combined with mechanical workability, excellent electrical and thermal conductivity, ease of soldering and brazing, and a resistance to macrofouling. Alloying nickel and iron into copper alters the corrosion product and improves corrosion resistance. CDA 706 (an alloy containing 88.5% copper, 10% nickel, and 1.5% iron) has been shown to be the most corrosion resistant copper-based alloy for seawater service.[1] Nickel alloys such as Monel 400 (containing 66.5% nickel and 31.5% copper and 1.25% iron) have been used extensively in highly aerated, fast-moving seawater environments such as evaporators, heat exchanger pumps and valves, diffusers for steam nozzles in steam ejectors, and turbine

132

blades.[2] A passive film similar in structure to that observed on pure nickel is formed on Ni-Cu alloys having more than 30% Ni, while alloys containing less than this amount of Ni behave like copper.[3]

Copper and nickel alloys are susceptible to several types of localized corrosion. Premature corrosion failures in predominantly copper alloys have been attributed to erosion corrosion caused by the removal or breakdown of the protective film by mechanical forces, such as local turbulence or impingement[1,4,5] and under-deposit corrosion.[6] In high-velocity seawater, Monel alloys are superior to predominantly copper alloys because the protective surface film remains intact under highly turbulent and erosive conditions.[7] Monel is susceptible to pitting and crevice corrosion attack under stagnant conditions.[8-10] Gouda et al.[11] described premature failures of Monel 400 cooler tubes in a refinery utilizing Arabian Gulf seawater. These failures were due to SRB under-deposit attack resulting in intergranular corrosion (selective leaching of nickel and iron), leaving copper-rich cavities. Gouda et al.[12] described the SRB attack of UNS N04400 (Monel 400) both in field tests in Arabian Gulf seawater and in laboratory tests. The SRB attack initiated beneath a black sulfide-rich deposit overlaid by a green chloride-rich deposit and a beige-colored calcareous scale. Both field and laboratory testing showed that the extent of the SRB attack increased with increasing exposure times (from 50 to 70 days) and absence of chlorination.[12] An SRB biofilm on Monel heat exchangers under low-flow chlorinated seawater conditions resulted in complete perforation of several tubes (thickness 2 mm) within three to eight months of service.[12]

Differential aeration,[13] selective leaching,[14] under-deposit corrosion,[15] and cathodic depolarization[16] have been reported as mechanisms for MIC of copper and nickel alloys. Pope[17] has proposed that the following microbial products accelerate localized attack: CO_2, H_2S, NH_3, organic and inorganic acids, metabolites that act as depolarizers, and sulfur compounds such as mercaptans, sulfides, and disulfides. Geesey et al.[18] have demonstrated that bacterial exopolymers can play a role in the corrosion of copper alloys. Mechanisms of metal deterioration based on metal-binding abilities of bacterial exopolymers have been reported by Bremer and Geesey[19] and Ford et al.[20] These include: (1) a reduction of free ion concentration at the metal surface that promotes further ionization to maintain equilibrium, (2) differential complexation by different exopolymers causing the formation of ion concentration cells, and (3) metals bound from solution reacting with surface ions.

This article describes collaboration between the biotechnology laboratory at the Naval Surface Warfare Center Dahlgren Division's White Oak Detachment and the Naval Research Laboratory Detachment (Stennis Space Center, Mississippi) on: (1) case studies of biocorrosion in a CDA 706 seawater piping system after a service life of approximately one year and in Monel 400 tubing after exposure to estuarine water for six months, (2) laboratory studies of copper-containing alloys exposed to anaerobic bacteria including SRB, and (3) the electrochemical measurements and surface analyses of copper coupons exposed to an aerobic, marine bacterium.

Materials And Methods

Case Histories

A heavily pitted section of CDA 706 piping (15 cm length x 2.5 cm inside diameter (I.D.), wall thickness 3.6 mm) was removed from the seawater piping system of a surface ship after approximately one year of seawater service. During operation of the ship, the seawater piping system had been maintained with continuously flowing seawater (1.6 m/sec) at a maximum temperature of 30°C. During the 12 to 18 months of the shipbuilding process, the system had been operated with estuarine water from the Gulf of Mexico with intermittent flow and long periods of stagnation. At the time of removal, the pitted piping was subsectioned for SRB enumeration in the biofilm and for surface chemical analyses. Subsections were placed in refrigerated 4 percent glutaraldehyde in filtered seawater. The fixed samples were taken through a series of distilled water washes, dehydrated through acetone and xylene washes, and air-dried.[20] Surface chemical analyses were performed with a KEVEX-7000 energy dispersive X-ray spectrometer (EDS) coupled to an AMRAY 1000A scanning electron microscope (SEM). Subsections were sputter-coated with gold for scanning electron micrographs.

Monel 400 tubes (6.0 meters x 20 mm I.D., wall thickness 1.9 mm) were maintained with intermittently flowing (1.5 m/sec) and with stagnant Gulf of Mexico water for approximately six months. After one month of continuous flow, the water in the tube sections was allowed to stagnate for one week, after which the flow was resumed. At the conclusion of the test period, tubes were cross sectioned, visually inspected, scraped for SRB enumeration, and prepared for SEM/EDS analyses as previously described.

133

Water Analyses

Water collected from the seawater piping system and from the Gulf of Mexico was analyzed for salinity,[21] dissolved oxygen,[21] pH, chlorinity,[22] total suspended solids,[22] total organic carbon,[22] and total dissolved sulfate.[22] Dissolved sulfides were measured using a modification of the method described by Strickland and Parsons[23] that uses a 10 cm cell to increase sensitivity (detection limit is 6.5 ppb). Numbers of SRB in the flow-through water and in the biofilm were estimated by the most probable number method, using a medium containing lactate as the electron donor and carbon source made to the salinity of the seawater.[24]

MIC by SRB in Laboratory Studies

The isolation, maintenance, and characterization of the mixed communities consisting of anaerobic (SRB) and facultatively anaerobic (non-sulfate reducers) microbes have been described previously.[25] Table 1 describes the original isolation of the seven mixed communities containing SRB and the hydrogenase test results for the SRB. Cu-containing alloys were exposed in the laboratory to anaerobic, mixed communities containing SRB. At the end of the exposure, surface topography and chemistry were documented using an Electroscan Model E-30 ESEM and a Tracor Northern Model 5502 EDS. Coupons were removed from the culture medium, taken through a series of salt water/distilled water washes, and examined directly from distilled water.

Aerobic, Bacterial Corrosion in Laboratory Studies

Wagner et al.[26] described aerobic corrosion experiments involving a gram negative, marine bacterium (tentatively identified as *Oceanospirillum* isolated from a cuprous-oxide-painted surface exposed to subsurface ocean water for two months. Electrochemical corrosion experiments involved 99 percent Cu, round disc electrodes (1 cm^2) placed in EG&G PARC corrosion cells. Baseline open-circuit potential (E_{corr}) and polarization resistance (R_p) measurements were obtained with the Cu electrodes in sterile, aerated artificial seawater; nutrients were then added, and E_{corr} and R_p were measured again; finally, the *Oceanospirillum* was added and the measurements were repeated. Bulk pH values were recorded when R_p measurements were taken. R_p data were analyzed to provide anodic and cathodic Tafel slopes and corrosion rates.

The metal-binding capacity of the bacterial exopolymers was evaluated by: (1) exposing Cu discs to the culture medium with and without the Cu-tolerant bacterium for 20 days and then measuring the amount of Cu in the two solutions with a Perkin-Elmer Model 3030 atomic absorption spectrometer coupled to an HGA 500 furnace, and (2) placing glass slides and a corroding metal disc (99% Cu, 316 stainless steel or 1018 carbon steel) in flasks which were inoculated with the Cu-tolerant bacterium. The metal bound by the biofilm on the glass slides was qualitatively measured with ESEM/EDS.

Table 1. Hydrogenase Activity in the Mixed, Microbial Populations Containing Sulfate-Reducing Bacteria (SRB)

Culture*	Isolated Originally On: Material + Topcoat(s)	Hydrogenase Activity** 2-1/2 h	4 h	24 h
I	4140 Steel + 5 Step Iron Phosphate	0	+1	+2
II	4140 Steel + 5 Step Iron Phosphate + Epoxy	+1	+1	+2
III	4140 Steel + Zinc Plate	+2	+2	+2
IV	4140 Steel + IVD-Aluminum + Nylon	+2	+2	+2
V	4140 Steel + 5 Step Iron Phosphate + Nylon	0	0	0
VI	Carbon Steel + Proprietary Primer and Topcoats	0	0	0
VII	Aluminum Alloy + Epoxy + Polyurethane	0	0	+2

* Cultures I-V were isolated from a constant immersion flume tank at the Dahlgren Division's Ft. Lauderdale, (Florida) Detachment. Culture VI was isolated from the seawater piping system of a surface ship at Long Beach Naval Station, Long Beach, California. SRB in cultures I-VI require NaCl for growth (halophilic). Culture VII was isolated from moisture trapped under the cargo ramp of a C-130 transport plane at NADEP, Cherry Point, North Carlina. SRB in culture VII are facultative halophiles (do not need NaCl for growth but can grow in seawater concentrations of NaCl).

** Activity of the hydrogenase enzyme is measured with a Caproco Hydrogenase Test Kit. The rating system is from 0 to 3. A negative reaction is rated as 0, weak reaction is +1 (0 to 0.5 nmol of hydrogen uptake/min), moderate reaction is +2 (0.05 to 5 nmol of hydrogen uptake/min) and a strong reaction is +3 (5 to 5,000 nmol of hydrogen uptake/min)

Results

Case Histories

The surface of the CDA 706 pipe was heavily pitted (Figures 1 and 2). Surface deposits were thick and multilayered, varying in color with depth. Outermost layers were dark green to reddish brown. Bright bluish-green deposits were found on the surface in unpitted areas. Pit interiors were black, and pit depths were typically 1.7 mm to 2.0 mm. A cross section through the pitted areas exposed subsurface bacteria within the thin, black deposit and a spongy subsurface (Figure 3). Scrapings from the area within the pits indicated the presence of 1×10^5 SRB cm^{-2}, compared to 1×10^1 SRB cm^{-2} detected within the surface film on the unpitted areas. The EDS spectrum of the base metal showing the relative concentrations of iron, nickel, and copper is shown in Figure 4a. An EDS spectrum taken in the bacterial layer showed concentrations of aluminum, silicon, phosphorus, sulfur, calcium, and chlorine in addition to elevated amounts of iron and nickel (Figure 4b,c). The EDS spectrum of the spongy layer under the bacteria indicated an accumulation of phosphorus and a depletion of nickel (Figure 4d).

Water removed from the failed pipe section was typical of seawater (salinity, 35 0/00; dissolved oxygen, 6.4 mg L^{-1}; pH, 8.2; total organic carbon, 1.8 mg L^{-1}; total suspended solids, 3.0 mg L^{-1}; and total dissolved sulfate, 2.4 g L^{-1}). Dissolved sulfides were below the detection limits. SRB concentration in the bulk seawater was typically 1×10^1-10^2 cc^{-1}.

Figure 2. SEM micrograph of a pit in CDA 706 piping after one year in seawater service.
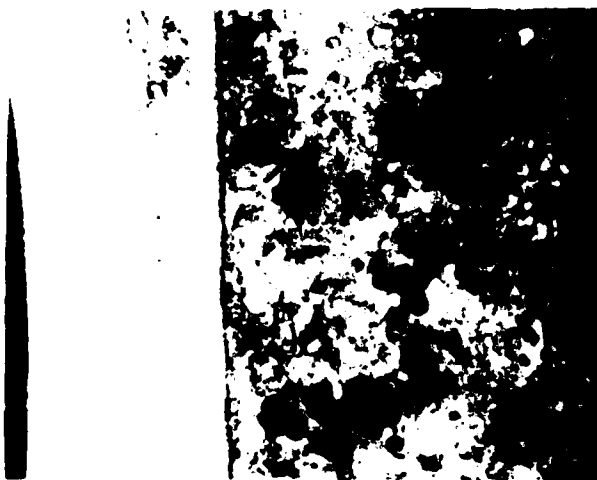

Figure 1. Cross sections of CDA 706 piping after one year in seawater service shows two examples of thick surface deposits and pitting.
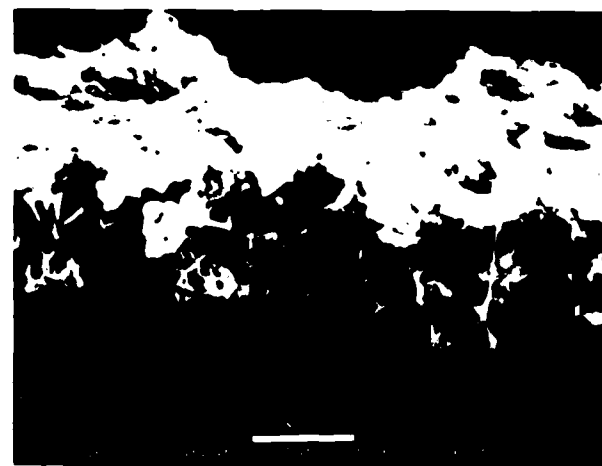

Figure 3. SEM micrograph of biofilm (bacteria, microbial metabolites, microbial polymers, and inorganic ion deposits) in cross section of CDA 706 pitted area.
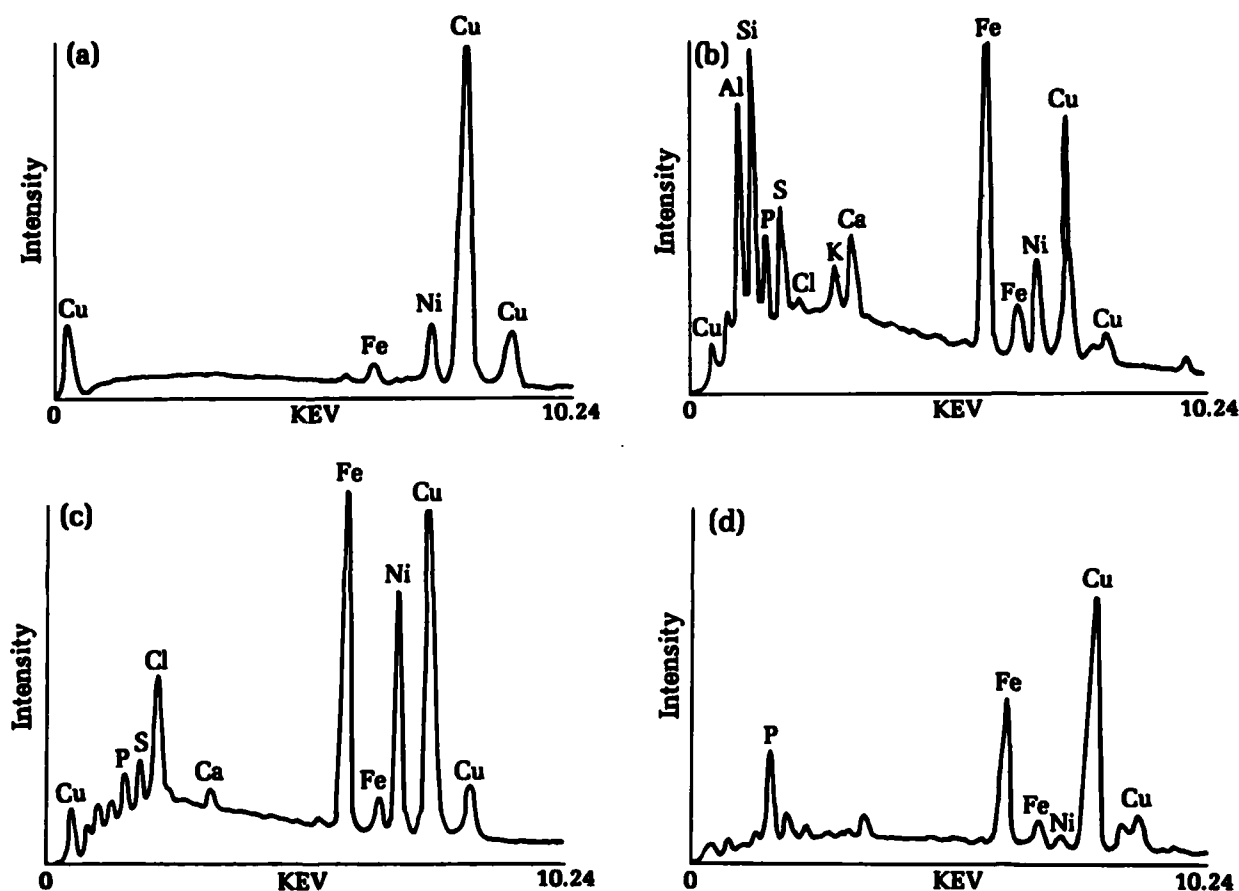
135

Figure 4. (a) EDS spectrum of clean CDA 706 before exposure; (b) EDS spectrum of pitted region of CDA 706 showing an accumulation of aluminum, silicon, phosphorus, sulfur, calcium, and elevated amounts of iron and nickel; (c) EDS spectrum of pitted region of CDA 706 showing the accumulation of chlorine and elevated amounts of nickel and iron; (d) EDS spectrum of the spongy material beneath bacteria showing an accumulation of phosphorus, an enrichment of iron, and a depletion of nickel in the base of the pit.

Visual examination of the Monel tubes indicated a multilayered scale and localized attack. The scales were characterized by surface blisters (Figure 5 a,c) that contained corrosion products and bacteria. The concentration of SRB within these surface deposits was typically 1×10^4 cm^{-2}. Removal of the scale exposed localized, irregular-shaped pits that averaged 0.4 mm wide x 1.0 mm deep (Figure 5 b,d). The EDS spectrum corresponding to unexposed Monel 400 indicated the relative amounts of copper, nickel, iron, and manganese in the alloy (Figure 6a). The EDS spectrum from the black layer within the pits shows an accumulation of sulfur and chlorine along with increased amounts of iron compared to the base alloy (Figure 6b). Physical removal of the biofilm from the pit exposed a copper-rich region that was depleted in nickel and iron (Figure 6c).

During the test period, the Gulf of Mexico estuarine water temperature varied from 9°C to 30°C; pH varied from 7.4 to 8.2; and chlorinity varied from 4.3 to 20.0 0/00 Cl⁻, which indicated a range of salinity from 7.7 to 37. Total

suspended solids ranged from 10 to 65 mg L^{-1}. Dissolved oxygen varied from 4.3 mg L^{-1} during the summer to 10.8 mg L^{-1} during the winter months. Dissolved sulfides were below the detection limits. The mean concentration for sulfates (SO_4^{-2}) was 2.5 gm L^{-1}. SRB concentration in the estuarine water was 1×10^2 to 10^3 cc^{-1}.

ESEM and EDAX Analyses of Wet Biofilms Established on Copper and Brass

All copper-containing metals exposed to anaerobic communities containing SRB were covered with black, sulfur-rich deposits (Figure 7 b,d), while samples exposed to growth medium only (no SRB) showed a thin, black, tenacious layer on 99 Cu and no black deposits on brass (Figure 7 a,c). ESEM micrographs of copper foils (Figure 8) and brass foils (Figure 9) showed heavy microbial colonization of the surfaces with a variety of cell morphologies. The extracellular microbial polymers (polysaccharides) produced by bacteria are a strong
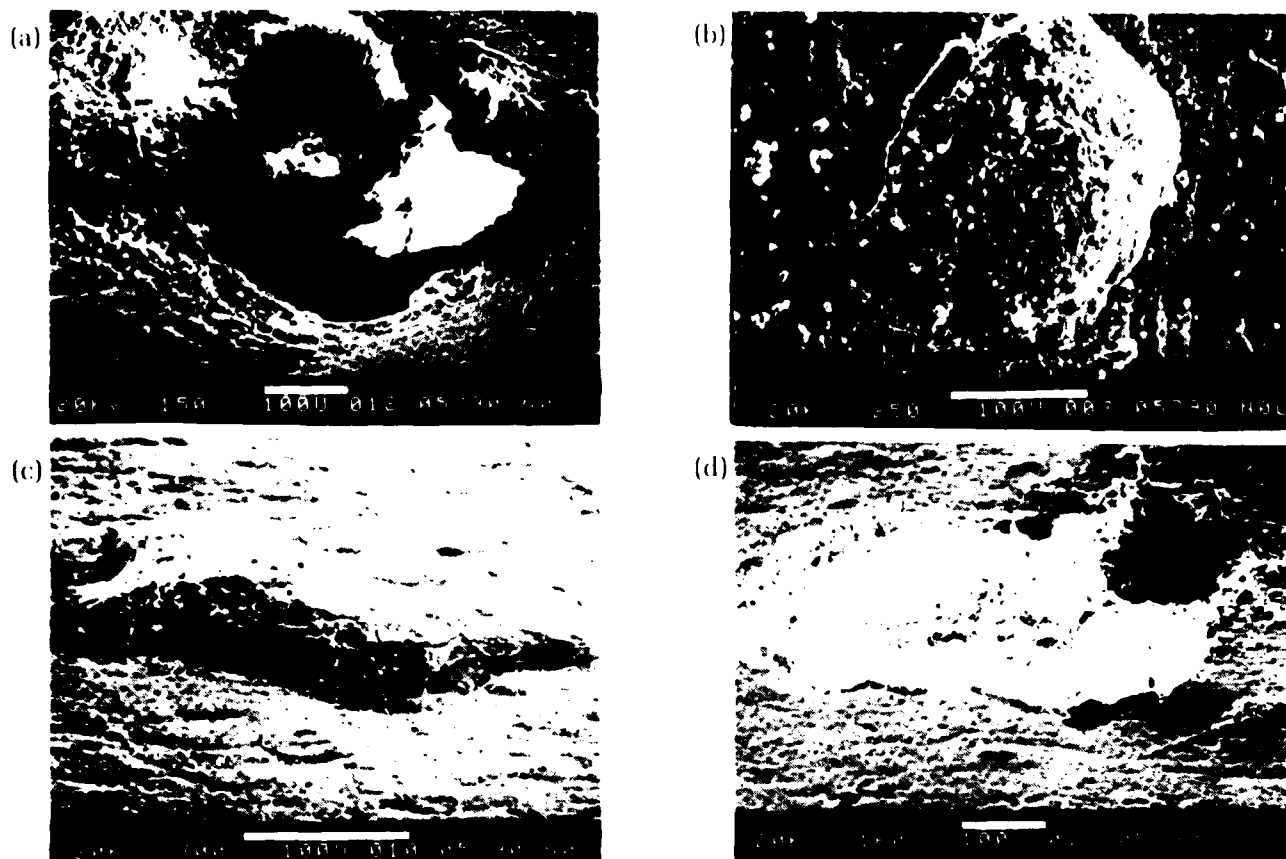
136

Figure 5. Blisters on the surface of Monel 400 tubing after six-month exposure to estuarine water (a,c); pits in Monel 400 tubing after six-month exposure to estuarine water. (b,d)
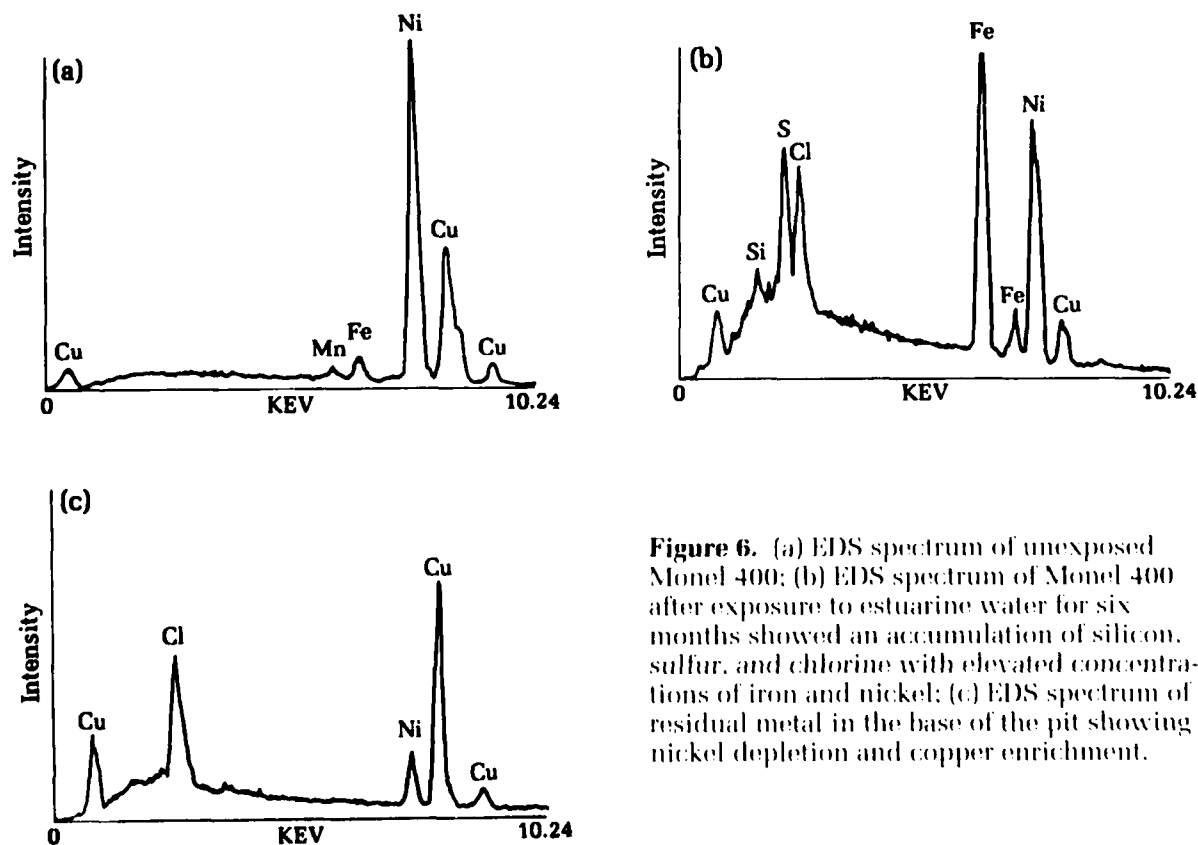

Figure 6. (a) EDS spectrum of unexposed Monel 400; (b) EDS spectrum of Monel 400 after exposure to estuarine water for six months showed an accumulation of silicon, sulfur, and chlorine with elevated concentrations of iron and nickel; (c) EDS spectrum of residual metal in the base of the pit showing nickel depletion and copper enrichment.

137

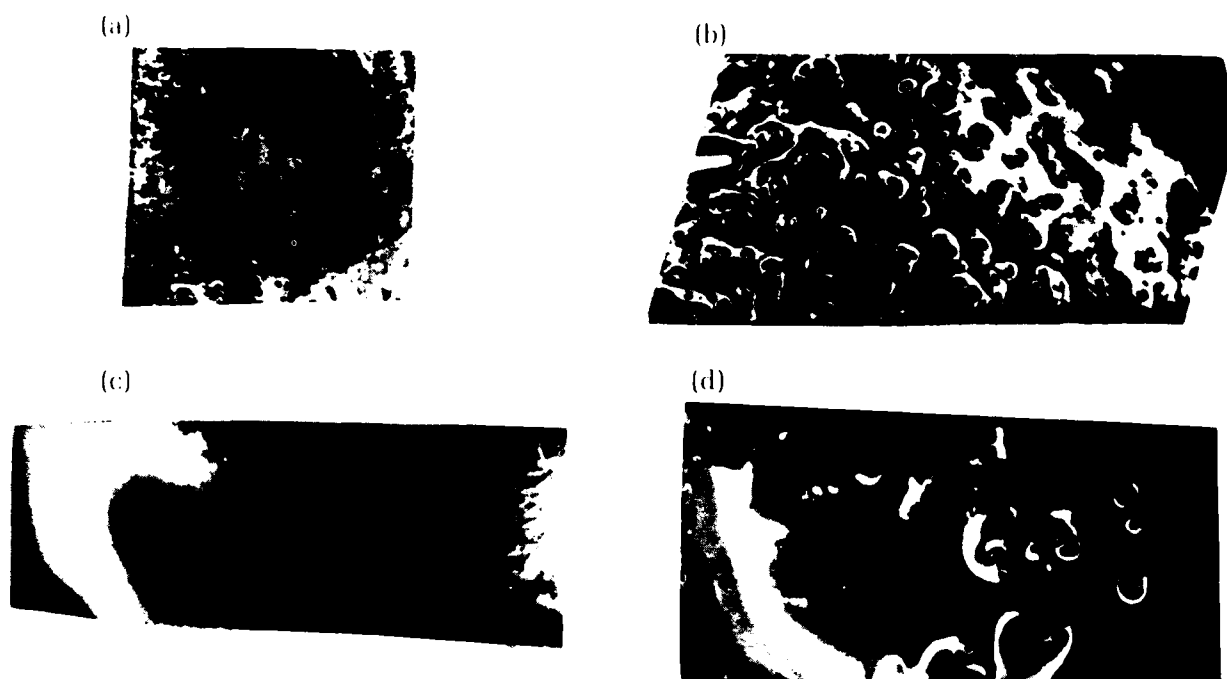**Figure 7.** (a) Surface of 99 Cu after four-month exposure to growth medium (-NaCl) with no SRB added; (b) surface of 99 Cu after four-month incubation with culture III; (c) surface of brass foil after four-month exposure to growth medium (-NaCl) with no SRB added; (d) surface of brass foil after four-month incubation with culture I.
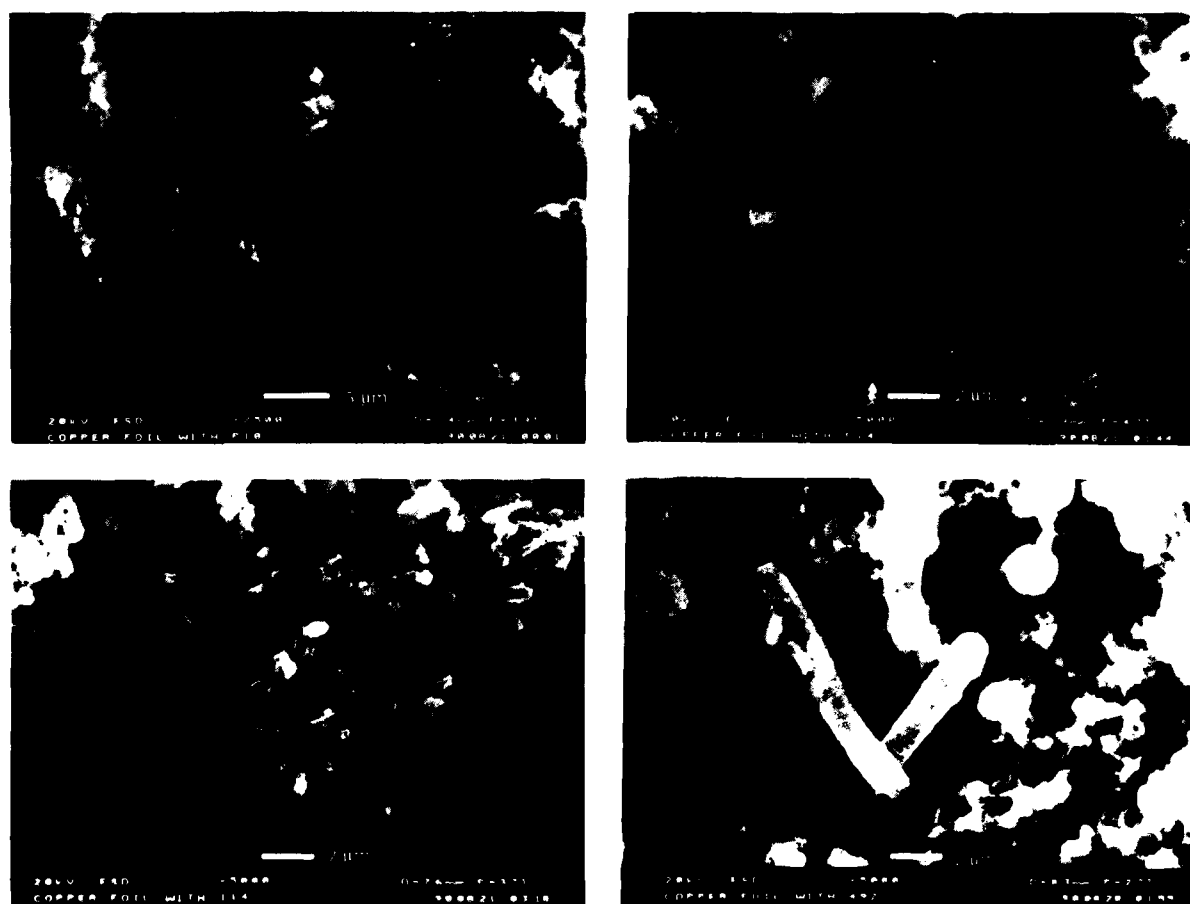

Figure 8. ESEM micrographs of four different mixed microbial communities containing SRB on copper foils.

138

adhesive for the bacteria, and this web-like fiber matrix (note patchiness and varied thicknesses of the biofilm) can easily be seen in the wet biofilms shown in Figures 8 and 9.

The thickness of the surface deposits on 99 Cu in the presence of SRB varied among the bacterial communities (Figure 10). The thickness of the surface deposits on 99 Cu
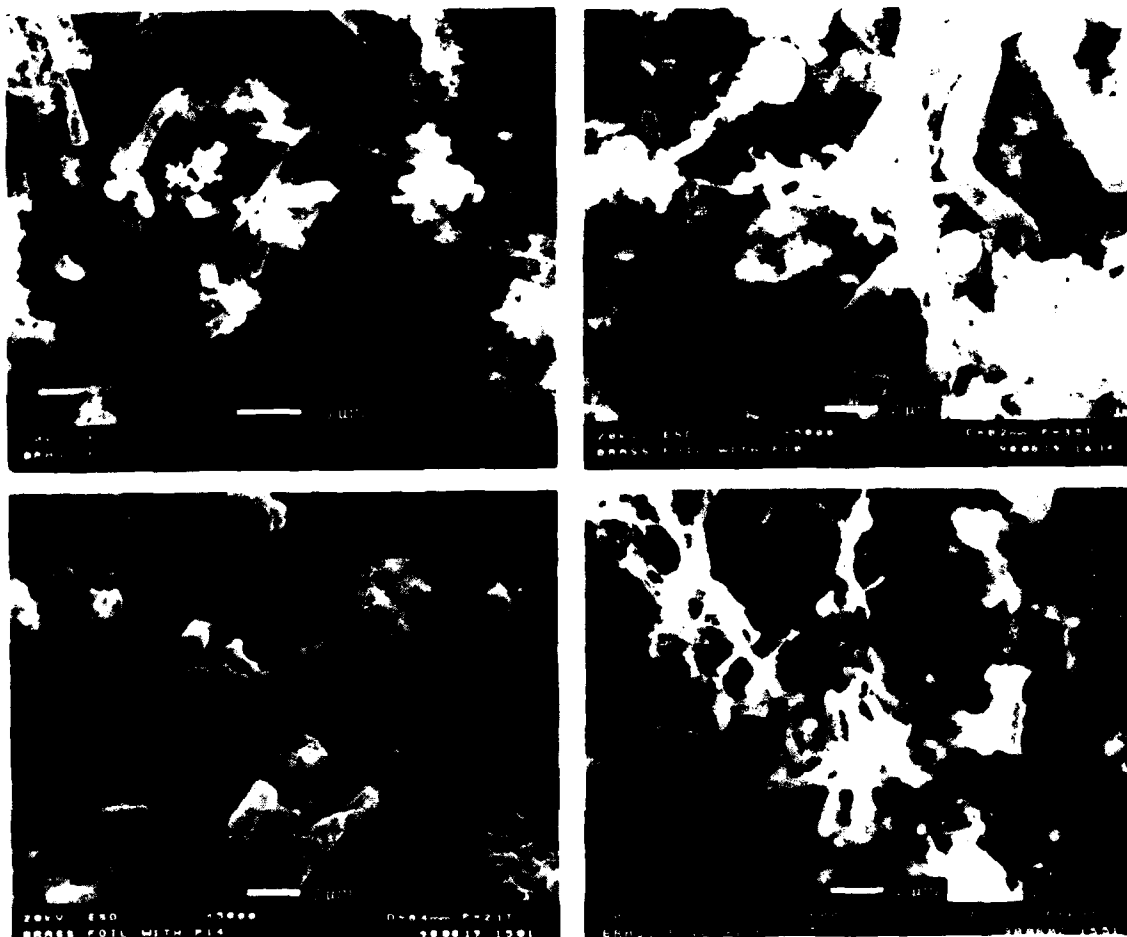
Figure 9. ESEM micrographs of three different mixed microbial communities containing SRB on brass foils.

Film Thickness
(6 µm)

Coupon Edge
(Thickness of
Base Metal
120 µm)

Biofilm Thickness
(8 µm)

Coupon Side
Edge
(60 µm)

139

Figure 10. Edge view of 99 Cu foil before exposure (coupon edge thickness of 120 microns) and edge view of 99 Cu foil after four-month incubation with marine, mixed culture III containing SRB (coupon edge thickness of 60 microns).

varied among the SRB cultures (see Table 2), but the sulfide layers on 99 Cu were consistently nonadherent, with much of the deposits sloughing off into the growth medium. Sulfide corrosion products on copper alloys were more

Table 2. Thickness of Copper Foils and Sulfide Layers After 4-Month Incubation

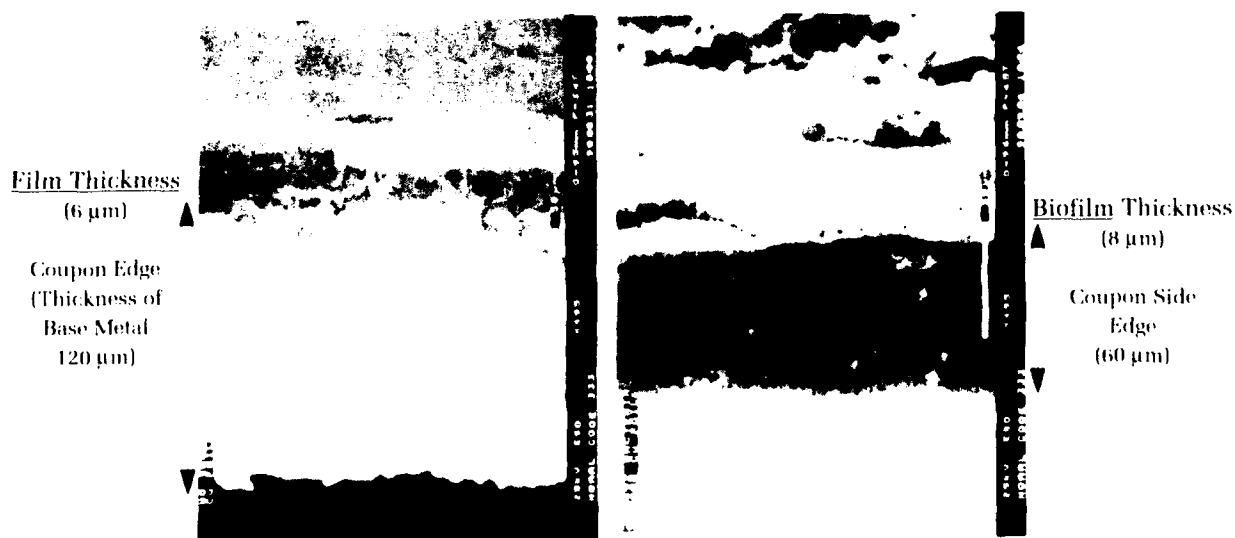| Copper Foils	Thickness of Base Metal (microns)	Thickness of Sulfide Layer (microns)
Sterile, Unexposed	128	0
Medium - NaCl	120	6
Medium + NaCl	110	12
Culture I	100	3-5
Culture II	80	6
Culture III	60	8
Culture IV	65	6
Culture V	80	6
Culture VI	70	4

adherent, while the sulfide layers on brass were thin and difficult to scrape from the surface. In all cases, bacteria were closely associated with the sulfur-rich deposits and many bacteria were encrusted with deposits of copper sulfides (data not shown). Table 3 is a summary of the elemental composition of 90 Cu:10 Ni and 70 Cu:10 Ni before and after colonization by cultures II and VII. The sulfide

layers were enriched in iron and nickel for both alloys, while the biofilm on 90 Cu:10 Ni contained elevated amounts of manganese.

Aerobic Bacterial Corrosion Studies

After three days in the minimal glutamate medium, the Cu-tolerant bacterium was used to inoculate the electrochemical cells. Fewer bacteria attached to 316 stainless steel and to nickel 201 discs compared to 99 Cu discs. The bacteria that were attached to the 99 Cu discs produced copious amounts of extracellular polymer. No localized corrosion was observed on the copper surface. The electrochemical data for copper in sterile artificial seawater, in sterile glutamate medium, and in the bacterial culture is shown in Table 4. E_{corr} increased by 145 mV within 37 days after bacteria were added, and a fivefold increase in corrosion rate was measured. There was not a significant change in Tafel constants when the discs were exposed to bacteria.

For evaluating the metal-binding capacity of the Cu-tolerant bacterium and its exopolymers, the bacteria were allowed to colonize glass slides in the presence of corroding metal discs. The EDS data for the elements concentrated on the glass slides indicate that the Cu-tolerant bacterium and its exopolymers are capable of

Table 3. Weight Percent of Elements as Determined by EDS Analyses

	90/10 Base Metal	90/10 Colonized with Culture II	90/10 With Biofilm Removed	70/10 Base Metal	70/30 Colonized with Culture VII	70/30 Under Biofilm
Si		0.67			0.69	
P		0.61			0.68	
S		7.44	14.57	0.006	11.06	9.31
Mn	0.5	0.92	0	0.78		
Fe	1.4	25.95	5.48	0.51	15.82	3.83
Ni	9.6	20.06	2.91	29.43	28.78	15.46
Cu	88.2	44.34	77.03	69.09	42.97	71.41
Zn	0.1			0.02		

Table 4. Electrochemical Corrosion Data for 99 Cu Exposed to Aerobic, Marine Bacteria

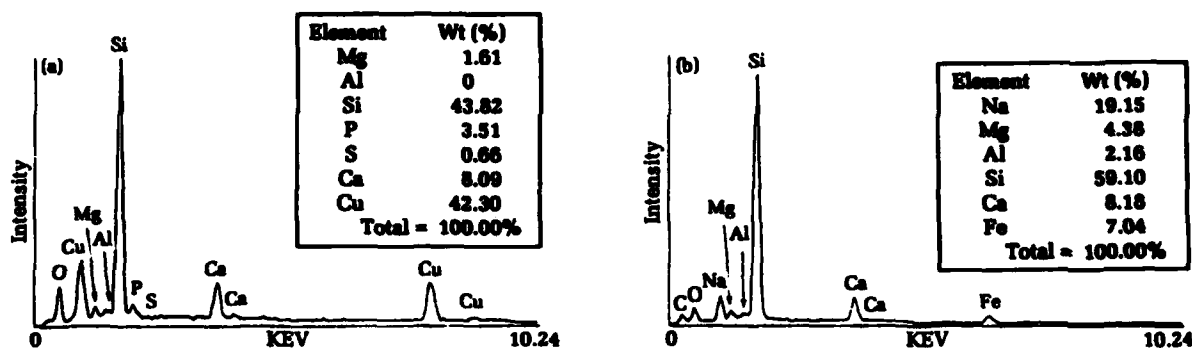|	3.5% Sterile Seawater (5 Days)	Sterile, Artificial Seawater/Glutamate (5 Days)	Artificial Seawater/ Glutamate and Bacteria 9 Days	Artificial Seawater/ Glutamate and Bacteria 37 Days
B_a (mV)	30.9	19.2	22.6	18.9
B_c (mV)	34.1	25	32.4	26.1
I_{corr} (uA/cm^2)	0.84	0.53	1.9	2.7
E_{corr} (mV SCE)	-327	-374	-283	-229
R_p (ohm-cm^2)	8418	7704	2722	582
pH	8	8.2	6.6	8.2

140

Figure 11. EDS spectra showing copper (a) and iron (b) uptake from solution.

binding copper and iron from solution (Figure 11). In a separate experiment, solutions from flasks with copper discs exposed to glutamate growth medium without bacteria and to the same media with Cu-tolerant bacteria were examined by atomic absorption spectroscopy. The data showed that copper solution concentrations were higher (430 ppm) in abiotic glutamate medium (no bacteria added) compared to the same medium with the Cu-tolerant bacterium (10 ppm). The copper removed from the corroding disc surface was bound within the biofilm.

Discussion

Copper alloys prevent or retard the settlement of macrofouling species such as barnacles and mussels.[27-29] However, bacteria, microalgae, protozoa, and their cellular exudates form a slime layer on copper-containing surfaces.[30,31] Marszalek et al.[32] documented that copper fouled at a slower rate than stainless steel and glass surfaces, that fungi were conspicuously absent on copper surfaces, and that diatoms appeared only after copper surfaces were covered with a microfouling layer of bacteria/extracellular polymer. There are some microorganisms that survive elevated levels of copper by using detoxification mechanisms such as extracellular complexation[33] and intracellular complexation.[34] Copper is strongly bound by organic material;[35,36] therefore, organic-complex formation is an important factor in determining the toxicity of the metal in aquatic environments. The aerobic marine bacterium *Vibrio alginolyticus* responds to copper added during logarithmic growth with a lag in growth proportional to the amount of copper added.[37] During the lag period, copper-inducible compounds with molecular masses of about 26 kDa and 28 kDa are produced, and these compounds bind copper extracellularly.[37,38]

A thick biofilm of copper-tolerant marine bacterium was present on copper-containing surfaces. The EDS data (see Figure 11) and the atomic absorption data described above demonstrate that this copper-tolerant bacterium can bind metal from solution as well as from a corroding substratum. Electrochemical measurements showed a fivefold increase in the corrosion rate of copper in the presence of this copper-tolerant bacterium. Geesey et al.[18] have demonstrated that bacterial exopolymers promoted deterioration of metallic copper and exhibited saturation binding of copper ions in aqueous solutions. Microcolonies within a biofilm could form copper concentration cells with adjacent areas in the biofilm that contain less reactive polymer, thereby promoting deterioration of copper surfaces. From the experiments described here, it is not possible to verify how the copper is bound by the bacterium and its exopolymers.

Corrosion can range from highly uniform to highly localized. Pitting in predominately copper alloys has been attributed to under-deposit attack. Under-deposit corrosion is extremely important for these alloys because it initiates a series of events that are individually or collectively extremely corrosive.[4] In the two case studies reported here, SRB were isolated from localized deposits associated with pits. SRB, a diverse group of anaerobic bacteria, can be isolated in many anaerobic habitats, but their principal habitat is the marine environment where the concentration of sulfate in seawater is high (typically 2 gm L^{-1}) and fairly constant.[39] Seawater piping systems have high surface areas at which nutrients can concentrate, predisposing these systems to biofilm formation.[40] Once a biofilm reaches a thickness of 200 um, the metal/biofilm interface can become anaerobic and provide a niche for sulfide production by SRB.[41]

The impact of sulfides on the corrosion of copper alloys has received a considerable

141

amount of attention. Little et al.[42,43] documented localized corrosion of copper alloys by SRB in estuarine environments. In the case reported here, EDS spectra for the pitted CDA 706 indicate that the nickel had been selectively removed from the alloy in the presence of SRB. A detailed discussion of mechanisms for selective attack and dealloying has been addressed by Schreir.[4]

Because the pitting potential of Monel is 20 mV to 30 mV below the open circuit potential, Monel has a tendency for the initiation of pitting in chloride-containing environments where the passive film can be disturbed. Under stagnant conditions, chlorides can penetrate the passive film at weak points, causing pitting attack. Sulfides can cause either a modification of the oxide layer as for copper or a breakdown of the oxide film of Ni-based alloys. Pit initiation and propagation depend on the depth of exposure, temperature, and presence of surface deposits.[8,9,11] Gouda et al.[11,12] demonstrated pitting of Monel 400 tubes exposed in Arabian Gulf seawater. Pits developed under deposits of SRB and nickel had been selectively dealloyed.[11,12]

In the case reported here, biocorrosion of the Monel 400 tube was characterized by pit formation under blisters containing SRB. Differential aeration cells appear to have been created, with low concentration of oxygen immediately underneath the deposits, which creates an anaerobic environment for SRB. The surface area under the deposit becomes anodic and corrodes while the electrons that are generated react at the cathodic region of high oxygen concentration. Chlorine and sulfur had accumulated within the pit and had reacted with the iron and nickel in the alloy. There was a selective leaching of nickel from the alloy, leaving a spongy, copper-rich material in the base of the pit.

ESEM offers a nondestructive method for observing the activity of microbial biofilms. Scientists at the Naval Research Laboratory Detachment (NRL Det.) were the first investigators to use ESEM to evaluate aerial coverage, topography, and microbiological and chemical composition of marine biofilms on metal surfaces. Much of the data on biofilm formation and chemical composition have been generated using traditional SEM/EDS analyses which result in preparation artifacts. ESEM allows one to examine wet biofilms on surfaces taken directly from liquid medium without any sample preparation. Also, EDS analysis can be performed at the same time the sample is being viewed and photographed.

This article contains photographs from wet biofilms of the same marine, mixed culture on copper foil and brass foil. Experiments are ongoing in our laboratories to compare wet

biofilms using ESEM/EDS analyses with biofilm images and EDS analyses obtained after sample fixation and dehydration. Several marine mixed cultures and a non-marine mixed culture were incubated with copper foil, brass foil, 90:10 copper-nickel, and 70:30 copper-nickel. The data obtained from these studies will provide a more accurate image of natural biofilms on metal surfaces, including the amount of polymer-bound metals in the biofilms.

Summary

Alloying iron and nickel into copper alters the corrosion product and improves corrosion resistance. Microbiologically produced sulfides appear to react preferentially with nickel and iron in copper alloys. Therefore, any benefit these alloying constituents provide to the corrosion protection of the alloy are lost in the presence of SRB where selective dealloying is suggested.

ESEM/EDS offer a nondestructive method for imaging wet biofilms on surfaces taken directly from liquid medium without any sample preparation. ESEM/EDS studies of copper and brass foils showed a diverse assemblage of microbes colonizing these surfaces, as well as the chemical composition of the wet biofilm/corrosion layers.

An aerobic, copper-tolerant bacterium (isolated from a Cu-containing marine coating) produced large amounts of extracellular polymer that had metal-binding ability. Biofilms of this microbe resulted in a fivefold increase in the corrosion rate of Cu metal. The corrosion appeared to be uniform, with no localized attack. The increased corrosion rate accompanied by an increased E_{corr} suggests that the enhanced corrosion rate is mainly due to an acceleration of the rate of the cathodic reaction which might involve the Cu^{2+}/Cu^{+} couple. There is also the possibility that the exopolymers are acidic, thereby promoting the deterioration of copper.

Acknowledgments

References

1. Bates, J. F. and Popplewell, J. M., "Corrosion of Condenser Tube Alloys in Sulfide Contaminated Brine," *Corrosion*, Vol. 31, 1975, pp. 269-275.
2. Tipton, D. G. and Kain, R. M., "Effect of Temperature on the Resistance to Pitting of Monel Alloy 400 in Seawater," *Proceedings of Corrosion80*, Paper No. 36, National Assoc. Corrosion Engineers, Houston, TX, 1980.
3. Friend, W. Z., *Corrosion of Nickel and Nickel-Based Alloys*, John Wiley & Sons, Inc., New York, NY, 1980.
4. Schreir, L. L., *Corrosion. Vol. 1 Metal/Environment Reactions*, Newnes-Butterworths, London, 1977.
5. Sato, S. and Nagata, K., "Factors Affecting Corrosion and Fouling of Condenser Tubes of Copper Alloys and Titanium," *Light Metal Technical Reports*, 1978.
6. LaQue, F. L., *Marine Corrosion: Causes and Prevention*, John Wiley & Sons, Inc., New York, NY, 1975.
7. Fink, F. W. and Boyd, W. K., "Corrosion of Metals in Marine Environments," *DMIC Report*, Batelle Memorial Inst., Columbus, OH, 1972.
8. Maylor, J. B., "Corrosion Resistance of High Nickel Alloys in Sea Water," *Anti-Corrosion Methods and Materials*, Vol. 25, 1978, pp. 3, 5-9.
9. Southwell, C. R. and Alexander, A. L., *Corrosion of Metals in Tropical Environments, Part 8. Nickel and Nickel-Copper Alloys: Sixteen Years Exposure*, Naval Research Laboratory, NRL Report 6592, Washington, DC, 1967.
10. Stover, H. E., "Premature Failure of Copper-Nickel Alloys in Sea Water," *Corrosion*, Vol. 17, 1961, pp. 461t-462t.
11. Gouda, V. K., et al., "Microbial-Induced Corrosion of Monel 400 in Seawater," *Corrosion/90*, Paper No. 107, National Assoc. Corrosion Engineers, Houston, TX, 1990.
12. Gouda, V. K., et al., "Microbiologically Induced Corrosion of UNS NO4400 in Seawater," *Corrosion*, Vol. 49, 1993, pp. 63-73.
13. Pope, D. H., *MIC in U.S. Industries-Detection and Prevention*, Argentine-USA Workshop on Biodeterioration (CONICET-NSF), Aquatica Quimica, San Paulo, Brazil, 1985, p. 105.
14. Alanis, I., et al., "A Case of Localized Corrosion in Underground Pipes," in Dexter, S. C., Ed., *Biologically Induced Corrosion*, National Assoc. Corrosion Engineers, 1986, pp. 102-108.
15. Pope, D. H., *A Study of Microbiologically Influenced Corrosion in Nuclear Power Plants and a Practical Guide for Countermeasures*, Electric Power Research Institute, Palo Alto, CA, 1986.
16. Miller, J. D. A., *Microbial Aspects of Metallurgy*, American Elsevier Pub. Co., New York, NY, 1970
17. Pope, D. H., et al., "Microbiologically Influenced Corrosion of Industrial Alloys," *Materials Performance*, Vol. 23, 1984, p. 14.
18. Geesey, G. G., et al., "Role of Bacterial Exopolymers in the Deterioration of Metallic Copper Surfaces," *Materials Performance*, Vol. 25, 1986, pp. 37-40.
19. Bremer, P. J. and Geesey, G. G., "Laboratory-Based Model for Microbiologically Induced Corrosion of Copper," *Applied and Environmental Microbiology*, Vol. 57, 1991, pp. 1956-1962.
20. Ford, T., Black, J. P., and Mitchell, R., "Relationship Between Bacterial Exopolymers and Corroding Metal Surfaces," *Corrosion/90*, Paper No. 110, National Assoc. Corrosion Engineers, Houston, TX, 1990.
21. American Public Health Association, *Standard Methods for the Examination of Water and Wastewater*, 14th Edition, American Public Health Assoc., American Water Works Assoc., and Water Pollution Control Assoc., Washington, DC, 1975.
22. American Society for Testing and Materials, *Annual Book of ASTM Standards (Part 31)*, ASTM, Philadelphia, PA, 1978.
23. Strickland, J. D. H. and Parsons, T. R., *A Practical Handbook of Seawater Analysis*, J. C. Stevenson, Ed., Fisheries Board of Canada, Ottawa, Ont., Canada, 1968.
24. Pfenning, N., Widdel, F., and Truper, H. G., "The Dissimilatory Sulfate-Reducing Bacteria," M. P. Starr, et al., Eds., *The Prokaryotes: A Handbook on Habitats, Isolation and Identification of Bacteria*, Springer-Verlag, New York, NY, 1981, pp. 926-940.
25. Jones, J. M., Walch, M., and Mansfeld, F., "Microbial and Electrochemical Studies of Coated Steel Exposed to Mixed Microbial Communities," *Corrosion/91*, Paper No. 108, National Assoc. Corrosion Engineers, Houston, TX, 1991.
26. Wagner, P. A., Little, B. J., and Stiffey, A. V., "An Electrochemical Evaluation of Copper Colonized by a Copper-Tolerant Marine Bacterium," *Corrosion/91*, Paper No. 109, National Assoc. Corrosion Engineers, Houston, TX, 1991.
27. Roberts, D., "Mussels and Pollution," B. L. Bayne, Ed., *Marine Mussels: Their Ecology and Physiology*, Cambridge Univ. Press, London, UK, 1976.
28. Moreton, B. B. and Glover, T. J., "New Marine Industry Applications for Corrosion and Biofouling Resistant Copper-Nickel Alloys," Biologia Marina, *Proc. 5th International Congress on Marine Corrosion and Fouling*, Barcelona, Spain, 1980, p. 267-278.
29. Fischer, E. C., et al., "Technology for Control of Marine Biofouling – A Review," J. D. Costlow, and R. C. Tipper, Eds., *Marine Biodeterioration: An Interdisciplinary Study*, Naval Institute Press, Annapolis, MD, 1981, pp. 261-299.
30. Purkiss, B. E., *Microbial Aspects of Metallurgy*, American Elsevier Pub. Co., New York, NY, 1970.
31. Field, B., "Marine Biofouling and Its Control: History and State-of-the-Art Review," *Oceans '81 Conference Record: I*, Boston, MA, 1981.
32. Marszalek, D. S., Gerchakov, S. M., and Udey, L. R., "Influence of Substrate Composition on Marine Microfouling," *Applied and Environmental Microbiology*, Vol. 38, 1979, pp. 987-995.
33. Schreiber, D. R., Millero, F. J., and Gordon, A. S., "Production of an Extracellular Copper Binding Compound by the Heterotrophic Marine Bacterium *Vibrio alginolyticus*," *Marine Chemistry*, Vol. 28, 1990, pp. 275-284.
34. Olafson, R. W., "Physiological and Chemical Characterization of Cyanobacterial Metallothioneins," *Environmental Health Perspectives*, Vol. 65, 1986, pp. 71-75.
35. Leckie, J. O. and Davis, J. A., "Aqueous Environmental Chemistry of Copper," J. O. Nriagu, Ed., *Copper in the Environment, Part 1*, John Wiley & Sons, Inc., New York, NY, 1979, pp.89-121.
36. Mantoura, R. F. and Riley, J. P., "The Analytical Concentration of Humic Substances From Natural Waters," *Anal. Chim. Acta*, Vol. 76, 1975, pp. 97-106.

143

37. Schreiber, D. R., Gordon, A. S., and Millero, F. J., "The Toxicity of Copper to the Marine Bacterium *Vibrio alginolyticus*," *Canadian J. Microbiology*, Vol. 31, 1985, pp. 83-87.

38. Harwood-Sears, V. and Gordon, A. S., "Copper-Induced Production of Copper-binding supernatant proteins by the marine bacterium *Vibrio alginolyticus*," *Applied and Environmental Microbiology*, Vol. 56, 1990, pp. 1327-1332.

39. Battersby, N. S., "Sulphate-Reducing Bacteria," B. Austin, Ed., *Methods in Aquatic Bacteriology*, John Wiley & Sons Ltd, New York, NY, 1988, pp. 269-299.

40. Costerton, J. W., et al., "Bacterial Biofilms in Nature and Disease," *Annual Review of Microbiology*, Vol. 41, 1987, pp. 435-464.

41. Little, B., et al., "Electrochemical Behavior of Stainless Steels in Natural Seawater," *Corrosion/90*, Paper No. 150, National Assoc. Corrosion Engineers, Houston, TX, 1990.

42. Little, B., Wagner, P., and Jacobus, J., "The Impact of Sulfate-Reducing Bacteria on Welded Copper-Nickel Seawater Piping," *Materials Performance*, Vol. 27, 1988, pp. 57-61.

43. Little, B., et al., "Evaluation of Microbiologically Induced Corrosion in an Estuary," *Estuaries*, Vol. 12, 1989, pp. 138-141.

44. Little, B., Wagner, P., Ray, R., and Jones, J., "Microbiologically Influenced Corrosion of Copper Alloys in Saline Waters Containing Sulfate-Reducing Bacteria," *Corrosion91*, Paper No. 101, National Assoc. Corrosion Engineers, Houston, TX, 1991.

The Authors

JOANNE M. JONES-MEEHAN received a B.S. degree in education with a major in biological sciences and a minor in chemistry from Illinois State University, a master's degree in biological sciences from Illinois State University and a Ph.D. degree in microbiology from Iowa State University. She did a three-year postdoctoral research fellowship at the University of Michigan in microbiology/molecular biology. Since June 1988, Dr. Jones has worked at the White Oak Detachment in the Biotechnology Laboratory and she has been a group leader for the past three years. She has published twenty-nine papers. She is a member of the American Society for Microbiology (ASM), a recipient of the Young Investigator's Award in 1986 (from ASM at the Second International Conference on Streptococcal Genetics), and the recipient of the 1992 Washington Academy of Sciences Award for Outstanding Achievement in Biological Sciences.

BRENDA J. LITTLE received a B.S. degree from Baylor University in biology and chemistry and a Ph.D. degree from Tulane University in chemistry. For the past 16 years she has worked for the Department of the Navy, currently the Naval Research Laboratory Detachment at Stennis Space Center, Mississippi, in the area of microbiologically influenced corrosion. Dr. Little has published over 70 papers on this topic. She is a member of the American Chemical Society, the National Association of Corrosion Engineers, the Electrochemical Society, the Adhesion Society, Sigma Xi, and the Mississippi Academy of Sciences.

144

PATRICIA A. WAGNER received a bachelor's degree in biological sciences from Cornell University and a master's degree in statistics from the University of Southern Mississippi. She has been an oceanographer for 10 years with the U.S. Navy, now at the Naval Research Laboratory Detachment at the *Stennis Space Center, Mississippi,* where she has performed research in microbiologically influenced corrosion with over 40 publications. Ms. Wagner is a member of the National Association of Corrosion Engineers, American Society for Testing Materials, Sigma Xi, Mississippi Academy of Sciences, and the American Geophysical Union.

RICHARD I. RAY received his bachelor's of science degree in biology and chemistry from the University of Southern Mississippi in Hattiesburg in 1978. He has worked for the U.S. Navy, first as a contractor for three years and for the past nine years at the Naval Research Laboratory Detachment, Stennis Space Center, Mississippi. He has worked as a technician with several investigators and has co-authored 10 papers. He is the operator of the Naval Research Laboratory's environmental scanning electron microscope facility.

145

Radiation Hardness of New Thulium-Doped Calcium Sulfate Dosimeters

K. Chakrabarti, J. Sharma, V. K. Mathur, and R. J. Abbundi

Thulium-doped calcium sulfate is the thermoluminescent material of choice for the new personnel dosimetry system developed by the Dahlgren Division, the Navy's Lead Laboratory and Technical Direction Agent for radiation detection. This very sensitive material can easily be heated and read by using a carbon dioxide laser. Although this system is primarily being developed for low-level personnel dosimetry, it also has the potential for application to battlefield dosimetry. We are therefore investigating the integrity of this thermoluminescent material under high dose and high dose rate. X-ray photoelectron spectroscopy studies have shown that the material remains in its proper chemical state even after radiation doses up to the 10 gray (100 rad = 1 gray) range. In terms of robustness to radiation damage, only in the 10,000 gray dose range does the phosphor show partial decomposition.

Introduction

For some years now researchers and regulators alike have sought to improve the method of accurately measuring an individual's exposure to ionizing radiation. Most of these efforts in dosimetry focus on producing stable, sensitive thermoluminescent (TL) phosphors. These phosphor materials are capable of absorbing radiation and storing this energy by the creation and distribution of charge carriers. Heating the phosphors at a later time causes redistribution of charge carriers in the material, with subsequent release of stored energy in the form of light. The amount of light given off is proportional to the initial exposure to radiation.

The subject of dosimetry is of particular interest due to the unique environment in which the Navy operates. Because personnel assigned to nuclear-powered ships may be confined to those vessels for extended periods of time, the Navy maintains an extensive radiation detection and personnel protection program both aboard ships and in shipyards.

The White Oak Detachment of the Dahlgren Division is the designated Lead Laboratory and Technical Direction Agent for the Naval Sea Systems Command in the area of radiation detection. For well over a decade, this laboratory has played a major role in the calibration, standardization, and quality assurance of the Navy's personnel dosimetry system. In addition to these programs, we are involved in research, development, and testing of a new-generation dosimetry system based on rapid laser heating.

The work reported here deals with investigation of the properties of thulium (Tm^{3+}) doped calcium sulfate $(CaSO_4)$. Dysprosium (Dy^{3+}) or thulium (Tm^{3+}) doped calcium sulfate $(CaSO_4)$ is by now a well established thermoluminescence dosimetry material with a very desirable dosimetric peak at approximately 220°C. This peak is stable at room temperature and sensitive to low

146

radiation doses. Moreover, this material is quite suitable for heating by an infrared carbon dioxide laser through strong photon-phonon coupling. Thus, thulium-doped calcium sulfate is the phosphor of choice for the Navy's state-of-the-art personnel dosimetry system, currently under full-scale development. Although the system is intended primarily for personnel dosimetry, it is considered desirable that it also have the potential of performing battlefield dosimetry. Therefore, it is important to investigate the integrity of this TL material under high dose and high dose rate.

Although these materials are considered to be among the best for personnel dosimetry, ambiguity still exists about the mechanism of TL emissions and the nature of charge trapping. Besides the dosimetric peak, there exist two low-intensity, lower-temperature peaks at approximately 80°C and 120°C. There is also a higher temperature peak observed[1,2,3,4] near 300°C. Several investigators have attempted to identify the origins of these TL peaks. Hazimura et al.[1] have attributed the 300°C peak to hypersulfite (SO_5^-) radicals, and the 120°C and 220°C peaks to sulfate (SO_4^-) and sulfite (SO_3^-) radicals, respectively. Nambi et al.[5] also observed electron spin resonance (ESR) signals from SO_4^-, SO_3^-, and O_3^- radicals. Morgan and Stoebe[2] have suggested that the TL peak at ~200°C is due to the release of the first hole from the center with two trapped holes, and the peak ~300°C is due to the release of the second hole from the same center. Las et al.[6] considered a V$^-$ center as a deep trap and a V^0 center as a shallow trap. (V$^-$ indicates a positive ion vacancy holding a positive charge, thus the term "deep trap center." V^0, a "shallow trap center," has two units of positive charge.) A V-type center[7,8] consists of a cation vacancy with a hole trapped in it, the hole being shared by the adjacent anions. Exposure to ionizing radiations such as γ rays and x-rays produces electron hole pairs. The holes trapped at the cation vacancies and shared by the adjacent SO_4 ions form V-type centers. The cation vacancies are formed in the lattice for charge compensation when the trivalent ions as Dy^{3+} or Tm^{3+} replace the divalent Ca^{2+} ions.

In well established V-type centers in magnesium oxide (MgO), a cation vacancy and the adjacent oxygen (O$^-$) ion form a V$^-$ center with a configuration[9]: O^{2-} - [Mg vacancy] - O$^-$. The O$^-$ ions are paramagnetic, and ESR signals are observed from these centers.[10] Hazimura et al.[1] and Nambi et al.[5] observed ESR signals from SO_4^- ions in $CaSO_4$, which by definition appear to be similar to V-type centers observed by Las et al.[6] However, they also reported formations of other radicals. We investigated Tm^{3+} doped $CaSO_4$ by x-ray photoelectron spectroscopy

(XPS), which revealed the partial decomposition of $CaSO_4$ at a high x-ray dose and the formation of sulfite, thiosulfate, and some sulfide. The decomposition is clearly evidenced by the development of structure in the core levels of the XPS spectra of sulfur. Also, new peaks appear and grow in the valence-level spectra. The highest occupied state shows structure and broadens towards smaller binding energy, indicating that the band gap has decreased. This indication is accompanied by a sharp increase in the optical absorption spectrum at a wavelength of 225 nanometers (nm), and the material begins to exhibit ultraviolet (UV) induced thermoluminescence.

Experimental

$CaSO_4$:Tm in fine powder form was obtained from Teledyne Isotopes, Inc. Samples in the form of pellets were prepared by pressing the powder at 5000 psi in a hydraulic press and sintering at a temperature of approximately 1000°C in air for 12 to 20 hours. A cesium[137] (Cs^{137}) source with a dose rate of 20 gray (gy) per hour was used for γ irradiation. TL glow curves were recorded with a Harshaw Reader 4000 with an X-Y recorder attached to its output. The heating rate was 2°C/S^{-1}. Optical absorption measurements were made by the technique of diffuse reflectivity between wavelengths of 220 nm to 800 nm using a Varian 2300 spectrophotometer. The sensitivity of the diffuse reflecting barium sulfate ($BaSO_4$) coated sphere restricts measurements to wavelengths above 220 nm. The XPS spectra were investigated by using a Kratos ES 300 instrument without an x-ray monochromator. For the study of radiation damage, the x-ray source of the XPS instrument (15 KV, 12 ma) was used to irradiate the material. It provided a dose rate of 4 Kgy per minute. As the material did not easily show radiation damage, rather high doses (up to 37.2 Mgy) were used to follow the changes. A control XPS spectrum is defined as the spectrum prior to radiation damage, i.e., when the exposure level is below 0.03 gy.

Experimental Results

Figure 1 shows a sequence of TL glow curves from a single sintered sample of $CaSO_4$:Tm. Curve 1 represents the glow curve measured from 40°C to 360°C after the sample is exposed to an unfiltered mercury (Hg) lamp for one minute. After the first glow curve measurement, the sample was γ irradiated at a dose of 0.30 gy and the TL glow curve was measured, as shown by curve 2. The sample was then

147
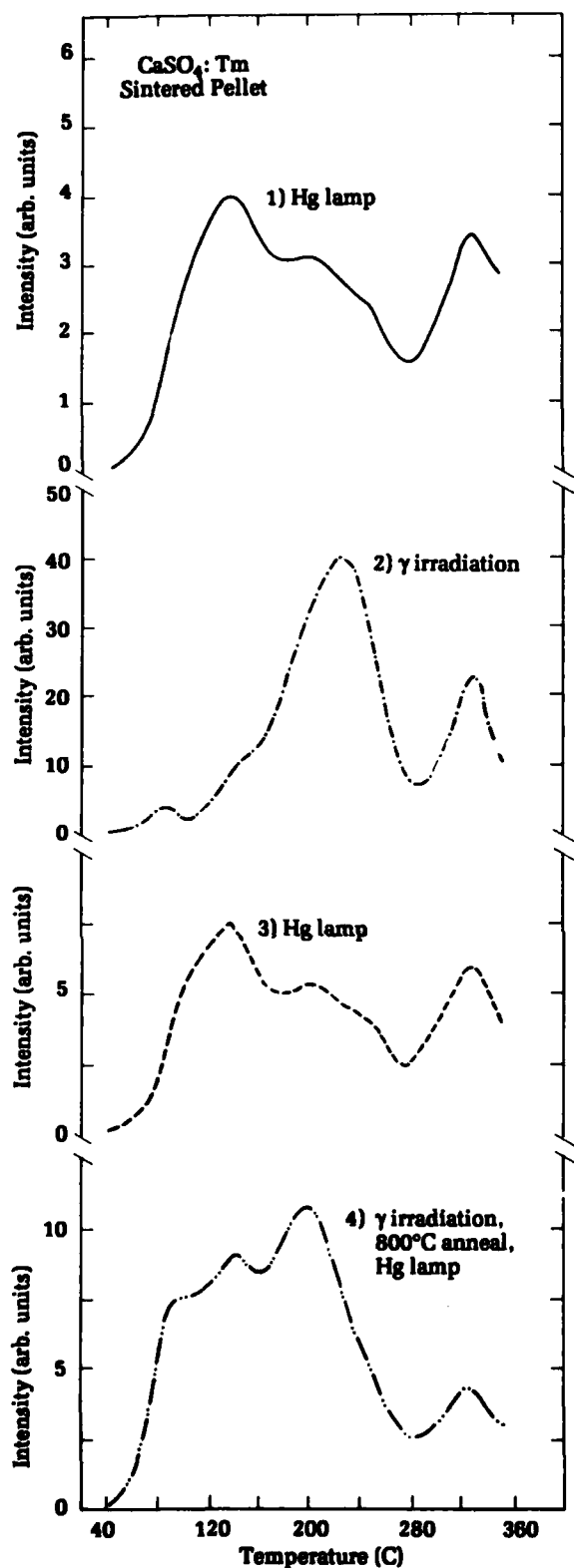
Figure 1. A sequence of thermoluminescence spectra observed at a temperature range 40°C - 360°C from the same sintered sample of CaSO$_4$:Tm following: (1) exposure to an Hg lamp, (2) gamma irradiation, (3) exposure to an Hg lamp, (4) gamma irradiation, an 800°C anneal, and exposure to an Hg lamp.
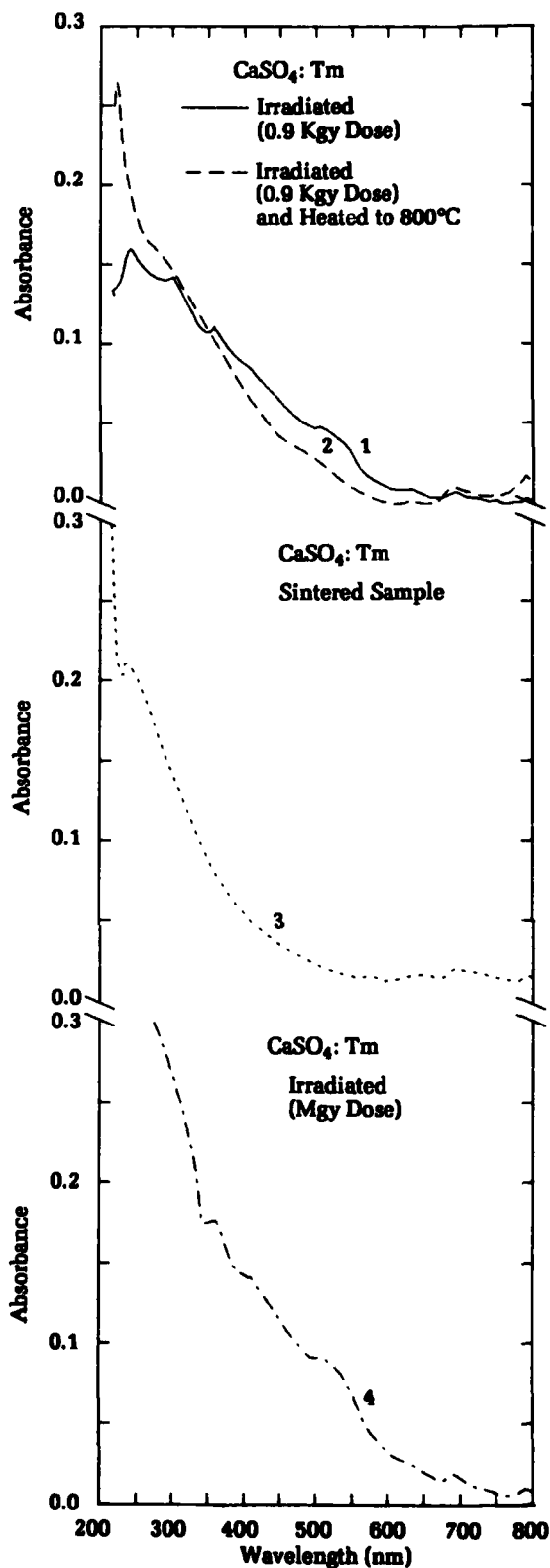
Figure 2. Optical absorption spectra of CaSO$_4$:Tm. Curve 1 is for γ irradiated (<1 Kgy dose) powder sample and Curve 2 is for the same powder sample after it is annealed to 800°C following γ irradiation. Curve 3 is for the sintered sample, and Curve 4 is for the heavily γ-irradiated (Mgy dose) powder sample.

exposed to the unfiltered Hg lamp again for one minute, and the results shown in curve 3 were observed. Finally, the sample was γ irradiated at a dose of 0.30 gy, annealed to 800°C for half an hour, and then exposed to the Hg lamp for one minute. The result is seen in glow curve 4.

The TL glow curves of sintered CaSO₄:Tm (Figure 1) show a TL peak at approximately 300°C, which can be generated only by UV light. Shinde et al.[11] observed that γ radiation of $CaSO_4$:Dy produces TL peaks as high as ~420°C and 520°C. They also observed that UV light phototransfers charge carriers from the traps responsible for the 420°C and 520°C TL peaks to the 220°C dosimetric peak. In order to avoid the phototransfer process, we annealed the material to 800°C following γ irradiation. The sample was then exposed to UV light. The TL peak at approximately 300°C was still observed (curve 4). This indicates that in sintered $CaSO_4$:Tm. UV light can produce the ~300°C TL peak. Both glow curves 1 and 4 were generated by UV light. However, curve 3 might be due to a combination of the UV-generated TL glow curve plus a contribution from the phototransfer process.

Figure 2 shows the optical absorption spectra of $CaSO_4$:Tm. Curve 1 represents the powder sample after being γ irradiated with a dose of 0.9 Kgy. A weak absorption peak at approximately 240 nm is observed. This peak shifts to a lower wavelength at ~230 nm, and sharply increases when this γ irradiated sample is heated at 800°C for half an hour (curve 2). Curve 3 represents the optical absorption spectrum of the unirradiated sintered sample. In this sample, the absorption band continues to grow at 220 nm, the minimum wavelength we could scan using the diffused reflecting sphere.
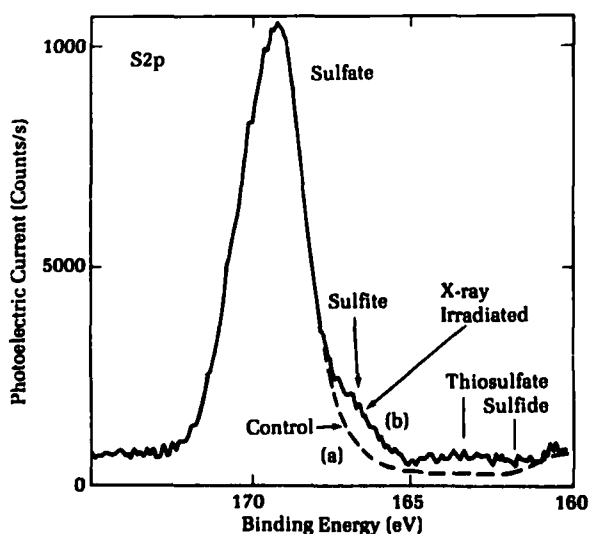
Evidently, this absorption band is further peak-shifted to a lower wavelength. A similar absorption spectrum with absorbance >3.0 in the UV region is observed in a powder sample irradiated by x-ray at a high dose (1 Mgy). Upon observing this pattern in the optical absorption spectra, we conclude that the heat treatment and radiation damage causes this material to absorb in the UV region of about 6 eV. Our further study of x-ray photoelectron spectra confirmed this view. The results of XPS studies also helped us to understand the mechanism leading to the increase in the absorption band in the UV region, and consequently the 300°C peak generated by the UV light. This peak was not observed in unsintered powder $CaSO_4$:Tm, as reported earlier.[4]

Figure 3 shows the sulfur (2p) core level from XPS spectra of (a) a control sample and (b) a heavily irradiated sample (1 Mgy) of $CaSO_4$:Tm powder. The development of three small peaks on the right-hand side of the main peak is evidence of new products from radiation damage. Based on the results of Prins[12,13] and Novakov,[12] these peaks are interpreted to arise from the decomposition of sulfate into sulfite, thiosulfate, and sulfide. In order to show the trend of the decomposition, a series of such measurements was made with doses up to 37.2 Mgy; the results are shown in Figure 4. It is obvious that even at the massive 37.2 Mgy dose, no more than 10 percent of the material is affected. In fact, at a dose of 0.1 Mgy, no sign of decomposition was observed. Thus, the $CaSO_4$:Tm powder is very resistant to radiation damage. Generally this type of dosimeter is used for measuring irradiation that is a hundred million times smaller than 1 Mgy.

The above results are upheld by the changes in the valence-band region of the XPS spectra. Figure 5 shows the growth of a new peak at 6 eV in a heavily irradiated (37.2 Mgy) sample. Thus, the changes experienced by the core levels of the atoms due to chemical alterations are also reflected in the valence band.
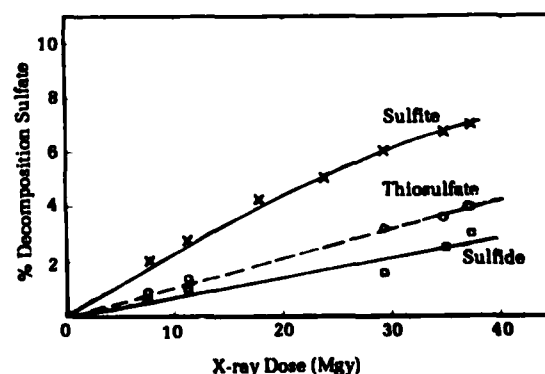

Figure 3. X-ray photoelectron spectrum of the sulfur (2p) core level in (a) control and (b) x-ray damaged $CaSO_4$:Tm.

Figure 4. Percent decomposition of sulfate into sulfite, thiosulfate, and sulfide as a function of x-ray dose.

149

The XPS study of the valence-band region has also provided an explanation of the increased optical absorption in the 220-nm region. As mentioned earlier, sintering at excessively high temperature causes an increase in the optical absorption spectrum at 220 nm, as shown by curves 3 and 4 in Figure 2. XP spectrum of the valence-band region of the sintered material (Figure 6) gives a peak at 6 eV in the XP spectrum, similar to that caused by x-ray irradiation as seen in Figure 5. It can be concluded from the work described above that sintering causes damage to the material similar to that of high-dose x-rays. During preparation of the samples, excessive heating is to be avoided.

Conclusion

The current work has demonstrated that $CaSO_4$:Tm is an excellent material to be used in dosimetry. As is well known, it is sensitive and reliable for measuring radiation doses over a wide range. In terms of susceptibility to radiation damage, it is also quite robust. In these experiments, no signs of any decomposition were observed up to 0.1 Mgy dose, which is a few million times larger than doses generally encountered. The material shows significant radiation damage only above 1 Mgy, when the sulfate begins to partially break up into sulfite,

thiosulfate, and sulfide. The current work also provides an explanation of the optical absorption in the 220-nm range seen in some samples. This phenomenon arises from sintering at excessively high temperature, which should therefore be avoided in sample preparation. It is therefore concluded that, when exposed to a surface warfare environment, $CaSO_4$:Tm would not lose its integrity as a dosimetric material.

References

1. Hazimura, R., Asahi, K., and Takenaga, M., "An ESR Study of Thermoluminescent Process in $CaSO_4$ Phosphors," Nucl. Instrum. Methods 175, 1980, pp. 8-9.

2. Morgan, M. D. and Stoebe, T. A., "Thermoluminescent Mechanism in $CaSO_4$:Dy Single Crystals," Radiat. Prot. Dosim., 17, 1986, pp.455 - 458.

3. Drazic, G. and Trontelj, M., "Properties of Sintered $CaSO_4$-Dy Dosimeters," Radiat. Prot. Dosim. 6, 1984, pp. 344-346.

4. Chakrabarti, K., Mathur, V. K., Abbundi, R. J. and Hill, M. D., "UV Induced Trapping in Powder and in Sintered $CaSO_4$:Tm and $CaSO_4$:Dy," Radiat. Prot. Dosim. 33, 1990, pp. 35-38.

5. Nambi, K. S. V., Bapat, V. N., and Ganguly, A. K., "Thermoluminescence of $CaSO_4$ Doped with Rare Earths," J. Phys. Chem. 7, 1974, pp. 4403-4415.

6. Las, W. L., Mathews, R. J., and Stoebe, T. G., "Mechanisms of Thermoluminescence in MgO and $CaSO_4$," Nucl. Instrum. Methods 175, 1980, pp. 1-3.

7. Hughes, A. E. and Henderson, B., Point Defects in Solids, Ed. J. H. Crawford and L. Slifkin (New York, Plenum Press, 1972), pp. 381-490.

8. Chakrabarti, K., Mathur, V. K., Thomas, L. A., and Abbundi, R. J., "Evidence of V⁻ Centere in Rare Earth Doped MgS," Phys. Rev. B 38, 1988, pp. 10894-10896.
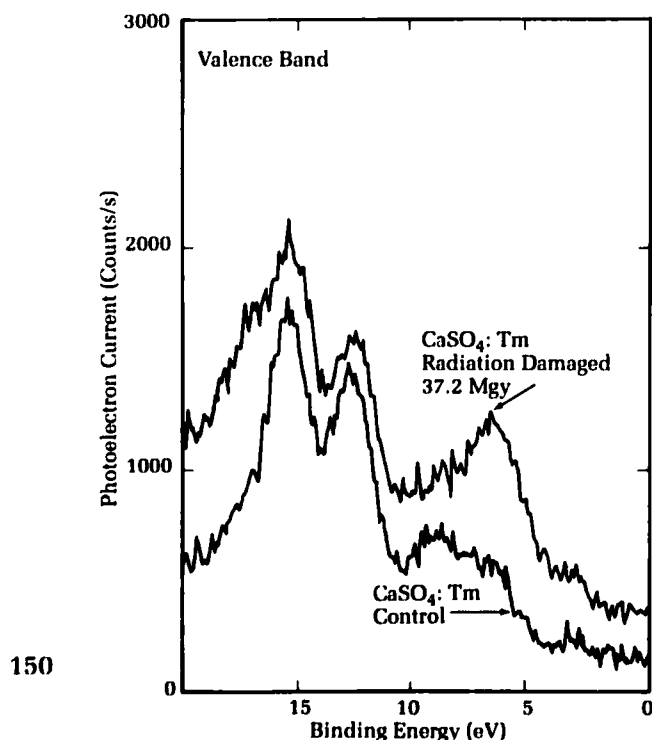
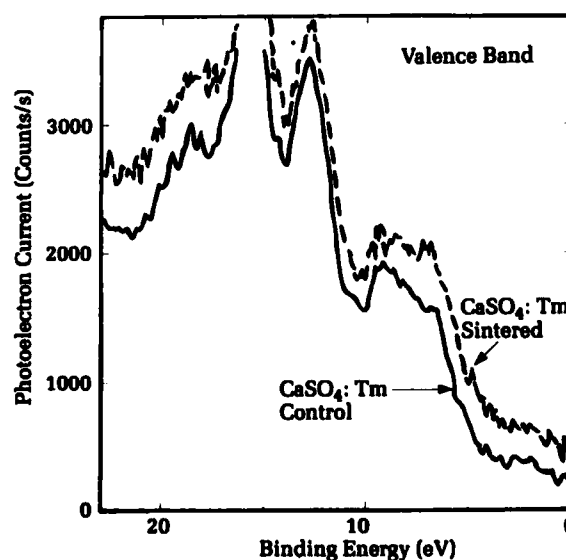**Figure 5.** Valence band XPS spectra of control and radiation damaged powder phosphor of $CaSO_4$:Tm.

Figure 6. Valence band XPS spectra of control and sintered phosphor of $CaSO_4$:Tm showing changes in the valence region similar to those caused by radiation damage, but to a much smaller extent.

150

9. Chen, Y. and Abraham, M. M., "Trapped Hole Centers in Alkaline Earth Oxides," *J. Phys. Chem. Solids,* 51, 1990, pp. 747-764.

10. Wertz, J. E., et al., *Interaction of Radiation with Solids,* Ed. A. Bishay (Plenum Press, N.Y.), 1967, pp. 617-627.

11. Shinde, S. S., et al., "Photo-transfer Thermoluminescence in CaSO$_4$:Dy - Grain Size Dependence," *Nucl. Instrum. Methods* B31, 1988, pp. 592-596.

12. Prins, R. and Novakov, T., "X-ray Photoelectron Spectra and Molecular Orbital Interpretation of the Valence Band Region of CLO$_4^{-1}$ and SO$_4^{-2}$," *Chem. Phys. Lett.* 9, 1971, pp. 593-596.

13. Prins, R., "Intensities in the X-ray Photoelectron Spectra and Electronic Structure of the Oxyions of Si, P, S, Cl, Mn and Cr," *J. Chem. Phys.* 61, 1974, pp. 2580-2591.

The Authors

KISHALAYA CHAKRABARTI received a Ph.D. in physics from Oklahoma State University in 1984, and served as an assistant professor of physics at Southwestern Oklahoma State University from 1984 to 1989. Since 1987 he has worked at the White Oak Detachment as a consultant research physicist. In the field of radiation defects in solids and spectroscopy of laser materials, he has published and presented more than 75 papers and holds two U.S. patents. He is a member of Phi Kappa Phi and *Sigma Pi Sigma* honor societies and was on the National Dean's List, 1983-84. He is a member of the American Physical Society, the Health Physics Society, and the Materials Research Society.

JAGADISH SHARMA received a Ph.D. in physics (1953) from Calcutta University, India. He served on the faculty of the Indian Institute of Technology, was a research associate at Princeton University and Brookhaven National Laboratory, and a Research Fellow with the National Research Council of Canada. He has worked on defects in solids and on radiation damage, especially in explosives and propellants. Formerly with Picatinny Arsenal, Dr. Sharma was the first to apply the techniques of x-ray photoelectron spectroscopy (XPS) to examine explosives and propellants. At White Oak since 1981, his work has provided the first determination of the chemical nature of "hot spots," which sensitize explosives and propellants and make them too dangerous to handle. His results opened up the possibility of detecting sensitized explosives from normal batches so that accidents can be prevented. He has received special awards for applying XPS to difficult explosives-related investigations, including the La Guardia Bombing incident and an Army-Navy proximity fuze failure.

VEERENDRA K. MATHUR is a senior research physicist in the Radiation Dosimetry Group. Since joining the White Oak Detachment in 1982, he has performed basic research on optical properties of thermoluminescent dosimeters. Currently, he is project manager for the development of a state-of-the-art laser-heated thermoluminescence dosimetry system for the Navy. The project, sponsored by the Naval Sea Systems Command and now in full-scale development, is intended to replace the personnel dosimetry system for the nuclear-propulsion Navy. This system is also capable of environmental and accidental dosimetry. Dr. Mathur received his M.S. degree from Agra University, India, in 1955 and a Ph.D. from Saugor University, India, in 1963. He was on the faculty of Kurukshetra (1963-82) and Saugor University (1961-63) in India and visited the U.K. as a Commonwealth Academic Staff Exchange Fellow in 1975-76. He came to White Oak from the University of Maryland. His research interests include interaction of ultra-short optical pulses with solids, luminescence, and optical properties of non-linear materials.

RAYMOND J. ABBUNDI received a Ph.D. in physics from The American University in 1976 and began his career at White Oak upon graduating. His research has encompassed several different areas centering around experimental investigations of the fundamental properties of solids. These include the magnetic and magnetoelastic interactions in rare earth intermetallic compounds, electronic transport properties of semiconductors, and his current area of interest, luminescence properties of dosimetric materials. He has been examining the fundamental optical properties of phosphors in an effort to develop more sensitive, stable, long-life dosimeters. Dr. Abbundi also supervises the calcium fluoride quality assurance dosimetry program for the Naval Sea Systems Command. This program maintains the integrity of the entire gamma radiation detection system for Navy personnel. This requires certifying the accuracy of those dosimeters used to calibrate instrumentation in the fleet and those used to monitor exposure to individuals. He has co-authored numerous publications for the scientific literature and for presentation at international conferences.

151